Enhancing the confidence in estimates of effective radiative forcing by aerosol through improved global modelling

Inger Helene Hafsahl Karset

Dissertation for the degree of Philosophiae Doctor (PhD)

Section for Meteorology and Oceanography

Department of Geosciences

University of Oslo

November 2019

Series of dissertations submitted to the
Faculty of Mathematics and Natural Sciences, University of Oslo
No. 2224

ISSN 1501-7710

Cover: Hanne Baadsgaard Utigard.
Print production: Reprosentralen, University of Oslo.

:Preface

This synthesis and collection of papers are submitted for the degree of pilosophiae doctor (PhD) in atmospheric physics and chemistry at the Section for Meteorology and Oceanography (MetOs), Department of Geosciences, University of Oslo. The work has been performed from March 2015 until November 2019, interrupted by a maternity leave. The reseach has been supervised by Terje Koren Berntsen (MetOs, Cicero), Trude Storelvmo (Metos), Kari Alterskjær (Cicero) and Jón Egill Kristjánsson (MetOs, Deceased 14th August 2016). The project was funded by the Norwegian Research Council through the project EVA (Earth System modelling of climate Variations in the Anthropocene), project number NFR - 229771. The thesis consists of an introduction part and the following papers. Summary of all four papers, including author contributions, are specified in Chapter 4.2 of the introdution part.

Paper I: Alf Kirkevåg, Alf Grini, Dirk Olivié, Øyvind Seland, Kari Alterskjær, Matthias Hummel, **Inger H. H. Karset**, Anna Lewinschal, Xiaohong Liu, Risto Makkonen, Ingo Bethke, Jan Griesfeller, Michael Schulz, and Trond Iversen, (2018), "A production-tagged aerosol module for Earth system models, OsloAero5.3 - extensions and updates for CAM5.3-Oslo", Geoscientific Model Development, doi:10.5194/gmd-11-3945-2018

Paper II: **Inger Helene Hafsahl Karset**, Terje Koren Berntsen, Trude Storelvmo, Kari Alterskjær, Alf Grini, Dirk Olivié, Alf Kirkevåg, Øyvind Seland, Trond Iversen, Michael Schulz, (2018), "Strong impacts on aerosol indirect effects from historical oxidant changes", Atmospheric Chemistry and Physics, doi:10.5194/acp-18-7669-2018

Paper III: Florent F. Malavelle, Jim M. Haywood, Andy Jones, Andrew Gettelman, Lieven Clarisse, Sophie Bauduin, Richard P. Allan, **Inger Helene H. Karset**, Jón Egill Kristjánsson, Lazaros Oreopoulos, Nayeong Cho, Dongmin Lee, Nicolas Bellouin, Olivier Boucher, Daniel P. Grosvenor, Ken S. Carslaw, Sandip Dhomse, Graham W. Mann, Anja Schmidt, Hugh Coe, Margaret E. Hartley, Mohit Dalvi, Adrian A. Hill, Ben T. Johnson, Colin E. Johnson, Jeff R. Knight, Fiona M. O'Connor, Daniel G. Partridge, Philip Stier, Gunnar Myhre, Steven Platnick, Graeme L. Stephens, Hanii Takahashi and Thorvaldur Thordarson, (2017), "Strong constraints on aerosol-cloud interactions from volcanic eruptions", Nature, doi:10.1038/nature22974

Paper IV: **Inger Helene Hafsahl Karset**, Andrew Gettelman, Trude Storelvmo, Kari Alterskjær, Terje Koren Berntsen, (2019), ”Exploring impacts of size-dependent evaporation and entrainment in a global model", Journal of Geophysical Research - Atmospheres, *in review*

Other publications from the PhD period that are not included in the thesis:

I Moa K. Sporre, Sara M. Blichner, **Inger H. H. Karset**, Risto Makkonen, and Terje K. Berntsen, (2019), "BVOC-aerosol-climate feedbacks investigated using NorESM", Atmospheric Chemistry and Physics, doi:10.5194/acp-19-4763-2019

II Giulia Saponaro, Moa K. Sporre, David Neubauer, Harri Kokkola, Pekka Kolmonen, Larisa Sogacheva, Antti Arola, Gerrit de Leeuw, **Inger H. H. Karset**, Ari Laaksonen, Ulrike Lohmann, and Philip Stier, (2019) "Evaluation of aerosol and cloud properties in three climate models using MODIS observations and its corresponding COSP simulator, and their application in aerosol-cloud interaction", Atmospheric Chemistry and Physics Discussions , doi:10.5194/acp-2019-631

III Moa K. Sporre, Sara M. Blichner, Roland Schrödner, **Inger H. H. Karset**, Terje K. Berntsen, Twan van Noije, Tommi Bergman, Declan O'Donnell and Risto Makkonen, (2019), "BVOC emissions and SOA yield impact on the direct and indirect aerosol effects in three ESMs Large difference in aerosol radiative effects from BVOC-SOA", *submitted to Atmospheric Chemistry and Physics*

:Acknowledgements

First and foremost, I would like to thank all my supervisors for guidance and support:
Jón Egill Kristjánsson, who initiated this PhD position and encouraged me to apply for it. I am sad to never know how this journey could have been with you.
Kari Alterskjær, the only one who has been supervising me since the beginning. Thanks for always being supportive.
Terje Koren Berntsen and Trude Storelvmo, thanks for gladly stepping in as supervisors after Jon Egill died, for sharing your knowledge and for always being positive and helpful.

I would also like to thank:
Colleagues at the EVA-project and MetOs for scientific and unscientific discussions, making life as a PhD student more interesting and less lonely.
Florent Malavelle and Jim Haywood for letting me participate in the Holuhraun study.
Christine for providing me this LaTeX template and for advising me on how to write a thesis.

Friends and family also deserve a special thanks for every day reminding me that life is good even though simulations are crashing and results don't make sense.

Oslo, November 2019
Inger Helene Hafsahl Karset

Contents

Part I

Thesis

Chapter 1

:Introduction

1.1 Motivation

Despite strong evidence of human impact on climate over the last century, large uncertainties are still associated with the contributions from the different climate drivers, with the lowest level of confidence linked to cloud adjustment due to atmospheric aerosol changes (*IPCC*, 2013).

Cloud droplets form when water vapor condenses onto liquid or solid particles suspended in air, also known as aerosols, that can act as cloud condensation nuclei (CCN). Given a fixed cloud liquid water content, more numerous CCN are associated with more numerous, but smaller droplets that brighten the clouds and scatter more of the incoming solar radiation back to space (*Twomey*, 1974). This is known as the first aerosol indirect effect. The reduction in cloud droplet size can also be followed by modulation of cloud water content, lifetime and/or extent through rapid cloud adjustments, known as the second aerosol indirect effect. *Albrecht* (1989) was the first to present the idea of an enhanced aerosol indirect effect caused by rapid cloud adjustments, arguing that precipitation formation is suppressed when droplets are smaller, leading to more water retention and extended cloud lifetime. While global models tend to only capture increased cloudiness due to suppressed precipitation, observations have shown both positive, negative and negligible responses in cloudiness when the aerosol concentration is enhanced (*Ackerman et al.*, 2004; *Gryspeerdt et al.*, 2019; *Malavelle et al.*, 2017; *McCoy et al.*, 2018; *Michibata et al.*, 2016; *Quaas et al.*, 2009; *Toll et al.*, 2017, 2019; *Wang et al.*, 2012; *Zhou and Penner*, 2017), indicating other mechanisms occurring in addition to that proposed by *Albrecht* (1989). Identifications and investigations of these processes that can buffer cloud responses to aerosol perturbations are needed to improve confidence.

The aerosol concentration in the atmosphere has changed since preindustrial times, contributing to the total anthropogenic radiative forcing (RF). RF is ”the net change in the energy balance of the Earth system due to some imposed perturbation” (*Myhre et al.*, 2013, p. 664), and with its positive value from preindustrial to present day, the Earth system receives more energy now in present day (+2.29 [1.13 to 3.33] Wm^{-2}) (*IPCC*, 2013). Together with its following feedback processes, RF results in a changing climate. Changes in atmospheric aerosol concentrations impact RF directly through

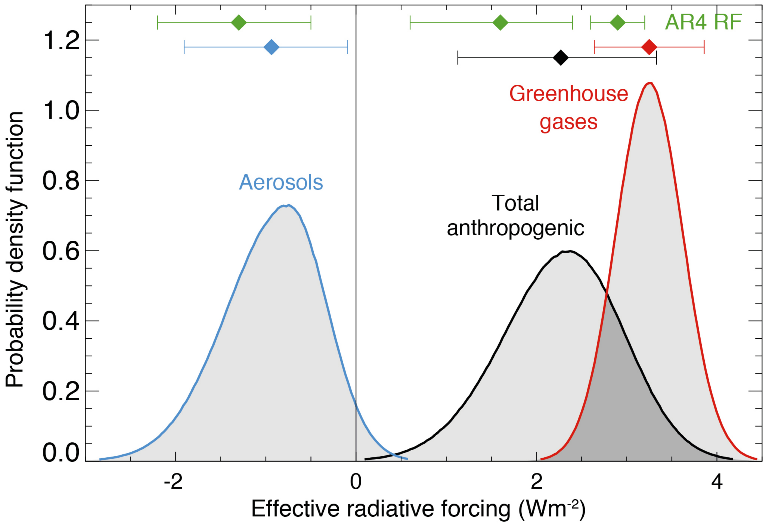

Figure 1.1: *Probability density function (PDF) of ERF due to total greenhouse gases (red), aerosol forcing (blue, both ERFaci and ERFari) and total anthropogenic forcing (black). The large spread in the blue curve is dominated by uncertainties in ERFaci. Figure from Myhre et al. (2013).*

changes in absorption and reflection of radiation by the aerosols, and indirectly through clouds. Cloud adjustments due to aerosols are referred to as Effective Radiative Forcing through Aerosol Cloud Interactions (ERFaci), including both RFaci (the first aerosol indirect effect) and the following rapid cloud adjustments (the second aerosol indirect effect). ERFaci has been estimated to contribute with -0.55 [-1.33 to -0.06] Wm^{-2} to the total anthropogenic forcing over the industrial era (*IPCC*, 2013). Together with the direct impact aerosols can have on radiation (Effective Radiative Forcing through Aerosol Radiation Interactions, ERFari), it most likely suppresses the warming of the greenhouse gases, which is illustrated in Fig. 1.1.

With the large spread in estimates of ERFaci+ari (and especially the aci-component), we do not know how much warming from the greenhouse gases has been modified by the cooling effect of aerosols and clouds. With projected reductions in emissions of aerosols driven by the desire to improve air quality, some of this warming is expected to be unmasked in the near future. For this reason, strong effort within the community is put into research on aerosol-cloud interactions to reduce the uncertainty and enhance the confidence in estimates of ERFaci. Increased understanding of how aerosols and clouds interact, and more certain estimates of how much cooling they have been contributing with over the last centuries are needed in order to better predict the climate for the future. The climate sensitivity, a measure of the temperature response to the forcing by a doubling of the CO_2-concentration in the atmosphere, is crucial to know to be able to predict future climate. Attempts have been made to derive the climate sensitivity by combining observed temperature and CO_2 records with modelled forcing estimates (*Hoffert and Covey*, 1992), but large uncertainties are introduced by the contribution from ERFaci. Since aerosol-cloud interactions are among the key factors controlling the hydrological cycle, improvements in how they are modelled will also improve predicted changes in precipitation.

Challenges in retrieving ERFaci are two-fold. Firstly, observations of how aerosols and clouds interact are limited on a global scale, and especially observations from preindustrial times are limited. Secondly, ERFaci seems difficult to model, witnessed by the large spread in global model estimates from the latest years that spans more than 1 Wm^{-2} (*Boucher et al.*, 2013; *Grandey et al.*, 2018; *Neubauer et al.*, 2017; *Zelinka et al.*, 2014; *Zhou et al.*, 2018), and the low level of confidence in estimates of ERFaci presented in the latest report by the Intergovernmental Panel on Climate Change (IPCC. See Fig. SPM.5 in *IPCC* (2013)). This thesis will focus on the second issue.

Reasons for the large uncertainty and low level of confidence in global model estimates of ERFaci are many. This is due to the dependency on correct representations of both radiation, cloud and aerosol processes, in addition to correct treatment and concentrations of gases in the atmosphere. Inadequate or uncertain cloud parameterizations are large sources of uncertainty (*Gettelman*, 2015). Aerosol-cloud interactions occur on microscales, while global models that are needed to get global radiation estimates have grid cells that span several tens of kilometers. Since it is not possible to resolve the clouds in these models, parameterizations are applied to describe the many processes that aerosols and cloud droplets may go through. Even though many of these parameterizations are evaluated against observations from selected places, they may not represent aerosols and clouds in different locations, at different times, or when other components of the model are modified, tuned or replaced through model development. Some parameterizations may also be lacking, for example representations of processes that can explain reduced cloudiness when the aerosol concentration increases (positive second indirect effect).

To be able to achieve the most accurate and credible estimate of how anthropogenic activities have contributed to ERFaci, model setups also need to be optimized. ERF, as introduced by *Myhre et al.* (2013) allows all physical variables, except for those concerning the ocean and sea ice, to respond to perturbations. This includes changes in rapid cloud adjustments and land surface temperatures, among others. A common way to model this is by replacing the ocean and sea ice components by fixed datasets with prescribed sea surface temperatures (SSTs) and sea ice extent, and carry out two simulations with emissions of aerosols and aerosol precursor gases from preindustrial times (PI) and present day (PD), respectively. As models have developed over the last decades, more of the emissions that previously were prescribed are now replaced with interactive emission algorithms, and more of the aerosol life cycle is represented by physical parameterizations rather than concentrations read in from files. Although this improves the model performances in many ways, it also introduces challenges when it comes to modelling ERFaci. One of these challenges is linked to the treatment of the oxidants, which impact the aerosol processes in the atmosphere by converting volatile gases into gases that more easily can condense and form new aerosol particles, or condense onto pre-existing aerosols making them grow larger. If anthropogenic activities have directly been impacting the oxidant levels, and not only through temperature feedbacks as a response to a warmer ocean, the question arises of whether these differences between PI and PD should be taken into account when modelling ERFaci. As the impacts of historical oxidant changes on ERFaci, and on aerosol growth and formation mechanisms in general, have not been studies before the work with this thesis, it was a need for investigations of this topic to enhance confidence in model estimates of ERFaci.

Another challenge that occurs when modelling ERFaci is the natural variability. Both aerosol concentrations and cloud properties affected by aerosol changes are highly dependent on variable meteorological conditions. As a result, long and computationally expensive simulations are required to separate the radiative effects caused by aerosol-cloud interactions from that of the natural variability. If not, uncertainties are introduced. This is also an issue for model intercomparison studies, or comparisons between models and observations where the modelled circulation can be very different from that observed. As a solution, methods for constraining the circulation by relaxing meteorological fields toward pre-defined conditions (*Jeuken et al.*, 1996), also known as nudging, are implemented in global models (*Kooperman et al.*, 2012), but it has been a need for upgrades (*Zhang et al.*, 2014).

1.2 Objective

The overall objective of this thesis is to contribute towards **enhancing the confidence in estimates of ERFaci through improved global modelling.** This is done through applying and developing the Norwegian Earth System Model, NorESM. As a part of the research project EVA (Earth system modelling of climate Variations in the Anthropocene), which aimed to ”further develop, extend, quality check, and apply the Norwegian Earth System Model (NorESM) to key research questions in the field of climate science” (*Bjerknes Centre*, 2015), the aim of this thesis has been to contribute to this work, with a more narrow focus on the field of aerosol-cloud interactions. As the reasons for the large uncertainty and low level of confidence in model estimates of ERFaci are many, several approaches are made in this thesis to seek for improvement strategies. This includes improvements to

- technical aspects of the model, with extra focus on the nudging capabilities
- pre-industrial to present day changes in factors controlling aerosol formation and growth, with extra focus on changes in the oxidant level
- cloud parameterizations impacting modelled rapid cloud adjustments, with extra focus on processes capable of reducing cloudiness under conditions with increased aerosol concentrations

The more specific sub objectives and their relation to the papers and specific chapters of the thesis are as follows:

1. To investigate, apply and improve the nudging capabilities in NorESM. (Paper I and Chapter 4.1)
2. To develop and apply a reanalysis dataset for nudging in NorESM, enabling comparisons of modelled aerosol-cloud interactions to observations. (Paper I, III and IV, and Chapter 4.1)

3. To investigate the impact of historical oxidant changes on ERFaci, and propose improved treatment of oxidants when modelling ERFaci (Paper II)

4. To identify issues linked to global modelling of rapid cloud adjustments by taking part in an intercomparison study that uses a recent volcanic eruption as a testbed to evaluate model performance in simulating aerosol-cloud interactions. (Paper III)

5. To explore impacts on rapid cloud adjustments by implementing size-dependency on two processes with the potential to reduce cloudiness with increased aerosol concentrations (evaporation and entrainment). (Paper IV).

Chapter 2

:Background

While each paper presents the scientific background relevant for the individual paper, with an overview of updated research with new findings within the given research field, the following chapter covers a broader and more basic background necessary for understanding all of the work carried out and presented in this thesis.

2.1 Forcing and feedback

This thesis focuses on effective radiative forcing through aerosol-cloud interactions, which is a measure of how interactions between aerosols and clouds affect climate. A perturbation imposed on the Earth system (for example a change in the concentration of aerosols or greenhouse gases in the atmosphere) can result in an imbalance in Earth's energy budget (i.e., the balance between incoming shortwave and outgoing longwave radiation). This imbalance, measured in units of $\mathrm{Wm^{-2}}$, is defined as the radiative forcing (RF) caused by the perturbation. On short time scales, rapid adjustments within the Earth system caused by fast responses to the imposed perturbation can occur. This can lead to adjustments to the initial RF, which together with RF results in an Effective Radiative Forcing (ERF), appearing as an imbalance measured at the top of the atmosphere (*Myhre et al.*, 2013). Regarding enhanced anthropogenic emissions of aerosols, the ERF is not just including the direct radiative impact aerosols have on radiation (ERFari), but also their impact through changes in cloud droplet (or ice crystal) number and size (RFaci) and possible following rapid adjustments of the cloud water content, extent and lifetime.

An imbalanced Earth system gains or loses energy, which eventually will lead to temperature changes that can result in more changes in the components of the Earth system, impacting the climate even more. To separate the effect of these changes from those leading to ERF, the definition of feedbacks is introduced. Feedbacks include adjustments in the Earth system that follow a change in the sea surface temperature. Due to the large heat capacity of the ocean, feedbacks occur on a much longer time scale than the rapid adjustments, but a clear time separation is not defined. The resulting total imbalance of the Earth system, ΔN, can be expressed as seen in Eq. (2.1)

$$\Delta N = \Delta F + \alpha \Delta T, \tag{2.1}$$

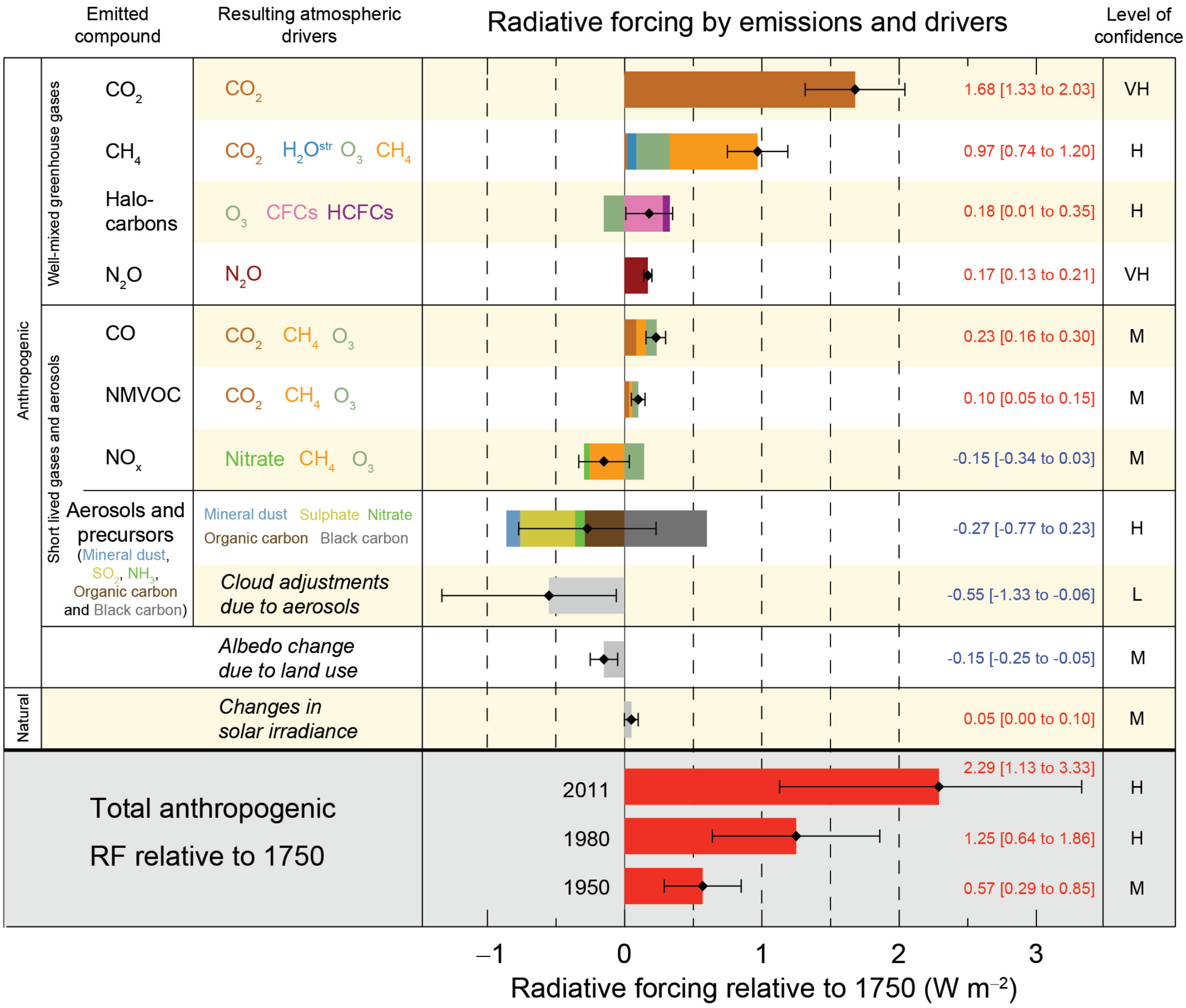

Figure 2.1: *Radiative forcing estimates in 2011 relative to 1750. For well-mixed greenhouse gases, aerosols and clouds, rapid adjustments are included, thus their values represent ERF. ERFaci is represented the bar named "Cloud adjustments due to aerosols", while ERFari is representd by the bar named "Aerosols and precursor gases". Figure SPM.5 from IPCC (2013).*

where ΔF (Wm^{-2}) is the ERF-part and $\alpha\Delta T$ is the feedback part, where ΔT (°C) is the change in global mean near surface air temperature and α ($\mathrm{Wm}^{-2}\,^{\circ}\mathrm{C}^{-1}$) is the feedback parameter expressing how much the imbalance is affected per unit of global warming (*Rotstayn and Penner*, 2001). While ΔN represents the actual imbalance, many studies focus on ERF and the feedbacks separately to better understand the processes behind the observed climate change.

This thesis focuses on ERF, and only on its contribution from aerosol-cloud interactions. Figure 2.1 shows forcing estimates from the many different drivers affecting the Earth's energy imbalance. As mentioned in the introductory chapter and shown in Fig. 2.1 by the black error bars, aerosols and clouds are the largest contributors to the uncertainty in the total preindustrial-to-present-day anthropogenic forcing. As seen in the right column of Fig. 2.1, the lowest level of confidence is linked to cloud adjustments due to aerosols. The level of confidence in Fig. 2.1 is a qualitative measure, based on the evaluations of the underlying scientific understanding by the author teams of the fifth Assessment Report (AR5) from the Intergovernmental Panel on Climate Change (IPCC). According to the report, confidence is "the validity of a finding, based on the type, amount, quality, and consistency of evidence (e.g., data, mechanistic understanding, theory, models, expert judgment) and the degree of agreement." (*Cubasch et al.*, 2013, p. 139). The level of confidence is thus a measure of how much we can trust the estimates.

2.2 Aerosols and oxidants

Aerosols are liquid or solid particles suspended in air, with highly variable sizes and chemical compositions (*Heintzenberg et al.*, 2000; *Putaud et al.*, 2010). In addition to naturally originating aerosols, such as sea salt, mineral dust, organic matter, bacteria and sulfate from volcanic eruptions, anthropogenic activities also contribute substantially to the aerosol burden (*Boucher et al.*, 2013). This happens directly through emissions from industrial and agricultural activities, but also through modifications of natural emissions caused by for example land use change (*Lathière et al.*, 2010; *Pacifico et al.*, 2012; *Unger*, 2013). Aerosols can either be injected directly into the atmosphere, or formed in situ by gaseous or aqueous phase oxidation of precursor gases to condensable species (*Kulmala et al.*, 2004). The first is the case for larger aerosols, such as sea salt, mineral dust, organic matter and black carbon. The latter is the case for secondary organic aerosols (SOA) and part of the sulphate (SO_4) aerosol. SOA can be produced when Biogenic Volatile Organic Compounds (BVOCs) are oxidized by ozone (O_3), nitrate radical (NO_3) or hydroxyl radical (OH), producing several different products with low volatility. These products can condense onto existing aerosol, or even take part in new particle formation, also called nucleation of aerosols (*Shrivastava et al.*, 2017). Some sulfate (SO_4) aerosols are emitted directly into the atmosphere, but most of them are produced in situ either through gas phase oxidation of SO_2 by OH forming sulphuric acid (H_2SO_4) or aqueous phase oxidation inside cloud droplets by O_3 or hydrogen peroxide (H_2O_2) (*Seinfeld and Pandis*, 2016). Natural aerosols and aerosol precursor gases can stem from both land and ocean. In addition to the release of sea salt when bubbles burst or drops are teared from waves, primary organic matter,

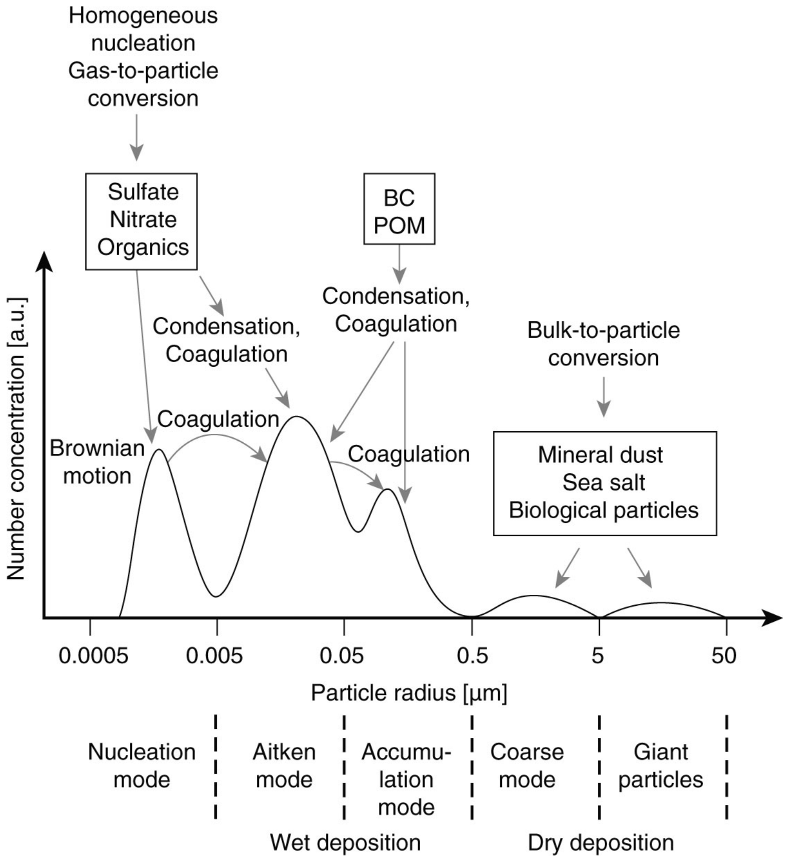

Figure 2.2: *Schematic of the main aerosol sources, groups and processes as a function of size. Note the logarithmic scale on the x-axis. BC refers to black carbon, while POM refers to particulate organic matter. Figure from Lohmann et al. (2016). Reprinted with permission from Cambridge University Press.*

BVOCs and dimethyl sulfide (DMS) are also injected from the ocean into the atmosphere (*Lovelock et al.*, 1972; *Shaw et al.*, 2010). DMS can be oxidized by OH or NO_3 to SO_2 (*Andreae et al.*, 1985) and methanesulfonic acid (MSA). In recent years, MSA has also been found to contribute to aerosol growth by condensation onto pre-existing aerosols, and possibly also participation in new particle formation (*Bork et al.*, 2014; *Hodshire et al.*, 2019; *Mäkelä et al.*, 2001).

As mentioned in the previous section and in Chapter 1, anthropogenic activities have contributed substantially to changes in the aerosol burden by increasing emissions of both primarily aerosols and secondary aerosol precursor gases. Since the formation of secondary aerosols is initiated by oxidation of precursor gases, changes in the oxidation capacity of the atmosphere will also impact the aerosols. In addition to reacting with aerosol precursor gases, oxidants also react with several other gases, like methane (CH_4), nitrogen oxide (NO_x) and carbon monoxide (CO) (*Seinfeld and Pandis*, 2016). With the strong increase in emissions of these gases since preindustrial times, the oxidation capacity of the atmosphere has changed due to changes in chemical loss rates (*Crutzen and Lelieveld*, 2001). The work in this thesis represents the first investigation into the impact of changes in the oxidant levels over the industrial era to ERFaci.

Figure 2.2 shows a size-distribution of aerosols with an overview of which aerosols we find in the different size categories. The smallest aerosols are called nucleation mode particles since they typically form through nucleation. These can grow either by condensation or coagulation into Aitken mode aerosols, named after the meteorologist John Aitken. The growth by condensation and coagulation slows down as the aerosols become larger, and since they still are too small to fall out by dry deposition at a significant rate, they accumulate in an accumulation mode. Larger aerosols, such as sea salt, mineral dust and bacteria form the coarse and giant mode. Dry deposition is the dominant deposition mechanism for the largest aerosols due to their weight, while wet deposition through uptake in cloud droplets and fall out by rain is dominating for the smaller ones (*Ginoux et al.*, 2001; *Textor et al.*, 2007; *Zhang and Vet*, 2006).

To what extent aerosols can impact the radiative budget through aerosol-cloud interactions depends on various factors, such as their size, composition, atmospheric lifetime and burden. Larger sizes and higher solubility favor the ability of the aerosols to act as CCN and thus cloud droplet growth, which will be described more in detail in the next section. Aerosols with surfaces not suitable for water uptake, such as black carbon, can still turn into CCN if they are coated through condensation of more hydrophilic components, for example sulfate or SOA (*Bond et al.*, 2013; *Dalirian et al.*, 2018). As already mentioned, the atmospheric lifetime of aerosols can also be important for their impact on climate through aerosol-cloud interactions. In models, it is common to define the atmospheric aerosol lifetime as the ratio between the aerosol burden (integrated mass from the ground and all the way up to the top of the atmosphere) and the rate of deposition or emission. Aerosols with long atmospheric lifetime can be transported to more remote regions with low cloud droplet number concentrations, where their impact on radiation, both directly and indirectly through clouds, can be more efficient than in polluted areas (*Twomey*, 1991).

2.3 Clouds

2.3.1 Physics

Collections of liquid water droplets, ice crystals, or a mix between the two, form the clouds that we observe in the atmosphere all over the globe. To limit the scope for this thesis, the work is focused on warm clouds, which only consists of liquid water droplets.

Cloud droplets can form when water vapor molecules grow into large clusters. Whether this process will happen or not depends on the supersaturation, defined as one minus the ratio of the atmospheric partial pressure of water vapor and partial pressure of water vapor needed for balance between evaporation and condensation above a flat, pure surface of liquid water. The supersaturation required for a droplet to continue to grow, and not evaporate, is calculated by Köhler theory (*Köhler*, 1936). This theory combines Raoult's solute effect, expressing that a lower supersaturation is required if the solubility is high, and Kelvin's surface area effect, expressing that the smaller the cluster or droplet is, the higher the supersaturation required for it to grow is because more work is required to maintain their surface tension. The supersaturation required for

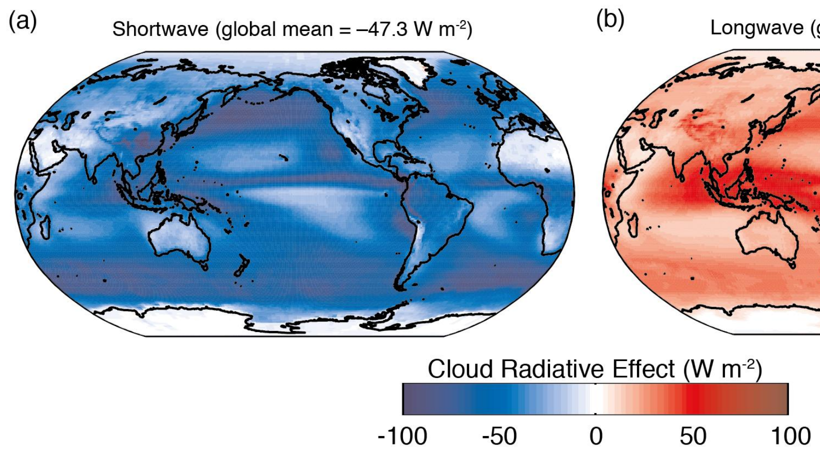

Figure 2.3: *(a) Shortwave and (b) longwave cloud radiative effect from CERES-EBAF. The values are averaged over the period 2001-2011. Figure from AR5, IPCC, Boucher et al. (2013).*

water vapor to cluster and form cloud droplets without any help from an aerosol to increase solubility or size is so high that this usually only happens in laboratories, and not in typical atmospheric conditions. During the initial phase of droplet creation, the aerosol will swell by taking up water. This will dilute the solute effect, and thus requiring higher supersaturations for further growth. At a certain size, the droplet is large enough that the surface tension effect will dominate and then the supersaturation required for further growth will decrease. At this size we say that the droplet is activated. Under typical atmospheric conditions, activation of cloud droplets will not occur without the presence of an aerosol with diameter above 50-100 nm, but the exact size will depend among others on the solubility of the aerosol (*Seinfeld and Pandis*, 2016).

Supersaturation can be achieved by adding water vapor in the air (increase in moisture sources), or by reducing temperatures. The latter can happen either through (1) cooling of lifted air caused by convective motions or forced orographic or frontal lifting, (2) by mixing of air masses with different temperature and saturation, or by (3) radiative or evaporative cooling. When the vapor pressure above the droplet surface is so high that the energy barrier is passed, the droplet will continue to grow by condensation. This growth mechanism is efficient for small droplets, since the surface area exposed to vapor compared to the volume is large. As this relation shifts when the droplets become larger, growth by collision and coalescence, also named collection or autoconversion, takes over. This is the process where liquid cloud water droplets merge and it is needed to form raindrops. Many other processes, beside growth by condensation and collection, also occur in clouds. These involve both vapor, liquid water and ice, in additon to interactions between them (*Lohmann et al.*, 2016). An overview of many of the processes included in the model applied in this study is found in the documentation of the microphysics scheme in NorESM (*Gettelman et al.*, 2008; *Morrison and Gettelman*, 2008), which will be returned to in Chapter 3.

2.3.2 Radiative impact

Covering more than two thirds of the globe, clouds have a strong impact on the radiative budget, both when it comes to reflecting incoming shortwave radiation from the sun (cooling) and absorbing longwave radiation from the Earth (warming) (*Boucher et al.*, 2013). Figure 2.3 shows the annual mean global cloud radiative effect estimated by ”Clouds and the Earth’s Radiant Energy System - Energy Balanced And Filled” (CERES-EBAF), which is a product based on satellite retrievals of radiation fluxes, adjusted to be consistent with the ocean heat storage (*Loeb et al.*, 2018). When having in mind that the top of the atmosphere receives ∼342 Wm^{-2} from the sun, Fig. 2.3(a) shows that as much as 14 % of this energy is reflected back to space by clouds. The strength of the shortwave effect depends on the difference in reflectivity between the bright clouds and the underlying surface. Figure 2.3(a) shows that this is large in areas covered by ocean. Figure 2.3(b) shows that, like greenhouse gases, clouds in the atmosphere also absorb and emit longwave radiation, contributing to a warming effect. The strength of the longwave effect depends on the temperature difference between the cloud and the underlying surface. Since the temperature drops with height in the troposphere, higher clouds contribute the most to this warming. By comparing Figs. 2.3(a)-(b), we can see that clouds are cooling the planet on a global scale, which means that their ability to reflect radiation contributes more to the global average radiative budget than their longwave effect. This is especially the case for low level subtropical clouds, like marine stratocumulus clouds, which have a low cloud top height, overlay a much darker ocean surface, and have a large horizontal extent (*Wood*, 2012).

2.4 Aerosol-cloud interactions

As mentioned in the introductory chapter, humans have not only contributed to perturbing Earth’s energy budget through emissions of greenhouse gases, but also through emissions of aerosols and aerosol precursor gases. Enhanced aerosol concentrations lead to enhanced competition for water vapor between cloud droplets during growth. This can result in smaller and more numerous cloud droplets, which reflect more of the incoming solar radiation back to space (*Twomey*, 1974). A common example of this is the clearly visible ship tracks in satellite images, as seen in Fig. 2.4. Several rapid cloud adjustments can follow the reduction in cloud droplet size. Some of these, and their impact on the total amount of integrated liquid cloud water from the ground and all the way up in the atmosphere (LWP - Liquid Water Path) are seen in Fig. 2.5. While suppressed precipitation (left branch) due to dampened autoconversion rate for smaller droplets generally increase LWP (*Albrecht*, 1989), smaller more numerous droplets also favor processes that can reduce LWP. These are illustrated by the middle and the right branches in Fig. 2.5. As for the growth of cloud droplets by condensation, evaporation of cloud droplets also depends on the total droplet surface area. Given the same conditions and a fixed cloud water content, more numerous and smaller droplets are associated with large total droplet surface area, which again is associated with stonger evaporation rate compared to that of fewer, larger droplets (*Squires*, 1952a,b). Enhanced evaporation can also lead to so-called evaporation-entrainment feedbacks (*Ackerman et al.*, 2004; *Altaratz et al.*, 2008; *Feingold et al.*, 2006; *Hill et al.*, 2009; *Jiang*

Figure 2.4: *Ship tracks observed by NASA's MODIS instrument on board the Aqua satellite. Figure from NASA (2010), retrieved from* `https://svs.gsfc.nasa.gov/3667` *October 9, 2019. More information about the instrument is found in Chapter 3.*

and Feingold, 2006; *Xue and Feingold*, 2006; *Xue et al.*, 2008). When evaporation is enhanced, the cloud top experiences enhanced evaporative cooling, which promotes sinking of air masses. This can induce enhanced turbulent mixing, entraining air from above the cloudtop into the cloud. If this air is dry, cloud water can evaporate, and LWP is reduced. Most global models include a size-dependent parameterization of the autoconversion process that dampens precipitation formation and increases LWP when cloud droplets become more numerous and smaller due to aerosol perturbations *Gettelman* (2015); *Quaas et al.* (2009); *Wang et al.* (2012). On the other hand, parameterizations of evaporation and entrainment processeses usually lack size-dependency *Stevens and Feingold* (2009); *Zhou and Penner* (2017). The result is that the models only include processes that could lead to increased LWP due to aerosol increase, while neglecting the possible LWP reducing processes. This issue is the focus of Paper IV, where impacts of adding size-dependent evaporation and entrainment to a global model are explored. The rightmost branch in Fig. 2.5 illustrates evaporation-sedimentation feedbacks (*Bretherton et al.*, 2007), which also has the potential to reduce LWP. When droplets are small, sedimentation of cloud droplets from the cloud top is suppressed since smaller droplets fall slower than larger droplets. This accumulation of droplets in the cloud top increases the mass of cloud water in the cloud top relative to the rest of the cloud. Combining this increase in available liquid water at the cloud top with enhanced evaporation and entrainment for smaller droplets, the overall result could be an even stronger reduction in LWP. This process is, however, not the focus in this thesis. More detailed information about rapid cloud adjustments are found in Paper IV.

Aerosol-cloud interactions also occur in ice clouds and mixed-phase clouds (both liquid and ice). While pure cloud droplets can freeze to ice crystals when temperatures drop below -38 °C (*Pruppacher and Klett*, 1997), ice crystals are formed in the atmosphere at higher temperatures with help of aerosols acting as Ice Nucleating Particles (INPs). Aerosol precursor gases can also condense on INPs, suppressing their ability to initiate nucleation. For these reasons, enhanced emissions of aerosols and aerosol precursor gases can impact where, when, how, and if ice nucleation occur. This can impact the cloud radiative effect through modifications of the cloud optical thickness,

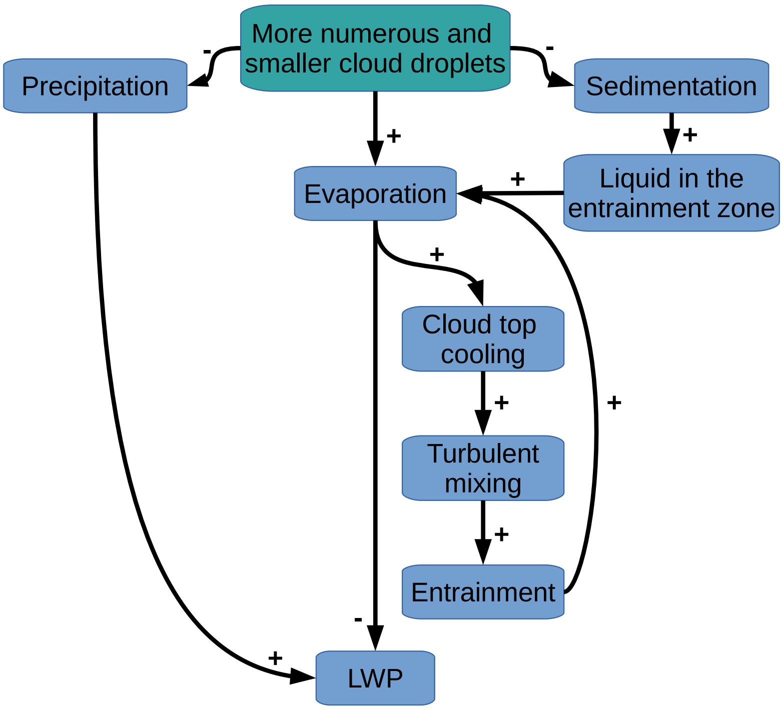

Figure 2.5: *Schematic of some rapid cloud adjustments that can follow an aerosol perturbation that resulted in more numerous and smaller cloud droplets. Some processes result in increased LWP (+), while some reduces LWP (-). Figure from Paper 4.*

which is low for clouds with few, large ice crystals compared to clouds with many, small droplets (*Lohmann*, 2017; *Storelvmo*, 2017). The mechanisms in ice clouds and mixed-phase clouds are many and complex, and not the focus of this thesis.

In addition to all processes mentioned above, aerosols may also cause invigoration of deep convective clouds (deepening and expanding their anvil), resulting in both enhanced warming effect due to reduced cloud top temperature and enhanced cooling effect due more reflection of incoming solar radiation by the larger and longer lasting clouds (*Koren et al.*, 2010; *Rosenfeld et al.*, 2014). The magnitude of the effect is uncertain and the opposite (suppression) has also been found (*Liu et al.*, 2019).

This thesis mainly focus on aerosol-cloud interactions in warm and shallow clouds, which mainly is the Twomey effect and the rapid-cloud adjustments described in the first part of this section.

2.5 Global modelling of ERFaci

While aerosol effects on clouds in the present-day atmosphere can be observed, information about aerosol-cloud interactions and their impact on Earth's energy budget back in time is missing. Global observations only exist from the beginning of the satellite era at the end of the 70's, centuries after humans began to impact the global climate with the industrial revolution at the end of the 18th century. For this reason, in order to be able to find out how much of the greenhouse gas warming the aerosols may be masking through aerosol-cloud interactions, global models are applied, where the latest and most advanced types are the Earth System Models (ESMs).

2.5.1 Earth System Models

Global climate models consist of a network of grid boxes covering the surface of the globe, upwards in the atmosphere and downwards in the ocean. Equations describing physical processes are solved within the boxes, in addition to interactions between them. Figure 2.6 illustrates the first decades of evolution of global climate models, with increased complexity and more numerous components included. Today's Earth System Models (ESMs) are even more advanced, also including biogeochemical processes and feedback cycles. The resolution has also become finer, with ESMs today generally applying a resolution of 1×1 degree ($\sim$100 km grid space near equator) or finer for the atmospheric component (*Eyring et al.*, 2016). ESMs can be applied as fully coupled versions, with all components (atmosphere, ocean, land, sea ice, etc.) running interactively, or just with one or few interactive components, with the others prescribed. The first is necessary for transient climate simulations, simulating the evolution of climate over longer time periods to capture a whole and realistic evolution of climate change. When only studying effective radiative forcings, only one or a few components are usually applied. This is computationally less expensive than running the fully coupled version, and makes it easier to separate out the forcings from the feedbacks. As mentioned in the introductory chapter, it is common to prescribe the SSTs and sea ice extent when modeling ERFaci, and only use a fully interactive atmosphere and a partly interactive land component (*Hansen et al.*, 2005). This method is known as ”the fixed-SST method”. Another way to model ERF is to use the so-called ”regression method” (*Gregory et al.*, 2004), where a fully coupled model carries out two transient simulations, with and without a perturbation by a forcing agent (for example increased emissions of aerosols), and linear regression of the response in the energy imbalance to the temperature change is applied to estimate the initial ERF. Being more computationally affordable and making it easier to separate the forcings from the freedbacks, the fixed-SST method is applied in the work carried out as a part of this thesis. The model and setups applied are described in more detail in Chapter 3, as well as in the description of the model and the experimental setups in the individual papers.

2.5.2 Nudging

Nudging, also known as Newtonian relaxation, is used to relax meteorological fields towards pre-defined conditions (*Jeuken et al.*, 1996). Since different meteorological conditions can have a much stronger impact on the studied variable than the impact from the forcing of interest, nudging is useful when comparing modelled fields to that of observations, or for model intercomparison studies (*Kipling et al.*, 2016; *Koffi et al.*, 2016; *Malavelle et al.*, 2017; *Mann et al.*, 2014; *Schulz et al.*, 2006). It is also commonly used to reduce computational costs (*Ghan et al.*, 2016; *Kooperman et al.*, 2012; *Lin et al.*, 2016). When for example modelling ERFaci, *Kooperman et al.* (2012) showed that even after 100 years of simulations with free running (not nudged) meteorology, the standard error was larger than that of 10 years with nudged meteorology.

Equation (2.2) shows the concept of nudging.

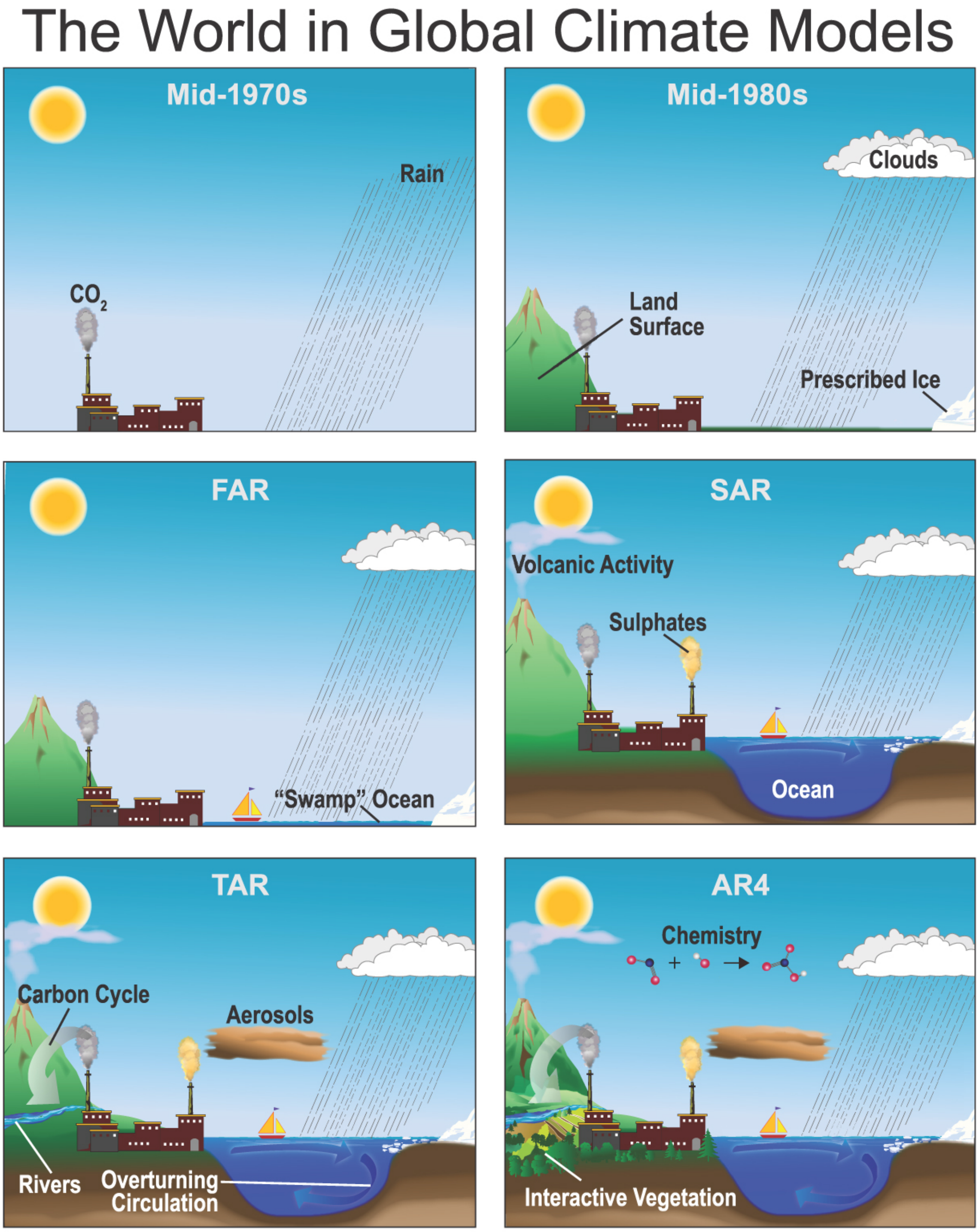

Figure 2.6: *Schematic of the increase in complexity of global climate models from the Mid-1970's to the Assessment Report number 4 (AR4) from the Intergovernmental Panel on Climate Change (IPCC) back in 2007. FAR, SAR and TAR are the first, second and third assessment report from IPCC. Today's Earth System Models are even more advanced. Figure from Treut et al. (2007).*

$$X_{m,new} = \left(1 - \frac{\Delta t}{\tau}\right) X_{m,old} + \frac{\Delta t}{\tau} X_p \tag{2.2}$$

$X_{m,old}$ is a modelled variable, for example temperature, before entering the nudging code. X_p is a predefined value of the same variable, taken from an input file that either stems from observations, reanalysis or from a previous model simulation. Δt is the length of a timestep in the model, while τ is the relaxation time that gives the strength of the nudging. $X_{m,new}$ is the updated variable after the nudging is applied. If Δt is 0.5 h and τ is 6 h, the new updated variable consists of ∼8.3 % of the value of X_p and 91.7 % of the modelled value of $X_{m,old}$.

The nudging capabilities in NorESM are investigated and updated, and the method is applied in all studies presented as a part of this thesis.

Chapter 3

:Research tools

This chapter provides an overview of the model, satellite and reanalysis dataset applied in the thesis. Note that the work with preparing and analysing the satellite data in Paper III were performed by two other authors of the paper; Florent Malavelle and Jim Haywood.

3.1 NorESM

3.1.1 General information

All papers in this thesis make use of the Norwegian Earth System Model (NorESM). It is based on the Community Earth System Model (CESM), developed primarily at the National Center for Atmospheric Research (NCAR). The simulations carried out for this thesis do not apply the fully coupled version of NorESM, but a setup where only the atmospheric component runs fully interactively. This component in NorESM is based on the Community Atmosphere Model (CAM) (*Liu et al.*, 2016; *Neale et al.*, 2012). The first version of NorESM, that participated in the Coupled Model Intercomparison Project Phase 5 (CMIP5), applied CAM4 as its base (*Bentsen et al.*, 2013; *Iversen et al.*, 2013; *Kirkevåg et al.*, 2013), while the second version used for the Coupled Model Intercomparison Project Phase 6 (CMIP6) is based on CAM6. During the process of developing CAM6-Oslo, an intermediate version, CAM5.3-Oslo was applied, which is documented in Paper I of this thesis (*Kirkevåg et al.*, 2018).

3.1.2 OsloAero and AeroTab

The main difference between CAM5.3 and CAM5.3-Oslo is the online aerosol module OsloAero and the offline size-resolving sectional model AeroTab. While the aerosol size distributions in CAM5.3 are represented by three or seven log-normal functions, aerosols in CAM5.3-Oslo are so called ”production tagged”. 15 lognormal background modes represent the aerosols coming directly from emissions or from production by nucleation in the atmosphere. The 13 tracers representing the direct emissions are consisting of various sizes of sea salt, dust, black carbon, organic matter and sulfate, while the 2 tracers representing the newly formed aerosols through nucleation are sulfate and SOA. These background tracers contribute to the aerosol number concentration.

Through microphysical aerosol processes calculated by OsloAero, such as condensation (2 tracers), coagulation (3 tracers) and production within cloud droplets (1 tracer), 6 process tracers change the chemical composition and shape of the background modes. After these processes, aerosol size-distributions are no longer modal, and are therefore referred to as ”mixtures” rather than ”modes”. Information about the mass and composition of each mixture are fed into preprocessed lookup tables generated by the offline sectional model, AeroTab, consisting of 44 size bins. AeroTab gives information about the size and the optical properties of each mixture, which later is used in calculations of cloud microphysics and radiation. In addition to the background and process tracers, 8 aerosol precursor and oxidant gas tracers are also transported by the model.

AeroTab only treats aerosol particles with diameter larger than 23.6 nm. Primarily emitted aerosols are assumed to be larger than this, but secondary aerosols need to grow up to this size by condensation to be included in the model as nucleation particles. This new particle formation process is included in the model for SOA and SO_4, and is based on *Makkonen et al.* (2014), with modifications described in *Kirkevåg et al.* (2018). It includes both binary homogeneous nucleation of SO_4 based on *Vehkamäki et al.* (2002), and boundary layer activation type nucleation based on Eq. (18) in *Paasonen et al.* (2010). The gas-phase and oxidant chemistry leading to the condensable species suited for nucleation and condensation are described in detail in Paper II.

Many of the emissions of aerosols and aerosol precursor gases in NorESM are prescribed by monthly averaged files based on CMIP5-data provided by *Lamarque et al.* (2010). A full overview of the emissions, burdens, lifetimes and loss rates of the different species in the model is provided in Paper I. As global models have developed and become more complex, also more of the emissions are calculated interactively as the models run. For NorESM, this is the case for BVOC, dust, sea salt, DMS and oceanic primary organic aerosols. These emission algorithms are described in Paper I.

For more information about the aerosol module and its predecessor model versions, see Paper I and *Seland and Iversen* (1999), *Iversen and Seland* (2002), *Kirkevåg et al.* (1999), *Kirkevåg and Iversen* (2002) *Kirkevåg et al.* (2005), *Seland et al.* (2008), *Kirkevåg et al.* (2008) and *Kirkevåg et al.* (2013).

3.1.3 Cloud treatment

Clouds are affected by several parts of the model, which is illustrated by the simplified workflow in Fig. 3.1. When OsloAero and AeroTab have calculated updated properties and sizes of the different aerosol mixtures, an activation scheme based on *Abdul-Razzak and Ghan* (2000) activates cloud droplets. Ice nucleation parameterizations based on *Hoose et al.* (2010) and *Wang et al.* (2014) also form ice crystals by heterogeneous ice nucleation with black carbon and dust acting as ice nucleating particles. The droplets and ice crystals in stratiform clouds are treated by the double moment bulk microphysics scheme MG1.5 (*Gettelman et al.*, 2008; *Morrison and Gettelman*, 2008), which is almost the same as MG1, but with activation moved before the microphysics (*Gettelman*, 2015). ”Double moment” means that it is prognostic both when it comes to mass and number. Deep and shallow convective clouds include calculations of the mass

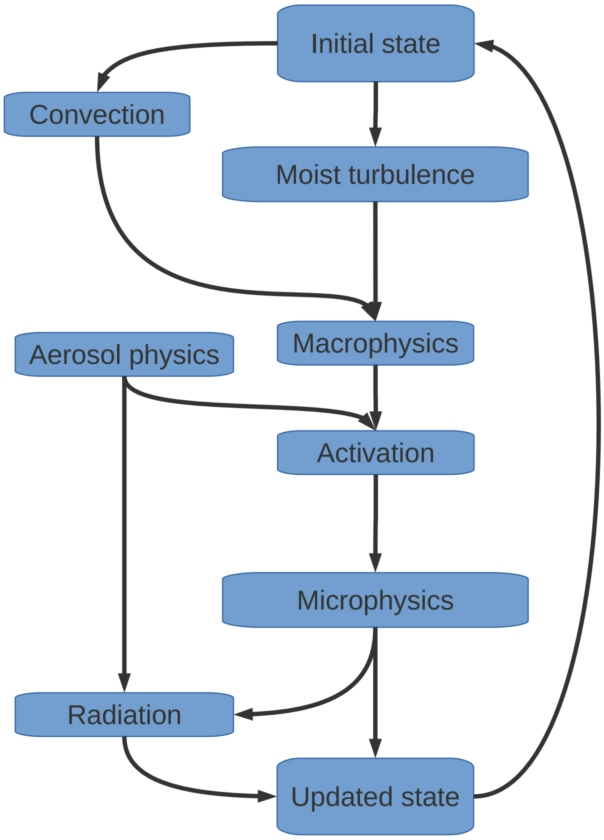

Figure 3.1: *Simplified workflow in CAM5.3-Oslo, showing the order of some of the most important processes in the model that affect cloud mass. Figure adapted from Paper IV.*

of water vapor, ice and liquid detrained from these clouds. The corresponding change in cloud droplet number is calculated based on the detrained mass and predefined constant cloud droplet sizes. This means that aerosol-cloud interactions only are included in the stratiform clouds of the model. Parameterizations of the deep convective clouds follow *Zhang and McFarlane* (1995), while the treatments of the shallow convective clouds and moist turbulence are based on work done at the University of Washington (*Bretherton and Park*, 2009; *Park and Bretherton*, 2009). The macrophysics, which includes saturation adjustment, is described in *Park et al.* (2014).

3.1.4 Why NorESM?

NorESM is a very well suited tool to apply when studying aerosol-cloud interactions on a global scale. With its participation in previous and upcoming global model intercomparison projects, and a model base similar to that of many other CESM-based models, research on aerosol-cloud interactions carried out with NorESM can be representative for other global models as well. With its production tagged aerosol scheme, the NorESM results can also represent novel and unique contributions to the research field.

3.2 ERA-Interim

3.2.1 General information

ERA-Interim is a global atmospheric reanalysis product created by the European Centre for Medium-Range Weather Forecasts (ECMWF), spanning the period from 1979 to August 2019 (*Berrisford et al.*, 2011). Atmospheric reanalysis products are mainly used to initialize numerical weather prediction models, but can also be applied in ESMs to constrain the meteorology, as is done in Paper I, III and IV of this thesis. ERA-Interim is produced through data assimilation, where the output from a forecast model is corrected by several observations, before the corrections again are used to initialize the forecast model in the next time step. 4D atmospheric products describing the state of the general circulation are produced every 6 hours on 60 model levels in the vertical up to 0.1 hPa, and on the horizontal spectral grid T255 ($\sim$80 km).

3.2.2 Why ERA-Interim?

The reanalysis dataset used in this thesis was chosen in order to be able to contribute to Paper III and an upcoming model intercomparison project. For the main model of the study of Paper III, HadGEM, ERA-Interim was applied to constrain its meteorology, so this reanalysis was also chosen for NorESM for better comparisons. ERA-Interim is one of the most frequently used reanalysis datasets, with high documented performance skill in several studies (*Boilley and Wald*, 2015; *Hofer et al.*, 2012; *Lindsay et al.*, 2014).

3.3 MODIS-Aqua

3.3.1 General information

Satellite data is used to evaluate modelled cloud properties over large areas. Paper III in this thesis compares modelled cloud effective radius and liquid water path with MODIS-Aqua products (*King et al.*, 2003; *Platnick et al.*, 2003). The spectroradiometer MODIS (Moderate Resolution Imaging Spectroradiometer) is placed on the satellite Aqua, which is a part of the sun-synchronised satellite constellation A-train. MODIS measures radiation with wavelengths in 36 bands between 0.405 μm and 14.385 μm, thus both reflected solar radiation and emitted longwave radiation from the Earth system. After applying calibration (L0 $\rightarrow$ L1) and retrieval algorithms (L1 $\rightarrow$ L2) to the rawdata, level 2 products (L2) describing microphysical properties, such as effective radius, cloud optical thickness and liquid water path, are generated. Several spectral bands are applied during the retrievals, but the combination of reflectances from the bands at 1.24 μm and 2.13 μm are typically used for retrieving both effective radius and cloud optical thickness at the same time. The calibration and retrieval algorithms have been updated several times since the launch of the satellite, resulting in several different collections of products. Paper III in this thesis applied products from collection 5.

3.3.2 Why MODIS-Aqua?

MODIS is also placed on the satellite Terra, but data from this instrument were not chosen because it has experienced a degradation in some of the channels, resulting in significant trends in several products, where LWP, r_e and cloud optical thickness are among these (see supplementary of Paper III). Other instruments for measuring cloud properties from satellites also exists, such as AVHRR on the NOAA satellites or VIIRS on the NPP satellites, but MODIS was chosen to both get a long record (which is not possible with a newly launched satellites, like NPP), and high resolution (which is better with MODIS compared to AVHRR).

Chapter 4

:Presentation of findings

In this chapter, the research conducted as a part of this thesis is presented. The section is divided into three parts. The first part gives an overview of the work done with improving the nudging capabilities in NorESM. This work is the base for all simulations carried out for this thesis, but is not fully documented through any of the papers. The second part briefly presents the different papers, with objectives, summaries, author contributions, main findings and main conclusions, while the last part summarizes the specific answers to the sub objectives of the thesis. Note that only a limited contribution to Paper I, and contributions specifically to the modelling part of Paper III are included in this thesis, thus only some of the findings from those papers are listed here.

4.1 Improved nudging capabilities in NorESM

4.1.1 Description of modifications

To be able to participate in model intercomparison studies, compare model outputs to observations, or reduce computational costs when simulating aerosol-cloud interactions, the nudging capabilities in NorESM were sought to be improved.

Before, NorESM was only set up to nudge to model produced meteorology. Through the work with this thesis, 19 years (2000-2018) of ERA-Interim nudging data with a temporal resolution of 6 hours were generated. This work included downloading the rawdata, converting it to a suitable format (NetCDF, Network Common Data Form), interpolating it to the NorESM-grid and modifying the files to include all information needed to serve as input for NorESM-simulations. Instructions on how to generate more nudging data, for example for different periods or different grids, were also produced. The Climate Data Operator (CDO), developed at the Max Planck Institute for Meteorology, was used for interpolation (*Schulzweida*, 2019). This method makes sure that mass is conserved by adjusting the surface pressure, without influencing the geostrophic velocities.

By using the old setup in NorESM for self-nudging, simulated cloud variables, such as LWP, differed greatly from those obtained with a free running version of the model. Figure 4.1(a) shows how LWP differed between simulations from a model version running with free meteorology, and simulations carried out with nudging towards mete-

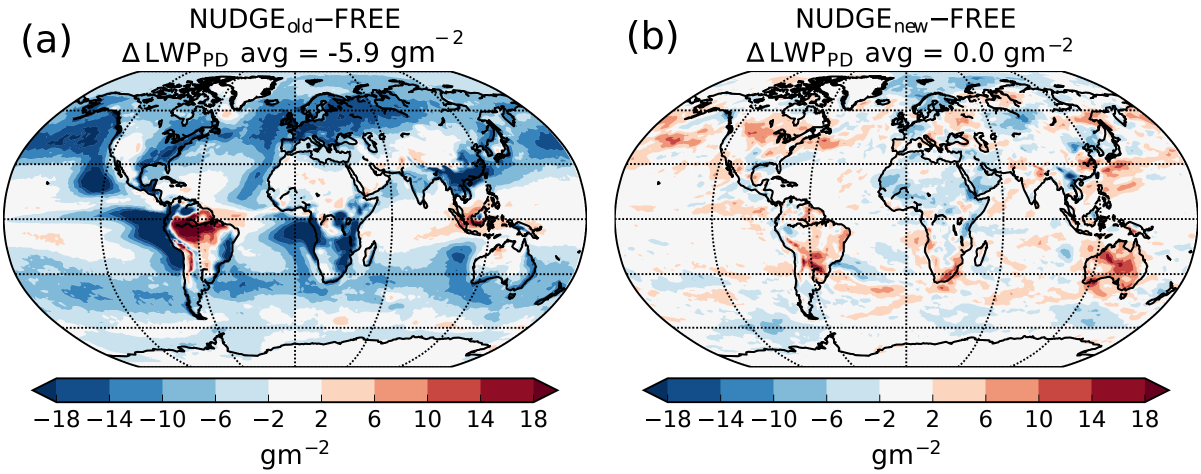

Figure 4.1: *Difference in total gridbox averaged Liqud Water Path (LWP) between a nudged and a free running version of the model. The values in the headers are global annual mean, averaged over the four last years of a simulation of six years. Both setups have fixed SSTs and sea-ice extent. The nudged simulation applied meteorology from the same free running version that it is compared to.* $NUDGE_{old}$ ***(a)*** *used the old nudging setup with a relaxation time scale of 0.5 h and nudging towards many fields (U, V, PS, TS, T, Q, QFLX, LHFLX, TAUX, TAUY), while* $NUDGE_{new}$ ***(b)*** *used the new setup with a relaxation time scale of 6 h and nudging towards only U, V and PS.*

orological fields produced by the free running model. Both setups have fixed SSTs and sea-ice extent. For the results obtained when nudging to represent the free running model version, they should not deviate as seen in Fig. 4.1(a). In order to solve this issue, the relaxation time scale was increased to 6 hours rather than 30 minutes, and the fields applied when nudging were reduced from 10 to just 3 (the horizontal wind components and the surface pressure). The results from the simulations in Fig. 4.1 and Tab. 4.1 show improvements.

According to Eq. (2.2), a relaxation time scale of only 30 minutes practically means that the meteorological fields were forced rather than nudged, since the time step of the model is 30 minutes. The meteorological fields from the free running version of NorESM applied for nudging are only written to files every 6 hours. For time steps in

Table 4.1: *Overview of simulations exploring nudging changes in NorESM.* ΔLWP_{PD} *is the difference in global annual mean LWP between a nudged and a free running version of the model. The nudged simulation applied meteorology from the same free running version that it is compared to. MANYVARS stands for all these variables: U, V, PS, TS, T, Q, QFLX, LHFLX, TAUX, TAUY.* τ *is the relaxation time scale.*

Case name	τ **[h]**	**Nudging variables**	ΔLWP_{PD} **[gm^{-2}]**
$NUDGE_{old}$	0.5	MANYVARS	-5.9
$NUDGE_{relax}$	6.0	MANYVARS	-1.7
$NUDGE_{UVPS}$	0.5	U, V, PS	0.6
$NUDGE_{new}$	6.0	U, V, PS	0.0

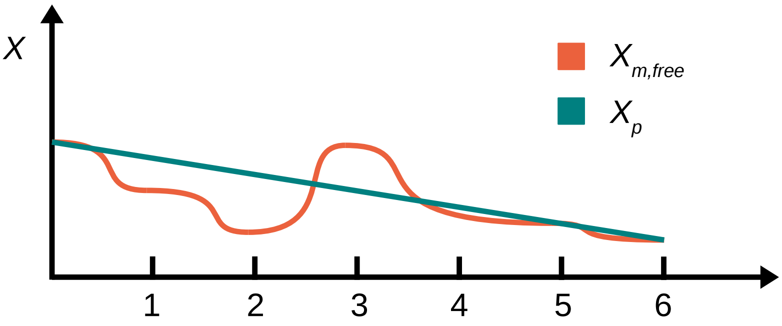

Figure 4.2: Illustration of a meteorological field from the free running version of the model, $X_{m,free}$ and the resulting inputdata, X_p, applied for nudging the same meteorological field in another simulation with constrained meteorology, following Eq. (2.2).

between, linear interpolation is applied, as illustrated in Fig. 4.2. Strong nudging or forcing to X_p can make a meteorological variable differ a lot from that of the free running model, $X_{m,free}$. Since many cloud properties strongly depend on meteorological conditions, too strong nudging or forcing could make modelled cloud properties from nudged simulations deviate considerably from the ones obtained with the free running model version.

The default setup in NorESM nudged the horizontal wind components (U, V), surface pressure (PS), surface temperature (TS), atmospheric temperature (T), atmospheric humidity (Q), surface fluxes of latent and sensible heat (QFLX, SHFLX) and surface drag (TAUX, TAUY). In one way, more variables nudged means more similar meteorology between the free running and the nudged version of the model, but it also means putting more control on the system, possibly dampening or removing rapid adjustments that we want to capture when modelling ERFaci. When for instance carrying out two sets of simulations, nudged to the same meteorological fields, but with different aerosol perturbations, we want to allow them to respond differently. Different responses to aerosol perturbations in for example temperature or humidity profiles could lead to different rapid cloud adjustments, which will not be captured if these profiles are strongly nudged. An increase in the relaxation time scale can help, while turning off all nudging of these fields will allow more of the rapid adjustments to be captured. Through the work with this thesis, the option of choosing which fields to nudge was included in NorESM, and the practice from now on is only nudging horizontal wind components and surface pressure. *Zhang et al.* (2014) shows that this is especially important when it comes to nudging to reanalysis data. They point out that nudging variables with known systematic biases in a model to that of reanalysis could result in different behavior in the model performance in simulating cloud responses to aerosol perturbations that is not representative for the model.

4.1.2 Overview of the use of nudging in the different papers

Nudging is applied in all papers of this thesis. Each paper gives a detailed description of the use and the results, but here follows a brief summary of the advantages of applying nudging in the studies.

- Paper I documents differences and similarities between modelled aerosol, cloud and radiation properties from a simulation with the free running version of CAM5.3-Oslo to a simulation nudged to ERA-Interim meteorology, as well as to various observations.

- Paper II applies nudging towards meteorology generated by the model itself in a previous simulation (self-nudging) to be able to carry out several sensitivity simulations to investigate the physical mechanisms behind the signal from the main simulations of the study. This would have been too computationally expensive to do with a free running version of the model.

- In Paper III, cloud responses to a volcanic eruption are compared between models and observations. Without the use of nudging towards meteorology from ERA-Interim reanalysis data, the results would have been biased by natural variability.

- Paper IV uses nudging towards meteorology generated by the model itself in a previous simulation to be able to carry out several sensitivity simulations without the need for long and expensive simulations. It also uses nudging towards ERA-Interim meteorology to simulate the same volcanic eruption as in Paper III.

4.2 Summary of papers

4.2.1 Paper I: ”A production-tagged aerosol module for Earth system models, OsloAero5.3 - extensions and updates for CAM5.3-Oslo”

Objective

To document updates of the aerosol module OsloAero5.3 and the atmospheric model CAM5.3-Oslo, and present, validate and discuss the model performance.

Summary

After documenting all updates, this paper presents the model performance through two sets of simulations, with free and nudged meteorology. Various aerosol, cloud and radiation properties generated by the different simulations are compared to one-another, to those generated by CAM5.3-Oslo's predecessor, and to those generated within model intercomparison studies and derived from observations.

Author contribution

I developed the ERA-Interim nudging data set applied for constraining the meteorology, updated the source code for nudging, and carried out one of the four main simulations in the paper (NUDGE_PD). I also modified the source code to carry out extra CDNC diagnostics, compared it to a dataset based on observations, produced the corresponding figures and participated in the discussion and writing of Chapter 4.3 - Cloud droplet concentration. I also participated in the discussions and writing of Chapter 5 - Interactions with radiation and clouds. Test simulations concerning the treatment of MSA (p. 3957) and the semi-direct effect (p. 3971) were also carried out by me.

Main findings

Only the findings presented below are the ones linked to the author contribution.

- ERFaci was modelled to be -1.34 Wm^{-2} when nudging the meteorology to that of ERA-Interim, and -1.3 ± 0.2 Wm^{-2} when not constraining the meteorology.

- With the model setup applied, estimates of ERFaci also includes the semi-direct effect, but test simulations found it to be small (-0.02 Wm^{-2}).

- Including the MSA contribution to SOA impacts the indirect effect (+0.10 Wm^{-2}). Whether MSA can participate in nucleation or only to condensation is found to be subordinate.

- Modelled values of CDNC are underestimated when considering averages over the oceanic areas between 60 °N and 60 °S, but overestimated downwind of major emission sources of mineral dust and biomass burning aerosols.

Main conclusion

The main conclusion related to the author contribution is that nudging can be applied to study aerosol-cloud interactions, without impacting the main results.

4.2.2 Paper II: ”Strong impacts on aerosol indirect effects from historical oxidant changes”

Objective

To investigate the impact of historical oxidant changes on the PD-PI aerosol indirect effect (ERFaci), and propose improved treatment of oxidants when modelling ERFaci.

Summary

In this paper, aerosol precursor gases in the PI-simulation, when modelling ERFaci with CAM5.3-Oslo, are exposed to PI-oxidants rather than PD-oxidants. The latter is common practice in the community when carrying out global model estimates of ERFaci. We argue that the precursor gases should be exposed to oxidants of its era for new particle formation and aerosol growth to be correct. Through several sensitivity tests, where impacts from the different oxidants were separated and the role of different chemical reactions were studied, the mechanisms behind the change in aerosol indirect effects were discovered.

Author contribution

I initiated and designed the study, carried out all model simulations, modified the source code and the input data files for all sensitivity simulations, generated the nudging data files and produced all figures. I also analysed the model output and wrote the text for the paper with help from the co-authors.

Main findings

These bullet points are copied from Section 5 in Paper II:

- The total aerosol indirect effect is reduced from -1.32 to -1.07 Wm^{-2} , mainly due to a cloud brightening in the modified PI simulation.

- NO_3 is the oxidant that contributes the most to the changes.

- When the precursor gases are exposed to an atmosphere with relatively lower oxidative power (PI oxidants vs. PD oxidants), their lifetimes increase and they are transported higher up in the atmosphere and horizontally towards more remote areas before they are oxidized.

- The increased lifetime of the precursor gases contributes to an increase in the formation of new aerosol and a decrease in the deposition and in the coagulation sink of the newly formed aerosols, contributing to an increase in the aerosol number concentration.

- A large portion of the new aerosol formation and the increase in aerosol number concentration occurs where the cloud-weighted susceptibility is high, giving a large impact on the radiative effects.

- The change from PD to PI oxidants in the PI simulation yields a shift in the chemical reactions towards increased production of condensate relative to the amount of gases that can nucleate, which increases the size of the aerosols, making it easier for them to activate.

Main conclusion

ERFaci is highly impacted by the oxidant changes between PI and PD, suggesting that historical oxidant changes should be taken into account for more credible model estimates of ERFaci.

4.2.3 Paper III: ”Strong constraints on aerosol–cloud interactions from volcanic eruptions”

Objective

To use the 2014-2015 fissure eruption in Holuhraun on Iceland as a testbed to study and constrain aerosol-cloud interaction, and evaluate associated model performances.

Summary

In this paper, satellite observations of cloud property changes caused by the eruption, and corresponding modelled changes by four global models, are presented.

Author contribution

I have carried out the simulations with CAM5.3-Oslo after preparing the model for the study. This includes generating emission files and reanalysis meteorology suited for this model. I was also involved in the discussions about the results in general.

Main findings

- Reduced cloud droplet size caused by the eruption was detected by satellite observations, while cloud adjustments through changes in LWP were not.
- The observations indicate that clouds are buffered against LWP change, and that forcing caused by rapid cloud adjustments (the second aerosol indirect effect) is small.
- Four global models, including CAM5.3-Oslo, were able to model the sign of the observed effect on cloud droplet size, but their LWP response differed.
- Most models, including CAM5.3-Oslo, showed large positive responses in LWP that were not identified in the observations.

Main conclusion

While the study enhance our confidence in a negative first aerosol indirect effect, it indicates that LWP are well buffered against aerosol changes, constraining estimates of ERFaci by abling rejections of results from climate models with an excessive response in LWP. It should be noted that this conclusion can be dampened by a more recent study indicating that cloud water content in clouds in cyclonic regions in the area was impacted by the eruption (*McCoy et al.*, 2018).

4.2.4 Paper IV: ”Exploring impacts of size-dependent evaporation and entrainment in a global model”

Objective

To investigate possible results of implementing size-dependent evaporation and entrainment in global models.

Summary

In this paper, LWP and LWP changes caused by aerosol perturbations in CAM5.3-Oslo are studied when letting evaporation and entrainment vary with the cloud droplet size. Both processes are scaled to be proportional to the total cloud droplet surface area. Effects on LWP changes caused by aerosol differences between PI and PD, and differences caused by the Holuhraun eruption, are studied. The results are also compared to those from simulations with other suggested modifications to the model that can impact aerosol indirect effects, such as the autoconversion parameterization and the inclusion of aerosol-cloud interactions in more cloud types than the stratiform ones.

Author contribution

I was involved in the planning of the project, carried out all model simulations, modified the source code for all sensitivity simulations, generated the nudging data files and produced all figures. I also analysed the model output and wrote the text for the paper with guidance from the co-authors.

Main findings

These bullet points are copied from Section 5 in Paper IV:

- Size-dependent entrainment, implemented by varying a tuning parameter in the expression for the entrainment efficiency between its maximum recommended values, had a moderate impact on the PD-PI total aerosol indirect effect (ERFaci), with a dampening from -1.07 Wm^{-2} to -0.98 Wm^{-2}. The result was mostly caused by a reduction in the PD-PI change in LWP.

- The same size-dependent entrainment reduced the LWP-response of the Holuhraun eruption slightly from +8.2 % to +7.8 %, much less than the impact of adding a suggested dampening of the dependency of cloud droplet number concentration to the autoconversion rate (+4.6 %).

- An additional size-dependent evaporation was also implemented, but the resulting change in the total aerosol indirect effect was caused by susceptibility changes due to enhanced evaporation rather than the size-dependency.

- Scaling the additionally implemented evaporation by the surface area differences between the PI- and the PD-droplets gave too small differences between the eras to impact aerosol indirect effects.

- Enhanced evaporation of small droplets only resulted in large impacts on LWP when either increasing the evaporation factor up to very large values, or allowing for mixing of moist air between the cloudtop layer and the layer above.
- When allowing for mixing between the layers, LWP increased in some areas as a response to enhanced evaporation. This increase in LWP was caused by enhanced shallow convection due to stability changes. It was also shown that the stability changes can have the opposite effect on LWP through altering the estimated inversion strength.

Main conclusion

Implementations of size-dependency on entrainment and evaporation processes in global models may not result in strong suppressions of initial increases in LWP when aerosol concentrations increase. The reasons are that droplet sizes between polluted and clean clouds can be too small, and that feedback processes linked to stability changes can be counteracting.

4.3 Summary of answers to the sub objectives

This section summarizes the specific answers to the sub objectives of the thesis.

1. **To investigate, apply and improve the nudging capabilities in NorESM.** Results carried out with the old nudging setup in NorESM were found to differ from results carried out with a version of the model running with free meteorology. This was improved by reducing the number of constrained variables, in addition to reducing the nudging intensity (increasing the relaxation time scale). The method of nudging was applied in all papers of the thesis.

2. **To develop and apply a reanalysis dataset for nudging in NorESM, enabling comparisons of modelled aerosol-cloud interactions to observations.** A nudging dataset suited for NorESM, based on 19 years of reanalysis data from ERA-Interim, was generated. This was applied in Paper III and IV to be able to compare modelled cloud responses to the Holuhraun eruption to those of satellite retrievals. It was also used in Paper I to show that various modelled aerosol, cloud and radiation properties carried out by a nudged version of the model were mostly similar to the same properties carried out by a version of the model running with free meteorology.

3. **To investigate the impact of historical oxidant changes on ERFaci, and propose improved treatment of oxidants when modelling ERFaci.** Paper II found that including oxidant changes between PI and PD is very important for the magnitude of the modelled ERFaci (+0.25 $\mathrm{Wm^{-2}}$, 19 % change), mainly because of its impact on the lifetime of the precursor gases, affecting both where, when and how aerosol formation, aerosol growth and cloud droplet activation occur. When modelling changes in aerosol-cloud interactions between different eras, the findings of this thesis suggest that not only aerosols and aerosol precursor gases should be switched between the two simulations, but also the oxidant fields. Aerosol precursor gases should be exposed to oxidants of its era.

4. **To identify issues linked to global modelling of rapid cloud adjustments by taking part in an intercomparison study that uses a recent volcanic eruption as a testbed to evaluate model performance in simulating aerosol-cloud interactions.** While satellite retrievals from the time of the eruption indicate that LWP are well buffered against aerosol changes, global models in Paper III did not find the same, indicating their inadequacy of simulating rapid cloud adjustments properly. Regarding the first aerosol indirect effect, global models were able to capture its sign and magnitude, as found from satellite retrievals, enhancing our confidence in it being both negative and of importance.

5. **To explore impacts on rapid cloud adjustments by implementing size-dependency on two processes with the potential to reduce cloudiness with increased aerosol concentration (evaporation and entrainment).** Paper IV found that implementations of size-dependency on entrainment and evaporation processes in global models may not result in strong suppressions of initial increases in LWP when aerosol concentrations increase. The reasons

for this result are that droplet sizes can be too small between polluted and clean clouds, and that feedback processes linked to stability changes can be counteracting. This highlights more complex aspects of the previously proposed buffering mechanisms of rapid cloud adjustments that has been in focus before.

Chapter 5

:Discussion, future outlook and concluding remarks

The overall objective of this thesis was to contribute towards enhancing the confidence in estimates of ERFaci through improved global modelling. This was addressed by three main topics in focus: (1) nudging, (2) historical changes impacting aerosol processes, and (3) rapid cloud adjustments. The first part of this chapter provides discussions of the results related to each of these topics, in addition to point out directions for future research within the field. The chapter ends with some concluding remarks, and a discussion on how the main objective was achieved and which relevance the findings from this thesis has to the larger scientific community.

5.1 Nudging

The advantages of the work with improving the nudging capabilities in NorESM are already discussed in Chapter 4.1. This work made it possible to achieve both objectives by applying NorESM in all the other papers, with the opportunity of constraining the meteorology to that of the observed and also enabling numerous sensitivity simulations due to lowered computational costs. When using the method of nudging, energy and momentum is not conserved. This means that one should be careful using this method when dynamical feedbacks are involved (*Lin et al.*, 2016; *Lohmann and Hoose*, 2009). Since ERFaci allows for rapid adjustments, e.g. feedbacks on a short time scale, all parts of ERFaci may not be captured when nudging. When studying ERFaci, one should be aware of the links between the nudged variables and the emissions and concentrations of aerosols. One example is that enhanced aerosol concentrations can lead to changes in the heating rates, and thus changes in the wind fields, which again can impact the wind-driven emissions of aerosols (sea salt, dust, DMS, oceanic OM, etc.) and further change the radiative impact of an aerosol perturbation. Only in cases where dynamical feedbacks are weak, results from model simulations with nudged meteorology will be comparable to those from a free running model.

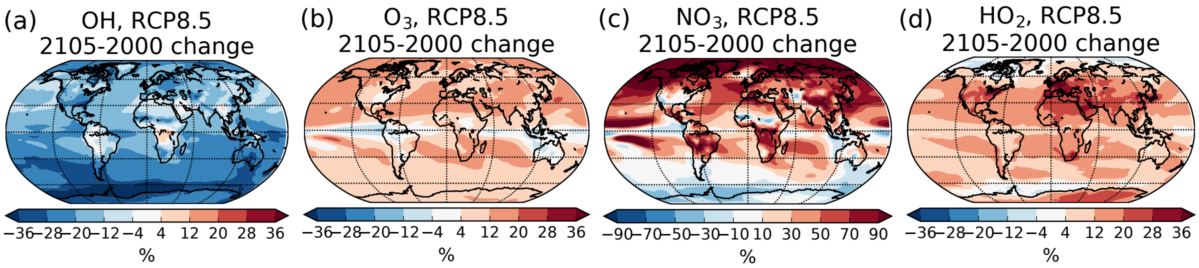

Figure 5.1: *Relative change in annual mean oxidant mixing ratio (mol mol^{-1}) from the surface and up to 550 hPa between present-day (year 2000) and year 2105, following RCP8.5. Note the different scales on the color bars.*

5.2 Historical changes impacting aerosol processes

5.2.1 Including historical oxidant changes

Through the work with Paper II, the treatment of the oxidants when carrying out model estimates of ERFaci was investigated, and an improved setup, with the use of different oxidant concentrations in PI and PD, was presented. This setup provides a more realistic aerosol formation and growth in the PI atmosphere, which is important to include in all global model estimates of ERFaci for reduced uncertainties and enhanced confidence. It should be emphasized that the results presented in this study only stem from one model, with its unique combination of treatments of physics and chemistry regarding aerosols and clouds. Although the strong modelled impact on ERFaci (+0.25 Wm^{-2}) could have been of a different magnitude if another model was used, the study contributes with new knowledge within the field by being the first to reveal and highlight changes in atmospheric processes regarding aerosol-cloud interactions when oxidant levels change. The process changes revealed are not unique for the studied period, thus also expected if studying oxidant changes over other time periods, for example in future projections. Exactly how much oxidant changes in the future will impact forcing estimates caused by aerosol-cloud interactions depends strongly on the level of future emissions. Figure 5.1 shows how the full chemistry model CAM-chem v3.5 in the study of *Lamarque et al.* (2010) predicted oxidant changes between year 2000 and year 2105, following the Representative Concentration Pathway 8.5 (RCP8.5). With reductions in the hydroxyl radical (OH), mainly due to loss through reactions with methane, and predominantly increases in the other oxidants, the overall effect is unknown and has yet to be simulated by global models. This is of interest in order to retrieve better estimates of how aerosols impact on clouds will impact global warming in the future. It should be pointed out that the RCP8.5-scenario is the most extreme scenario with a policy of ”business as usual” when it comes to emission pathways and mitigation strategies, and that oxidant changes will be different in other scenarios. Ozone (O_3), for instance, is projected to decrease under the RCP2.6, RCP4.5, and RCP6.0 scenarios due to reduced emissions of pollutants that favor O_3 production (*Kim et al.*, 2015). Also worth noting when modelling future projections is that the RCP-scenarios have a much more narrow range of outcomes regarding future air pollutant trajectories than the newly developed Shared Socioeconomic Pathways (SSP) scenarios that will serve as inputs for the simulations of future climate in CMIP6 (*Rao et al.*, 2017).

5.2.2 Including human impacts on natural emissions

In addition to the question of how oxidants should be treated when modelling ERFaci, questions of how to treat other parts of the model code can also be raised. Natural emissions are an example. Changed emission rates of aerosols and aerosol precursor gases are not only caused by enhancements through human activities like fossil fuel combustion and biomass burning. Changes also occur through our impact on natural emissions, but are generally not included in model estimates of ERFaci carried out using the fixed SST method (*Myhre et al.*, 2013). If anthropogenic activities have directly impacted natural emissions, and not only indirectly through temperature feedbacks, this raises the question of whether these differences in the natural emissions over the industrial era should be taken into account when modeling anthropogenic radiative forcings. Uncertainties in the magnitude of natural emissions have been highlighted by several studies as large contributors to uncertainties in ERFaci, since the impact of an aerosol perturbation depends on the initial concentration (*Carslaw et al.*, 2013; *Hoose et al.*, 2009; *Kirkevåg et al.*, 2008; *Lohmann et al.*, 2000; *Rap et al.*, 2013; *Scott et al.*, 2014). However, there is a lack of studies that have modeled how changes in these emissions directly caused by human activities may have impacted ERFaci.

Deforestation can be used as an example of how humans directly have impacted natural emissions. Previous model setups have included the additional emissions of organic matter, black carbon and SO_4 when trees are burned, but have not included the corresponding reduction in emissions of BVOCs due to fewer trees, or the increase in emissions of dust due to more crops and bare soil. To the extent that this has been included in models, it has been a part of the contribution to the total ERF over the historical period from land use change (*Myhre et al.*, 2013). *Scott et al.* (2014) presented model estimates of how the inclusion of several different representations of SOA formation from BVOCs affect the radiative effect in both PI and PD, but did not include changes in emissions of BVOCs between the eras. A representation of the second aerosol indirect effect was also lacking in the model applied. *Unger* (2014) simulated changes in radiative forcings caused by the reduction in BVOC emissions since PI, but focused on the impact on O_3, CH_4 and the direct aerosol effect of SOA, while excluding aerosol-cloud interactions in the simulations. *Scott et al.* (2018) modelled several different radiative forcings from PD and into the future caused by deforestation, including the effect of changes in short lived climate forcers. They point out that the inclusion of the first aerosol indirect effect due to reduced emissions of BVOCs shifts the RF from the short lived climate forcers from -0.08 Wm^{-2} to +0.12 Wm^{-2} for the greatest deforestation case, indicating that we also might had an effect between PI and PD. A recent study by *Zhu et al.* (2019) let the BVOC emissions in the PI simulation be impacted by both climate and land use from PI. The resulting ERFaci was 3.5 % less negative (+0.06 Wm^{-2}) compared to that of the setup using the same climate and land use in both PI and PD, but a separation of the impacts by land use change (forcing) and climate change (including feedbacks) was missing.

The direct anthropogenic impact on natural emissions, and the resulting change in ERFaci, could be an interesting topic for future studies. As an attempt to investigate how two such emission changes can impact ERFaci, simulations applying NorESM and the

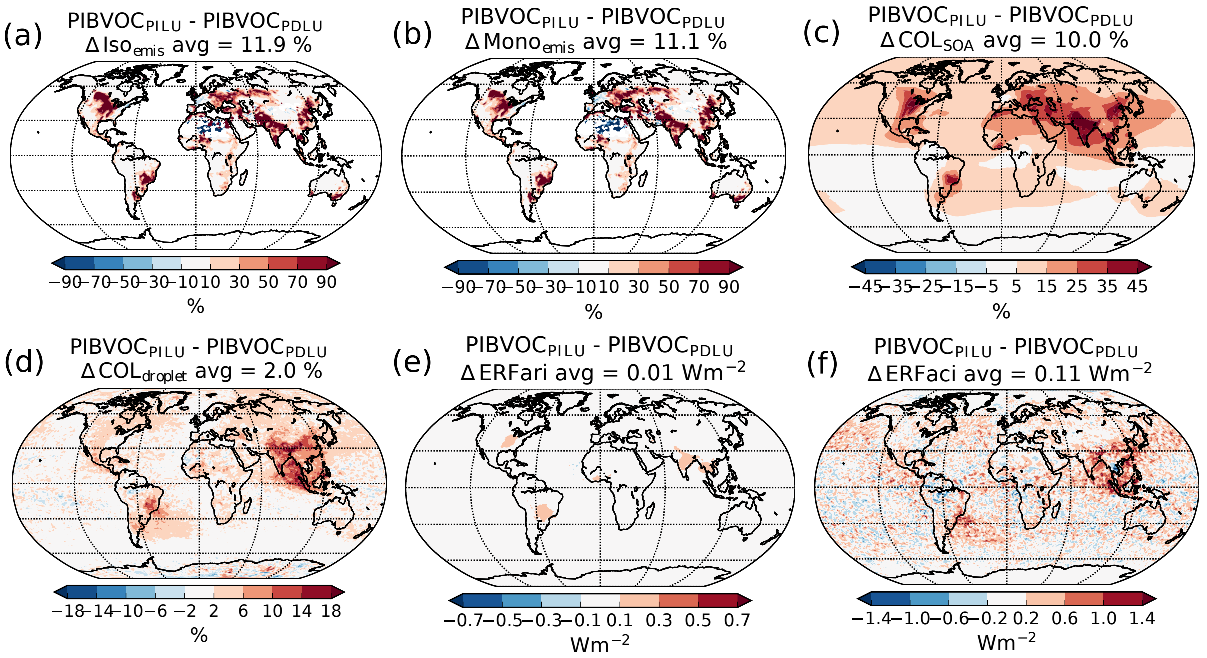

Figure 5.2: ***(a-d)*** *Relative change in aerosol and cloud properties from the default PI simulation PIBVOC$_{PDLU}$, to the modified PI simulations PIBVOC$_{PILU}$, where BVOC emissions are impacted by land use from PI rather than PD.* ***(a)*** *Emissions of isoprene,* ***(b)*** *emissions of monoterpene,* ***(c)*** *column burden of SOA and* ***(d)*** *column integrated cloud droplet number.* ***(e-f)*** *The resulting change in the direct aerosol effect (ERFari) and the total aerosol indirect effect (ERFaci) when replacing the simulation PIBVOC$_{PDLU}$ with PIBVOC$_{PILU}$.*

same setup as in Paper II (PDAER_PDOXI and PIAER_PIOXI) have already been carried out, but with different emissions of BVOCs and dust (separately) in the PI-simulation. Instead of using BVOC emissions impacted by land use from PD, emissions generated in a previous simulations that applied land use and land cover information from PI instead of PD were read from file every model timestep. The results from the simulation where the BVOC emissions were changed are shown in Fig. 5.2. More land covered by forests in PI results in moderate enhancements of the emissions of BVOCs and a resulting 10 % increase in the column burden of SOA in PI. While Fig. 5.2 shows that this results in a negligible impact on ERFari, the impact on ERFaci is moderate (+0.11 $\pm$ 0.01 Wm^{-2}, 10 %) due to enhanced activation of cloud droplets giving brighter clouds in PI, reducing the difference in reflectance between the eras. The corresponding effect of dust emission changes were negligible, both for ERFari (-0.01 $\pm$ 0.01 Wm^{-2}) and ERFaci (+0.01 $\pm$ 0.01 Wm^{-2}). A deeper analysis of the results, in addition to several simulations of other emission types or using other models for the same purpose can be the focus in future research studies. The question of whether these emissions changes should be included in model estimates of ERFaci should also be addressed in order to retrieve the full ERFaci, in addition to make modelling groups agree upon a setup for reduced uncertainties and enhanced confidence.

5.3 Rapid cloud adjustments

5.3.1 Advances in recent years

Paper III (*Malavelle et al.*, 2017) was one of the pioneering studies in its field using satellite observations to identify the lack of increase in LWP due to aerosol perturbations on a larger scale, despite reductions in cloud droplet size. It also presented large discrepancies in LWP response to aerosol perturbations between the satellite products and most models of the study. This highlighted the importance of further development of parameterizations involving rapid cloud adjustments in the models for improved model estimates of ERFaci. Although only few years have passed since Paper III was published, progress has been made within the field of research on rapid cloud adjustments to aerosol perturbations. Advances have been made in the observational constraints on the relationship between LWP and the cloud droplet number concentration (N_d) through the use of improved satellite products, which no longer need to rely on the crude assumption of Aerosol Optical Depth (AOD) being a measure of N_d (*Gryspeerdt et al.*, 2019; *Rosenfeld et al.*, 2019). In addition, *Toll et al.* (2017, 2019) have presented several satellite based observations of LWP-differences between clean clouds and polluted clouds downwind of know emissions sources, like volcanoes, cities, ship tracks and fires. All these studies indicated weak average response in LWP to N_d, underpinning the results in Paper III.

5.3.2 Separating the components of ERFaci

Toll et al. (2019) also uses their results to put numbers on the contributions to the radiative forcing from the Twomey effect (RFaci, -0.52 Wm^{-2}) and the LWP change (rapid cloud adjustments, +0.12 Wm^{-2}). A clear separation of the two effects can not at this point be calculated directly by the standard setup in NorESM or by using the monthly mean outputs from the model. Previous studies (*Gettelman*, 2015; *Malavelle et al.*, 2017) carried out new simulations with a constant value of the cloud droplet number concentration (N_d) in the autoconversion parameterization, and used the difference between this value and the result from simulations with the main setup as a measure of the radiative effect caused by the LWP change (rapid cloud adjustments). Although the autoconversion parameterization, which allows for suppressed rain formation when N_d increases, is the only process in most global models that can result in rapid cloud adjustments, this method of separating the effects has weaknesses. By using a constant value of N_d, even if using the global mean value of N_d in the default model setup, the clouds in this sensitivity setup can be very different due to the large spatial variability in N_d. This method will introduce too many droplets over ocean and too few over land, resulting in clouds with different susceptibility to aerosol perturbations than in the main model setup. For this reason, modelled estimates using this method to separate rapid cloud adjustments and RFaci may not represent the actual contribution from the different processes in the model.

Mülmenstädt et al. (2019) showed how the Partial Radiative Perturbations (PRP, *Colman and Mcavaney* (1997); *Wetherald and Manabe* (1988) approach can be applied to separate the contributions to ERFaci from changes in in-cloud droplet number, in-cloud

LWP and cloud fraction. Since the method is computationally expensive and time consuming by requiring 3 hourly output, in addition to new radiative transfer simulations, it is beyond the scope of this thesis to make use of it. While the method of *Mülmenstädt et al.* (2019) should be used in upcoming modelling studies regarding different components of ERFaci, a more simplified and crude separation of the components is introduced to get a first hint of the magnitude of the components relative to each other, enabling first comparisons to that of *Toll et al.* (2019). First, expressions of the cloud albedo (A) and the cloud optical thickness given by *Hobbs* (1993) are combined into Eq (5.1) to express how A varies with the effective radius of the cloud droplets (r_e) and LWP. If using the change in A caused by an aerosol perturbation as a measure of the shortwave component of ERFaci, dA due to changes in r_e (Eq. (5.2)) can be used as a measure of the Twomey effect (RFaci), while dA due to changes in LWP (Eq. (5.3)) can be a measure of the rapid cloud adjustments. If using this method on the output from simulations in paper II (PIAER_PIOXI and PDAER_PDOXI), the results show that 34 % of the albedo change from PI to PD is caused by the change in r_e, while 66 % is caused by the change in LWP. Converting this to forcings by using the modelled shortwave component of ERFaci from Paper II results in RFaci of -0.37 Wm^{-2} and rapid cloud adjustments of -0.66 Wm^{-2}. Even though this method is very crude compared to that of *Mülmenstädt et al.* (2019), using monthly mean output, not taking into account albedo differences due to zenith angle differences, and neglecting the longwave contribution, it is clear that the model produces far too much cooling caused by the LWP-change relative to RFaci if compared to the respective numbers of *Toll et al.* (2019) of -0.52 Wm^{-2} and +0.12 Wm^{-2}.

$$A = \left(1 + \frac{2}{3} \cdot \frac{6.7\rho_L r_e}{LWP}\right)^{-1} \tag{5.1}$$

$$dA_{re} = -\frac{4467LWP}{(LWP + 4467r_e)^2} dr_e \tag{5.2}$$

$$dA_{LWP} = \frac{4467r_e}{(LWP + 4467r_e)^2} d(LWP) \tag{5.3}$$

5.3.3 Proposed solutions to remaining challenges

Even if including buffering effects represented by enhanced entrainment feedback for small droplets as explored and proposed in Paper IV, the measure of the contributions to ERFaci by its two different components are still far away from those of *Toll et al.* (2019). Explored implementations of size-dependent evaporation in Paper IV can not solve this issue, due to small differences in evaporation between PI and PD, and the revealed counteracting feedback processes caused by stability changes. While observational constraints on the response of LWP to changes in $\mathrm{N_d}$ have improved over recent years, challenges linked to reducing the differences between models and observations still remain. *Rosenfeld et al.* (2019) highlight several important aspects concerning this issue. First, they show that even though LWP averaged over a larger domain does not increase much when N_d increases, they find high sensitivity of the cloud fraction to changes in N_d. Increased cloud fraction linked to increased N_d was also found by *Gryspeerdt et al.* (2016), which used satellite retrievals to find that aerosol influence on the liquid cloud fraction gives a contribution to ERFaci of -0.48 Wm^{-2} (-0.1 to -0.64 Wm^{-2}). With constant liquid content, clouds expanding horizontally impact radiation differently than clouds expanding vertically. The simulations carried out as a part of this thesis (for example PIAER_PIOXI and PDAER_PDOXI in Paper II) do not give any significant changes in cloud fraction between clean (PI) and polluted (PD) clouds. Reasons why the cloud fraction in NorESM, and probably in many other models as well, does not behave in the same way as found by *Rosenfeld et al.* (2019) is beyond the scope of this thesis, but should be an interesting topic for future studies. In these upcoming studies, the cloud fraction parameterization, and especially the one for the stratiform clouds which is often just based on relative humidity, should be examined. Secondly, *Rosenfeld et al.* (2019) speculate that enhanced cooling due to increases in cloud fraction might be compensated by enhanced warming caused by aerosol-cloud interactions in convective clouds, which are yet to be implemented in most global models. As pointed out in Paper IV, NorESM only include aerosol-cloud interactions in stratiform clouds. For reduced uncertainties and enhanced confidence in global model estimates of ERFaci in future studies, aerosol-cloud interactions should be implemented in all clouds.

5.3.4 An upcoming study

As a follow-up to Paper 3, the intercomparison project ”Volcanic ACI experiment (VolcACI)”, is ongoing within the framework of Aerosol Comparisons between Observations and Models (AEROCOM). In addition to further exploring the mechanisms behind the model responses to the Holuhraun eruption, it also includes more models, several sensitivity simulations and simulations of two other volcanic eruptions from Kilauea, Hawaii, in 2008 (*Yuan et al.*, 2011) and 2018. I am contributing to this study with simulations from NorESM.

5.4 Concluding remarks and implications

The overall objective of this thesis was to contribute towards enhancing the confidence in estimates of ERFaci through improved global modelling. As pointed out in Chapter 1, aerosols and clouds are the largest contributors to the uncertainty in the total preindustrial-to-present-day anthropogenic forcing, and the estimates of effective radiative forcing caused by cloud adjustments due to aerosols have the lowest level of confidence. As given in the description of the concept of confidence (see Chapter 2.1 and *Cubasch et al.* (2013)), it will be low if the agreement is low between estimates from observations, between estimates from models, and between estimates from both categories. Several parts of this thesis have facilitated for future estimates to show better agreement. One example is the ability to carry out model estimates of forcings related to aerosol-cloud interactions under approximately equal meteorological conditions as the observations to which they are compared. Another example is the proposed guidelines in Paper II of exposing the precursor gases to oxidants of its era when carrying out model estimates of ERFaci. If all models in an intercomparison study follow these guidelines, the results from models are expected to show better agreement than if the treatment of the oxidants vary between modelling groups. The level of confidence is also affected by how well the relevant physical and chemical processes are understood. In Paper II we show that model simulations can indeed capture aerosol-cloud related forcings due to different atmospheric oxidation capacaties. This enhances our confidence in the results being credible. Paper III enhances confidence in the negative first aerosol indirect effect, by increasing the amount of evidence. In this paper the effect was both detected in satellite retrievals and simulated by all models in the study. Paper III also claimed to constrain aerosol-cloud interactions by being able to reject model estimates of ERFaci with an excessive response in LWP, supported by several other recent studies presented in Chapter 5.3 (*Gryspeerdt et al.*, 2019; *Toll et al.*, 2017, 2019). However, conflicting results from recent studies regarding cloud water responses in cyclonic cloud systems (*McCoy et al.*, 2018) and impacts on the cloud fraction by aerosol changes (*Gryspeerdt et al.*, 2016; *Rosenfeld et al.*, 2019), in addition to implications of the findings in Paper IV, indicate that further research on rapid-cloud adjustments and associated model parameterizations still is needed.

As presented above, this thesis has improved global modelling of aerosol-cloud interactions, with results contributing to enhanced confidence in global model estimates of ERFaci. Although emissions of aerosols and aerosol precursor gases are predicted to be reduced by the policies aimed at improving air quality, enhanced confidence and reduced uncertainty in ERFaci are still crucial. Without knowing ERFaci, we do not know how much of the greenhouse gas warming the aerosols may be masking through aerosol-cloud interactions. This means that we are not able to attribute observed temperature changes to previous emissions of CO_2 and use this to find the climate sensitivity (introduced in Chapter 1). Knowing the climate sensitivity, which includes temperature changes directly caused by the forcing and by the following feedback processes, is needed to predict how much warming future emissions will entail. Improved estimates of climate sensitivity also lead to improved estimates of the remaining carbon budget, which is the amount of CO_2 we have left to emit to stay below a certain temperature limit (*Enting et al.*, 1994). Since aerosol-cloud interactions also are amongst the key factors controlling the hydrological cycle (see Chapter 1), the contributions from this thesis to enhancing the confidence in ERFaci can also improve predicted changes in precipitation.

While it is intrinsically difficult to provide certain answers to questions concerning the climate impact of aerosol-cloud interactions, this thesis has contributed in several ways to enhancing the confidence in ERFaci through global modelling.

Bibliography

Abdul-Razzak, H., and S. J. Ghan (2000), A parameterization of aerosol activation 2. Multiple aerosol types, *Journal of Geophysical Research Atmospheres*, *105*(D5), 6837–6844, doi:10.1029/1999JD901161. 3.1.3

Ackerman, A. S., M. P. Kirkpatrick, D. E. Stevens, and O. B. Toon (2004), The impact of humidity above stratiform clouds on indirect aerosol climate forcing., *Nature*, *432*(7020), 1014–1017, doi:10.1038/nature03137.1. 1.1, 2.4

Albrecht, B. A. (1989), Aerosols, cloud microphysics, and fractional cloudiness, *Science*, *245*(4923), 1227–1230, doi:10.1126/science.245.4923.1227. 1.1, 2.4

Altaratz, O., I. Koren, T. Reisin, A. Kostinski, G. Feingold, Z. Levin, and Y. Yin (2008), Aerosols' influence on the interplay between condensation, evaporation and rain in warm cumulus cloud, *Atmospheric Chemistry and Physics*, *8*(1), 15–24, doi:10.5194/acp-8-15-2008. 2.4

Andreae, M. O., R. J. Ferek, F. Bermond, K. P. Byrd, R. T. Engstrom, S. Hardin, P. D. Houmere, F. LeMarrec, H. Raemdonck, and R. B. Chatfield (1985), Dimethyl sulfide in the marine atmosphere., *Journal of Geophysical Research - Atmospheres*, *90*(D7), 12,891–12,900, doi:10.1029/JD090iD07p12891. 2.2

Bentsen, M., I. Bethke, J. B. Debernard, T. Iversen, A. Kirkevåg, Ø. Seland, H. Drange, C. Roelandt, I. A. Seierstad, C. Hoose, and J. E. Kristjánsson (2013), The Norwegian Earth System Model, NorESM1-M – Part 1: Description and basic evaluation of the physical climate, *Geoscientific Model Development*, *6*(3), 687–720, doi:10.5194/gmd-6-687-2013. 3.1.1

Berrisford, P., D. Dee, P. Poli, R. Brugge, K. Fielding, M. Fuentes, P. Kallberg, S. Kobayashi, S. Uppala, and A. Simmons (2011), The ERA-Interim Archive Version 2.0, *ERA report series*, *2*. 3.2.1

Bjerknes Centre (2015), EVA - Earth system modelling of climate Variations in the Anthropocene. Retrieved from https://www.bjerknes.uib.no/en/project/eva October 22, 2019. 1.2

Boilley, A., and L. Wald (2015), Comparison between meteorological re-analyses from ERA-Interim and MERRA and measurements of daily solar irradiation at surface, *Renewable Energy*, *75*, 135–143, doi:10.1016/j.renene.2014.09.042. 3.2.2

Bond, T. C., S. J. Doherty, D. W. Fahey, P. M. Forster, T. Berntsen, B. J. Deangelo, M. G. Flanner, S. Ghan, B. Kärcher, D. Koch, S. Kinne, Y. Kondo, P. K. Quinn,

M. C. Sarofim, M. G. Schultz, M. Schulz, C. Venkataraman, H. Zhang, S. Zhang, N. Bellouin, S. K. Guttikunda, P. K. Hopke, M. Z. Jacobson, J. W. Kaiser, Z. Klimont, U. Lohmann, J. P. Schwarz, D. Shindell, T. Storelvmo, S. G. Warren, and C. S. Zender (2013), Bounding the role of black carbon in the climate system: A scientific assessment, *Journal of Geophysical Research Atmospheres*, *118*(11), 5380–5552, doi:10.1002/jgrd.50171. 2.2

Bork, N., J. Elm, T. Olenius, and H. Vehkamäki (2014), Methane sulfonic acid-enhanced formation of molecular clusters of sulfuric acid and dimethyl amine, *Atmospheric Chemistry and Physics*, *14*(22), 12,023–12,030, doi:10.5194/acp-14-12023-2014. 2.2

Boucher, O., D. Randall, P. Artaxo, C. Bretherton, G. Feingold, P. Forster, V.-m. Kerminen, Y. Kondo, H. Liao, U. Lohmann, P. Rasch, S. Satheesh, S. Sherwood, B. Stevens, and X. Zhang (2013), Clouds and aerosols, in *Climate Change 2013 the Physical Science Basis: Working Group I Contribution to the Fifth Assessment Report of the Intergovernmental Panel on Climate Change*, vol. 9781107057, edited by T. Stocker, G.-K. D. Qin, M. Plattner, S. Tignor, J. Allen, A. Boschung, Y. Nauels, V. Xia, B. Midgley, and P.M., chap. 8, pp. 571–658, Cambridge University Press, Cambridge, United Kingdom and New York, NY, USA., doi:10.1017/CBO9781107415324.016. 1.1, 2.2, 2.3, 2.3.2

Bretherton, C. S., and S. Park (2009), A new moist turbulence parameterization in the community atmosphere model, *Journal of Climate*, *22*(12), 3422–3448, doi:10.1175/2008JCLI2556.1. 3.1.3

Bretherton, C. S., P. N. Blossey, and J. Uchida (2007), Cloud droplet sedimentation, entrainment efficiency, and subtropical stratocumulus albedo, *Geophysical Research Letters*, *34*(3), doi:10.1029/2006GL027648. 2.4

Carslaw, K. S., L. A. Lee, C. L. Reddington, K. J. Pringle, A. Rap, P. M. Forster, G. W. Mann, D. V. Spracklen, M. T. Woodhouse, L. A. Regayre, and J. R. Pierce (2013), Large contribution of natural aerosols to uncertainty in indirect forcing, *Nature*, *503*(7474), 67–71, doi:10.1038/nature12674. 5.2.2

Colman, R. A., and B. J. Mcavaney (1997), A study of general circulation model climate feedbacks determined from perturbed sea surface temperature experiments, *Journal of Geophysical Research*, *102*(D16), 19,383–19,402. 5.3.2

Crutzen, P., and J. Lelieveld (2001), HUMAN IMPACTS ON ATMOSPHERIC CHEMISTY, *Annual Review of Earth and Planetary Sciences*, *29*, 17–45. 2.2

Cubasch, U., D. Wuebbles, D. Chen, M. C. Facchini, D. Frame, N. Mahowald, and J.-G. Winther (2013), Introduction, in *Climate Change 2013: The Physical Science Basis. Contribution of Working Group I to the Fifth Assessment Report of the Intergovernmental Panel on Climate Change*, edited by Y. Ding, L. Mearns, and P. Wadhams, chap. 1, pp. 119–158, Cambridge University Press. 2.1, 5.4

Dalirian, M., A. Ylisirniö, A. Buchholz, D. Schlesinger, J. Ström, A. Virtanen, and I. Riipinen (2018), Cloud droplet activation of black carbon particles coated with organic compounds of varying solubility, *Atmospheric Chemistry and Physics*, *18*(16), 12,477–12,489, doi:10.5194/acp-18-12477-2018. 2.2

Enting, I. G., T. M. L. Wigley, and M. Heimann (1994), Future Emissions and Concentrations of Carbon Dioxide, *CSIRO Division of Atmospheric Research*, *31*. 5.4

Eyring, V., S. Bony, G. A. Meehl, C. A. Senior, B. Stevens, R. J. Stouffer, and K. E. Taylor (2016), Overview of the Coupled Model Intercomparison Project Phase 6 (CMIP6) experimental design and organization, *Geoscientific Model Development*, *9*(5), 1937–1958, doi:10.5194/gmd-9-1937-2016. 2.5.1

Feingold, G., H. Jiang, H. Xue, A. Teller, and Z. Levin (2006), Aerosol effects on the lifetime of shallow cumulus, *12th Conference on Cloud Physics, and 12th Conference on Atmospheric Radiation*, *33*(February), 2–5, doi:10.1029/2006GL026024. 2.4

Gettelman, A. (2015), Putting the clouds back in aerosol-cloud interactions, *Atmospheric Chemistry and Physics*, *15*(21), 12,397–12,411, doi:10.5194/acp-15-12397-2015. 1.1, 2.4, 3.1.3, 5.3.2

Gettelman, A., H. Morrison, and S. J. Ghan (2008), A new two-moment bulk stratiform cloud microphysics scheme in the community atmosphere model, version 3 (CAM3). Part II: Single-column and global results, *Journal of Climate*, *21*(15), 3660–3679, doi:10.1175/2008JCLI2116.1. 2.3.1, 3.1.3

Ghan, S., M. Wang, S. Zhang, S. Ferrachat, A. Gettelman, J. Griesfeller, Z. Kipling, U. Lohmann, H. Morrison, D. Neubauer, D. G. Partridge, P. Stier, T. Takemura, H. Wang, and K. Zhang (2016), Challenges in constraining anthropogenic aerosol effects on cloud radiative forcing using present-day spatiotemporal variability, *Proceedings of the National Academy of Sciences of the United States of America*, *113*(21), 5804–5811, doi:10.1073/pnas.1604888113. 2.5.2

Ginoux, P., M. Chin, I. Tegen, T. Goddard, J. Prospero, B. Holben, O. Dubovik, and S.-J. Lin (2001), Sources and distributions of dust aerosols simulated with the GOCART model, *Journal of Geophysical Research*, *106*, 20,255–20,273. 2.2

Grandey, B. S., D. Rothenberg, A. Avramov, Q. Jin, H.-h. Lee, X. Liu, Z. Lu, S. Albani, and C. Wang (2018), Effective radiative forcing in the aerosol–climate model CAM5.3-MARC-ARG, *Atmospheric Chemistry and Physics*, *18*, 15,783–15,810, doi:10.5194/acp-18-15783-2018. 1.1

Gregory, J. M., W. J. Ingram, M. A. Palmer, G. S. Jones, P. A. Stott, R. B. Thorpe, J. A. Lowe, T. C. Johns, and K. D. Williams (2004), A new method for diagnosing radiative forcing and climate sensitivity, *Geophysical Research Letters*, *31*(3), 2–5, doi:10.1029/2003GL018747. 2.5.1

Gryspeerdt, E., J. Quaas, and N. Bellouin (2016), Constraining the aerosol influence on cloud fraction, *Journal of Geophysical Research - Atmospheres*, *121*, 3566–3583, doi:10.1002/2015JD023744. 5.3.3, 5.4

Gryspeerdt, E., T. Goren, O. Sourdeval, J. Quaas, J. Mülmenstädt, S. Dipu, C. Unglaub, A. Gettelman, and M. Christensen (2019), Constraining the aerosol influence on cloud liquid water path, *Atmospheric Chemistry and Physics*, *19*(8), 5331–5347, doi: 10.5194/acp-19-5331-2019. 1.1, 5.3.1, 5.4

Hansen, J., M. Sato, R. Ruedy, L. Nazarenko, A. Lacis, G. A. Schmidt, G. Russell, I. Aleinov, M. Bauer, S. Bauer, N. Bell, B. Cairns, V. Canuto, M. Chandler, Y. Cheng, A. Del Genio, G. Faluvegi, E. Fleming, A. Friend, T. Hall, C. Jackman, M. Kelley, N. Kiang, D. Koch, J. Lean, J. Lerner, K. Lo, S. Menon, R. Miller, P. Minnis, T. Novakov, V. Oinas, J. Perlwitz, J. Perlwitz, D. Rind, A. Romanou, D. Shindell, P. Stone, S. Sun, N. Tausnev, D. Thresher, B. Wielicki, T. Wong, M. Yao, and S. Zhang (2005), Efficacy of climate forcings, *Journal of Geophysical Research D: Atmospheres*, *110*(18), 1–45, doi:10.1029/2005JD005776. 2.5.1

Heintzenberg, J., D. C. Covert, and R. Van Dingenen (2000), Size distribution and chemical composition of marine aerosols: A compilation and review, *Tellus, Series B: Chemical and Physical Meteorology*, *52*(4), 1104–1122, doi:10.3402/tellusb.v52i4.17090. 2.2

Hill, A. A., G. Feingold, and H. Jiang (2009), The influence of entrainment and mixing assumption on aerosol-cloud interactions in marine stratocumulus, *Journal of the Atmospheric Sciences*, *66*(5), 1450–1464, doi:10.1175/2008JAS2909.1. 2.4

Hobbs, P. V. (1993), *Aerosol-Cloud-Climate Interactions*, 1 ed., 235 pp., Academic Press. 5.3.2

Hodshire, A. L., P. Campuzano-Jost, J. K. Kodros, B. Croft, B. A. Nault, J. C. Schroder, J. L. Jimenez, and J. R. Pierce (2019), The potential role of methanesulfonic acid (MSA) in aerosol formation and growth and the associated radiative forcings, *Atmospheric Chemistry and Physics*, *19*(5), 3137–3160, doi:10.5194/acp-19-3137-2019. 2.2

Hofer, M., B. Marzeion, and T. Mölg (2012), Comparing the skill of different reanalyses and their ensembles as predictors for daily air temperature on a glaciated mountain (Peru), *Climate Dynamics*, *39*(7-8), 1969–1980, doi:10.1007/s00382-012-1501-2. 3.2.2

Hoffert, M. I., and C. Covey (1992), Deriving global climate sensitivity from paleoclimate reconstructions, *Nature*, *360*, 573–576. 1.1

Hoose, C., J. E. Kristjánsson, T. Iversen, A. Kirkevåg, Seland, and A. Gettelman (2009), Constraining cloud droplet number concentration in GCMs suppresses the aerosol indirect effect, *Geophysical Research Letters*, *36*(12), 1–5, doi:10.1029/2009GL038568. 5.2.2

Hoose, C., J. E. Kristjánsson, J.-P. Chen, and A. Hazra (2010), A Classical-Theory-Based Parameterization of Heterogeneous Ice Nucleation by Mineral Dust, Soot, and Biological Particles in a Global Climate Model, *Journal of the Atmospheric Sciences*, *67*, 2483–2503, doi:10.1175/2010JAS3425.1. 3.1.3

IPCC (2013), Summary for Policymakers, in *Climate Change 2013: The Physical Science Basis. Contribution of Working Group I to the Fifth Assessment Report of the Intergovernmental Panel on Climate Change*, edited by T. F. Stocker, D. Quin, G.-K. Plattner, M. Tignor, S. K. Allen, J. Boschung, A. Nauels, Y. Xia, V. Bex, and P. M. Midgley, pp. 3–30, Cambridge University Press, Cambridge, United Kingdom and New York, NY, USA, doi:10.1017/CBO9781107415324.004. 1.1, 1.1, 2.1

Iversen, T., and Ø. Seland (2002), A scheme for process-tagged SO4 and BC aerosols in NCAR CCM3: Validation and sensitivity to cloud processes, *Journal of Geophysical Research Atmospheres*, *107*(24), doi:10.1029/2001JD000885. 3.1.2

Iversen, T., M. Bentsen, I. Bethke, J. B. Debernard, A. Kirkevåg, Ø. Seland, H. Drange, J. E. Kristjansson, I. Medhaug, M. Sand, and I. A. Seierstad (2013), The Norwegian Earth System Model, NorESM1-M – Part 2: Climate response and scenario projections, *Geoscientific Model Development*, *6*(2), 389–415, doi:10.5194/gmd-6-389-2013. 3.1.1

Jeuken, A. B., P. C. Siegmund, L. C. Heijboer, J. Feichter, and L. Bengtsson (1996), On the potential of assimilating meteorological analyses in a global climate model for the purpose of model validation, *Journal of Geophysical Research Atmospheres*, *101*(D12), 16,939–16,950, doi:10.1029/96JD01218. 1.1, 2.5.2

Jiang, H., and G. Feingold (2006), Effect of aerosol on warm convective clouds: Aerosol-cloud surface flux feedbacks in a new coupled large eddy model, *Journal of Geophysical Research Atmospheres*, *111*(1), 1–12, doi:10.1029/2005JD006138. 2.4

Kim, M. J., R. J. Park, C. H. Ho, J. H. Woo, K. C. Choi, C. K. Song, and J. B. Lee (2015), Future ozone and oxidants change under the RCP scenarios, *Atmospheric Environment*, *101*, 103–115, doi:10.1016/j.atmosenv.2014.11.016. 5.2.1

King, M. D., W. P. Menzel, Y. J. Kaufman, D. Tanré, B. C. Gao, S. Platnick, S. A. Ackerman, L. A. Remer, R. Pincus, and P. A. Hubanks (2003), Cloud and aerosol properties, precipitable water, and profiles of temperature and water vapor from MODIS, *IEEE Transactions on Geoscience and Remote Sensing*, *41*(2 PART 1), 442–456, doi:10.1109/TGRS.2002.808226. 3.3.1

Kipling, Z., P. Stier, C. E. Johnson, G. W. Mann, N. Bellouin, S. E. Bauer, T. Bergman, M. Chin, T. Diehl, S. J. Ghan, T. Iversen, A. Kirkevåg, H. Kokkola, X. Liu, G. Luo, T. Van Noije, K. J. Pringle, K. Von Salzen, M. Schulz, Ø. Seland, R. B. Skeie, T. Takemura, K. Tsigaridis, and K. Zhang (2016), What controls the vertical distribution of aerosol? Relationships between process sensitivity in HadGEM3-UKCA and inter-model variation from AeroCom Phase II, *Atmospheric Chemistry and Physics*, *16*(4), 2221–2241, doi:10.5194/acp-16-2221-2016. 2.5.2

Kirkevåg, A., and T. Iversen (2002), Global direct radiative forcing by process-parameterized aerosol optical properties, *Journal of Geophysical Research D: Atmospheres*, *107*(20), doi:10.1029/2001JD000886. 3.1.2

Kirkevåg, A., T. Iversen, and A. Dahlback (1999), On radiative effects of black carbon and sulphate aerosols, *Atmospheric Environment*, *33*(17), 2621–2635, doi:10.1016/S1352-2310(98)00309-4. 3.1.2

Kirkevåg, A., T. Iversen, Ø. Seland, and J. E. Kristjánsson (2005), Revised schemes for optical parameters and cloud condensation nuclei, (128), 1–29. 3.1.2

Kirkevåg, A., T. Iversen, Ø. Seland, J. B. Debernard, T. Storelvmo, and J. E. Kristjánsson (2008), Aerosol-cloud-climate interactions in the climate model CAM-Oslo, *Tellus, Series A: Dynamic Meteorology and Oceanography*, *60 A*(3), 492–512, doi:10.1111/j.1600-0870.2008.00313.x. 3.1.2, 5.2.2

Kirkevåg, A., T. Iversen, Ø. Seland, C. Hoose, J. E. Kristjánsson, H. Struthers, A. M. L. Ekman, S. Ghan, J. Griesfeller, E. D. Nilsson, and M. Schulz (2013), Aerosol–climate interactions in the Norwegian Earth System Model – NorESM1-M, *Geoscientific Model Development*, *6*(1), 207–244, doi:10.5194/gmd-6-207-2013. 3.1.1, 3.1.2

Kirkevåg, A., A. Grini, D. Olivié, Ø. Seland, K. Alterskjær, M. Hummel, I. H. Karset, A. Lewinschal, X. Liu, R. Makkonen, I. Bethke, J. Griesfeller, M. Schulz, and T. Iversen (2018), A production-tagged aerosol module for earth system models, OsloAero5.3-extensions and updates for CAM5.3-Oslo, *Geoscientific Model Development*, *11*(10), 3945–3982, doi:10.5194/gmd-11-3945-2018. 3.1.1, 3.1.2

Koffi, B., M. Schulz, Bréon F.-M., F. Dentener, S. B. M., J. Griesfeller, D. Winker, Y. Balkanski, S. E. Bauer, N. Bellouin, T. Berntsen, H. Bian, M. Chin, T. Diehl, R. Easter, S. Ghan, U. L. . Didier A. Hauglustaine 3 , Trond Iversen 2, 13 , Alf Kirkevåg 2 , Xiaohong Liu 12, 14, S. D. S. . Gunnar Myhre 9 , Phil Rasch 10 , Øyvind Seland 2 , Ragnhild B. Skeie 9, . Philip Stier 16 , Jason Tackett 17 , Toshihiko Takemura 18 , Kostas Tsigaridis 5, 6 , Maria Raffaella Vuolo 3, and . Jinho Yoon 12, 20 , and Kai Zhang 12 (2016), Evaluation of the aerosol vertical distribution in global aerosol models through comparison against CALIOP measurements: AeroCom phase II results, *Journal of Geophysical Research: Atmospheres*, pp. 7254–7283, doi:10.1002/2015JD024639. 2.5.2

Köhler, H. (1936), The nucleus in and the growth of hygroscopic droplets, *Transactions of the Faraday Society*, *32*(1152), 1152–1161, doi:10.1039/TF9363201152. 2.3.1

Kooperman, G. J., M. S. Pritchard, S. J. Ghan, M. Wang, R. C. Somerville, and L. M. Russell (2012), Constraining the influence of natural variability to improve estimates of global aerosol indirect effects in a nudged version of the Community Atmosphere Model 5, *Journal of Geophysical Research Atmospheres*, *117*(23), doi:10.1029/2012JD018588. 1.1, 2.5.2

Koren, I., L. A. Remer, O. Altaratz, J. V. Martins, and A. Davidi (2010), Aerosol-induced changes of convective cloud anvils produce strong climate warming, *Atmospheric Chemistry and Physics*, *10*, 5001–5010, doi:10.5194/acp-10-5001-2010. 2.4

Kulmala, M., H. Vehkamäki, T. Petäjä, M. Dal Maso, A. Lauri, V. M. Kerminen, W. Birmili, and P. H. McMurry (2004), Formation and growth rates of ultrafine atmospheric particles: A review of observations, *Journal of Aerosol Science*, *35*(2), 143–176, doi: 10.1016/j.jaerosci.2003.10.003. 2.2

Lamarque, J. F., T. C. Bond, V. Eyring, C. Granier, A. Heil, Z. Klimont, D. Lee, C. Liousse, A. Mieville, B. Owen, M. G. Schultz, D. Shindell, S. J. Smith, E. Stehfest, J. Van Aardenne, O. R. Cooper, M. Kainuma, N. Mahowald, J. R. McConnell, V. Naik, K. Riahi, and D. P. Van Vuuren (2010), Historical (1850-2000) gridded anthropogenic and biomass burning emissions of reactive gases and aerosols: Methodology and application, *Atmospheric Chemistry and Physics*, *10*(15), 7017–7039, doi: 10.5194/acp-10-7017-2010. 3.1.2, 5.2.1

Lathière, J., C. N. Hewitt, and D. J. Beerling (2010), Sensitivity of isoprene emissions from the terrestrial biosphere to 20th century changes in atmospheric CO 2 concentration, climate, and land use, *Global Biogeochemical Cycles*, *24*(1), n/a–n/a, doi:10.1029/2009gb003548. 2.2

Lin, G., H. Wan, K. Zhang, Y. Qian, and S. Ghan (2016), Can nudging be used to quantify model sensitivities in precipitation and cloud forcing?, *Journal of Advances in Modeling Earth Systems*, *8*, 1289–1309, doi:10.1002/2013MS000282.Received. 2.5.2, 5.1

Lindsay, R., M. Wensnahan, A. Schweiger, and J. Zhang (2014), Evaluation of seven different atmospheric reanalysis products in the arctic, *Journal of Climate*, *27*(7), 2588–2606, doi:10.1175/JCLI-D-13-00014.1. 3.2.2

Liu, H., J. Guo, I. Koren, O. Altaratz, G. Dagan, Y. Wang, P. Zhai, J. H. Jiang, and Y. L. Yung (2019), Non-Monotonic Aerosol Effect on Precipitation in Convective Clouds over Tropical Oceans, *Nature Scientific Reports*, *9*(7809), 1–7, doi:10.1038/s41598-019-44284-2. 2.4

Liu, X., P. L. Ma, H. Wang, S. Tilmes, B. Singh, R. C. Easter, S. J. Ghan, and P. J. Rasch (2016), Description and evaluation of a new four-mode version of the Modal Aerosol Module (MAM4) within version 5.3 of the Community Atmosphere Model, *Geoscientific Model Development*, *9*(2), 505–522, doi:10.5194/gmd-9-505-2016. 3.1.1

Loeb, N. G., D. R. Doelling, H. Wang, W. Su, C. Nguyen, J. G. Corbett, L. Liang, C. Mitrescu, F. G. Rose, and S. Kato (2018), Clouds and the Earth'S Radiant Energy System (CERES) Energy Balanced and Filled (EBAF) top-of-atmosphere (TOA) edition-4.0 data product, *Journal of Climate*, *31*(2), 895–918, doi:10.1175/JCLI-D-17-0208.1. 2.3.2

Lohmann, U. (2017), Anthropogenic Aerosol Influences on Mixed-Phase Clouds, pp. 32–44, doi:10.1007/s40641-017-0059-9. 2.4

Lohmann, U., and C. Hoose (2009), Sensitivity studies of different aerosol indirect effects in mixed-phase clouds, *Atmospheric Chemistry and Physics*, *9*(22), 8917–8934, doi:10.5194/acp-9-8917-2009. 5.1

Lohmann, U., J. Feichter, J. Penner, and R. Leaitch (2000), Indirect effect of sulfate and carbonaceous aerosols: A mechanistic treatment, *Journal of Geophysical Research: Atmospheres*, *105*(D10), 12,193–12,206, doi:10.1029/1999JD901199. 5.2.2

Lohmann, U., F. Luond, and F. Mahrt (2016), *An Introduction to Clouds*, 1 ed., Cambridge University Press, doi:10.1017/cbo9781139087513. 2.2, 2.3.1

Lovelock, J. E., R. E. Maggs, and Rasmussen R. A. (1972), Atmospheric Dimethyl Sulphide and the Natural Sulphur Cycle, *Nature*, *237*, 452–453, doi:10.1038/237452a0. 2.2

Mäkelä, J. M., S. Ylikoivisto, V. Hiltunen, W. Seidl, E. Swietlicki, K. Teinilä, M. Sillanpää, I. K. Koponen, J. Paatero, K. Rosman, and K. Hämeri (2001), Chemical composition of aerosol during particle formation events in boreal forest, *Tellus, Series B: Chemical and Physical Meteorology*, *53*(4), 380–393, doi:10.3402/tellusb.v53i4.16610. 2.2

Makkonen, R., Ø. Seland, A. Kirkevåg, T. Iversen, and J. E. Kristjánsson (2014), Evaluation of aerosol number concentrations in NorESM with improved nucleation parameterization, *Atmospheric Chemistry and Physics*, *14*(10), 5127–5152, doi:10.5194/acp-14-5127-2014. 3.1.2

Malavelle, F. F., J. M. Haywood, A. Jones, A. Gettelman, L. Clarisse, S. Bauduin, R. P. Allan, I. H. H. Karset, J. E. Kristjánsson, L. Oreopoulos, N. Cho, D. Lee, N. Bellouin, O. Boucher, D. P. Grosvenor, K. S. Carslaw, S. Dhomse, G. W. Mann, A. Schmidt, H. Coe, M. E. Hartley, M. Dalvi, A. A. Hill, B. T. Johnson, C. E. Johnson, J. R. Knight, F. M. O'Connor, P. Stier, G. Myhre, S. Platnick, G. L. Stephens, H. Takahashi, and T. Thordarson (2017), Strong constraints on aerosol-cloud interactions from volcanic eruptions, *Nature*, *546*(7659), 485–491, doi:10.1038/nature22974. 1.1, 2.5.2, 5.3.1, 5.3.2

Mann, G. W., K. S. Carslaw, C. L. Reddington, K. J. Pringle, M. Schulz, A. Asmi, D. V. Spracklen, D. A. Ridley, M. T. Woodhouse, L. A. Lee, K. Zhang, S. J. Ghan, R. C. Easter, X. Liu, P. Stier, Y. H. Lee, P. J. Adams, H. Tost, J. Lelieveld, S. E. Bauer, K. Tsigaridis, T. P. Van Noije, A. Strunk, E. Vignati, N. Bellouin, M. Dalvi, C. E. Johnson, T. Bergman, H. Kokkola, K. Von Salzen, F. Yu, G. Luo, A. Petzold, J. Heintzenberg, A. Clarke, J. A. Ogren, J. Gras, U. Baltensperger, U. Kaminski, S. G. Jennings, C. D. O'Dowd, R. M. Harrison, D. C. Beddows, M. Kulmala, Y. Viisanen, V. Ulevicius, N. Mihalopoulos, V. Zdimal, M. Fiebig, H. C. Hansson, E. Swietlicki, and J. S. Henzing (2014), Intercomparison and evaluation of global aerosol microphysical properties among AeroCom models of a range of complexity, *Atmospheric Chemistry and Physics*, *14*(9), 4679–4713, doi:10.5194/acp-14-4679-2014. 2.5.2

McCoy, D. T., P. R. Field, A. Schmidt, D. P. Grosvenor, F. A. Bender, B. J. Shipway, A. A. Hill, J. M. Wilkinson, and G. S. Elsaesser (2018), Aerosol midlatitude cyclone indirect effects in observations and high-resolution simulations, *Atmospheric Chemistry and Physics*, *18*(8), 5821–5846, doi:10.5194/acp-18-5821-2018. 1.1, 4.2.3, 5.4

Michibata, T., K. Suzuki, Y. Sato, and T. Takemura (2016), The source of discrepancies in aerosol–cloud–precipitation interactions between GCM and A-Train retrievals, *Atmospheric Chemistry and Physics*, *16*, 15,413–15,424, doi:10.5194/acp-16-15413-2016. 1.1

Morrison, H., and A. Gettelman (2008), A new two-moment bulk stratiform cloud microphysics scheme in the community atmosphere model, version 3 (CAM3). Part I: Description and numerical tests, *Journal of Climate*, *21*, 3642–3659, doi:10.1175/2008JCLI2105.1. 2.3.1, 3.1.3

Mülmenstädt, J., E. Gryspeerdt, M. Salzmann, S. Dipu, and J. Quaas (2019), Separating radiative forcing by aerosol–cloud interactions and fast cloud adjustments in the ECHAM–HAMMOZ aerosol–climate model using the method of partial radiative perturbations, *Atmospheric Chemistry and Physics Discussions*, (January), 1–20, doi:10.5194/acp-2018-1304. 5.3.2

Myhre, G., D. Shindell, F.-M. Bréon, W. Collins, J. Fuglestvedt, J. Huang, D. Koch, J.-F. Lamarque, D. Lee, B. Mendoza, T. Nakajima, A. Robock, G. Stephens, T. Takemura, and H. Zhang (2013), Anthropogenic and Natural Radiative Forcing, in *Climate Change 2013: The Physical Science Basis. Contribution of Working Group I to the Fifth Assessment Report of the Intergovernmental Panel on Climate Change*, edited by T. Stocker, G.-K. Qin, M. Plattner, S. Tignor, J. Allen, A. Boschung, Y. Nauels, V. Xia, and B. Midgley, chap. 7, pp. 657–740, Cambridge University Press, doi:10.1017/CBO9781107415324.018. 1.1, 1.1, 2.1, 5.2.2

NASA (2010), Ship Tracks Reveal Pollution's Effects on Clouds. Retrieved from https://svs.gsfc.nasa.gov/3667 October 9, 2019. 2.4

Neale, R. B., C.-C. Chen, A. Gettelman, P. H. Lauritzen, S. Park, D. L. Williamson, A. J. Conley, R. Garcia, D. Kinnison, J.-F. Lamarque, D. Marsh, M. Mills, A. K. Smith, S. Tilmes, F. Vitt, H. Morrison, P. Cameron-Smith, W. D. Collins, M. J. Iacono, R. C. Easter, S. J. Ghan, X. Liu, P. J. Rasch, and M. A. Taylor (2012), CAM5 Description. 3.1.1

Neubauer, D., W. M. Christensen, A. C. Poulsen, and U. Lohmann (2017), Unveiling aerosol-cloud interactions - Part 2: Minimising the effects of aerosol swelling and wet scavenging in ECHAM6-HAM2 for comparison to satellite data, *Atmospheric Chemistry and Physics*, *17*(21), 13,165–13,185, doi:10.5194/acp-17-13165-2017. 1.1

Paasonen, P., T. Nieminen, E. Asmi, H. E. Manninen, T. Petäjä, C. Plass-Dülmer, H. Flentje, W. Birmili, A. Wiedensohler, U. Hõrrak, A. Metzger, A. Hamed, A. Laaksonen, M. C. Facchini, V. M. Kerminen, and M. Kulmala (2010), On the roles of sulphuric acid and low-volatility organic vapours in the initial steps of atmospheric new particle formation, *Atmospheric Chemistry and Physics*, *10*(22), 11,223–11,242, doi:10.5194/acp-10-11223-2010. 3.1.2

Pacifico, F., G. A. Folberth, C. D. Jones, S. P. Harrison, and W. J. Collins (2012), Sensitivity of biogenic isoprene emissions to past, present, and future environmental conditions and implications for atmospheric chemistry, *Journal of Geophysical Research Atmospheres*, *117*(22), 1–13, doi:10.1029/2012JD018276. 2.2

Park, S., and C. S. Bretherton (2009), The University of Washington shallow convection and moist turbulence schemes and their impact on climate simulations with the community atmosphere model, *Journal of Climate*, *22*(12), 3449–3469, doi:10.1175/2008JCLI2557.1. 3.1.3

Park, S., C. S. Bretherton, and P. J. Rasch (2014), Integrating Cloud Processes in the Community Atmosphere Model, Version 5, *Journal of Climate*, *27*(18), 6821–6856, doi:10.1175/JCLI-D-14-00087.1. 3.1.3

Platnick, S., M. D. King, S. A. Ackerman, W. P. Menzel, B. A. Baum, J. C. Riédi, and R. A. Frey (2003), The MODIS cloud products: Algorithms and examples from Terra, *IEEE Transactions on Geoscience and Remote Sensing*, *41*(2 PART 1), 459–472, doi:10.1109/TGRS.2002.808301. 3.3.1

Pruppacher, H. R., and J. D. Klett (1997), *Microphysics of Clouds and Precipitation*, 2 ed., 954 pp., Kluwer Academic Publishers. 2.4

Putaud, J. P., R. Van Dingenen, A. Alastuey, H. Bauer, W. Birmili, J. Cyrys, H. Flentje, S. Fuzzi, R. Gehrig, H. C. Hansson, R. M. Harrison, H. Herrmann, R. Hitzenberger, C. Hüglin, A. M. Jones, A. Kasper-Giebl, G. Kiss, A. Kousa, T. A. Kuhlbusch, G. Löschau, W. Maenhaut, A. Molnar, T. Moreno, J. Pekkanen, C. Perrino, M. Pitz, H. Puxbaum, X. Querol, S. Rodriguez, I. Salma, J. Schwarz, J. Smolik, J. Schneider, G. Spindler, H. ten Brink, J. Tursic, M. Viana, A. Wiedensohler, and F. Raes (2010), A European aerosol phenomenology - 3: Physical and chemical characteristics of particulate matter from 60 rural, urban, and kerbside sites across Europe, *Atmospheric Environment*, *44*(10), 1308–1320, doi:10.1016/j.atmosenv.2009.12.011. 2.2

Quaas, J., Y. Ming, S. Menon, T. Takemura, M. Wang, J. E. Penner, A. Gettelman, U. Lohmann, N. Bellouin, O. Boucher, A. M. Sayer, G. E. Thomas, A. McComiskey, G. Feingold, C. Hoose, J. E. Kristjánsson, X. Liu, Y. Balkanski, L. J. Donner, P. A. Ginoux, P. Stier, B. Grandey, J. Feichter, I. Sednev, S. E. Bauer, D. Koch, R. G. Grainger, A. Kirkevåg, T. Iversen, Ø. Seland, R. Easter, S. J. Ghan, P. J. Rasch, H. Morrison, J.-F. Lamarque, M. J. Iacono, S. Kinne, and M. Schulz (2009), Aerosol indirect effects - general circulation model intercomparison and evaluation with satellite data, *Atmospheric Chemistry and Physics*, *9*(22), 8697–8717, doi:10.5194/acp-9-8697-2009. 1.1, 2.4

Rao, S., Z. Klimont, S. J. Smith, R. Van Dingenen, F. Dentener, L. Bouwman, K. Riahi, M. Amann, B. L. Bodirsky, D. P. van Vuuren, L. Aleluia Reis, K. Calvin, L. Drouet, O. Fricko, S. Fujimori, D. Gernaat, P. Havlik, M. Harmsen, T. Hasegawa, C. Heyes, J. Hilaire, G. Luderer, T. Masui, E. Stehfest, J. Strefler, S. van der Sluis, and M. Tavoni (2017), Future air pollution in the Shared Socio-economic Pathways, *Global Environmental Change*, *42*, 346–358, doi:10.1016/j.gloenvcha.2016.05.012. 5.2.1

Rap, A., C. E. Scott, D. V. Spracklen, N. Bellouin, P. M. Forster, K. S. Carslaw, A. Schmidt, and G. Mann (2013), Natural aerosol direct and indirect radiative effects, *Geophysical Research Letters*, *40*(12), 3297–3301, doi:10.1002/grl.50441. 5.2.2

Rosenfeld, D., S. Sherwood, R. Wood, and L. Donner (2014), Climate Effects of Aerosol-Cloud Interactions, *Science*, *343*(January), 379–381. 2.4

Rosenfeld, D., Y. Zhu, M. Wang, Y. Zheng, T. Goren, and S. Yu (2019), Aerosol-driven droplet concentrations dominate coverage and water of oceanic low-level clouds, *Science*, *363*(6427), doi:10.1126/science.aav0566. 5.3.1, 5.3.3, 5.4

Rotstayn, L. D., and J. E. Penner (2001), Indirect aerosol forcing, quasi forcing, and climate response, *Journal of Climate*, *14*, 2960–2975, doi:10.1175/1520-0442(2001)014<2960:IAFQFA>2.0.CO;2. 2.1

Schulz, M., C. Textor, S. Kinne, Y. Balkanski, S. Bauer, T. Berntsen, T. Berglen, O. Boucher, F. Dentener, S. Guibert, I. S. Isaksen, T. Iversen, D. Koch, A. Kirkevåg, X. Liu, V. Montanaro, G. Myhre, J. E. Penner, G. Pitari, S. Reddy, Seland, P. Stier, and T. Takemura (2006), Radiative forcing by aerosols as derived from the AeroCom present-day and pre-industrial simulations, *Atmospheric Chemistry and Physics*, *6*(12), 5225–5246, doi:10.5194/acp-6-5225-2006. 2.5.2

Schulzweida, U. (2019), CDO User Guide. Climate Data Operator. Version 1.9.6. 4.1.1

Scott, C. E., A. Rap, D. V. Spracklen, P. M. Forster, K. S. Carslaw, G. W. Mann, K. J. Pringle, N. Kivekäs, M. Kulmala, H. Lihavainen, and P. Tunved (2014), The direct and indirect radiative effects of biogenic secondary organic aerosol, *Atmospheric Chemistry and Physics*, *14*(1), 447–470, doi:10.5194/acp-14-447-2014. 5.2.2

Scott, C. E., S. A. Monks, D. V. Spracklen, S. R. Arnold, P. M. Forster, A. Rap, M. Äijälä, P. Artaxo, K. S. Carslaw, M. P. Chipperfield, M. Ehn, S. Gilardoni, L. Heikkinen, M. Kulmala, T. Petäjä, C. L. Reddington, L. V. Rizzo, E. Swietlicki, E. Vignati, and C. Wilson (2018), Impact on short-lived climate forcers increases projected warming due to deforestation, *Nature Communications*, *9*(1), 1–9, doi:10.1038/s41467-017-02412-4. 5.2.2

Seinfeld, J. H., and S. N. Pandis (2016), *Atmospheric Chemistry and Physics: From Air Pollution to Climate Change*, 3 ed., Wiley. 2.2, 2.3.1

Seland, Ø., and T. Iversen (1999), A scheme for black carbon and sulphate aerosols tested in a hemispheric scale, Eulerian dispersion model, *Atmospheric Environment*, *33*(17), 2853–2879, doi:10.1016/S1352-2310(98)00389-6. 3.1.2

Seland, Ø., T. Iversen, A. Kirkevåg, and T. Storelvmo (2008), Aerosol-climate interactions in the CAM-Oslo atmospheric GCM and investigation of associated basic shortcomings, *Tellus, Series A: Dynamic Meteorology and Oceanography*, *60 A*(3), 459–491, doi:10.1111/j.1600-0870.2008.00318.x. 3.1.2

Shaw, S. L., B. Gantt, and N. Meskhidze (2010), Production and Emissions of Marine Isoprene and Monoterpenes: A Review, *Advances in Meteorology*, *2010*(1), 1–24, doi:10.1155/2010/408696. 2.2

Shrivastava, M., C. D. Cappa, J. Fan, A. H. Goldstein, A. B. Guenther, J. L. Jimenez, C. Kuang, A. Laskin, S. T. Martin, N. L. Ng, T. Petaja, J. R. Pierce, P. J. Rasch, P. Roldin, J. H. Seinfeld, J. Shilling, J. N. Smith, J. A. Thornton, R. Volkamer, J. Wang, D. R. Worsnop, R. A. Zaveri, A. Zelenyuk, and Q. Zhang (2017), Recent advances in understanding secondary organic aerosol: Implications for global climate forcing, *Reviews of Geophysics*, *55*(2), 509–559, doi:10.1002/2016RG000540. 2.2

Squires, P. (1952a), The growth of cloud drops by condensation. I. General characteristics, *Australian Journal of Chemistry*, *5*(1), 59–86, doi:10.1071/CH9520059. 2.4

Squires, P. (1952b), The growth of cloud drops by condensation. I. General characteristics, *Australian Journal of Chemistry*, *5*(1), 59–86, doi:10.1071/CH9520059. 2.4

Stevens, B., and G. Feingold (2009), Untangling aerosol effects on clouds and precipitation in a buffered system, *Nature*, *461*(7264), 607–613, doi:10.1038/nature08281. 2.4

Storelvmo, T. (2017), Aerosol Effects on Climate via Mixed-Phase and Ice Clouds, *Annual Review of Earth and Planetary Sciences*, *45*, 199–222, doi:10.1146/annurev-earth-060115-012240. 2.4

Textor, C., M. Schulz, S. Guibert, S. Kinne, Y. Balkanski, S. Bauer, T. Berntsen, T. Berglen, O. Boucher, M. Chin, F. Dentener, T. Diehl, J. Feichter, D. Fillmore, P. Ginoux, S. Gong, A. Grini, J. Hendricks, L. Horowitz, P. Huang, I. S. Isaksen, T. Iversen, S. Kloster, D. Koch, A. Kirkevåg, J. E. Kristjansson, M. Krol, A. Lauer, J. F. Lamarque, X. Liu, V. Montanaro, G. Myhre, J. E. Penner, G. Pitari, M. S. Reddy, Seland, P. Stier, T. Takemura, and X. Tie (2007), The effect of harmonized emissions on aerosol properties in global models - An AeroCom experiment, *Atmospheric Chemistry and Physics*, *7*(17), 4489–4501, doi:10.5194/acp-7-4489-2007. 2.2

Toll, V., M. Christensen, S. Gasso, and N. Bellouin (2017), Volcano and Ship Tracks Indicate Excessive Aerosol-Induced Cloud Water Increases in a Climate Model, *Geophysical Research Letters*, *44*(24), 12,492–12,500, doi:10.1002/2017GL075280. 1.1, 5.3.1, 5.4

Toll, V., M. Christensen, J. Quaas, and N. Bellouin (2019), Weak average liquid-cloud-water response to anthropogenic aerosols, *Nature*, *572*(7767), 51–55, doi:10.1038/s41586-019-1423-9. 1.1, 5.3.1, 5.3.2, 5.3.3, 5.4

Treut, L., R. Somerville, U. Cubasch, Y. Ding, C. Mauritzen, A. Mokssit, T. Peterson, M. Prather, D. Qin, M. Manning, Z. Chen, M. Marquis, K. B. Averyt, M. Tignor, and U. Kingdom (2007), Historical Overview of Climate Change Science, in *Climate Change 2007: The Physical Science Basis. Contribution of Working Group I to the Fourth Assessment Report of the Intergovernmental Panel on Climate Change*, edited by S. Solomon, D. Qin, M. Manning, Z. Chen, M. Marquis, K. B. Averyt, M. Tignor, and H. L. Miller, chap. 1, Cambridge University Press, Cambridge, United Kingdom and New York, NY, USA. 2.6

Twomey, S. (1974), Pollution and the planetary, *Atmospheric Environment*, *8*, 1251–1256. 1.1, 2.4

Twomey, S. (1991), Aerosols, clouds and radiation, *Atmospheric Environment Part A, General Topics*, *25*(11), 2435–2442, doi:10.1016/0960-1686(91)90159-5. 2.2

Unger, N. (2013), Isoprene emission variability through the twentieth century, *Journal of Geophysical Research Atmospheres*, *118*(24), 13,606–13,613, doi:10.1002/2013JD020978. 2.2

Unger, N. (2014), Human land-use-driven reduction of forest volatiles cools global climate, *Nature Climate Change*, *4*(10), 907–910, doi:10.1038/nclimate2347. 5.2.2

Vehkamäki, H., M. Kulmala, I. Napari, K. E. J. Lehtinen, C. Timmreck, M. Noppel, and A. Laaksonen (2002), An improved parameterization for sulfuric acid–water nucleation rates for tropospheric and stratospheric conditions, *Journal of Geophysical Research*, *107*(D22), 4622, doi:10.1029/2002JD002184. 3.1.2

Wang, M., S. Ghan, X. Liu, T. S. L'Ecuyer, K. Zhang, H. Morrison, M. Ovchinnikov, R. Easter, R. Marchand, D. Chand, Y. Qian, and J. E. Penner (2012), Constraining cloud lifetime effects of aerosols using A-Train satellite observations, *Geophysical Research Letters*, *39*(15), 3–9, doi:10.1029/2012GL052204. 1.1, 2.4

Wang, Y., X. Liu, C. Hoose, and B. Wang (2014), Different contact angle distributions for heterogeneous ice nucleation in the community atmospheric model version 5, *Atmospheric Chemistry and Physics*, *14*, 10,411–10,430, doi:10.5194/acp-14-10411-2014. 3.1.3

Wetherald, R. T., and S. Manabe (1988), Cloud Feedback Processes in a General Circulation Model, *Journal of the Atmospheric Sciences*, *45*(8), 1397–1415. 5.3.2

Wood, R. (2012), Stratocumulus clouds, *Monthly Weather Review*, *140*(8), 2373–2423, doi:10.1175/MWR-D-11-00121.1. 2.3.2

Xue, H., and G. Feingold (2006), Large-eddy simulations of trade wind cumuli: Investigation of aerosol indirect effects, *Journal of the Atmospheric Sciences*, *63*(6), 1605–1622, doi:10.1175/JAS3706.1. 2.4

Xue, H., G. Feingold, and B. Stevens (2008), Aerosol effects on clouds, precipitation, and the organization of shallow cumulus convection, *Journal of the Atmospheric Sciences*, *65*(2), 392–406, doi:10.1175/2007JAS2428.1. 2.4

Yuan, T., L. A. Remer, and H. Yu (2011), Microphysical, macrophysical and radiative signatures of volcanic aerosols in trade wind cumulus observed by the A-Train, *Atmospheric Chemistry and Physics*, *11*(14), 7119–7132, doi:10.5194/acp-11-7119-2011. 5.3.4

Zelinka, M. D., T. Andrews, P. M. Forster, and K. E. Taylor (2014), Quantifying components of aerosol-cloud-radiation interactions in climate models, *Journal of Geophysical Research: Atmospheres*, *119*, 7599–7615, doi:doi:10.1002/2014JD021710. 1.1

Zhang, G. J., and N. A. McFarlane (1995), Sensitivity of climate simulations to the parameterization of cumulus convection in the canadian climate centre general circulation model, *Atmosphere - Ocean*, *33*(3), 407–446, doi:10.1080/07055900.1995.9649539. 3.1.3

Zhang, K., H. Wan, X. Liu, S. J. Ghan, G. J. Kooperman, P. L. Ma, P. J. Rasch, D. Neubauer, and U. Lohmann (2014), Technical note: On the use of nudging for aerosol-climate model intercomparison studies, *Atmospheric Chemistry and Physics*, *14*(16), 8631–8645, doi:10.5194/acp-14-8631-2014. 1.1, 4.1.1

Zhang, L., and R. Vet (2006), A review of current knowledge concerning size-dependent aerosol removal, *China Particuology*, *4*(6), 272–282, doi:10.1016/s1672-2515(07)60276-0. 2.2

Zhou, C., and J. E. Penner (2017), Why do general circulation models overestimate the aerosol cloud lifetime effect? A case study comparing CAM5 and a CRM, *Atmospheric Chemistry and Physics*, *17*(1), 21–29, doi:10.5194/acp-17-21-2017. 1.1, 2.4

Zhou, C., H. Zhang, S. Zhao, and J. Li (2018), On Effective Radiative Forcing of Partial Internally and Externally Mixed Aerosols and Their Effects on Global Climate, *Journal of Geophysical Research Atmospheres*, *123*, 401–423, doi:10.1002/2017JD027603. 1.1

Zhu, J., J. E. Penner, F. Yu, S. Sillman, M. O. Andreae, and H. Coe (2019), Decrease in radiative forcing by organic aerosol nucleation, climate, and land use change, *Nature Communications*, *10*(1), 1–7, doi:10.1038/s41467-019-08407-7. 5.2.2

Part II

Papers

Paper I

A production-tagged aerosol module for Earth system models, OsloAero5.3 - extensions and updates for CAM5.3-Oslo

Alf Kirkevåg, Alf Grini, Dirk Olivié, Øyvind Seland, Kari Alterskjær, Matthias Hummel, **Inger H. H. Karset**, Anna Lewinschal, Xiaohong Liu, Risto Makkonen, Ingo Bethke, Jan Griesfeller, Michael Schulz, and Trond Iversen
Geoscientific Model Development , 2018
doi:10.5194/gmd-11-3945-2018

Geosci. Model Dev., 11, 3945–3982, 2018
https://doi.org/10.5194/gmd-11-3945-2018

Geoscientific
Model Development
Open Access

A production-tagged aerosol module for Earth system models, OsloAero5.3 – extensions and updates for CAM5.3-Oslo

Alf Kirkevåg[1], Alf Grini[1], Dirk Olivié[1], Øyvind Seland[1], Kari Alterskjær[2,3], Matthias Hummel[3], Inger H. H. Karset[3], Anna Lewinschal[4], Xiaohong Liu[5], Risto Makkonen[6,7], Ingo Bethke[8], Jan Griesfeller[1], Michael Schulz[1], and Trond Iversen[1,2]

[1]Norwegian Meteorological Institute, P.O. Box 43, Blindern, 0313 Oslo, Norway
[2]CICERO Center for International Climate Research, 0349 Oslo, Norway
[3]Department of Geosciences, Section for Meteorology and Oceanography, University of Oslo, 1022 Oslo, Norway
[4]Department of Meteorology, Stockholm University, 10691 Stockholm, Sweden
[5]Department of Atmospheric Science, University of Wyoming, Laramie, Wyoming 82071, USA
[6]Institute for Atmospheric and Earth System Research/Physics, Faculty of Science, P.O. Box 64, 00014, University of Helsinki, Helsinki, Finland
[7]Climate System Research, Finnish Meteorological Institute, P.O. Box 503, 00101, Helsinki, Finland
[8]Uni Research Climate, Bjerknes Centre for Climate Research, P.O. Box 7810, 5020 Bergen, Norway

Correspondence: Alf Kirkevåg (alfk@met.no)

Received: 19 February 2018 – Discussion started: 31 May 2018
Revised: 28 August 2018 – Accepted: 30 August 2018 – Published: 1 October 2018

Abstract. We document model updates and present and discuss modeling and validation results from a further developed production-tagged aerosol module, OsloAero5.3, for use in Earth system models. The aerosol module has in this study been implemented and applied in CAM5.3-Oslo. This model is based on CAM5.3–CESM1.2 and its own predecessor model version CAM4-Oslo. OsloAero5.3 has improved treatment of emissions, aerosol chemistry, particle life cycle, and aerosol–cloud interactions compared to its predecessor OsloAero4.0 in CAM4-Oslo. The main new features consist of improved aerosol sources; the module now explicitly accounts for aerosol particle nucleation and secondary organic aerosol production, with new emissions schemes also for sea salt, dimethyl sulfide (DMS), and marine primary organics. Mineral dust emissions are updated as well, adopting the formulation of CESM1.2. The improved model representation of aerosol–cloud interactions now resolves heterogeneous ice nucleation based on black carbon (BC) and mineral dust calculated by the model and treats the activation of cloud condensation nuclei (CCN) as in CAM5.3. Compared to OsloAero4.0 in CAM4-Oslo, the black carbon (BC) mass concentrations are less excessive aloft, with a better fit to observations. Near-surface mass concentrations of BC and sea salt aerosols are also less biased, while sulfate and mineral dust are slightly more biased. Although appearing quite similar for CAM5.3-Oslo and CAM4-Oslo, the validation results for organic matter (OM) are inconclusive, since both of the respective versions of OsloAero are equipped with a limited number of OM tracers for the sake of computational efficiency. Any information about the assumed mass ratios of OM to organic carbon (OC) for different types of OM sources is lost in the transport module. Assuming that observed OC concentrations scaled by 1.4 are representative for the modeled OM concentrations, CAM5.3-Oslo with OsloAero5.3 is slightly inferior for the very sparsely available observation data. Comparing clear-sky column-integrated optical properties with data from ground-based remote sensing, we find a negative bias in optical depth globally; however, it is not as strong as in CAM4-Oslo, but has positive biases in some areas typically dominated by mineral dust emissions. Aerosol absorption has a larger negative bias than the optical depth globally. This is reflected in a lower positive bias in areas where mineral dust is the main contributor to absorption. Globally, the low bias in absorption is smaller than in CAM4-Oslo. The Ångström parameter exhibits small biases both globally and regionally, suggesting that the aerosol particle sizes are reasonably well represented. Cloud-top droplet number concentrations over oceans are generally underestimated compared to satellite retrievals, but seem to be overestimated downwind of major emissions of dust and biomass burning sources. Finally, we find small changes in direct radiative forcing at the top of the atmosphere, while the cloud radiative forcing due to anthropogenic aerosols is now more negative than in CAM4-Oslo, being on the strong side compared to the multi-model estimate in IPCC AR5. Although not all validation results in this study show improvement for the present CAM5.3-Oslo version, the extended and updated aerosol module OsloAero5.3 is more advanced and applicable than its predecessor OsloAero4.0, as it includes new parameterizations that more readily facilitate sensitivity and process studies and use in climate and Earth system model studies in general.

1 Introduction

Humans influence the production of aerosols (microscopic solid and liquid particles suspended in air) in various ways, giving rise to local and regional air pollution. Furthermore, Earth's climate can be influenced by aerosols, either directly through changes to the scattering and absorption of solar radiation or more indirectly through the effects these particles have on cloud properties and precipitation. Numerical modeling of Earth's climate therefore requires a description of aerosols in which mass and number concentrations and chemical composition as a function of size are important properties.

Even without going all the way in calculating how aerosols impact climate by including slow responses and feedbacks through atmospheric and ocean–atmosphere interactions that can be simulated in fully coupled climate models or Earth system models (ESMs), one may quantify a first-order effect on Earth's radiative budget in partly uncoupled model configurations through estimates of the so-called aerosol radiative forcing. It is common to distinguish between the traditional concepts of radiative forcing (RF) and the effective radiative forcing (ERF), which includes rapid adjustments that modify the radiative budget through fast atmospheric and surface changes (IPCC AR5: Boucher et al., 2013; Myhre et al., 2013). ERF from aerosols can furthermore be decomposed into a forcing term due to aerosol–radiation interactions (ERFari), which includes the traditional direct effect and semi-direct effects (as rapid adjustments to atmospheric heating by absorbing aerosols), and an aerosol–cloud interaction term (ERFaci) (Boucher et al., 2013), which includes the cloud albedo effect (Twomey, 1977) and associated adjustments in the form of lifetime effects (e.g., Albrecht, 1989). In this study we follow the method outlined by Ghan (2013) for calculating the effective radiative forcing of aerosols, which is decomposed into a direct radiative forcing, a cloud radiative forcing, and a surface albedo forcing term. In contrast to the terminology used in IPCC AR5, the semi-direct effect is integrated into the cloud radiative forcing term here.

Traditionally, mainly two methods have been used to calculate aerosol size and chemical composition. Modal approaches (e.g., Binkowski and Shankar, 1995) approximate the aerosol size distribution as lognormal distributions. Sectional methods (e.g., Bergman et al., 2012) discretize the size distribution into fixed size intervals that have constant properties. In a sectional aerosol module the size distribution does not have to be lognormal or of any other specified shape and is generally considered to be closer to "first principles".

An alternative "production-tagged" aerosol module is used in the atmospheric component (CAM-Oslo) of the Norwegian Earth System Model (NorESM) and in various predecessor model versions. This aerosol module has been documented in Kirkevåg et al. (2013) for CAM4-Oslo (NorESM1) and in earlier studies (Kirkevåg et al., 1999, 2005, 2008; Kirkevåg and Iversen, 2002; Iversen and Seland, 2002, 2003; Seland et al., 2008). The production-tagged method describes a number of "background" lognormal modes. These modes can change their size distribution due to condensation, coagulation, and cloud processing. The corresponding aerosol microphysical calculations are performed in a detailed size-resolving model and run offline. A selection of results in terms of bulk properties from these aerosol microphysics calculations are stored in lookup tables, which during the NorESM model simulation provide information about aerosol optical parameters as well as size and composition where needed (for details, see Sect. 2.1 in Kirkevåg et al., 2013). Production-tagged refers to the fact that the tracers which change the aerosol size distribution represent their production pathway (e.g., condensation, coagulation, and cloud processing). We will refer to the online aerosol module as OsloAero and to the offline size-resolving model that produces the lookup tables as AeroTab. Although the aerosol module has been developed over many years and already been used in numerous model versions, it has previously not been given any name or version number. For the purpose of simplicity and clarity in the intercomparison of the respective module versions, we hereafter denote the OsloAero module described and used by Kirkevåg et al. (2013) as OsloAero4.0 and the present version as OsloAero5.3. We similarly denote the respective versions of the offline size-resolving lookup table model as AeroTab4.0 (Kirkevåg et al., 2013) and AeroTab5.3.

In this work we have ported OsloAero to the Community Atmospheric Model version CAM5.3 (Neale et al., 2012; Liu et al., 2016) so that it exists as an option alongside the CAM modal aerosol modules (MAM3 and MAM7). We hereafter refer to the atmospheric model including OsloAero5.3 and the AeroTab5.3-produced lookup tables as CAM5.3-Oslo. CAM5.3 is part of the Community Earth System Model version 1.2, CESM1.2 (http://www.cesm.ucar.edu/models/cesm1.2, last access: 24 September

2018). The Norwegian Earth System Model version based on CESM1.2, which we name NorESM1.2, uses CAM5.3-Oslo instead of CAM5.3 and an updated MICOM version based on NorESM1 (Bentsen et al., 2013) instead of POP2 as the ocean model, while the land model CLM4.5, the sea ice model CICE4, and the coupler CPL7 are all as in CESM1.2. In this study we do not make use of the fully coupled model system, but prescribe sea surface temperatures and sea ice fractions (i.e., an AMIP setup). In the following discussions we therefore just refer to the model as CAM5.3-Oslo.

CAM5.3-Oslo is after some final updates and tuning planned to be merged with the atmospheric component, CAM6, from the upcoming release of the NCAR/DOE Community Earth System Model, CESM2 (http://www.cesm.ucar.edu/working_groups/Atmosphere/, last access: 24 September 2018). This merged version is expected to be the atmospheric component of NorESM2. NorESM2 is planned to participate in the Coupled Model Intercomparison Project 6 (CMIP6). NorESM1.2 (using a further adapted and tuned version of CAM5.3-Oslo) is at present a fallback version and may be used in the early phases of CMIP6 if NorESM2 is not finalized in time. Two versions of NorESM1, NorESM1-M (Bentsen et al., 2013; Iversen et al., 2013; Kirkevåg et al., 2013) and NorESM1-ME (Tjiputra et al., 2013), contributed with results for CMIP5 and were analyzed together with the other CMIP5-contributing models in IPCC AR5 (Myhre et al., 2013).

The main purpose of this study is to document the changes in the treatment of aerosols and aerosol–cloud interactions since the predecessor model version CAM4-Oslo, as well as to summarize the main principles behind the aerosol schemes applied in earlier and the present model versions. We then evaluate CAM5.3-Oslo's performance with respect to various aerosol and cloud droplet properties and present and discuss new estimates of effective radiative forcing, both for comparison with results from CAM4-Oslo and other CMIP5 models.

The article is organized as follows: Sect. 2 describes the model components that have changed since Kirkevåg et al. (2013), with an emphasis on the aerosol module. Section 3 describes the model configurations used in this study. Section 4 compares the aerosol and cloud droplet concentrations and optical properties to observations and remote retrievals, as well as to previous studies wherever feasible. Section 5 puts the results into a climate context by discussing the effective radiative forcing due to aerosol–radiation and aerosol–cloud interactions, before presenting the summary and conclusions in Sect. 6.

2 Aerosol model description

OsloAero5.3, as it is implemented in CAM5.3, applies the same method of aerosol activation (Abdul-Razzak and Ghan, 2000), transport, and transition between aerosols in the interstitial and cloud phase as in Liu et al. (2012), with the simplifications proposed by Ghan and Easter (2006) that cloud-borne aerosols are not advected, except by vertical turbulent mixing. An important feature of CAM5.3 is that it includes a general chemical solver (CAM-Chem) as well as a standardized chemical code preprocessor (MOZART; Emmons et al., 2010), which OsloAero5.3 (unlike earlier versions) makes use of. The sulfur chemistry is now also as in Liu et al. (2012), except for the DMS + OH addition reaction in which 75 % of the reaction product is SO_2 (as in Pozzoli et al., 2008) compared to 50 % in Liu et al. (2012). However, the treatments of nucleation and secondary organic aerosols differ, as in many other processes that are specific to CAM5.3-Oslo, i.e., to OsloAero5.3 and AeroTab5.3.

Since Kirkevåg et al. (2013) (CAM4-Oslo), several improvements have been made to OsloAero and AeroTab. These updates will be described in detail in this section, but may be briefly summarized as follows. Aerosol nucleation and secondary organic aerosols have been taken explicitly into account based on Makkonen et al. (2014), with some extensions. Sea salt emissions and emission sizes have been changed to those of Salter et al. (2015). Dimethyl sulfide (DMS) and oceanic primary organics are now emitted from concentration- and wind-driven parameterizations (Nightingale et al., 2000; Vignati et al., 2010), and dust emissions are calculated online based on Zender et al. (2003). Aerosol hygroscopicity and a few other microphysical properties have also been changed since CAM4-Oslo. Finally, heterogeneous ice nucleation is implemented based on Wang et al. (2014), which was based on a modified version of the scheme in CAM3-Oslo (Hoose et al., 2010).

2.1 The production-tagged aerosol module

The production-tagged aerosol module has been used previously in many studies. The life-cycling component of the online aerosol module we now call OsloAero was first developed and described by Seland and Iversen (1999) and Iversen and Seland (2002, 2003). The offline size-resolving aerosol model we call AeroTab, including table lookups and interpolations with respect to aerosol–radiation and aerosol–cloud interaction calculations in OsloAero, was first developed and described by Kirkevåg et al. (1999) and Kirkevåg and Iversen (2002), with some updates by Kirkevåg et al. (2005). Later versions of both components of the production-tagged aerosol module as a whole are described by Seland et al. (2008) and Kirkevåg et al. (2008), and Kirkevåg et al. (2013), hereafter referred to as K13. The essential difference to other aerosol module treatments is the division of tracers into "background" and "process" tracers. Background tracers, which are mainly primary emitted particles (nucleation being the exception), form lognormal modes and contribute to the aerosol number concentration. The process tracers change the shape and chemical composition of the initially lognormal background modes. Examples of pro-

Table 1. Transported aerosol tracers included in OsloAero5.3. The aerosol precursor and oxidant gas tracers transported by the model are SO_2, H_2SO_4, DMS, isoprene, monoterpene, SOAG_LV, SOAG_SV, and H_2O_2.

Tracer variable ID	Meaning S4: SO_4 (particulate sulfate); SOA: secondary organic aerosol; BC: black carbon; OM: primary organic matter; SS: sea salt; DU: DST (mineral dust)	Notation in Fig. 1
SO4_NA	SO_4 formed by co-nucleation with SOA	S4(n)
SO4_A1	SO_4 condensate on existing particles from H_2SO_4 (gas)	S4 (yellow)
SO4_A2	SO_4 formed from aqueous-phase chemistry	S4
SO4_AC	SO_4 particles coagulated with other particles	S4(ac), S4(c)
SO4_PR	SO_4 primary emissions, emitted as particles	S4(ac)
SOA_NA	SOA formed by co-nucleation with SO_4	SOA(a)
SOA_A1	SOA condensate on existing particles from $SOAG_{SV}$ (gas)	SOA (yellow)
BC_N	BC emitted externally mixed as nucleation sized mode	BC(n)
BC_AX	BC emitted externally mixed as fractal accumulation mode	BC(ac)
BC_NI	BC emitted internally mixed with OM, Aitken mode	OM/BC(a)
BC_A	BC coated with water-solubles, Aitken mode	OM/BC(a)
BC_AI	BC coexisting with OM and coated Aitken mode	OM/BC(a), BC(a)
BC_AC	BC particles coagulated with other aerosols (coagulate)	BC(ac), BC(c)
OM_NI	OM emitted internally mixed with BC, Aitken mode	OM/BC(a)
OM_AI	OM coexisting with BC and coated, Aitken mode	OM/BC(a)
OM_AC	OM and SOA particles coagulated with other aerosols (coagulate)	OM(ac), OM(c), SOA(ac), SOA(c)
DST_A2	Mineral dust, accumulation mode	DU(ac)
DST_A3	Mineral dust, coarse mode	DU(c)
SS_A1	Sea salt aerosol, Aitken mode	SS(a)
SS_A2	Sea salt aerosol, accumulation mode	SS(ac)
SS_A3	Sea salt aerosol, coarse mode	SS(c)

cess tracers are sulfate condensate, sulfate coagulate, sulfate from cloud processing (aqueous-phase chemistry in cloud droplets, followed by evaporation), and secondary organic aerosol (SOA) condensate. All tracers that are calculated explicitly are listed in Table 1.

For gas-phase and aqueous aerosol chemistry, concentrations of OH, NO_3, O_3, and HO_2 are prescribed (see also Karset et al., 2018) as time-varying climatological 3-D monthly mean fields from simulations with the global stratosphere–troposphere chemistry model CAM-chem v3.5 in the study of Lamarque et al. (2010), representative for conditions in the year 2000. H_2O_2 is calculated as in Liu et al. (2012) and depends on the prescribed (monthly averaged) HO_2 concentrations.

As soon as the aerosol background modes have changed composition and shape, we refer to them as "mixtures". Because the resulting size-distribution from AeroTab is no longer lognormal and "modes" are traditionally used for aerosol size distributions that are lognormal, the term mixture is used in order to avoid confusion. The resulting mixtures, which the lookup tables are based on, are given in Table 2. The table shows which tracers are assumed to be background tracers (lognormally distributed at the point of emission or production) and which tracers are purely size and composition modifying. OsloAero calculates how much of each "modifying" tracer should be distributed onto each of the background modes (thus forming mixtures of mass from the various tracers) within a time step. When that fraction is known, interpolations in the lookup tables (generated by AeroTab) return the optical properties or the best lognormal fit (in terms of modal median radius and standard deviation) of the final dry size distribution of that mode after growth. The assumed standard deviation of the initially lognormal size distributions and the accommodation coefficients for each of the mixtures are still as in Table 1 in K13.

Concerning the basic principles behind the production-tagged aerosol module (see K13 and references therein), we may look at it as a three-stage process over a time step in the model. First, during atmospheric transport the background aerosol tracers are assigned typical tropospheric dry sizes (i.e., the sizes at the point of emission, augmented to take into account atmospheric growth for the finest particles; mixture nos. 1–4 in Table 2). The size-modifying aerosol tracers are also assigned prescribed sizes (see Table 2). Their respective sizes after hygroscopic growth, calculated as in OsloAero4.0 (K13), are eventually used for the calculation of dry deposition, in which both types of aerosol tracers are treated as if they were separate particles. Secondly, when the size distribution resulting from aerosol microphysics is needed, the mass of the size-modifying tracers is distributed onto the dif-

Table 2. Distribution of aerosol tracers in the particle mixtures treated in the model. Tracer names in bold and italic fonts are background tracers, while the others are tracers that modify the size distribution. The initial number median dry radius (NMR) and standard deviation (SIGMA) of each background mode are listed in the second and third column. Also listed (with numbers in brackets) are the prescribed dry NMR values assumed during transport (including atmospheric growth) for the finest particle mixtures (nos. 1, 2, and 4). For other mixtures, the dry sizes of transported tracers are assumed to be identical to the initial sizes. Note that for historical reasons, particle mixture numbers 3, 11, and 13 do not exist in the present model version. For the sake of consistency and transparency, the numbering is the same as in the model code. Assumed dry size parameters for the size-modifying tracers during transport: NMR = 0.04 µm and SIGMA = 1.8 for SO4_A1; NMR = 0.1 µm and SIGMA = 1.59 for SO4_A2, SO4_AC, OM_AC, BC_AC, and SOA_A1.

Particle mixture no.	NMR (µm)	SIGMA	Aerosol tracers (cf. Table 1) contributing to the particle mixture						
0	0.0626	1.6	***BC_AX***						
1	0.0118 (0.025)	1.8	***SO4_NA***	***SOA_NA***	SO4_A1	SOA_A1			
2	0.024 (0.025)	1.8	***BC_A***	SO4_A1	SOA_A1				
4	0.04 (0.06)	1.8	***OM_AI***	***BC_AI***	SO4_A1	SO4_A2	SOA_A1		
5	0.075	1.59	***SO4_PR***	BC_AC	OM_AC	SO4_A1	SO4_AC	SO4_A2	SOA_A1
6	0.22	1.59	***DST_A2***	BC_AC	OM_AC	SO4_A1	SO4_AC	SO4_A2	SOA_A1
7	0.63	2.0	***DST_A3***	BC_AC	OM_AC	SO4_A1	SO4_AC	SO4_A2	SOA_A1
8	0.0475	2.1	***SS_A1***	BC_AC	OM_AC	SO4_A1	SO4_AC	SO4_A2	SOA_A1
9	0.3	1.72	***SS_A2***	BC_AC	OM_AC	SO4_A1	SO4_AC	SO4_A2	SOA_A1
10	0.750	1.6	***SS_A3***	BC_AC	OM_AC	SO4_A1	SO4_AC	SO4_A2	SOA_A1
12	0.024	1.8	***BC_N***						
14	0.04	1.8	***OM_NI***	***BC_NI***					

ferent background size modes according to how large the sink is for the tracer in question, estimated online following Kirkevåg et al. (1999). For example, the amount of condensate added to a background mode is proportional to the background mode's condensation sink (prior to growth). Finally, the mass of these mixture-apportioned tracers is fed into the interpolation code connected to the lookup tables, giving us estimated sizes and optical properties. The lookup tables have been calculated offline by using AeroTab5.3 based on the fully size-resolved (with 44 size bins) solution to the continuity equations for particle number and mass concentrations (Kirkevåg et al., 1999) after aerosol growth. Note that the full size distribution (i.e., number concentration for each size bin) is not stored in these lookup tables, but rather the subsequent bulk (i.e., size-integrated) parameters that are required by the atmospheric model, such as single scattering albedo, asymmetry factor, and mass specific extinction, in addition to lognormal fits to the dry size distributions after growth. Tabulated aerosol optical parameters include the effect of humidity swelling.

Using this technique, we lose information about which sizes were modified by which tracer in the past, since the detailed size information is lumped back into a limited number of tracers before atmospheric transport. However, we gain computational efficiency since the technique requires fewer transported tracers. The size of the aerosol mixtures, i.e., of background tracers including growth by process tracers, could in principle be estimated by using the tabulated size parameters for the particle mixtures in the previous time step. Such a link has not yet been implemented in the model, but is something that should be investigated and tested in future model versions.

The total number of transported aerosol and gas tracers in OsloAero5.3 is 29 (21 aerosol and 8 gas tracers; see Table 1) compared to 20 (15 and 5) in MAM3 and 37 (31 and 6) in MAM7. Comparing CAM5.3-Oslo simulations using OsloAero5.3 with MAM3, we find a ca. 49 % increase in model cost (50 % for the atmosphere module alone). Much of the relatively large increase in model cost compared to MAM3 is due to the multidimensional table lookups and interpolation calculations for aerosol optical properties and sizes in OsloAero5.3. For comparison, according to Liu et al. (2012), CAM5.1 set up with MAM7 runs about 30 % slower than with MAM3.

2.2 Secondary organic aerosols and nucleation

The treatment of secondary organic aerosol (SOA) and nucleation has been much improved since K13, for which SOA was simply prescribed as a monthly surface source, and nucleation (sulfate only) was implicitly determined by the amount of available H_2SO_4 left after condensation during a model time step. The treatment is now based on Makkonen et al. (2014), hereafter referred to as M14, who implemented emissions of monoterpene and isoprene in a research version of NorESM1-M (see also Boy et al., 2018). These SOA precursors are oxidized by OH, O_3, and NO_3.

The chemical reactions and assumed yields (0.15 and 0.05) are given below, with reaction rates (not shown) taken from IUPAC (Atkinson et al., 2004, 2006). These yields are similar to values used in other studies (e.g., Mann et al., 2010;

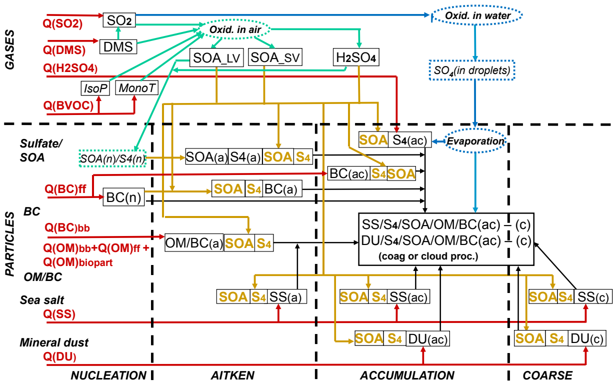

Figure 1. Flow diagram of processes in the aerosol module OsloAero5.3. The source terms to the left, labeled $Q(X)y$, where X is the constituent name and y is the source type, can be primary emissions or secondary production. The source labels $y = \mathrm{bb}$, ff, or biopart indicate biomass burning, fossil fuel or biofuel combustion, and biogenic particle sources. Primary particles are emitted (red arrows) as accumulation-mode sulfate (S4(ac)), nucleation- and accumulation-mode black carbon (BC(n), BC(ac)), Aitken-mode BC (BC(a)), internally mixed Aitken-mode organic matter and black carbon (OM/BC(a)), Aitken-, accumulation-, and coarse-mode sea salt (SS(a), SS(ac), SS(c)), and accumulation- and coarse-mode mineral dust (DU(ac), DU(c)). Model-calculated gas-phase components are DMS, SO_2, isoprene (IsoP), monoterpene (MonoT), H_2SO_4, and gaseous secondary organics ($SOAG_{LV}$ and $SOAG_{SV}$). $SOAG_{LV}$ partly co-nucleates with nucleation-mode sulfate (S4(n), SOA(n), turquoise arrows) and partly condensates (yellow arrows) on existing particle surfaces, while $SOAG_{SV}$ only forms SOA through condensation. Sulfate produced in cloud water droplets (SO4(in droplets), blue arrow) is partly added to S4(ac) and partly to a broad internal mixture of accumulation- and coarse-mode particles coagulated with either mineral dust or sea salt. Black arrows represent coagulation that contributes to the latter two particle types. Components in dashed boxes are not explicitly calculated.

Tsigaridis et al., 2014).

$$\text{monoterpene} + O_3 \rightarrow 0.15 \cdot SOAG_{LV} \quad \text{(R1)}$$

$$\text{monoterpene} + OH \rightarrow 0.15 \cdot SOAG_{SV} \quad \text{(R2)}$$

$$\text{monoterpene} + NO_3 \rightarrow 0.15 \cdot SOAG_{SV} \quad \text{(R3)}$$

$$\text{isoprene} + OH \rightarrow 0.05 \cdot SOAG_{SV} \quad \text{(R4)}$$

$$\text{isoprene} + O_3 \rightarrow 0.05 \cdot SOAG_{SV} \quad \text{(R5)}$$

$$\text{isoprene} + NO_3 \rightarrow 0.05 \cdot SOAG_{SV} \quad \text{(R6)}$$

The idea of separating $SOAG_{SV}$ and $SOAG_{LV}$ is that the SOA gas (SOAG) tracer labeled "SV" is assumed to be semi-volatile, with an equilibrium vapor pressure too high to contribute to new particle formation but instead goes to condensation. In addition to contributing to condensation, the tracer labeled "LV" is assumed to be low volatile enough to also contribute to particle nucleation and subsequent aerosol growth below the number median radius of the SO4_N/SOA_N mixture (mixture no. 1 in Table 2). Only low-volatile products are assumed to take part in new particle formation as described by Kulmala et al. (2004). In M14, low-volatile products are only assumed to form in the reaction between monoterpene and O_3. This choice is supported by an observed correlation between growth rates of 7–20 nm (in diameter) aerosol and monoterpene ozonolysis (Yli-Juuti et al., 2011), as well as the relatively higher yield of extremely low-volatility organic compounds (ELVOCs) from O_3 compared to OH reaction with monoterpenes (Jokinen et al., 2015). The fractions of monoterpene and isoprene that do not react to form SOA gas in Reactions (R1)–(R6) are not taken into account, assuming that they form other gas or aerosol products that we do not track in the model. This approach is a good way to resolve oxidant-mediated variations in SOA production and is suitable for global aerosol models with simplified aerosol precursor chemistry schemes (e.g., Spracklen et al., 2008). We also note that, since the model uses the "offline oxidant approach", Reactions (R1) to (R6) need only resolve one product, meaning that the products of the second reactants (the oxidants) do not need to be included on the right-hand side of the chemical equations. While methanesulfonic acid (MSA) in K13 was emitted directly into the OM_NI tracer as primary OM, we now also treat MSA as a biogenic VOC that may form SOA, assuming that 20 % and 80 % of the mass is added to the $SOAG_{LV}$ and $SOAG_{SV}$ tracers, respectively (see Fig. 1). The exact LV-to-SV ratio is unknown, but some of the MSA is of low enough volatility to contribute to nucleation and subsequent growth (Chen et al., 2017; Willis et al., 2016).

The concentrations of the condensable gases H_2SO_4, $SOAG_{LV}$, and $SOAG_{SV}$ are calculated based on the production rates from the gas-phase chemistry solver MOZART (Horowitz et al., 2003). The solver is configured to use the chemical mechanism used in K13 with the additional reactions for SOA. The chemical mechanisms in OsloAero5.3, for sulfur and oxidant chemistry as well as the SOA chemistry in Reactions (R1)–(R6), have been described in more detail by Karset et al. (2018, Sect. 2). For an overview of the chemical reactions and the respective reaction rate coefficients, see Table 2 in Karset et al. (2018).

Furthermore, only a fraction of the $SOAG_{LV}$ oxidation products (50 %, as in M14) is assumed to be low volatile enough to nucleate or condense onto nucleation-sized particles, while the remaining fraction and the semi-volatile tracer is allowed to condense on preexisting particles. Binary nucleation of H_2SO_4 vapor is based on Vehkamäki et al. (2002). Boundary layer nucleation is implemented according to several semi-empirical parameterizations from Paasonen et al. (2010). For the present model version and the simulations in this study we have used Eq. (18) in Paasonen et al. (2010).

After nucleation, particles grow further by condensation of sulfuric acid and organic vapors. Growth of nucleated clusters to the particle size of the corresponding mixture treated in the model (see Table 2) is based on Lehtinen et al. (2007).

The organic vapors available for this transition have been found to be very important for the growth of atmospheric particles (Riipinen et al., 2011; Keskinen et al., 2013).

The condensation sink is known from the surface area of the background aerosols. After the gas-phase chemistry is treated in the model, the concentrations of the condensable gases are set back to their value from the start of the time step, and the following equation is solved to obtain concentrations at the end of the time step:

$$\frac{\mathrm{d}C_{\mathrm{gas}}}{\mathrm{d}t} = P_{\mathrm{gas}} + L_{\mathrm{cond}} \cdot C_{\mathrm{gas}} - L_{\mathrm{nuc}} \cdot C_{\mathrm{gas}}, \tag{1}$$

where L_{cond} is the loss rate (s^{-1}) for condensation and L_{nuc} is the loss rate (s^{-1}) due to nucleation for the condensing gas. Since L_{nuc} is dependent on the concentration we perform one iteration before the equation is solved with an Euler backwards method to obtain the concentration at the end of the time step $C_{\mathrm{gas,new}}$. In the first iteration, L_{nuc} is zero. The resulting gas-phase concentration from the first iteration is used to calculate the nucleation rate. When the concentration at the end of the time step has been found with the Euler backwards method, the tendency is calculated as

$$\frac{\mathrm{d}C_{\mathrm{gas}}}{\mathrm{d}t} = (C_{\mathrm{gas,new}} - C_{\mathrm{gas,old}})/\mathrm{d}t. \tag{2}$$

Nucleated particles from $\mathrm{SOAG_{LV}}$ and H_2SO_4 have much smaller diameters ($d_{\mathrm{nuc}} \sim$ 1–3 nm) than the respective aerosol mixture in CAM5.3-Oslo (mixture no. 1 in Table 2), which has a median modal diameter (d_x) of 23.6 nm. The smallest particles can either coagulate with the background particles or grow by condensation of $\mathrm{SOAG_{LV}}$ and H_2SO_4 until they reach sizes that have a longer lifetime with respect to coagulation. The following formula (Eq. 7 in Lehtinen et al., 2007; see also M14) gives the rate J_x at which particles of size d_x form, growing from nucleation size to that of the corresponding mixture (no. 1) in the model:

$$J_x = J_{\mathrm{nuc}} \cdot \exp(-\gamma \cdot d_{\mathrm{nuc}} \frac{\mathrm{CoagS}(d_{\mathrm{nuc}})}{\mathrm{GR}});$$
$$\gamma = \frac{1}{m+1}[(\frac{d_x}{d_{\mathrm{nuc}}})^{m+1} - 1]. \tag{3}$$

Here J_{nuc} is the nucleation rate of d_{nuc} sized particles, CoagS is the coagulation sink, and GR is the rate of particle growth due to condensation. The factor γ is expressed as a function of d_{nuc} and d_x, as well as a background size-dependent exponent m. Here we simply let $m = -1.6$ (as in M14), which is a typical value for atmospheric conditions (Lehtinen et al., 2007). The formation rate is in other words determined by the concentration of sulfuric acid and organic vapors available for condensational growth and by the coagulation sink of the newly formed particles onto preexisting aerosols.

There are four important differences in the SOA treatment compared to M14.

1. We close the mass balance both for H_2SO_4 and for organic vapors, while M14 put nucleated mass into the model as H_2SO_4, thus allowing sulfur mass to be produced by organic vapors. Unlike the M14 study, which focused on changes in aerosol life cycling but not on the radiative effects of SOA, the lookup tables for optics and sizes with respect to aerosol–radiation and aerosol–cloud interactions are now also taking into account SOA.

2. We add the non-nucleated vapor as condensate. The condensate is only added through condensation on preexisting particles and does not produce new particles. In M14, non-nucleated vapor was added to the tracer representing primary organics. Since primary organics is a background tracer in OsloAero5.3, increasing primary organic mass also increases aerosol number concentration. In the updated treatment condensate does not increase particle number concentrations (unless it leads to increased nucleation rates).

3. M14 assumed secondary organic aerosol formation only from monoterpenes. In this work both monoterpenes and isoprene are assumed to produce SOA mass. Still only monoterpene ozonolysis products are allowed to produce new particles by nucleation (via $\mathrm{SOAG_{LV}}$).

4. We now also make use of interactive emissions of SOA precursors from CLM4.5 using the MEGAN v2.1 (Guenther et al., 2012) algorithm instead of reading them in from file. This allows us to study the effects of a changing climate on SOA formation and facilitates feedback studies. We lump 21 monoterpene species (myrcene, sabinene, limonene, 3-carene, t-β-ocimene, β-pinene, α-pinene, dimethyl styrene, p-cymene, o-cymene, α-phellandrene, α-thujene, α-terpinene, γ-terpinene, terpinolene, β-phellandrene, camphene, bornene, α-fenchene, allo-ocimene, and *cis*-β-ocimene) into one atmospheric monoterpene tracer.

The main advantages of the new treatment of SOA in this study compared to M14 are that the atmospheric composition influences the aerosol size distribution and particle number, as well as its optical properties, that SOA is allowed to form outside the boundary layer, and that the use of interactive biogenic volatile organic compound (BVOC) emissions, including MSA from the ocean surface, facilitates studies of the effects of climate change on SOA formation, as well as on subsequent feedbacks.

2.3 Aerosol microphysics

Diffusion coefficients for condensable gases have been calculated based on Eqs. (11)–(4.4) and Table 11-1 in Poling et al. (2001). For SOA, which was not explicitly treated in the predecessor model CAM4-Oslo (K13), we use a molecular weight of 168.2 ($\mathrm{g\,mol^{-1}}$), corresponding to $C_{10}H_{16}O_2$ as our assumed representative SOA molecule. Due to a lack of exact information about the large range of possible organic compounds we call SOA, for simplicity and computational efficiency we assume SOA to have the same microphysical properties (mass density, hygroscopicity, refractive index) as OM in the model, i.e., both in AeroTab5.3 and OsloAero5.3. A bug in the life cycle scheme (OsloAero4.0; K13) that produced too-slow growth by condensation has also been found and rectified in OsloAero5.3. The effect of this is discussed to some degree by Iversen et al. (2017).

Mass densities and refractive indices are unchanged from K13, except for BC and mineral dust. For BC we have adopted the recommendations by Bond and Bergström (2006) of using a monomer mass density of $1800\,\mathrm{kg\,m^{-3}}$ and a refractive index of $m = 1.95–0.79i$ (assumed to be wavelength independent). The refractive index for mineral dust has also been modified. This now follows Hess et al. (1998) for all wavelengths, which gives somewhat more light absorption by dust than in K13.

Modal number median radii and standard deviations for background tracers at the point of emissions (Table 2) are as in CAM4-Oslo, except for BC and sea salt (SS_A1, SS_A2, and SS_A3). Sea salt particle sizes have been changed to fit the new emission parameterization by Salter et al. (2015).

NMR for mixture nos. 2 and 12 (BC_A and BC_N from fossil fuel combustion) has been ca. doubled (to 24 nm) compared to CAM4-Oslo (11.8 nm) in order to account for some growth from the BC monomer size near the emission source to a more representative model grid mean value. This NMR is consistent with observations of somewhat aged BC mass size distributions of diesel exhaust and urban aerosol (Ning et al., 2013) and has also been shown to give more realistic aerosol number concentrations in a version of CAM4-Oslo with improved nucleation parameterization (M14). The new NMR is also more in line with the Aitken-mode fossil fuel carbonaceous particle size assumptions applied by the participating models in the multi-model AeroCom aerosol microphysics model intercomparison study (Mann et al., 2014), which were in the range 15–40 nm. We note, however, that most of those models emitted particles as mixed BC–POM particles, so the size for a pure BC emission mode is not exactly comparable.

The externally mixed BC_AX mixture is a "fluffy" fractal-structured agglomerate consisting of BC_N particles assumed to be formed by rapid self-coagulation in exhaust from fossil fuel combustion. We keep the standard deviation (SIGMA = 1.6) as in K13, but have reduced NMR from 0.1 to 0.0626 µm in order to conserve number concentrations as BC_AX gets coated and ages into BC_AI. We keep the assumed fractal dimension D (Ström et al., 1992) as in CAM4-Oslo; i.e., $D = 2.5$.

One aerosol tracer has been removed compared to CAM4-Oslo, namely the nucleation-mode sulfate (SO4_N, originally mixture no. 11 in Table 2). This was done in order to save computational cost and has been found to affect the overall life-cycling properties with respect to, e.g., sulfate concentrations and atmospheric residence times negligibly. This tracer was originally introduced to help mimic the growth in time from freshly nucleated sulfate particles (with a fixed size and composition) to aged particles. Since the assumed chemical composition (with respect to life cycling in OsloAero) in effect is quite similar to those of the aged particles, the division between those two aerosol tracers, despite their somewhat different sizes, has been found unnecessary in OsloAero5.3.

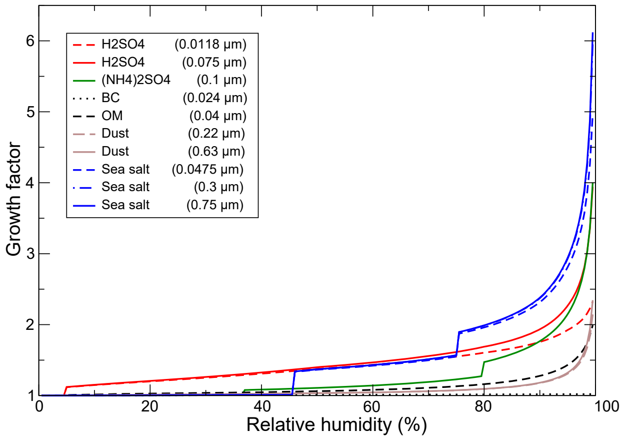

Figure 2. Hygroscopic growth factors (wet–ambient radius divided by dry radius) for aerosol components at some typical dry radii and for relative humidities up to $\mathrm{RH_{max}} = 99.5\,\%$, as treated in AeroTab5.3 and the optics lookup tables. Note that the growth factor curve for sea salt at dry radius 0.3 µm is not visible due to overlap with that for 0.75 µm. To relate this figure to the nomenclature in Table 2, H_2SO_4 (sulfuric acid) may come as SO4_NA, SO4_PR, or SO4_A1, $(NH_4)_2SO_4$ (ammonium sulfate) as SO4_A2, BC as BC_AX, BC_N, BC_NI, or BC_A, OM as OM_NI, OM_AI, SOA_NI, or SOA_A1, mineral dust as DST_A2 or DST_A3, and sea salt as SS_A1, SS_A2, or SS_A3.

Although the aerosol scheme is different from that of Liu et al. (2012), we use the same method for calculating the aging of externally mixed BC and organic aerosols. The layer thickness of SOA and sulfate condensate collected by the externally mixed species BC_N and BC_AX must exceed three monolayers (sulfate equivalent) before transitioning to the respective coated or aged particle mixtures is allowed. In K13 the BC_AX mixture was assumed to be large enough so that aging by condensation could be ignored, an assumption that was based on near-surface measurements of BC in the remote Arctic. However, the extreme conditions in Arctic winter are not representative of conditions elsewhere, and this assumption contributed to the somewhat exaggerated upper troposphere mass concentrations of BC that were modeled in CAM4-Oslo.

Hygroscopicities have also been modified somewhat, both with respect to internal consistency and simplicity. The new treatment ensures that the hygroscopicity of an aerosol mixture for humidity swelling (for use with the offline optics calculations in AeroTab5.3) at slight sub-saturation ($\mathrm{RH} = 99.5\,\%$) is the same as the value used for calculating activation to cloud droplets at supersaturated conditions (online in OsloAero5.3). These two cases were treated independently and could be slightly different in OsloAero4.0. The new growth factors (i.e., wet radius divided by dry radius) for RH values up to the cutoff value of 99.5 %, hereafter referred to as $\mathrm{RH}_{\mathrm{max}}$, are shown in Fig. 2.

For BC we now assume a very low hygroscopicity of $B = 5.0 \times 10^{-7}$ (Ghan et al., 2001) for all relative humidities. In CAM4-Oslo BC was assumed to be entirely hydrophobic ($B = 0$) in calculations of hygroscopic swelling, but $B = 8.9 \times 10^{-7}$ with respect to CCN activation. Although the hygroscopicity for CCN activation is nearly halved since CAM4-Oslo, the values are already so small that the effect of this on cloud droplet production is probably negligible.

For ammonium sulfate we assume that $B = 0.507$ (Ghan et al., 2001) at $\mathrm{RH}_{\mathrm{max}}$ and at supersaturated conditions. This value is the same as in CAM4-Oslo with respect to CCN activation, but larger than what was used for hygroscopic growth at $\mathrm{RH}_{\mathrm{max}}$ (0.434). Instead of imposing a linear growth in the hysteresis domain, i.e., for $\mathrm{RH} = 37$–$80\,\%$ (Tang and Munkelwitz, 1994; Tang, 1996) as in CAM4-Oslo, we simply assume here that B is reduced to the half ($B = 0.2535$) between the points of crystallization and deliquescence. Below the point of crystallization, the hygroscopicity is assumed to be the same as for BC (i.e., very low) compared to 0 in CAM4-Oslo.

While sulfate in OsloAero5.3 is consistently treated as ammonium sulfate, just as in CAM5.3 (Liu et al., 2012), in AeroTab5.3 we still (as in AeroTab4.0) treat both nucleated sulfate particles and condensate (SO4_NA and SO4_A1, respectively) as sulfuric acid with respect to hygroscopicity. This hygroscopicity is now parameterized to vary with RH in such a way that the growth factor equals that of H_2SO_4 (for a range of RH values from 50 % to 99 %) in Table 2 in Köpke et al. (1997). By solving the Köhler equation, B is then estimated to be 0.534 at $\mathrm{RH} = 99\,\%$ (and assumed to be the same at $\mathrm{RH}_{\mathrm{max}}$) compared to 0.646 in CAM4-Oslo.

For sea salt we have inferred the B values from Köpke et al. (1997) and then reduced the values by 50 % in the hysteresis domain, i.e., for $\mathrm{RH} = 46$–$75\,\%$ (Tang and Munkelwitz, 1994; Tang, 1996). This gives $B = 1.20$ at $\mathrm{RH}_{\mathrm{max}}$, which is slightly larger than the CAM4-Oslo B values of 1.15 at $\mathrm{RH}_{\mathrm{max}}$ and 1.16 for CCN activation (as in Ghan et al., 2001).

The OM hygroscopicity is assumed to be 0.14 (Ghan et al., 2001) for all RH values, slightly below the B value of 0.158 at $\mathrm{RH}_{\mathrm{max}}$ but the same B value with respect to CCN activation as in CAM4-Oslo.

For mineral dust a B value of 0.069 has been chosen, consistent with a ca. 10 % soluble mass fraction of dust. This is a high-range value of the “less-hygroscopic” dust category in Koehler et al. (2009). In CAM4-Oslo much lower values were assumed: $B = 4.8 \times 10^{-5}$ at $\mathrm{RH}_{\mathrm{max}}$ and $B = 0.015$ with respect to CCN activation. However, the new B value is still low compared to the value 0.14 assumed by Ghan et al. (2001).

In this model version, as in CAM4-Oslo, hygroscopicity with respect to CCN activation is not calculated within AeroTab. AeroTab instead provides lookup tables of aerosol size parameters for each mixture, which in addition to B is used as input to the activation code (Abdul-Razzak and Ghan, 2000). The hygroscopicity is calculated as a mass-weighted B for mixtures that are uncoated or have a thin coating of soluble components (i.e., sulfate, OM, and/or sea salt) and as a mass-weighted B of the coating itself when the coating is sufficiently thick. This threshold coating thickness is assumed to be 2 nm, as in K13.

2.4 Emission fluxes

DMS and biogenic OM emissions from the ocean have been updated to be wind driven. In K13 DMS emissions were taken from Dentener et al. (2006) and given as daily averages. Biogenic OM was assumed to have the same spatial distribution as the fine mode of sea salt emissions given in Dentener et al. (2006) and scaled to the global number in Spracklen et al. (2008). The DMS emissions are now instead given as the product of the transfer velocity and the ocean DMS molar concentration:

$$F_{\mathrm{DMS}} = C \cdot k_{600} \cdot M_{\mathrm{DMS}} \cdot C_{\mathrm{DMS}}. \tag{4}$$

Here $\mathrm{F}_{\mathrm{DMS}}$ is the flux of DMS ($\mathrm{kg\,m^{-2}\,s^{-1}}$), C is a unit conversion coefficient in the model code (not a tuning factor), C_{DMS} is the DMS concentration in the ocean given as monthly averages by Lana et al. (2011), M_{DMS} is the molar mass of DMS, and k_{600} is a transfer coefficient ($\mathrm{cm\,h^{-1}}$) from Nightingale et al. (2000):

$$k_{600} = 0.222 \cdot U_{10}^2 + 0.333 \cdot U_{10}, \tag{5}$$

where U_{10} is the 10 m wind speed.

The flux of oceanic primary organic aerosols is given by O’Dowd et al. (2008) and Vignati et al. (2010) to be proportional to the submicron sea salt flux of the finest mode (SS_A1) and to the (monthly) organic matter concentration fraction in the water. Vignati et al. (2010) give the OM fraction as

$$\mathrm{OM}_{\mathrm{frac}} = 0.435 \cdot \rho_{\mathrm{Chl\,a}} + 0.13805. \tag{6}$$

$\mathrm{OM}_{\mathrm{frac}}$ is saturated at 90 % according to O’Dowd et al. (2008). $\rho_{\mathrm{Chl\,a}}$ is the mass concentration of chlorophyll a ($\mathrm{mg\,m^{-3}}$) in the surface water using SeaWiFS climatology (O’Reilly et al., 2000). A tuning constant has been added to the equation so that the OM flux from the ocean (still) matches the estimate of Spracklen et al. (2008) of approximately $8\,\mathrm{Tg\,yr^{-1}}$.

The treatment of sea salt fluxes in K13 has been changed to the formulation used for CAM4-Oslo in Salter et al. (2015),

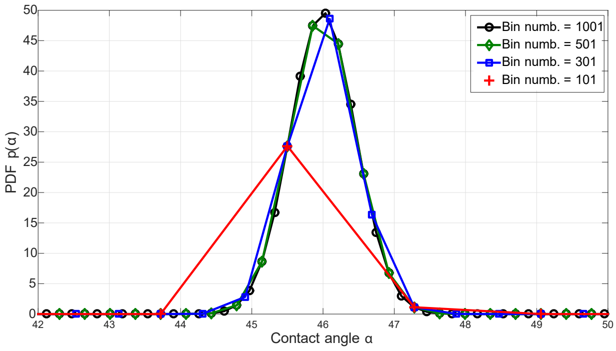

Figure 3. Probability $p(\alpha)$ of the α-PDF model used for calculating the contact angle for immersion freezing. Different bin numbers are tested in order to correct the numerical formulation that is used in Wang et al. (2014).

both being functions of near-surface wind and sea surface temperature. Dust sources were prescribed in K13. They are now wind driven and calculated from the Dust Entrainment and Deposition (DEAD) model (Zender et al., 2003), which is implemented in the Community Land Model and is made available to OsloAero5.3. The parameterization is the same as that used by Liu et al. (2012), but fitted to the dust aerosol sizes used in OsloAero5.3.

As described in Sect. 2.2, the biogenic emissions of monoterpene and isoprene are calculated online (called every time step, which is 30 min) from MEGAN (Guenther et al., 2012). The oxidant fields are prescribed as monthly averages but with a daily variation superimposed for OH and HO_2 and are therefore decoupled from the BVOC concentrations.

For aerosol and precursors not mentioned above, as in K13, the emissions are taken from the IPCC AR5/CMIP5 (Lamarque et al., 2010) for the year 2000 (for simplicity called present day, PD) and 1850 (preindustrial, PI) conditions. The emissions and their vertical distribution are essentially the same as those used by Liu et al. (2012): the IPCC AR5 emission data set includes anthropogenic emissions for primary aerosol species OC and BC, as well as the precursor gas SO_2. We assume that 2.5 % of the sulfur emissions are emitted directly as primary sulfate aerosols and the rest as SO_2. Anthropogenic emissions are defined as originating from industrial, energy, transportation, domestic, and agricultural activity sectors.

2.5 Heterogeneous ice nucleation

In this new version of CAM5.3-Oslo, the stochastic nature of freezing is considered for heterogeneous freezing in mixed-phase clouds, which is described according to classical nucleation theory (CNT; Pruppacher and Klett, 1997). Dust (DST_A2 and DST_A3) and black carbon (BC_AI) can act as ice nucleating particles (INP). Water molecules can form small agglomerates of ice on the surface of INP, and if these ice clusters reach a critical size the thermodynamic energy barrier ΔG of the water–ice transformation is passed.

A common formulation for the ice nucleation rate is used for deposition and immersion freezing, as well as for contact nucleation, which is identical to Eq. (1) in Wang et al. (2014). Deposition freezing and contact nucleation take place if the particles are uncoated or not completely coated. The coating thickness is calculated from the coated volume of the tracers and the volume of the dust and black carbon cores. The particle ability to act as INP in these mixtures is suppressed if the coated volume exceeds the thickness of one monolayer of sulfate. Particles can be coated according to Table 2. Immersion freezing is allowed to take place on cloud-borne dust and black carbon, which becomes cloud-borne when interstitial particles merge with an already existing droplet or act as condensation nuclei themselves.

Two different approaches are considered for describing the contact angle for immersion freezing. The single contact angle (α) model is similar to previous descriptions with CNT (Hoose et al., 2010). An α-PDF model can also be applied for dust immersion freezing, in which the contact angle is formulated by a lognormal probability density function (Wang et al., 2014). Thus, the inhomogeneity within the aerosol population can be represented by accounting for differences in the individual particle's ice nucleation properties (described in detail by Wang et al., 2014).

Compared to the study of Wang et al. (2014), we have used a small correction to the α-PDF model, which is also being taken into account in later releases of CAM versions by the National Center for Atmospheric Research (NCAR). The original calculation of the probability $p(\alpha)$ in the α-PDF model relies on a bin number of 101, which we have found to be too small to represent the lognormal distribution with a small standard deviation σ (e.g., 0.01) properly (Fig. 3). This resulted in an unphysical lower limit of the activated fraction of INP so that the INP activated fraction values were not able to fall below this limit and therefore stayed constant above a certain temperature (e.g., at $\sim 5 \times 10^{-5}$ for $T > -15\,°\mathrm{C}$ in Fig. 1 in Wang et al., 2014). By increasing the bin number to 501, the distribution can be described more accurately (Fig. 3) and the unphysical behavior of the activated fraction is no longer present.

3 Model configuration and simulation setup

All simulations have been run with 0.9° (latitude) by 1.25° (longitude) horizontal resolution and with 30 layers in the vertical. In hybrid sigma pressure coordinates, the uppermost eta level (or top of the level) mid-value is 3.64 (2.26) hPa, and for the lowermost level it is 992.56 (985.11) hPa. The number of layers below approximately 1 and 2 km of height a.s.l. are five and eight, respectively. CAM5.3, and therefore also CAM5.3-Oslo, has two choices for stratiform microphysical cloud schemes: MG1.0 (Morrison and Gettelman,

Table 3. Overview of the experiments in this study. Note that the land model (CLM4.5) setup is for a PD climate, so BVOC emissions are based on PD land use. All simulations have been run with 0.9° × 1.25° horizontal resolution and with 30 layers in the vertical.

Name	Meteorology	Emission year	Years simulated (years analyzed)
NUDGE_PD	ERA-Interim	2000	2004–2010 (2006–2010)
NUDGE_PI	ERA-Interim	1850	2004–2010 (2006–2010)
AMIP_PD	CAM5.3-Oslo/AMIP	2000	1–30 (3–30)
AMIP_PI	CAM5.3-Oslo/AMIP	1850	1–30 (3–30)

2008) and MG1.5 (Gettelman and Morrison, 2015). Both are double-moment (i.e., mass and number predicting) bulk cloud microphysics schemes with prognostic cloud droplet and cloud ice mass mixing ratios and number concentrations. MG1.5 is an update of the original formulation MG1, in which the location for updating prognostic droplet number mixing ratios with the tendency for droplet activation has been moved to the beginning of the scheme. We have in this study used MG1.5. The land model CLM4.5 (Oleson et al., 2013) is configured with satellite-observed phenology.

Two different configurations have been used to study and evaluate the aerosols: the nudged configuration (in the NUDGE_PD and NUDGE_PI simulations) and the AMIP configuration (in the AMIP_PD and AMIP_PI simulations); see Table 3 for an overview. The model has been run with aerosol and aerosol precursor emissions from year 2000 (PD) and 1850 (PI) for both configurations. We have also used PD oxidant levels in the PI simulations, as in K13. The effects of using PI oxidant levels on the effective radiative forcing in CAM5.3-Oslo, and on the indirect effects in particular, are being studied by Karset et al. (2018). Only the aerosol and aerosol precursor emissions or concentrations differ between the PD and PI simulations, while greenhouse gas concentrations, land use, and prescribed SSTs and sea ice concentrations are identical. The concentrations of DMS and biogenic OM in the ocean surface layer are also the same, although the emissions of these into the atmosphere differ slightly due to different meteorological conditions.

The difference between the AMIP and the nudged configuration is that the latter includes additional terms to the dynamical equations that push (nudge) the model meteorology towards the observed (or reanalyzed, read in 6-hourly, and interpolated in time) meteorology using a relaxation time of 6 h (Kooperman et al., 2012; Zhang et al., 2014). The main purpose of using the nudged configuration is to constrain natural variability, as a significantly higher number of simulated years is required to isolate statistically significant differences in cloud radiative forcing (due to anthropogenic aerosols) with the free AMIP configuration (Kooperman et al., 2012). Another objective is to obtain a model meteorology that more closely resembles actual meteorological conditions during the period of observations, which the model is compared with in the aerosol and cloud validation in Sect. 4. We have run both configurations in order to verify that the results are coherent and to be able to study how much the nudging affects the results.

In the nudged configuration, we use meteorological data from ERA-Interim (Berrisford et al., 2011) for the period 2004–2010. We nudge only to horizontal winds and surface pressures (Zhang et al., 2014). This way of nudging will allow the aerosols to influence temperatures and clouds. While nudging to observed temperatures might also improve the comparison of aerosol properties with observations, leaving the temperature un-nudged is important for the calculation of the indirect and semi-direct effect of aerosols (Zhang et al., 2014), since these are most realistically (or at least consistently) estimated with the model's own vertical temperature gradients, which again are crucial for atmospheric stability and vertical mixing.

4 Results and discussion

The predecessor model version CAM4-Oslo has been extensively validated and compared with other models through the AeroCom project (Aerosol Comparisons between Observations and Models: http://aerocom.met.no, last access: 24 September 2018) in studies by Jiao et al. (2014), Tsigaridis et al. (2014), Kipling et al. (2016), and Koffi et al. (2016), as well as in K13. A separate evaluation of CAM4-Oslo and other CMIP5 models by using the remote sensing of aerosols in the Arctic was made by Glantz et al. (2014). In this section we attempt to answer the following question: how does CAM5.3-Oslo perform with respect to aerosol and aerosol-related cloud properties compared with observations? We first compare some of the results with CAM4-Oslo (K13) and other studies, both in order to discuss properties that cannot easily (or at all) be compared with observations and to be able to see whether the updates and extended physical parameterizations have improved the model performance with respect to aerosols or not. The latter question is not straightforward, since the host model itself has undergone a great number of changes in moving from CAM4 to CAM5.3. Additionally, CAM4-Oslo was run with a coarser horizontal resolution of 2°.

4.1 Concentrations and budgets

4.1.1 Budgets and vertical profiles

Table 4 shows the budgets for the different species in the model simulations. For each term in the table, results from both present day (PD) and preindustrial (PI) conditions are listed, together with the respective values found in K13. Unless otherwise stated, the discussed model values are from the NUDGE_PD simulation.

Table 4. Aerosol budgets for the different components in the ERA-Interim nudged and the AMIP (shown in square brackets) simulations for year 2000 (PD) and 1850 (PI) emissions. Emission and burdens for DMS, SO_2, and SO_4 are given as Tg(S) yr^{-1} and Tg(S). For each cell the upper row shows results from NUDGE_PD [AMIP_PD], and the lower row shows results from NUDGE_PI [AMIP_PI]. The burdens are calculated from interstitial aerosols only. Results in round brackets are from the PD 2000 experiment in Kirkevåg et al. (2013) for comparison. Entries labeled N/A are not assessed, indicating that the respective processes are not defined or applicable for the model.

	DMS	SO_2	SO_4	Dust	Sea salt	BC	OM
Emissions ($Tg\,yr^{-1}$)	34.3 [34.6] (18.1) 34.3 [34.7] (18.1)	65.0 [65.0] (66.3) 14.6 [14.6] (16.4)	1.67 [1.67] (1.70) 0.373 [0.373] (0.42)	3104 [2508] (1672) 3135 [2552] (1672)	1937 [2003] (6462) 1937 [2005] (6462)	7.93 [7.93] (7.70) 3.15 [3.15] (3.06)	86.9 [87.4] (122) 61.4 [61.9] (97.5)
Chemical sources ($Tg\,yr^{-1}$)	N/A N/A	31.5 [31.8] (13.2) 31.5 [31.9] (13.2)	56.2 [56.4] (62.2) 26.5 [26.3] (23.2)	N/A N/A	N/A N/A	N/A N/A	87.3 [83.2] (16.2) 89.5 [85.3] (15.5)
Dry dep. (% of sinks)*	N/A N/A	22.5 [22.5] (23.0) 17.7 [18.0] (10.5)	13.2 [12.9] (8.4) 13.3 [13.1] (6.3)	80.7 [80.7] (74.8) 80.5 [80.5] (74.8)	43.6 [43.3] (54.6) 43.5 [43.2] (54.6)	24.8 [23.5] (28.1) 21.7 [20.7] (27.3)	13.6 [13.0] (21.4) 13.2 [12.8] (22.4)
Wet dep. (% of sinks)	N/A N/A	19.3 [19.2] (7.9) 24.6 [24.2] (11.1)	86.8 [87.1] (91.6) 86.7 [86.9] (93.7)	19.3 [19.3] (25.2) 19.5 [19.5] (25.2)	56.4 [56.7] (45.4) 56.5 [56.8] (45.4)	75.2 [76.5] (71.9) 78.3 [79.3] (72.7)	86.4 [87.0] (78.6) 86.8 [87.2] (77.6)
Chemical loss (%)	100 [100] (100) 100 [100] (100)	58.2 [58.3] (69.1) 57.7 [57.8] (78.4)	N/A N/A	N/A N/A	N/A N/A	N/A N/A	N/A N/A
Lifetime (days)	1.48 [1.50] (2.39) 1.48 [1.50] (2.39)	1.35 [1.33] (1.11) 1.25 [1.26] (1.07)	3.70 [3.65] (3.80) 3.25 [3.21] (3.21)	1.92 [1.93] (2.55) 1.91 [1.94] (2.55)	1.07 [1.04] (0.28) 1.07 [1.04] (0.28)	4.98 [4.77] (8.12) 5.03 [4.83] (7.12)	5.13 [4.84] (7.58) 4.87 [4.62] (7.32)
Burden (Tg)	0.140 [0.143] (0.12) 0.140 [0.144] (0.12)	0.357 [0.352] (0.24) 0.158 [0.160] (0.087)	0.584 [0.579] (0.59) 0.239 [0.238] (0.21)	16.3 [13.3] (11.7) 16.4 [13.6] (11.7)	5.70 [5.72] (4.94) 5.67 [5.71] (4.94)	0.108 [0.103] (0.17) 0.043 [0.042] (0.060)	2.44 [2.26] (2.87) 2.01 [1.86] (2.27)

*Calculated as 100 % minus chemical loss (%) minus wet deposition (%).

The result of the change in DMS emission parameterization described in Sect. 2.4 is an almost doubled DMS emission (34–35 $\mathrm{Tg\,S\,yr^{-1}}$) compared to the 18.1 $\mathrm{Tg\,S\,yr^{-1}}$ found in K13, accompanied by a similar increase in the SO_2 source term from the oxidation of DMS. The main reason for the increase is that the DMS emissions in Dentener et al. (2006) (applied in K13) were based on the DMS climatology of Kettle and Andreae (2000), with generally lower DMS concentrations in seawater than in the updated version of Lana et al. (2011). An experiment with wind-driven DMS emissions in a research version of CAM4-Oslo using the same transfer function gave 22.0 $\mathrm{Tg\,S\,yr^{-1}}$ with the Kettle and Andreae (2000) data and 34.2 $\mathrm{Tg\,S\,yr^{-1}}$ with the Lana et al. (2011) data. The shorter lifetime of DMS (1.5 days) compared to K13 (2.4 days) is likely caused by the use of different oxidant fields. Liu et al. (2012) obtain a lifetime of 1.3 days using nearly the same chemical mechanism (see Sect. 2) and the same oxidant fields as in the present work, but with emissions from Dentener et al. (2006). An additional test simulation with CAM5.3-Oslo with the AMIP PD setup and 2° resolution shows that the effect of increased resolution (to 1°) on DMS emissions and lifetime alone is only about 5 % and 0.2 %, respectively (not shown). Note also that the increase in column burden from CAM4-Oslo to CAM5.3-Oslo is much smaller than the increase in emissions (see Table 1), going from 0.12 to 0.14 Tg S. These both lie well within the range of estimates (0.015–0.17 Tg S) from other model studies reported by Liu et al. (2007); see their Table 1.

The chemical source for SO_4 is divided into clear-air sources through the $SO_2 + OH$ reaction and production in cloud water. The chemical sources of OM (via SOA) are mainly from monoterpene and isoprene. This gives a total of 78 $\mathrm{Tg(OM)\,yr^{-1}}$ of SOA produced from terpenes, which lies within the range of AeroCom models published by Tsigaridis et al. (2014). For comparison, the total amounts of BVOC emitted as isoprene and monoterpene are 438 and 119 $\mathrm{Tg\,yr^{-1}}$, respectively. There is also a source from the oxidation of DMS to MSA assumed to form organics (ca. 9 $\mathrm{Tg(OM)\,yr^{-1}}$), adding up to a total of 87 $\mathrm{Tg(OM)\,yr^{-1}}$. As mentioned in Sect. 2.2, for the MSA contribution to SOA, 20 % and 80 % of the MSA mass is added to the $SOAG_{LV}$ and $SOAG_{SV}$ tracers, respectively. The exact LV-to-SV ratio is unknown, but we find a quite low sensitivity of the anthropogenic change in cloud effective radiative forcing (i.e., the indirect effect, which is the most important in a climate change perspective) to the assumed apportionment of MSA: test simulations indicate that the total shortwave and longwave indirect effect only changes by about $-0.03\,\mathrm{W\,m^{-2}}$ if all MSA goes into $SOAG_{SV}$ (no nucleation) and by $0.00\,\mathrm{W\,m^{-2}}$ if we instead feed all MSA into the $SOAG_{LV}$ tracer. The effect of neglecting the MSA contribution to SOA altogether is similarly estimated to give a $-0.10\,\mathrm{W\,m^{-2}}$ change.

The zonal mean mass mixing ratios and their variation with height for SO_2, BC, OM, sulfate, mineral dust, and sea salt (SS) are shown in Fig. 4, both for NUDGE_PD and AMIP_PD. The figure shows that some BC is transported to the stratosphere where the lifetime is longer. OM and sulfate also have this secondary maximum in the stratosphere, but the concentrations aloft are smaller in CAM5.3-Oslo than in CAM4-Oslo (not shown). Dust and sea salt do not exhibit the same clear secondary maxima in the stratosphere, since these particles are generally larger and more readily removed by sedimentation. The additional 2° test simulation with CAM5.3-Oslo reveals that the effect of increased resolution on vertical profiles is very small compared to the differences between the two model versions for all species (not shown).

For BC we can compare the model with profiles from the HIAPER (High-Performance Instrumented Airborne Platform for Environmental Research) Pole-to-Pole Observations (HIPPO) of carbon and greenhouse gases study over the (mainly remote) Pacific Ocean in January and November 2009, March–April 2010, and June–July and August–September 2011 (Wofsy et al., 2011; Schwarz et al., 2013); see Fig. 5. It is clear that the new model version does produce less excessive BC concentrations in the upper troposphere and in the stratosphere globally (Fig. 5a) and that it now compares better with the HIPPO observations in the Pacific (Fig. 5b), although the concentrations are still too high in the upper troposphere and lower stratosphere for this region, similar to the findings for CAM5.3-MAM4 in Liu et al. (2016). This is probably related to the way aerosols are transported and scavenged in deep convective clouds in the model (see, e.g., Kipling et al., 2013, 2016). There are currently ongoing tests with alternative treatments of convective transport and mixing (see Sect. 2.1.5 of K13 for a sensitivity test on this in CAM4-Oslo); these are improved treatments which will possibly be included in the upcoming CAM6-Oslo version for CMIP6. The additional 2° test simulation reveals that the effect of increased resolution on the lifetime of BC is only about 0.3 % (not shown). Note that NUDGE_PD and AMIP_PD yield almost identical results in the troposphere. This indicates that the nudging, as long as we are not nudging the temperature, only has modest effects on the convective transport and mixing of BC in the model (see also Fig. 4).

Some of the changes in aerosol concentration fields are connected to changes in cloud microphysics in the host model. Two major factors that affect both aerosols and aerosol precursors are the amount of liquid cloud water and the cloud fraction. Globally averaged, CAM5.3-Oslo has only about one-third as high cloud liquid water path (LWP) as CAM4-Oslo, while the precipitation rate is slightly (7 %) larger. Since the loss rate of aerosol activated to cloud droplets in the model is assumed to be proportional to the precipitation-to-LWP ratio, an increased scavenging efficiency and a subsequent reduction in aerosols away from source regions as a result of the reduced LWP is to be expected. A reduction in aerosol transport to remote regions is

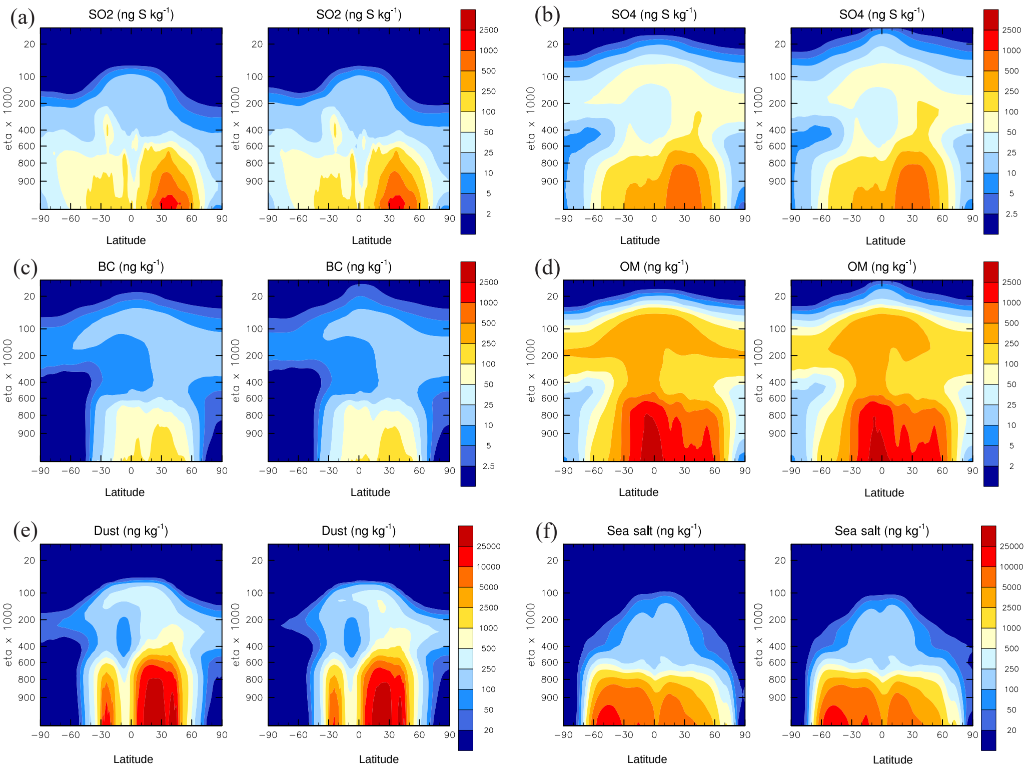

Figure 4. Modeled zonal mean mass mixing ratios of **(a)** SO_2, **(b)** sulfate (as S), **(c)** BC, **(d)** OM, **(e)** dust, and **(f)** sea salt in the NUDGE_PD (left panels) and the AMIP_PD (right panels) simulation (eta × 1000 is the model hybrid coordinate eta level multiplied by 1000). Note the different scales for mineral dust and sea salt vs. the other components.

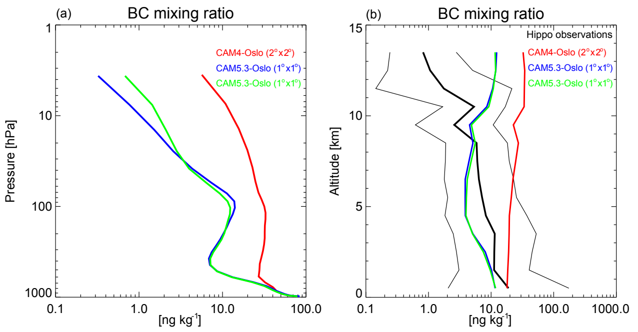

Figure 5. (a) Globally averaged annual BC mass mixing ratio profiles as modeled in the NUDGE_PD (blue line) and AMIP_PD (green line) experiments and in CAM4-Oslo (red line) for comparison. **(b)** Modeled BC mass mixing ratio profiles from the same simulations as in **(a)** compared to HIPPO aircraft campaigns averaged over the areas and months in which the campaign took place (Schwarz et al., 2013; see also Samset et al., 2014).

indeed found for all aerosol components and is particularly pronounced in the Arctic and Antarctic regions. At the same time, the total (low) cloud cover has increased from 53 % (34 %) in CAM4-Oslo to 66 % (43 %) in CAM5.3-Oslo, with the largest changes at high latitudes. This increase in cloud cover likely also gives an increase in the frequency of precipitation events, which tends to reduce aerosol lifetimes. The additional 2° test simulation (note that this by default setup has a slightly different cloud tuning) reveals that the effect of increased resolution on LWP and on total (low) cloud cover is small compared to the differences between the two model versions, only about 1 % and −1 % (−3 %), respectively (not shown).

Even sea salt burdens have been reduced away from the source regions, despite an almost 4 times increase in global lifetime, which is now 1.07 days. This is to a large degree due to the shift towards more long-lived (i.e., accumulation mode) particle sizes (compare Table 2 with Table 1 in K13). While the lifetime is now longer, the emissions have decreased even more so that the overall sea salt burdens are about 35 % smaller than in CAM4-Oslo. In Liu et al. (2012), the sea salt lifetime lies between CAM4-Oslo and CAM5.3-Oslo, but is quite dependent on the aerosol microphysics (0.76 days in MAM3 and 0.55 days in MAM7). The effect of increased resolution from 2 to 1° is found here to be 11 % for the emissions (due to stronger winds), 9 % for the burden, and only −2 % for the lifetime (not shown).

As for BC, the concentrations of OM, sulfate, and mineral dust have also dropped in the upper troposphere and lower stratosphere when going from CAM4-Oslo to CAM5.3-Oslo. This reduction is more substantial for carbonaceous aerosols than for the other species, however. In addition to the increased overall scavenging efficiency, BC and primary OM now experience a more rapid transition from external to internal mixtures; see Sect. 2.3. The lifetimes of BC and OM of approximately 5 days in CAM5.3-Oslo are now more comparable to the MAM7 values in Liu et al. (2012), which are 4.4, 4.9, and 4.1 days for BC, OM, and SOA, respectively. The additional 2° test simulation reveals that the effect of increased resolution on the OM lifetime is only about 1 % (not shown).

The situation for sulfur is more complex. While the scavenging efficiency of SO_2 is increased on the one hand, as for aerosols, the lower liquid water content in CAM5.3-Oslo, on the other hand, acts to reduce the aqueous-phase reaction rates. The net effect of all changes is a ca. 20 % increase in lifetime. Furthermore, while SO_2 (and thus the potential for the formation of sulfate) is now transported higher into the atmosphere, the increase in aerosol activation scavenging tends to counteract the effect of this enhanced transport. The combined effect of a longer lifetime for SO_2 and increased aerosol loss rates in the lower troposphere is just a 3 % overall reduction in the atmospheric residence time of SO_4. The estimate at 3.70 days is very close to the sulfate lifetimes in Liu et al. (2012): 3.72 days for MAM7 and 3.77 days for MAM3. The additional 2° test simulation reveals that the effect of increased resolution on the SO_2 lifetime is only about -0.4 % (not shown).

As for carbonaceous aerosols, the lifetime of mineral dust is also reduced. The main reason for this reduction is most likely the general increase in activation scavenging. Below-cloud collection efficiencies are still as in Seland et al. (2008), so any changes in below-cloud scavenging are due to changes in precipitation and aerosol life cycling. The relative amount of dust emitted in the accumulation mode (DST_A2) in the new emission parameterization (13 %) is larger than for the prescribed emissions in CAM4-Oslo (11 %), which should rather contribute to a longer dust lifetime in CAM5.3-Oslo due to reduced gravitational settling. A test simulation performed with an earlier model version showed that a tuning of the relative amount of emissions taking place through the accumulation mode from 13 % to 20 % led to a 20 % increase in lifetime globally. The inherent assumption of OsloAero that there is a constant size background aerosol – the particles cannot shrink to smaller sizes than that of the background as the largest particles are deposited – may result in a shorter lifetime of the coarse mode compared to the modal aerosol schemes (MAM3 and MAM7) in Liu et al. (2012). Since Liu et al. (2012) calculate number and mass independently, the size of the coarse-mode particles may decrease with time, thereby increasing the lifetime of that mode. The estimated dust lifetime of 1.9 days is shorter than in both MAM3 (2.6 days) and MAM7 (3.1 days) in Liu et al. (2012). The additional 2° test simulation reveals that the effect of increased resolution on the mineral dust lifetime is only about 2 % (not shown).

According to Kok et al. (2017), mineral dust in global models is probably often too fine based on constrained atmospheric dust properties and abundance. AeroCom emission rates and loadings (Textor et al., 2006) are below the central estimates in Kok et al. (2017) of 1000–2700 $\mathrm{Tg\,yr^{-1}}$ and 13–29 Tg, respectively. We get a slightly higher global emission rate of 3100 $\mathrm{Tg\,yr^{-1}}$ in NUDGE_PD, but 2500 $\mathrm{Tg\,yr^{-1}}$ in the AMIP_PD simulation. The estimated global dust burden of 13 (NUDGE_PD) or 16 Tg (AMIP_PD) that follows, however, falls within the central estimates of Kok et al. (2017). The global emission rate may be adjusted by a tuning factor (a constant in the emission flux term) in CAM5.3, but in the present version we have retained the value used in the original CAM5.3 code.

Some of the aerosol burden changes from CAM4-Oslo to CAM5.3-Oslo are due to differences in meteorology. To roughly estimate the magnitude of such an effect, we compare the NUDGE_PD and AMIP_PD results in Table 4.

The globally averaged burdens of DMS and SO_2 differ by less than 2 %, and SO_4 and sea salt by less than 1 %, while BC and OM and mineral dust are ca. 5 % and 7 % lower in the free-running AMIP simulations, respectively. So for these species the differences between NUDGE and AMIP are quite small. We would probably have obtained even smaller changes if the model was self-nudged, i.e., being nudged to a meteorology produced by the model itself (e.g., the AMIP_PD simulation) instead of the ERA meteorology. In a similar comparison by Liu et al. (2016), they obtain as much as ca. 20 % lower BC and OM burdens with nudged (towards 1-year recurrent meteorology) vs. a free simulation (10 years). They partly attribute this to interannual variability, but mainly to (climatological) differences in the meteorological conditions between the free and nudged model simulations, which affect aerosol transport and cloud processing. Unlike the nudging procedure applied here, Liu et al. (2016) also nudged the model meteorology to reanalyzed temperatures (Tilmes et al., 2015), which may explain the larger difference in simulated aerosol burdens between their nudged and free AMIP simulations. A similar effect was found in an older version of CAM5.3-Oslo as we went from nudging temperatures, specific humidity, and U, V, PS, and some surface fields to only nudging U, V, and PS: the difference in globally averaged LWP between the nudged and free simulations was reduced by an order of magnitude. An important effect of nudging is that it constrains the model's natural variability (Kooperman et al., 2012), which is useful in calculations of the indirect effect of aerosols since it reduces the simulation length required to obtain sufficiently high signal-to-noise ratios. When nudging to an atmospheric circulation produced by the model itself (self-nudging) instead of using data from reanalysis (such as the ERA data), the circulation mean and variability characteristics are less affected, resulting in ERF estimates more consistent with the

Table 5. Seasonal and annual normalized mean biases (NMBs) and Pearson correlation coefficients (R) for NUDGE_PD vs. observed climatological surface concentrations (see http://aerocom.met.no, last access: 24 September 2018; cf. Fig. 6). NMBs with absolute values of 50 % or more are listed in bold font.

	BC		SO_2		SO_4		OM (OA)		SS		DUST	
	NMB	R	NMB	R	NMB	R	NMB	R	NMB	R	NMB	R
DJF	**−53 %**	0.32	**154 %**	0.45	−19 %	0.66	−34 %	0.31	20 %	0.49	−8.4 %	0.43
MAM	−21 %	0.47	**124 %**	0.23	19 %	0.69	**63 %**	0.44	13 %	0.57	−39 %	0.82
JJA	8.2 %	0.61	**143 %**	0.21	46 %	0.87	**294 %**	0.37	28 %	0.59	**−52 %**	0.47
SON	−28 %	0.38	**180 %**	0.26	31 %	0.70	**96 %**	0.25	26 %	0.53	−42 %	0.45
ANN	−28 %	0.38	**150 %**	0.35	22 %	0.72	**122 %**	0.29	22 %	0.54	−39 %	0.52

model's own innate behavior. However, since the circulation variability is not "synchronized" here with the observed variability of a specific time period, self-nudging does not facilitate a comparison of modeled aerosol properties with observations for that time period.

The 3 % increase in sea salt emissions in going from NUDGE_PD to AMIP_PD, which is consistent with larger simulated 10 m wind speeds in the extratropical storm track regions, is almost offset by a reduction in lifetime (more wet scavenging), giving only a 1 % net increase in column burden. There is one exception for which the difference between NUDGE_PD and AMIP_PD seems to be important, namely for mineral dust. This is most readily seen from the global dust emissions, varying with wind speed and soil humidity, which are 19 % lower in AMIP_PD than in NUDGE_PD, very close to the 18 % difference in atmospheric burden.

The contribution by interannual variations in the NUDGE_PD simulation to global aerosol or aerosol precursor burdens, given here as normalized standard deviations, is found to be about 3.6 % for DMS, 0.8 % for SO_2, 1.2 % for SO_4, only 0.1 % for BC, 1.0 % for OM, 2.6 % for sea salt, and 2.5 % for mineral dust. Hence, the above-estimated changes in burdens from NUDGE_PD to AMIP_PD are actually smaller than 1 standard deviation of the interannual variation (in NUDGE_PD) for DMS, SO_4, and sea salt so that only SO_2, BC, OM, and mineral dust can be said with some confidence to be different (smaller) in the AMIP_PD than the NUDGE_PD simulation.

4.1.2 Evaluation of near-surface mass concentrations

Column burdens cannot be measured and observed surface concentrations are used here for validating the aerosol masses in the model. Figure 6 and Table 5 show surface mass concentrations of BC, SO_2, OA (modeled OM vs. observed OC*1.4; see explanation in the figure caption and below), SS (sea salt), SO_4 (sulfate), and DUST (mineral dust) in NUDGE_PD compared with various observations as available via the AeroCom intercomparison project (http://aerocom.met.no, last access: 24 September 2018). Note that the amount of data and spatiotemporal coverage available for the different parameters is inhomogeneous because of data network fluctuations and incomplete storage in the databases used (EBAS: Tørseth et al., 2012; see also http://ebas.nilu.no, last access: 25 September 2018; AEROCE: Arimoto et al., 1995; Huneeus et al., 2011). Tables 6–8 give an overview of statistical evaluation for the NUDGE_PD and AMIP_PD simulations as well as a range of AeroCom Phase II (AP2) and AeroCom Phase III (AP3) models. These are compared for different years, both for individual years (meteorology of 2006 for AP2 and 2010 for AP3) and our model climatology against a climatology from the observational data.

We find that the model mainly overestimates SO_2 concentrations. One possible explanation for the large positive bias is the low vertical and horizontal resolution in the model. With such low resolution the model does not capture the dispersion of primary emissions of SO_2 well from large point sources or shipping routes. A part of this bias probably comes from the fact that we are comparing concentrations at the midpoint of the lowermost model layer ($\sim$ 50 m) with ground-based observations (see discussion in Simpson et al., 2012). For the climatologically averaged SO_2 data, the Pearson correlation coefficient R (hereafter often just referred to as the correlation) is slightly better for the nudged than for the un-nudged AMIP simulation, in which instead the normalized mean bias (NMB; hereafter often just referred to as the bias) is slightly better. The bias and correlation for each of the continents are 216 % and 0.52 for Europe, 134 % and 0.94 for North America, and −53 % and −0.02 for Asia. None of the AP3 models have available SO_2 statistics, while four of the five AP2 models that do exhibit higher biases than ours. The correlations are also lower than ours in all the AP2 models, while three of them have a higher percentage of monthly model values within a factor of 2 of the observed values (Fact2).

Sulfate is also somewhat overestimated, with a positive bias of 22 % and a correlation as high as 0.72 for the monthly climatological data, slightly above that of the free AMIP simulation. CAM4-Oslo exhibits a smaller, slightly negative bias, but is less correlated with the observations. The new model version still yields a lower Fact2 value, all in all performing slightly worse than the predecessor. Biases and correlations for each of the continents are 15 % and 0.54 for

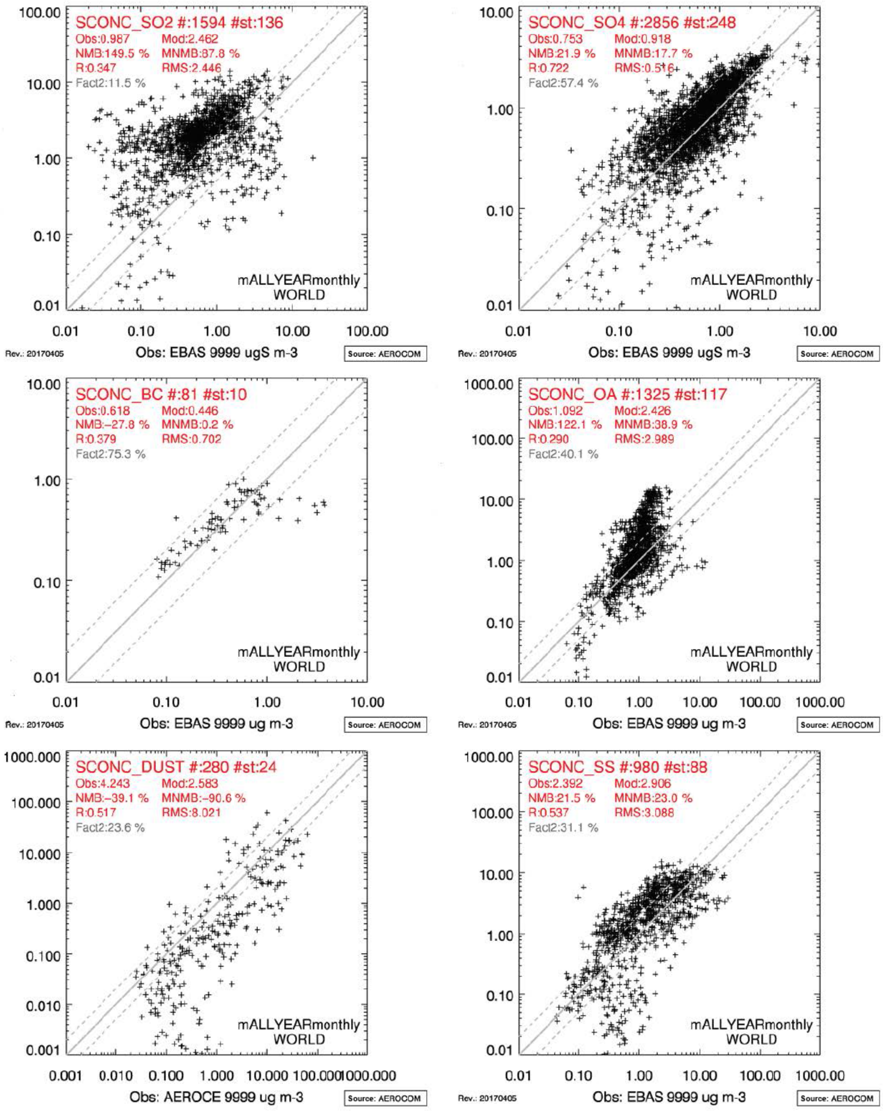

Figure 6. Surface concentrations in the NUDGE_PD experiment compared with EBAS and AEROCE data through the AeroCom tools. OA represents modeled OM concentrations vs. observed OC concentrations multiplied by 1.4 (the assumed OM/OC ratio for fossil fuel OC in the model).

Europe, 38 % and 0.92 for North America, and −9 % and 0.59 for Asia. The bias for sulfate is better than in four of the eight AP3 models with available concentration data (for year 2010), while the correlation falls just below the AP3 range. Comparing against the 23 AP2 models (for year 2006), however, CAM5.3-Oslo has a lower bias than only 6 of the AP2 models, while outperforming or matching 14 models with respect to correlation.

We see that the model mainly underestimates BC, especially the highest concentrations. The bias is −28 % and the correlation 0.38, which is also higher here than for the AMIP simulation. CAM4-Oslo has an almost twice as large bias and a much lower correlation coefficient, so apparently there has been an improvement in modeled BC surface concentrations for the very limited number and geographical coverage of stations available (in Europe only). As much as 75 % of the model values lie within a factor of 2 of the observed values, compared to 68 % for CAM4-Oslo. The BC bias is also better than in six of the eight AP3 models. Although the correlations for BC are quite low for all the AP3 models, only one has a lower correlation than CAM5.3-Oslo. Similarly, comparing against the 23 AP2 models, CAM5.3-Oslo outperforms only 7 of the models bias-wise and 6 with respect to correlation.

For the calculation of mass concentrations of OM from OC the model does not distinguish between tracers from different source types, since they are lumped together for each of the background and size-modifying tracers. This has been

Table 6. Normalized mean bias (NMB, in %) statistics from 1 year of monthly data (see AeroCom web interface for details on coverage and networks). Compared are NMBs for the near-surface aerosol mass concentrations and column-integrated optical properties for CAM5.3-Oslo, as well as for CAM4-Oslo and AeroCom models in the aerocom.met.no database (represented here by an NMB range). The top row indicates the meteorological year for observations and nudged simulations; climatology means that all available years from the model or observations are used for the statistics. The regional coverage areas for observations are abbreviated as follows: E: Europe, N: North America, A: Asia, global: nearly all continents or world oceans (island sites) are represented. The control versions of the AeroCom Phase II (AP2) and Phase III (AP3) models used in the model intercomparison are listed below the table, with names as on the AeroCom web interface. Optics diagnostics listed for most of the AP2 and AP3 models (exact number is not available) are clear-sky values, in the sense that the clear-sky humidity of the grid cell is used for calculating hygroscopic swelling of the aerosol (Michael Schulz, personal communication, 6 September 2018). Supplementary information as provided by AeroCom modeling teams about optics diagnostics for 11 of the AP2 models included in this study may be found at https://wiki.met.no/aerocom/optical_properties (last access: 25 September 2018). CAM4-Oslo and CAM5.3-Oslo compute all-sky optical properties using the average humidity (RH) of the grid cell. Clear-sky (CS) properties are instead represented by a 2-D cloud-free fraction-weighted average of the all-sky properties. Only a few other AeroCom models follow a similar clear-sky optics definition, and the optics data submitted to AeroCom for a few of the models are all-sky values both in terms of cloud conditions and RH for hygroscopic growth. Data from CAM4-Oslo and the two simulations with CAM5.3-Oslo, all run with 2000 (PD) emissions, can be found in the aerocom.met.no database under the project label NorESM, subset NorESM-Ref2017. NMBs with absolute values of 50 % or more are listed in bold font. Entries labeled N/A indicate that the respective model data are not available.

NMB (%)	Climatology			2006			2010		
	Coverage	CAM4-Oslo	CAM5.3-Oslo NUDGE_PD (AMIP_PD)	Coverage	AP2 range (≤ 23models*)	CAM5.3-Oslo NUDGE _PD	Coverage	AP3 range (≤ 8models*)	CAM5.3-Oslo NUDGE _PD
SO_2 conc.	E; N; A	16	**150 (137)**	E; N	**65–977**	223	E	NA	**328**
SO_4 conc.	E; N; A	−5	22 (27)	E; N	**−61–186**	37	E	−40–**199**	31
BC conc.	E	**−54**	−28 (−34)	E	−40–**64**	−32	E	**−65**–35	-16
OA (OM) conc.	E; N	**108**	**122 (125)**	E; N	**−60**–335	141	E	**−70–71**	23
Sea salt conc.	E; N; A	**50**	22 (40)	E; N	**−97–477**	66	E	**−56–301**	36
Dust conc.	Global	−14	−39 (−24)	Global	**−64–106**	−34	Global	**−82**–4	−46
OD550CS	Global	−22	−16 (−27)	Global	**−50–133**	−18	Global	**−53**–−3	−24
OD550	Global	−8	15 (3)	Global		11	Global		12
ABS550CS	Global	−32	−25 (−30)	Global	**−80**–21	−38	Global	NA	−36
ABS550	Global	−33	−20 (−30)	Global		−30	Global		−35
ANG4487CS	Global	NA	−17 (−15)	Global	−30–31	−15	Global	NA	−16
ANG4487	Global	−19	−44 (−42)	Global		−44	Global		−45

*Excluding models with missing data or with NMB < −99 % or NMB > 1000 % (see the main text for more details). AP2 models: CAM5.1-MAM3-PNNL.A2.CTRL, ECHAM-SALSA.A2.CTRL, ECHAM-SALSA.A2.CTRL.emi2000, GISS-MATRIX.A2.CTRL, GISS-modelE.A2.CTRL, GLOMAPbin1pt1.A2.CTRL, GLOMAPmodev4.A2.CTRL, GLOMAPmodev6R.A2.CTRL, GMI.A2.CTRL, GMI-v3.A2.CTRL, GOCART-v4.A2.CTRL, GOCART-v4Ed.A2.CTRL, HADGEM2-ES.A2.CTRL, HADGEM3-A-GLOMAP.A2.CTRL, INCA.A2.CTRL, MPIHAM_V1_KZ.A2.CTRL, MPIHAM_V2_KZ.A2.CTRL, OsloCTM-v2.A2.CTRL, OsloCTM.A2.CTRL, SALSA_v1_TB.A2.CTRL, SPRINTARS-v384.A2.CTRL, SPRINTARS-v385.A2.CTRL, and TM5.V3.A2.CTRL. AP3 models: CNRM-CM6.2Nut127_AP3-CTRL2015, CNMR-CM6.2t127_AP3-CTRL2015, ETHZ-ECHAM-HAM2_CTRL2015, GEOS-Chem-v10-01_AP3-CTRL2015, OsloCTM3_AP3-CTRL2015, SPRINTARS-T106_AP3-CTRL2015, SPRINTARS-T213_AP3-CTRL2015, and TM5_AP3-CTRL2015.

done in order to limit the CPU requirements as much as possible, as the model (when fully coupled with the ocean and sea ice modules) is built for use in long climate simulations. We compare modeled OM with observed OC values that have been multiplied by 1.4 (defined as OA for the observations in Fig. 6, while OA simply means OM for the model values) to account for the conversion factor in going from fossil fuel OC to OM in the model (K13). For OM from biomass burning, defined as agricultural waste burning, grass fires, and forest fires in the model, the respective conversion factor is assumed to be 2.6 (K13; see also Formenti et al., 2003), i.e., 1.86 that of the fossil fuel emissions. If all OM originated from biomass burning, the bias would therefore be 19 % instead of 122 %. The latter value is simply based on the assumption of zero OC contribution from biomass burning. The truth concerning the validation probably lies somewhere between these two estimates, even though OM / OC ratios exceeding 2.6 might be more representative for some sources, such as MSA (see Sect. 4.2.1 in K13). For comparison, the respective bias values in CAM4-Oslo are 108 % and 12 %. The correlation coefficient for OM in CAM5.3-Oslo's NUDGE_PD is substantially lower than for both BC and SO_4, but very close to that for OM in both AMIP_PD and CAM4-Oslo. Regional bias and correlation values are 143 % and 0.44 for North America, where most of the observation sites are located, and −26 % and 0.01 for Europe.

Assuming that OA is representative for the modeled OM, in North America the concentrations are most overestimated in the months JJA, while being underestimated in DJF. In Europe OM is overestimated only in JJA. This may indicate that OC is overestimated in summer or that sources with OM/OC ratios exceeding 1.4 dominate during summer, as should be expected since relative contributions to OM from SOA (e.g., Gelencsér et al., 2007) and forest fires are gener-

Table 7. Pearson correlation coefficient (R) statistics for the same data as in Table 6.

R	Climatology			2006			2010		
	Coverage	CAM4-Oslo	CAM5.3-Oslo NUDGE_PD (AMIP_PD)	Coverage	AP2 range (≤ 23models*)	CAM5.3-Oslo NUDGE _PD	Coverage	AP3 range (≤ 8models*)	CAM5.3-Oslo NUDGE _PD
SO_2 conc.	E; N; A	0.28	0.35 (0.32)	E; N	0.27–0.57	0.61	E	NA	0.59
SO_4 conc.	E; N; A	0.61	0.72 (0.70)	E; N	0.47–0.76	0.70	E	0.34–0.65	0.32
BC conc.	E	0.14	0.38 (0.17)	E	0.15–0.57	0.42	E	0.20–0.43	0.24
OA (OM) conc.	E; N	0.31	0.29 (0.28)	E; N	0.15–0.39	0.25	E	0.00–0.52	−0.02
Sea salt conc.	E; N; A	0.60	0.54 (0.51)	E; N	0.12–0.83	0.80	E	0.34–0.72	0.71
Dust conc.	Global	0.45	0.52 (0.59)	Global	0.25–0.74	0.35	Global	0.27–0.66	0.55
OD550CS OD550	Global Global	0.67 0.67	0.59 (0.62) 0.64 (0.69)	Global Global	0.44–0.77	0.53 0.61	Global Global	0.40–0.76	0.57 0.63
ABS550CS ABS550	Global Global	0.58 0.58	0.47 (0.50) 0.47 (0.50)	Global Global	0.45–0.70	0.45 0.42	Global Global	0.60	0.40 0.47
ANG4487CS ANG4487	Global Global	NA 0.47	0.75 (0.74) 0.46 (0.46)	Global Global	0.56–0.72	0.68 0.45	Global Global	NA	0.69 0.43

*Excluding models with missing data.

Table 8. Percentage of model near-surface concentration and column-integrated optical parameter values within a factor of 2 of the observations (Fact2, given in %) for the same data as in Table 6.

Fact2 (%)	Climatology			2006			2010		
	Coverage	CAM4-Oslo	CAM5.3-Oslo NUDGE_PD (AMIP_PD)	Coverage	AP2 range (≤ 23models*)	CAM5.3-Oslo NUDGE _PD	Coverage	AP3 range (≤ 8models*)	CAM5.3-Oslo NUDGE _PD
SO_2 conc.	E; N; A	36	12 (12)	E; N	4–33	10	E	NA	7
SO_4 conc.	E; N; A	68	57 (53)	E; N	17–85	45	E	14–70	39
BC conc.	E	68	75 (72)	E	20–51	46	E	26–64	50
OA (OM) conc.	E; N	36	40 (40)	E; N	12–53	35	E	21–52	39
Sea salt conc.	E; N; A	34	31 (28)	E; N	0–37	31	E	2–40	34
Dust conc.	Global	34	24 (18)	Global	9–32	18	Global	7–23	19
OD550CS OD550	Global Global	75 69	42 (41) 68 (71)	Global Global	45–80	39 64	Global Global	38–74	49 58
ABS550CS ABS550	Global Global	54 53	47 (51) 50 (50)	Global Global	10–51	45 49	Global Global	NA	40 48
ANG4487CS ANG4487	Global Global	NA 81	83 (85) 49 (52)	Global Global	68–90	82 54	Global Global	NA	83 51

*Excluding models with missing data or with NMB < −99 % or NMB > 1000 % (see the main text for more details).

Table 9. Globally and annually averaged PD mass extinction coefficients at 550 nm for each of the main aerosol components in CAM5.3-Oslo compared to CAM4-Oslo and to AeroCom Phase I models. For a component X we calculate $\mathrm{MEC}_X = \mathrm{AOD}_X / B_X$, where B_X is the burden of the component.

MEC ($\mathrm{m}^2\,\mathrm{g}^{-1}$) decomposition	CAM4-Oslo	CAM5.3-Oslo NUDGE_PD (AMIP_PD)	AeroCom Phase I median (min–max)
Sulfate (SO_4)	6.7	5.84 (5.78)	8.5 (4.2–28.3)
OM	8.6	5.99 (6.06)	5.7 (3.2–11.4)
BC	6.5	7.56 (7.64)	8.9 (5.3–18.9)
Dust	1.4	1.64 (1.66)	0.95 (0.46–2.1)
Sea salt	3.1	5.04 (5.05)	3.0 (0.88–7.5)
Reference	Kirkevåg et al. (2013)	This work	Kinne et al. (2006)

Table 10. Globally and annually averaged aerosol radiative forcing (RF) and effective radiative forcing (ERF) decomposed into its SW and LW components for CAM5.3-Oslo and CAM4-Oslo compared with the respective mean values and ranges reported in IPCC AR5. Note that the estimates from IPCC AR5 are only available as sums of the SW and LW contributions and have been estimated for the period 1750 to 2011 (with one exception, see the footnote), whereas the CAM4-Oslo and CAM5.3-Oslo estimates are for year 1850 to 2000.

RF/ERF decomposition	CAM4-Oslo RF ($\mathrm{W\,m^{-2}}$)	CAM5.3-Oslo ERF ($\mathrm{W\,m^{-2}}$) NUDGE_PD (AMIP_PD)	IPCC AR5 RF ($\mathrm{W\,m^{-2}}$)	IPCC AR5 ERF ($\mathrm{W\,m^{-2}}$)
SW ari	−0.10	−0.095 (−0.092)*	−0.35 (−0.85 to 0.15)	−0.45 (−0.95 to 0.05)
LW ari	–	0.026 (0.026)*		
SW aci	−0.91	−1.50 (−1.45)*	Not assessed	−0.45 (−1.20 to 0.0)
LW aci	0.01	0.161 (0.155)*		
ari & aci	−1.00	−1.41 (−1.36)*	Not assessed	−0.9 (−1.9 to −0.1) −1.08 (−1.40 to −0.76)**
Reference	Kirkevåg et al. (2013)	This work	Boucher et al. (2013)	Boucher et al. (2013)

* The semi-direct effect is embedded here in the ERFaci term (Ghan, 2013), not in ERFaci as in the IPCC AR5 estimates. ** Mean ± 1 standard deviation for CMIP5 and ACCMIP models for the period 1850–2000.

ally larger in this season. As discussed in K13, in addition to the various OM/OC ratios in the model, as in nature, a further complicating factor comes from the use of different standards and methods for measuring OC mass concentrations. While being integrated over all particle sizes in the model, the measured quantities may be based on PM2.5 or PM10 values in different observation networks, as is the case for North America (PM2.5 in IMPROVE) vs. Europe (PM10 in EMEP). This hampers reliable validation of OM in the model in its present form. Ideally the model should carry separate tracers for OC from SOA (preferably speciated), fossil fuel, and biomass burning sources and also have separate mass diagnostics for the different size intervals, which would better facilitate a more comprehensive evaluation of organic matter in the model.

Compared to the eight AP3 models, the bias (i.e., modeled OM–measured OA) is found to be smaller than in all but one model. The correlation, however, is just below the range for the AP3 models. It is slightly negative for the whole year of 2010 (Europe only), as for the months MAM that year, while being 0.15 or higher in the other seasons. Comparing against the 22 AP2 models (1 model is missing surface concentration data), CAM5.3-Oslo has a smaller bias than only 1 of the models, while it performs better than 6 models with respect to correlations for the year 2006. The Pearson correlation in our model varies between 0.16 and 0.25 for years 2004–2006, when both North American and European stations are included, while being closer to zero or negative in 2007–2010 based only on European station data, in which it varies between −0.12 and 0.12. It is surprising that there has been practically no change in correlation for the all-year climatology since K13 (CAM4-Oslo in Table 7), for which the SOA treatment was very simplistic. This should be investigated in future studies.

For the sea salt surface concentrations we obtain a bias of 22 % and a correlation of 0.54, and 31 % of the model values are within a factor of 2 of the observations. Compared to CAM4-Oslo this is much better bias-wise, but with nearly

Table 11. All-sky and clear-sky aerosol optical depth (OD) and absorptive optical depth (ABS) at 550 nm, liquid water path (LWP), in-cloud cloud droplet number concentrations (CDNCs)* and effective cloud droplet radius (Reffl)** at 860 hPa (model layer 24), and ice water path (IWP). Also shown are the column-integrated CDNC (CDNCcol) and ice crystal number concentration values (ICNCcol, calculated as part of the post-processing).

Experiment	OD550 (OD550CS)	ABS550 (ABS550 CS)	LWP ($g\,m^{-2}$)	CDNCcol (1.e6 cm^{-2})	CDNC 860 hPa (cm^{-3})	Reffl 860 hPa (m)	IWP ($g\,m^{-2}$)	ICNCcol (cm^{-2})
NUDGE PD	0.152 (0.124)	0.0048 (0.0049)	53.85	1.39	58.93	11.25	10.00	6874.16
NUDGE PI	0.128 (0.109)	0.0036 (0.0037)	50.29	1.10	49.12	11.56	10.03	6876.01
NUDGE PD–PI	0.025 (0.015)	0.0012 (0.0012)	3.56	0.29	9.81	−0.31	−0.03	−1.9
AMIP PD	0.142 (0.113)	0.0042 (0.0044)	53.52	1.37	57.57	11.50	10.25	6882.92
AMIP PI	0.119 (0.098)	0.0031 (0.0032)	50.10	1.08	47.78	11.86	10.29	6882.97
AMIP PD–PI	0.023 (0.014)	0.0011 (0.0012)	3.42	0.29	9.79	−0.36	−0.04	−0.05

*CDNC is calculated as the average cloud water concentration AWNC (a grid average multiplied with the fractional occurrence of liquid at each time step) divided by the fractional occurrence of liquid, FREQL. **Reffl is calculated as the average cloud droplet effective radius AREL (a grid average multiplied with the fractional occurrence of liquid at each time step) divided by the fractional occurrence of liquid, FREQL.

the same Fact2 value. The bias is also about half of that in the free-running AMIP_PD simulation. Regional biases and correlations are 59 % and 0.76 for Europe, 19 % and 0.72 for North America, and 31 % and -0.04 for Asia. A considerable number of the observation stations for sea salt are coastal and inland, however, and are perhaps therefore not very representative for sea salt aerosol as such in the model. CAM5.3-Oslo performs better than all the AP3 models bias-wise, and only one of the AP3 models has a higher Pearson correlation for sea salt. Our model is also less biased than 20 of the 23 AP2 models, and with higher correlation than 21 models.

For mineral dust we only have climatological observations to compare with. The bias for all stations and months is found to be −39 %, with a correlation of 0.52, which is slightly lower here than in the free AMIP_PD simulation. The observation stations for mineral dust surface concentrations are all quite distant from the largest dust source regions. Hence, the negative bias found in CAM5.3-Oslo may very well be a result of underestimated long-range transport rather than too-small emissions. This is corroborated by the fact that aerosol optical depths in the largest source regions (see Sect. 4.2) are biased high compared to the remotely retrieved values. Although the correlation coefficient is slightly better than in CAM4-Oslo, in which mineral dust emissions are simply prescribed, CAM5.3-Oslo is more biased and has a lower Fact2 value. We note, however, that even for the nudged simulation, the year-to-year variation for mineral dust is large enough to affect these validation results. Comparing monthly data from each individual model year with the observed climatological dust concentrations, the bias here varies between −46 % and −23 % and the correlation between 0.29 and 0.71. Part of this variability may be due to a varying number of stations for which there are enough data to be included in the multiyear climatology. Compared to the eight AP3 models, our model performs better than only three models bias-wise, but lies above the middle of the AP3 range with respect to correlations. It is also less biased than 14 of the 23 AP2 models and has a higher correlation than 7 of the models.

4.2 Optical properties

4.2.1 Mass specific extinction and absorption

Table 9 gives the modeled mass extinction coefficients (MEC) for each of the aerosol components, calculated as the component's aerosol optical depth at 550 nm divided by its atmospheric burden. What determines MEC for a monodisperse aerosol consisting of spherical (which we assume) and homogeneous particles is the particle size (divided by the radiative wavelength of interest), its mass density, and refractive index. For an internally mixed component of an aerosol size distribution, the size-integrated and atmospheric column-averaged MEC depends on a range of factors in the model. In addition to the refractive index of the components in a given mixture and the mixture's lognormal modal parameters (median radii and standard deviations) at the point of emission or nucleation, the growth by added process tracers and by hygroscopic swelling also play important roles. Aerosol lifetimes and aerosol life cycling in general, including transport and deposition, can further affect the results by shifting the "center of mass" of the aerosol components in question to areas and altitudes with different relative humidity, which consequently also affects the globally averaged MEC value.

Since neither the assumed mass density nor the initial lognormal modal parameters of the sulfate background modes in mixture nos. 1 and 5 have changed relative to the treatment in K13, i.e., in CAM4-Oslo, the ca 14 % reduction in MEC globally must be due to changes in growth, including the effects of life cycling on growth. As outlined in Sect. 2.3, the hygroscopicity of sulfuric acid has been reduced by about 17 % for relative humidities close to RH_{max}, while for ammonium sulfate there has been an equally large increase for these highest RH values but a larger reduction in large parts of the hysteresis domain (RH $\approx$ 50–80 %), up to a 50 % reduction at RH $\approx$ 80 %. The net effect of this when introduced into the model at the time (in an older model version), however, was small compared to the change from CAM4-Oslo to the present model version, which points to changes in meteorology and life cycling as the main cause. Although the atmospheric residence times and burdens of sulfate are quite similar globally (Table 4), in CAM5.3-Oslo they are both considerably smaller at middle to high latitudes and somewhat larger in the subtropics. At these low latitudes the relative humidity (and cloud cover) in the lower troposphere is also somewhat lower in CAM5.3-Oslo. Hence the sulfate "center of mass" is in effect shifted towards typically less humid regions, which is consistent with less hygroscopic growth and the smaller MEC values found in CAM5.3-Oslo. Some of the reduction may in addition be a result of having relatively larger amounts of (less hygroscopic) OM internally mixed with sulfate in the present model version, due to the co-nucleation of sulfate and SOA (mixture no. 1) and to the condensation of sulfuric acid and $\mathrm{SOAG_{SV}/SOAG_{LV}}$ onto larger particles (mixture nos. 1–10). The sulfate MEC estimates lie within the inter-model variability of the AeroCom Phase I models (Kinne et al., 2006) for both configurations of CAM5.3-Oslo, as for CAM4-Oslo.

MEC for OM aerosol has decreased by about 30 % compared to CAM4-Oslo, also still within the range of the AeroCom I models, but now closer to the AeroCom I median value. Looking back on results from earlier model versions of CAM5.3-Oslo, we find that the larger part of this change is most likely due to a shift in OM burdens to less humid areas (mainly at lower latitudes), just as for sulfate. An additional change that might be of importance is that SOA now comes as nucleation- or Aitken-mode particles (mixture no. 1) and is distributed onto larger particles by condensation instead of in the internally mixed primary OM/BC(a) mode (mixtures 4 and 14), which generally has a higher specific extinction. For instance, MEC is about 0.4 (0.6) $\mathrm{m^2\,g^{-1}}$ for mixture 1 if only consisting of nucleated OM at RH = 0 % (80 %) compared to 3.0 (4.5) $\mathrm{m^2\,g^{-1}}$ for mixtures 4 and 14 when only consisting of OM (and condensed water).

Despite a shift in burdens towards lower latitudes also for BC, the mass specific extinction for BC (7.6 $\mathrm{m^2\,g^{-1}}$) has increased by about 17 % from CAM4-Oslo to CAM5.3-Oslo. This is also closer to the AeroCom I median value (8.9 $\mathrm{m^2\,g^{-1}}$). Regionally the increase is largest in areas downwind of relatively large sulfate and SOA or biomass burning sources in northern South America (where MEC is now at its largest at about 20 $\mathrm{m^2\,g^{-1}}$) and Indonesia ($\sim$ 15 $\mathrm{m^2\,g^{-1}}$), as well as over and downwind of eastern North America to eastern Europe ($\sim$ 10–15 $\mathrm{m^2\,g^{-1}}$). As mentioned, there is more growth by condensation in CAM5.3-Oslo since SOA is no longer treated as primary particles as in CAM4-Oslo. It is reasonable to assume that this extra aerosol growth may also be linked to the increase in MEC. Most importantly, however, the changes in BC emissions size, mass density, and refractive index (see Sect. 2.3) did change MEC for the pure and dry (RH = 0 %) background particles of mixture nos. 2 (when containing only BC) and 12 from about 7.0 to 8.5 $\mathrm{m^2\,g^{-1}}$, i.e., a 20 % increase from the background tracer with the largest mass-wise contribution (90 %) to fossil fuel BC emissions. For mixture no. 0, the fractal fossil fuel BC particles, the net change in MEC from altered size, density, and refractive index is just a 0.3 % increase to 8.2 $\mathrm{m^2\,g^{-1}}$, due to compensating effects. The increase in MEC is also very small ($\sim$ 3 %) for fresh BC particles from biomass burning in mixture nos. 4 and 14 if we assume that only BC is present in the OM/BC(a) mode.

MEC for mineral dust has increased by about 19 % globally and with a regional pattern quite similar to that of BC. Mass densities and particle sizes at the point of emission are the same here as in CAM4-Oslo for both tracers (DST_A2 and DST_A3). The effect of the change in refractive index (see Sect. 2.3) only yields a 0.4 % increase in MEC at 550 nm for pure dust in both mixture 6 and 7. Dust hygroscopicity has increased somewhat (see Sect. 2.3), which together with the extra growth potential from SOA is consistent with an increase in MEC. We note, however, that MEC is now higher even in the most arid source regions (e.g., Sahara) due to a slightly larger fraction of accumulation-mode (DST_A2) to total dust mass in the new emission parameterization (0.13) compared to CAM4-Oslo (0.11). With MEC = 2.44 $\mathrm{m^2\,g^{-1}}$ and 0.335 $\mathrm{m^2\,g^{-1}}$ for DST_A1 and DST_A2 (assuming no growth), this shift towards smaller sizes alone (i.e., before further growth and deposition) can account for a 7 % larger MEC for dust in CAM5.3-Oslo. Mineral dust MEC is still within the range of the AeroCom I models, although it is now closer to the highest model estimates. Note that the (common) assumption that dust particles are spherical leads to a substantial underestimate in MEC for coarse particles, while the error is much smaller for particles with geometric diameters below about 0.6 µm (Kok et al., 2017). The bias towards smaller emission sizes, however (see the discussion above), should lead to an opposite-directed bias in MEC, since coarse mineral dust has much lower MEC than submicron dust (e.g., 86 % lower for DST_A3 than for DST_A2).

The hygroscopicity of sea salt has increased by about 4 % for high ambient relative humidities, now being smaller throughout much of the hysteresis domain compared to CAM4-Oslo (see Sect. 2.3). Together with changes in particle growth by the process tracers, such as by the condensation of SOA (missing in K13 and M14), this might explain some of the changes in sea salt MEC in moving to CAM5.3-Oslo. The main cause of the about 63 % increase, however, is the shift in particle effective radii towards sizes with higher specific extinction: globally averaged MEC for sea salt in CAM5.3-Oslo (5.04 $\mathrm{m^2\,g^{-1}}$) is just 1 % lower than in the CAM4-Oslo development version of Salter et al. (2015), which used the same model parameters for sea salt as in Table 2 while otherwise being the same as in K13.

Note that these MEC estimates are based on the common assumption that an internally mixed component's contribution to the total extinction increases linearly with its volume fraction, which in our model (in AeroTab) is allowed to vary with size. The same goes for the absorption or scattering when we focus on either of their contributions to the extinction separately. In this way nonabsorbing aerosols, such as sulfate and sea salt, contribute to the total aerosol absorption wherever internally mixed with absorptive aerosols, such as BC. Although the total extinction, scattering, and absorption is thus correctly found by summing up the contributions from each of the aerosol components, the method is expected to give biased extinction estimates, especially for the absorption part, compared to in situ measurements for each aerosol component separately (or for less aged and/or internally mixed particles close to the sources). Furthermore, the refractive indices of mixtures consisting of absorbing and nonabsorbing components are calculated by using the semi-empirical Maxwell–Garnett mixing rule, which gives less absorption (in better agreement with measurements) than the volume mixing rule for homogeneous mixtures (Chýlek et al., 1998), but more absorption than for purely external mixtures (Chýlek et al., 1998; see also Fig. 6 in Kirkevåg et al., 2005).

To obtain a first rough estimate of the magnitude of at least parts of the uncertainty in connection with the choice of methodology for calculating BC MEC and the corresponding mass specific absorption, MAC (defined as absorption aerosol optical depth (AOD) divided by aerosol burden), we have also calculated the corresponding coefficients for the anthropogenic part (i.e., using PD–PI AODs and burdens). This means a shift towards sizes and specific extinctions more representative of fossil fuel sources. The anthropogenic MEC is found to be about 8 % larger than for PD BC, 8.18 $\mathrm{m^2\,g^{-1}}$ for NUDGE_PD and 8.28 $\mathrm{m^2\,g^{-1}}$ for AMIP_PD, and 10 % higher (7.14 $\mathrm{m^2\,g^{-1}}$) than for PD BC in CAM4-Oslo. Similarly, the anthropogenic MAC value is as much as 30 % higher than for PD BC, 3.15 $\mathrm{m^2\,g^{-1}}$ for NUDGE_PD and 3.27 $\mathrm{m^2\,g^{-1}}$ for AMIP_PD, and 31 % higher for anthropogenic BC (3.15 $\mathrm{m^2\,g^{-1}}$) than for PD BC in CAM4-Oslo. We note that this is still low compared to measured values and the recommended range of $7.5 \pm 1.2\,\mathrm{m^2\,g^{-1}}$ for fresh, uncoated BC in Bond and Bergström (2006). According to that review paper, MAC can drop to about 5 $\mathrm{m^2\,g^{-1}}$ for collapsed BC aggregates, while coating by negligibly absorbing aerosol typically enhances MAC by 50 % (to ca. 11 $\mathrm{m^2\,g^{-1}}$).

One may also calculate alternative MAC values from the PD simulations by assuming that nonabsorptive or less absorptive components do not contribute to the light absorption of the mixture containing BC. First, leaving out only sulfate and sea salt and letting $\mathrm{MAC} = \mathrm{ABS_{(BC+SO4+SS)}}/\mathrm{B_{BC}}$, we find that MAC = 4.82 and 4.95 $\mathrm{m^2\,g^{-1}}$ in NUDGE_PD and AMIP_PD, respectively, compared to 5.07 $\mathrm{m^2\,g^{-1}}$ in CAM4-Oslo. MAC here exceeds 7 $\mathrm{m^2\,g^{-1}}$ over large areas (for all the above simulations) somewhat downstream of major BC emissions in North and South America and over several smaller areas in Southeast Asia. Similarly, assuming that mineral dust and OM do not contribute to the absorption either (as in Stjern et al., 2017), which is a much less realistic assumption in many regions, we obtain global MAC values of 23.2 and 21.4 $\mathrm{m^2\,g^{-1}}$ in NUDGE_PD and AMIP_PD, respectively, and 13.6 $\mathrm{m^2\,g^{-1}}$ in CAM4-Oslo. Assuming that the truth lies somewhere between the two last assumptions we could even obtain globally averaged BC MAC values within the recommended range of Bond and Bergström (2006). The problem with this line of reasoning is, of course, that BC is not the only absorbing aerosol component and that nonabsorptive components also add to, and even enhance (e.g., Chen et al., 2017), the total absorption for internal mixtures. Finally, although both mineral dust and OM individually have small MAC values, they have much larger atmospheric burdens than BC and thus also contribute considerably to the total absorption, even dominating regionally. In a test simulation with less absorptive mineral dust at most wavelengths – the imaginary refractive index at 550 nm is reduced from 0.0055 to 0.0024 – otherwise being identical to NUDGE_PD, the latter BC MAC estimate is reduced by 25 % globally, from 23.2 to 17.5 $\mathrm{m^2\,g^{-1}}$. Assuming linearity in MAC with respect to the imaginary part of the refractive index, MAC for BC partially internally mixed with nonabsorptive dust can be estimated from this at ca. 10.1 $\mathrm{m^2\,g^{-1}}$. The absorption by OM is still included in this estimate, however.

4.2.2 Column-integrated optical properties

Figure 7 shows aerosol optical depth and absorptive optical depth at 550 nm as well as the Ångström parameter for wavelengths 440 to 870 nm in the NUDGE_PD simulation compared with AERONET (Holben et al., 1998). The results discussed and referred to below are shown in Fig. 7 and Tables 6–8.

We first look at modeled clear-sky aerosol optical depth at 550 nm (OD550CS). This is in the model calculated as the all-sky optical depth weighted (at each time step in the simulation) with the clear-sky fraction and with hygroscopic swelling calculated from average grid cell RH. This is the method adapted in K13, while a more common method for simulating the cloud-screened remote sensing assumes hygroscopic swelling based on the clear-sky RH fraction, but for all-sky conditions (no sampling or weighting). Due to the relatively large coverage (which we somewhat loosely call global here; see Fig. 7 and http://aerocom.met.no (last access: 25 September 2018) for the actual coverage) we find an apparently wide spread for modeled vs. observed (monthly) values, but with a relatively low NMB of −16 %, $R = 0.59$, and Fact2 = 42 %. The all-sky values (OD550) look slightly better, with a positive NMB of 15 %, $R = 0.64$, and Fact2 = 68 %. In comparison, CAM4-Oslo has a slightly

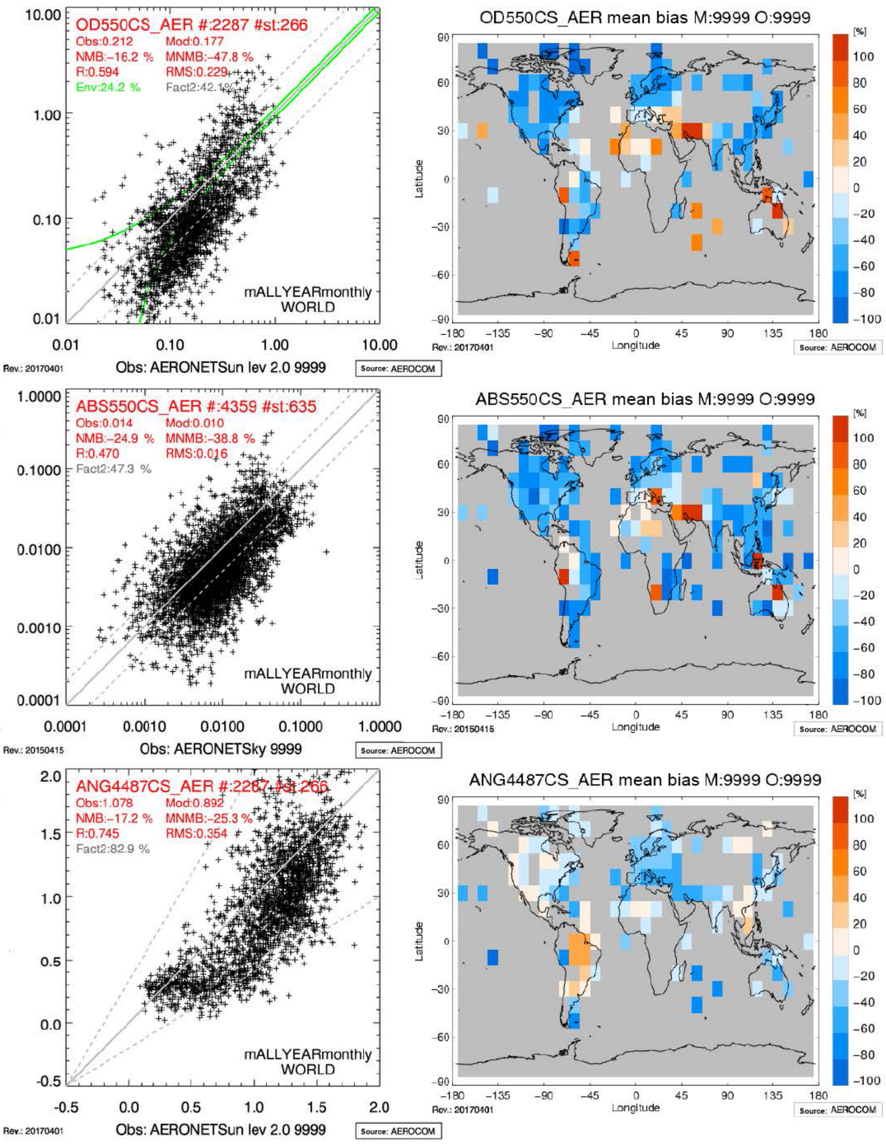

Figure 7. Scatter plots (left panels) and annual relative bias plots with respect to AERONET observations and retrievals (right panels) of clear-sky aerosol optical depth (top), all-sky absorption optical depth (middle) at 550 nm, and Ångström parameter (bottom) for the wavelength range 440–870 nm for the NUDGE_PD simulation.

stronger negative bias for OD550CS and a slightly smaller, but negative, bias for OD550.

Across the various available observation years 2004–2010, MNB for OD550CS varies between −27 % and −6 %. Regionally, OD550CS is most underestimated in East Asia (NMB = −59 %), followed by North America (−56 %), Europe (−38 %), South and Central America (−21 %), and India (−19 %). Europe is also defined here to include sites at the northern coast of Africa. For northern Africa, which again is defined to include sites at the Mediterranean coast in Europe, the bias is positive (12 %). The positive bias is even larger in Australia (71 %), where mineral dust is also estimated to dominate as the most optically thick aerosol. In spite of the apparent underestimation of near-surface dust mass concentrations discussed in Sect. 4.1.2, we may add here that the global all-sky optical depth contribution to mineral dust is biased by 65 % (not shown; see results at http://aerocom.met.no, last access: 25 September 2018), i.e., much more than the 15 % bias for total OD550. It is furthermore clear from Fig. 7 that OD550CS is underestimated at high latitudes. What is not known, however, is how much of this negative bias is caused by missing or inaccurate emissions (see, e.g., Stohl et al., 2013) and how much of it is a result of other systematic biases such as deficiencies in the modeling of transport, aerosol chemistry, microphysics, and subsequent scavenging or dry deposition.

Comparing OD550CS with the simulated aerosol optical depth from the same eight AP3 models as in Sect. 4.1.2, we find that four of the models have approximately the same (one model) or larger (in absolute value) NMB values than ours. The correlations are higher in six of the AP3 models, and five models also exhibit higher Fact2 values. Comparing with the 20 models with available data among the 23 AP2 models, we find that only 7 of these are less biased, but the correlations are smaller than ours in only 3 of the models. Although CAM5.3-Oslo performs well in terms of NMB, the spread is so large that the Fact2 value is lower than in all of these AP2 models.

Moving on to the clear-sky absorption aerosol optical depth at 550 nm (ABS550CS), we similarly find that NMB $= -25\,\%$, $R = 0.47$, and Fact2 $= 47\,\%$. The all-sky values also look slightly better here, with NMB $= -20\,\%$, $R = 0.47$, and Fact2 $= 50\,\%$. In comparison, CAM4-Oslo has a slightly stronger negative bias for both ABS550CS and ABS550.

Across the individual years 2004–2010, MNB for ABS550CS only varies very little between $-41\,\%$ and $-36\,\%$. Regionally it is most underestimated in India ($-52\,\%$), followed by East Asia ($-44\,\%$), North America ($-39\,\%$), Europe (defined as above, $-29\,\%$), South and Central America ($-20\,\%$), and Australia ($-13\,\%$). For northern Africa (defined as above), the bias is slightly positive (4 %). Regionally the biases in ABS550CS and OD550CS thus mainly have the same sign, which is consistent with too-low or too-high (depending on the sign of the bias) modeled aerosol burdens. Some exceptions are found, however, such as for Australia as a whole and in (e.g.) some mineral-dust-dominated areas over and downwind of the Sahara Desert where the absorption optical depth is underestimated, while the optical depth (at 550 nm) is overestimated. This may indicate that the assumed imaginary part of the refractive index at 550 nm is too small or that the effective size of the mineral dust particles is underestimated, which has been identified as a problem in many AeroCom models (Kok et al., 2017).

A few AP2 models and one AP3 model also have absorption data available (ABS550). Comparing with the AP3 model (MNB $= -56\,\%$) CAM5.3-Oslo is less biased ($-38\,\%$). Comparing with the 16 models with available data among the 23 AP2 models, we find that only 5 of these are less biased than our model. The correlations are higher than ours in all these AP2 models, however, and nine models have larger Fact2 values.

Finally, we look at the statistics for the clear-sky Ångström parameter, defined here through the clear-sky aerosol optical depths at the wavelengths 440 and 870 nm in OD440CS and OD870CS, respectively:

$$\mathrm{ANG4487CS} = \frac{-\ln(\mathrm{OD870CS}/\mathrm{OD440CS})}{\ln(870/440)}. \qquad (7)$$

Globally, for ANG4487CS we obtain NMB $= -17\,\%$, $R = 0.75$, and Fact2 $= 83\,\%$, a quite decent result indicating that the aerosol size for the clear-sky atmospheric column is fairly well modeled in terms of its relative abundance of large vs. small particles. The all-sky equivalent ANG4487, however, yields a much poorer match with AERONET, having NMB $= -44\,\%$, $R = 0.46$, and Fact2 $= 49\,\%$. In comparison, CAM4-Oslo has a smaller negative bias for ANG4487 (no clear-sky value is available from that model version), indicating that the effective particle sizes are indeed smaller there than in CAM5.3-Oslo. For all-sky conditions the aerosol sizes are biased much more towards large particles (small ANG values), which is consistent with higher relative humidities and thus more extensive hygroscopic swelling.

Across the individual years 2004–2010, the bias varies as little as between $-15\,\%$ and $-16\,\%$. Regionally, ANG4487CS is most underestimated in northern Africa (defined as above, i.e., extended to include sites along the European coast of the Mediterranean, $-35\,\%$), followed by Europe (defined as above, $-32\,\%$), Australia ($-31\,\%$), India ($-20\,\%$), East Asia ($-10\,\%$), and North America ($-7\,\%$). The pattern (see also Fig. 7) seems to point towards dust as a source of large negative biases, which is consistent with an excessive mineral dust contribution to the total aerosol (as also indicated by the regional OD550CS biases) or, alternatively, overestimated dust particles sizes (opposite of what we found as a potential cause of the positive bias in ABS550CS). For South and Central America NMB $= 15\,\%$, i.e., an overestimate indicating slightly too-fine particles. This positive bias is smallest (8 %) for the SON months, i.e., late in the biomass burning season for the region, while it is largest (22 %) for DJF. Since the negative biases for OD550CS and ABS550CS here are smallest ($-5\,\%$ and $-6\,\%$, respectively) in JJA and largest ($-32\,\%$ and $-35\,\%$) in DJF, there is still a theoretical possibility that the biomass burning aerosol contribution is exaggerated. This could be the case if contributions from other sources are generally underestimated, e.g., due to missing emissions or exaggerated scavenging. Just based on these results, however, we cannot conclude whether this is the case or not nor whether the assumed OM / OC ratio of 2.6 for biomass burning aerosols is too high or not.

None of the AP3 models but 13 of the AP2 models also have ANG4487 information available at http://aerocom.met.no (last access: 25 September 2018). Comparing with the 13 AP2 models, we find that 5 have larger biases than in ours. The correlations are smaller in six models, and the Fact2 values are also smaller than ours in six models.

The particle sizes globally seem to be well represented. Based on modeled ANG4487CS, the consistent low bias in OD550CS and ABS550CS, and the assumption that the intrinsic optical properties and other factors that might affect the result are fairly well represented, the modeled aerosol column burdens may be underestimated. For the surface concentrations, only BC and mineral dust are underestimated compared to in situ observations, as discussed in Sect. 4.1.2. However, considering that the available in situ measurements are very sparsely distributed globally and that we know little

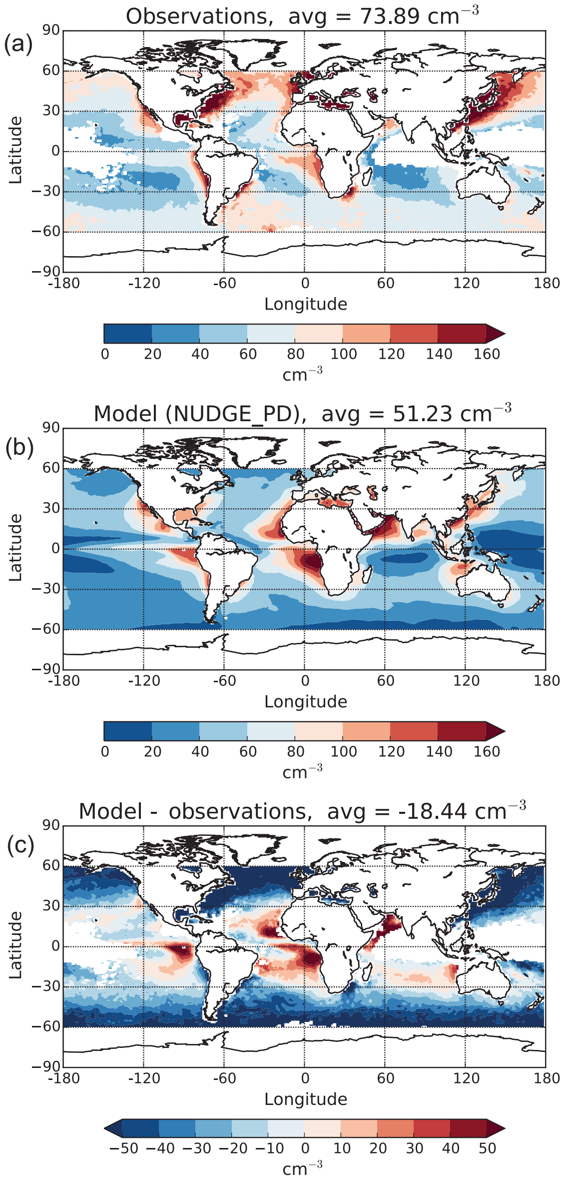

Figure 8. In-cloud cloud droplet number concentrations at cloud top in **(b)** CAM5.3-Oslo (NUDGE_PD) compared to **(a)** Bennartz and Rausch (2017), with the difference shown in **(c)**. White areas indicate a lack of observations from MODIS meeting the criteria on temperature and cloud fraction given by Bennartz and Rausch (2017).

about the model performance in terms of the vertical distribution of mass concentrations (except for BC), we cannot expect these very different measures of model performance to fully agree.

Further aerosol model validation is taking place through ongoing multi-model studies that include results from the present model version. These studies are the AeroCom Control EXPERIMENT 2016, the remote sensing evaluation for AeroCom Control 2016, the AeroCom in situ measurement comparison (for optical properties) (https://wiki.met.no/aerocom/phase3-experiments, last access: 25 September), and the BACCHUS CCN global model intercomparison exercise (http://lists.met.no/pipermail/aerocom-modeller/2017-January/000109.html, last access: 25 September 2018).

4.3 Cloud droplet concentrations

We also compare the modeled in-cloud droplet concentration (CDNC) to the data set provided by Bennartz and Rausch (2017). This data set is a climatology of cloud droplet number concentration (monthly mean, in-cloud 1° × 1° CDNC values plus associated uncertainties for warm clouds) based on 13 years of Aqua MODIS observations over the global ice-free oceans. To facilitate this comparison, we take out in-cloud droplet concentrations at the cloud top, defined as the first layer – starting from the model top – in which the stratiform liquid cloud fraction in a grid cell exceeds 10 % and the temperature criterion of Bennartz and Rausch (2017) is fulfilled, i.e., $268\,\mathrm{K} < T < 300\,\mathrm{K}$. The annually averaged result for the NUDGE_PD simulation is given in Fig. 8, which shows that, globally averaged, we calculate lower droplet number concentrations than what is observed. CAM5.3-Oslo mostly underestimates cloud droplet concentrations over coastal ocean areas in East Asia, Europe, and North America. The model overestimates the droplet concentrations close to mineral-dust- and biomass-burning-dominated areas, typically downwind of Saudi Arabia and Africa. The results from AMIP_PD (not shown) are very similar with an average of $49.8\,\mathrm{cm}^{-3}$ compared to $51.2\,\mathrm{cm}^{-3}$ for NUDGE_PD. One possible reason for the discrepancies between the model and observations is that we have not applied a satellite simulator, and the simple way of outputting the droplet concentration described above does not necessarily correspond to what the satellite is seeing. A comprehensive analysis of the discrepancies for the different regions, however, is beyond the scope of this study.

5 Interaction with radiation and clouds

The effective radiative forcing (ERF) of aerosols has been calculated using the method of Ghan (2013), in which radiative fluxes for a "clean" (no aerosol extinction) and a "clear" (cloud-free, but including aerosol extinction) atmosphere are used together with the standard all-sky (including aerosol extinction) radiative fluxes in order to decompose the ERF into its separate components. Differences between the PD and PI simulations thus yield the anthropogenic ERF as a direct radiative forcing, a cloud radiative forcing (note that this is the contribution by anthropogenic aerosols, not the total cloud forcing itself), and a surface albedo forcing term. We only show and discuss the results for the cloud forcing and the direct radiative forcing components here. The surface albedo forcing is small on a global scale and is not discussed. Neither is the semi-direct effect of aerosols, which is included as part of the cloud radiative forcing term (Ghan, 2013) but not calculated and shown separately, since this particular diagnostic requires extra sets of simulations in which (potentially) anthropogenic aerosols are assumed to be totally nonabsorptive (Ghan et al., 2012). Results from such simulations with an earlier, slightly differently tuned model version suggest that the semi-direct effect in CAM5.3-Oslo contributes very little to the total aerosol ERF. The globally averaged SW + LW semi-direct radiative forcing was estimated to be $-0.02\,\mathrm{W\,m^{-2}}$.

Figure 9 shows modeled shortwave (SW) and longwave (LW) direct radiative forcing at the top of the atmosphere (TOA) annually averaged from both the nudged simulations (i.e., NUDGE_PD–NUDGE_PI) and the longer AMIP simulations (AMIP_PD–AMIP_PI). Global averages are listed and compared to estimates from CAM4-Oslo (direct RF) and IPCC AR5 (direct RF and ERF) in Table 10. Regionally, the SW direct forcing is positive over some areas with high surface albedo or high cloud fractions for low clouds, mainly related to biomass burning activity, which compared to PI conditions has led to increased levels of light-absorbing aerosols such as fossil fuel or biomass burning BC (e.g., Sahara, the Arctic, and off the west coasts of South America and Africa). The direct forcing term is also positive in some areas with reduced absorption, where the scattering aerosol optical depth (mainly from OM) has decreased even more (such as in the eastern USA and parts of Australia and South America). However, negative SW direct forcing is dominant over the industrialized parts of the world due to the general increase in scattering aerosol of anthropogenic origin (sulfate and OM). The global annual average is estimated at $-0.095\,\mathrm{W\,m^{-2}}$ ($-0.092\,\mathrm{W\,m^{-2}}$ for the AMIP simulations). The LW direct forcing is much smaller, having a regional maximum over the Middle East where both large mineral dust and (internally mixed) anthropogenic aerosol are abundant: the sulfate column burden has a local maximum in this region. The global annual average here is $0.026\,\mathrm{W\,m^{-2}}$ for both the NUDGE and the AMIP simulations. Just as for CAM4-Oslo, the estimated total (joint SW and LW) global direct radiative forcing in CAM5.3-Oslo lies within the range of the ERFari estimates of IPCC AR5 (Boucher et al., 2013); see Table 10. Since the AR5 range has been evaluated for the period 1750–2011 and ERFari in AR5 includes the semi-direct effect, the numbers are not entirely comparable.

Figure 10 similarly shows the shortwave (SW) and longwave (LW) cloud radiative forcing (due to anthropogenic aerosols) at TOA. Here we also obtain positive SW forcing in some areas, mainly in the SH subtropics and at high latitudes, consistent with the lower PD than PI cloud droplet concentrations (CDNC) and liquid water path (LWP) found in these areas. Some of the positive cloud forcing is due to a reduction in organic emissions from biomass burning since 1850 (e.g., in England, Australia, and the eastern United States). Also over the Southern Ocean there are areas with slightly positive values, coinciding with areas with slightly smaller column vertically integrated CDNC and LWP values in the PD than in the PI simulations. This pattern has been found to be even more prominent when the PI simulations apply PI oxidant levels (instead of PD as in this study); see Karset et al. (2018) for a more thorough discussion on the effect of different oxidant levels on the cloud forcing. Areas with a negative SW cloud forcing term, however, are dominant due to the general increase in CDNC from PI to PD conditions, being large (negative) over oceans downstream of areas with high aerosol emissions from industrial activity, biofuel consumption, or biomass burning. The negative SW cloud forcing peaks over the northern Pacific Ocean near the coast of East Asia. The global annual average value is estimated at $-1.50\,\mathrm{W\,m^{-2}}$ ($-1.45\,\mathrm{W\,m^{-2}}$ for the AMIP simulations). The LW cloud forcing is smaller and is in most regions of opposite sign to the SW contribution. Its global and annual average is $0.161\,\mathrm{W\,m^{-2}}$ ($0.155\,\mathrm{W\,m^{-2}}$ for the AMIP simulations). Compared to the ERFaci estimates in Table 10, the total global cloud radiative forcing in CAM5.3-Oslo is thus on the high side, lying just outside the 5 to 95 % confidence range given by IPCC AR5. As mentioned, the AR5 range in Table 10 is for the period 1750–2011 instead of 1850–2000. Compared to this extended period we should expect a somewhat smaller negative forcing contribution, since the reference state in 1850 is less pristine than in 1750, while changes due to aerosols in the latter part of the period are of less importance (Carslaw et al., 2013). For the same time period, however, we should expect a stronger negative cloud forcing than that of AR5 since the second indirect effect is included in our model (although not calculated separately), whereas the ERFaci range in IPCC AR5 is (mainly) for the first indirect effect.

The expert judgment of a 5 to 95 % (medium confidence) uncertainty range for ERFari + ERFaci is in IPCC AR5 estimated to be -1.9 to $-0.1\,\mathrm{W\,m^{-2}}$, while the 17–83 % (likely) range is -1.5 to $-0.4\,\mathrm{W\,m^{-2}}$ (Boucher et al., 2013). These estimates take into account the fact that GCM studies calculate stronger aerosol ERF values than what is found in satellite studies. Our model values of $-1.4\,\mathrm{W\,m^{-2}}$ (NUDGE_PD–NUDGE_PI) and $-1.36\,\mathrm{W\,m^{-2}}$ (AMIP_PD–AMIP_PI) lie within both ranges of uncertainty. Our model estimates are also very close to 1 standard deviation away from the multi-model estimate for the period 1850–2000 in Boucher et al. (2013), which is given as $-1.08 \pm 0.32\,\mathrm{W\,m^{-2}}$ based on results from the CMIP5 and ACCMIP (Atmospheric Chemistry and Climate Model Intercomparison Project) models.

Table 11 lists some globally and annually averaged variables relevant for understanding the above estimates of effective radiative forcing by aerosols for both the NUDGE and AMIP simulations. Although the globally averaged all-sky aerosol optical depth at 550 nm (OD550) for PD is found to be larger than in CAM4-Oslo (0.135; see Table 7 in

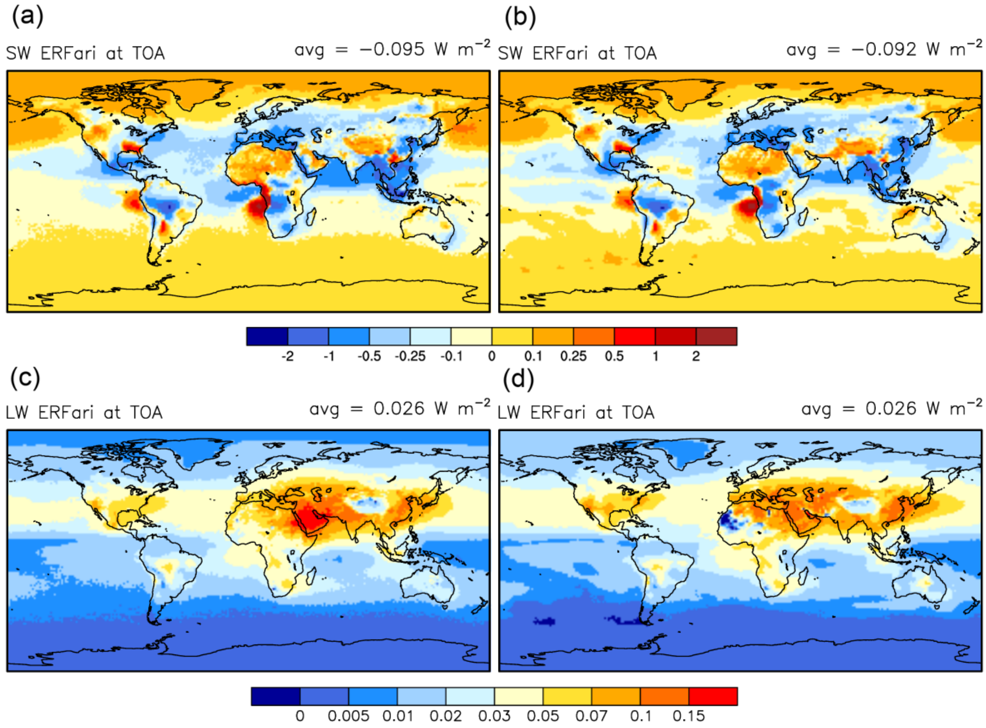

Figure 9. Shortwave (SW, **a** and **b**) and longwave (LW, **c** and **d**) ERFari at the top of the atmosphere (TOA) for the simulations NUDGE_PD–NUDGE_PI (**a** and **c**) and AMIP_PD–AMIP_PI (**b** and **d**). Note the different color scales. Note also that the semi-direct effect is not included here, since ERFari in this study corresponds to the "direct radiative forcing" component in Ghan (2013).

K13), we now obtain an anthropogenic (PD–PI) AOD that is 29 % smaller than in CAM4-Oslo, mainly due to lower atmospheric residence times and burdens of sulfate, BC, and OM. The simulated anthropogenic AOD fractions of total AOD (about 16 % in both NUDGE_PD and AMIP_PD) are therefore considerably smaller than in CAM4-Oslo (26 %), which is about the same as in the average AeroCom Phase I model (25 %; Schulz et al., 2006). Anthropogenic absorption AOD (ABS) is about 40–45 % smaller than in CAM4-Oslo (0.020), and the anthropogenic ABS fraction is estimated at about 25 % compared to 43 % in CAM4-Oslo. Considering that the anthropogenic absorption optical depth has decreased more (39 %) than the anthropogenic optical depth itself (28 %), one would perhaps expect a more negative direct radiative forcing in CAM5.3-Oslo. It is instead found to be nearly the same: −0.095 (or −0.092 for the AMIP simulations) vs. $-0.10\,\mathrm{W\,m^{-2}}$ (as an instantaneous direct forcing) globally averaged. This can be partly understood as an effect of the substantial increase in the cloud fraction (and thus planetary albedo) for low clouds, 0.43 vs. 0.34, with the largest increase found at middle to high latitudes. The surface albedo is also higher in CAM5.3-Oslo: 0.163 vs. 0.156 in CAM4-Oslo. Regionally the largest increases (> 0.1) are also found here at middle and high latitudes over continents in the NH. The shift towards smaller anthropogenic BC concentrations and to lower altitudes (Fig. 5), which reduces the absorption in the atmospheric column and therefore leads to a less positive direct RF (e.g., Samset et al., 2013), is in other words counteracted by the effect of increased surface or near-surface albedos from CAM4-Oslo to CAM5.3-Oslo. The reduction in anthropogenic atmospheric absorption is reflected in the difference in SW direct radiative forcing between the TOA and the surface, which in CAM5.3-Oslo is estimated at $0.51\,\mathrm{W\,m^{-2}}$ for NUDGE and $0.47\,\mathrm{W\,m^{-2}}$ for AMIP compared to $0.95\,\mathrm{W\,m^{-2}}$ in CAM4-Oslo (K13).

In-cloud cloud droplet number concentrations and effective droplet radii are defined here differently than in CAM4-Oslo by (for each time step) weighting the respective model variables with the stratiform liquid cloud fraction (a number between 0 and 1) in CAM5.3-Oslo instead of the frequency of cloud occurrence (being either 0 or 1). These two model parameters are therefore not directly comparable between the two model versions. We can see, however, that the vertically integrated liquid water path (LWP) in CAM5.3-Oslo ($\sim 54\,\mathrm{g\,m^{-2}}$) is much smaller than in CAM4-Oslo ($\sim 130\,\mathrm{g\,m^{-2}}$; see K13). Some of this drop in LWP may be due to the changes in aerosol treatment, but the relative low sensitivity of LWP to aerosol concentration levels (Table 11; Table 4 in K13) suggests that much of it is a result of switching from the RK cloud microphysics scheme (Rasch and Kristjánsson, 1998) in CAM4-Oslo to MG1.5 (see Sect. 3) in CAM5.3-Oslo and how the respective schemes are tuned.

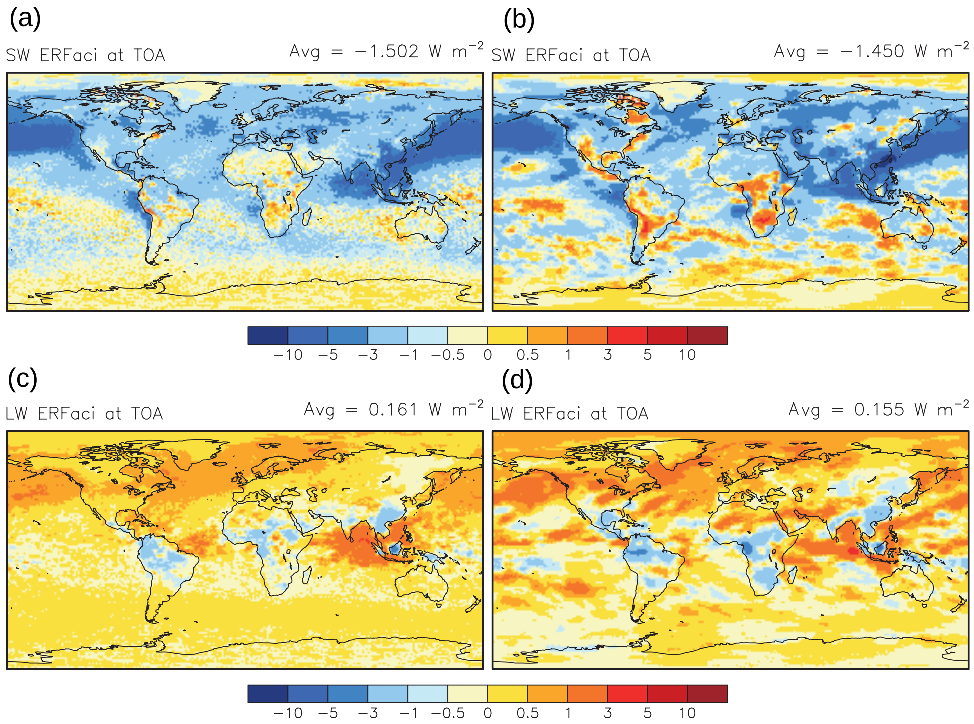

Figure 10. Shortwave (SW, **a** and **b**) and longwave (LW, **c** and **d**) ERFaci at the top of the atmosphere (TOA) for the simulations NUDGE_PD–NUDGE_PI (**a** and **c**) and AMIP_PD–AMIP_PI (**b** and **d**). Note that the semi-direct effect is embedded here in the ERFaci term, which corresponds to the "cloud radiative forcing" component in Ghan (2013).

This may have contributed to an increase in the modeled cloud susceptibility (Albrecht, 1989), thus leading to enhanced cloud forcing by anthropogenic aerosols. A more thorough investigation of this falls outside the scope of this study and has not been pursued. Note, however, that nudging to the ERA data instead of the model's own meteorology only has small impacts on anthropogenic cloud forcing: Karset et al. (2018), applying self-nudging (and when using the same oxidant levels as in the present study) in CAM5.3-Oslo, estimated it to $-1.32\,\mathrm{W\,m^{-2}}$, which is very close to our estimate of $-1.34\,\mathrm{W\,m^{-2}}$ (SW + LW ERFaci in Table 10).

The size and even sign of the Albrecht (lifetime) effect is very uncertain and has in a recent observationally based study been shown to be small or, more specifically, not detectable above the level of natural variability for the Holuhraun volcanic eruption (Malavelle et al., 2017). In CAM5.3-Oslo the anthropogenic change in LWP is estimated to be about $3.56\,\mathrm{g\,m^{-2}}$ in NUDGE_PD–NUDGE_PI ($3.42\,\mathrm{g\,m^{-2}}$ in the AMIP simulations). Compared to $4.37\,\mathrm{g\,m^{-2}}$ in CAM4-Oslo (K13), this constitutes a much larger relative change in LWP, being 6.6 % (6.4 %) instead of 3.4 %. The lifetime effect was in CAM4-Oslo calculated as a radiative forcing, however, by using double calls to both the radiation and stratiform cloud microphysics modules, following Kristjánsson (2002). Since the cloud cover is independent of liquid water content (mainly depending on RH), that approach does not take into account changes in cloud lifetime from changes in the cloud cover, which may result in a low-end estimate of the indirect effect (Kristjánsson, 2002). The relative (anthropogenic divided by total) change in vertically integrated CDNC is about the same in CAM5.3-Oslo (21 % in both NUDGE and AMIP) and in CAM4-Oslo (21 %, not shown). Hence, a considerable part of the increase in cloud effective radiative forcing from $-0.90\,\mathrm{W\,m^{-2}}$ to $-1.34\,\mathrm{W\,m^{-2}}$ is probably due to the very uncertain lifetime indirect effect.

Since the modeled ice crystal number concentrations (ICNCs) can be directly affected by aerosols only through the heterogeneous freezing of mineral dust and BC in mixed-phase clouds, it is quite insensitive to anthropogenic aerosols. Vertically integrated ICNC is practically unchanged from PI to PD in both the NUDGE and AMIP simulations (Table 11), so the effect of this on the total cloud radiative forcing is probably negligible.

6 Summary and conclusions

We have described in quite some detail changes in the treatment of aerosols and aerosol–cloud interactions in going from the predecessor model version CAM4-Oslo (Kirkevåg et al., 2013; Iversen et al., 2013) to CAM5.3-Oslo. In broad terms the changes consist of explicitly taking into account nucleation and secondary organic aerosols (based on Makkonen et al., 2014), using new sea salt emissions and emission sizes (Salter et al., 2015), applying interactive DMS and primary organics emissions by using prescribed ocean-surface-layer-concentration- and wind-driven parameterizations (Nightingale et al., 2000; Vignati et al., 2010), and now also online dust emissions (Zender et al., 2003). Aerosol hygroscopicity and some other microphysical properties have also been updated, and heterogeneous ice nucleation has been implemented based on Wang et al. (2014). An updated overview of the main principles behind the production-tagged aerosol module, which is used in CAM5.3-Oslo and a number of predecessor versions, has also been presented.

We have furthermore made an attempt to validate CAM5.3-Oslo with respect to its simulated aerosol properties and aerosol cloud interactions by comparing monthly model output with in situ observations and remote retrievals. This is meant to more thoroughly complement several ongoing intercomparison studies, mainly under the AeroCom project (see http://aerocom.met.no, last access: 25 September 2018), which focus on various model diagnostics at monthly as well as finer time resolutions (down to 1 h) using results from the same model version as in this study along with other AeroCom models.

It is shown that the simulated vertical profile of BC concentrations is more realistic in CAM5.3-Oslo than in CAM4-Oslo when comparing to in situ measurements from the HIPPO aircraft campaign in the Pacific Ocean. The new model version produces much less excessive BC mass concentrations in the upper troposphere and in the stratosphere, although the concentrations are still overestimated at the highest altitudes. This may be related to aerosol aging and to how aerosols are transported and scavenged in deep convective clouds (see, e.g., Kipling et al., 2016); the mass concentrations of the other aerosol components have also been reduced (aloft) from CAM4-Oslo to CAM5.3-Oslo. This issue is to a large degree dependent on the choice of host model (which is CAM5.3 in this case) and will most likely continue to be an area of focus in future research and development of the model. Note that there is a general tendency for models participating in the AeroCom project to overestimate BC compared to the aircraft measurements in the free troposphere in remote regions (Samset et al., 2014).

With an approximately doubled DMS emission and a subsequent increase in the SO_2 source term, near-surface mass concentrations of SO_2 now seem to be considerably overestimated (normalized mean bias NMB $\sim 150\,\%$) compared to in situ observations available via the AeroCom intercomparison project (http://aerocom.met.no, last access: 25 September 2018), more so than in CAM4-Oslo. However, the modeled concentrations are not adjusted with respect to representative height above the ground surface before comparing with observations, which is an important factor for SO_2 and therefore hampers reliable evaluation of the model performance.

Near-surface sulfate concentrations are biased slightly high (22 %), more so than in CAM4-Oslo (−5 %), which instead exhibits a slightly lower Pearson correlation coefficient, R. All eight AeroCom Phase III (AP3) models with available information at aerocom.met.no have higher correlations, and half of them also have smaller (in absolute value) biases. The sulfate concentrations in CAM5.3-Oslo are found to be less biased than only 6 of the 23 available AeroCom Phase II (AP2) models, although with similar or better correlations than 14 of the models.

Near-surface BC concentrations are mainly biased low (−28 %), but less than in CAM4-Oslo (−54 %), which together with the more realistic vertical profiles indicates an improvement in modeling of BC. The bias is also found to be smaller than in 6 of 8 AP3 models, but only in 7 of the 23 AP2 models. The correlation values lie within the ranges spanned by the AP2 and AP3 models, although in the lower range for both AeroCom phases.

Since OsloAero5.3 (like earlier module versions) does not trace OM from different source types with different assumed OM/OC ratios, a reliable evaluation of the modeled mass concentrations for OM cannot be obtained without doing further work with this particular aim in mind. However, if we simply assume that the OM/OC ratio in the model is 1.4 or 2.6 for all OC, which is assumed to be representative for cases with *no* biomass burning and *only* biomass burning emission sources, respectively, we find respective biases of 122 % or 19 % compared to 108 % or 12 % in CAM4-Oslo. Unless the sparsely distributed in situ observation data represent OC very poorly globally (which is a possibility since only North America and Europe are represented), these results do indicate an overestimation that is now slightly larger than in the predecessor model despite the increased level of sophistication in the new parameterization of SOA and primary biogenic OM emissions from the ocean. The correlation value of 0.29 is just below that of CAM4-Oslo. The correlation is also lower than in most of the AP2 models and all of the AP3 models. If we assume that $\mathrm{OM/OC} = 1.4$, the bias is also larger than in the AP3 models and in all but one of the AP2 models. Although CAM4-Oslo apparently performs slightly better in this particular evaluation and for the current OM/OC ratio assumption, we should keep in mind that both SOA (treated as primary OM) and biogenic OC from the ocean use prescribed emissions, rendering that model version less useful for Earth system modeling and studies of past and future climates, as well as for more detailed process studies and sensitivity studies in general.

The sea salt aerosol concentrations are found to have a bias of 22 %, which is an improvement compared to CAM4-Oslo, although the correlation is slightly lower. Both model versions apply wind- and temperature-dependent emissions, but CAM5.3-Oslo is using particle size parameters at the point of emission that are closer to observed values in (and fully consistent with) the updated treatment. Our model outperforms the AP3 models bias-wise and has the second highest Pearson correlation. It also ends up among the best in comparison to the AP2 models.

The surface concentrations of mineral dust are biased low by −39 %, but with a decent correlation of 0.52. The available observation sites are not representative for the source regions of dust, however, and we have reasons to believe that the negative bias is a result of an underestimate in dust transport rather than in the emissions; see the summary for aerosol optics below. The dust concentrations have quite large year-to-year variations and differ the most between the nudged and the free-running AMIP simulations, for which the bias is smaller. Compared to the eight AP3 models, CAM5.3-Oslo performs better than three bias-wise and four with respect to correlation. Compared to the 23 AP2 models it performs better than 14 models bias-wise, but only 7 with respect to correlations. CAM4-Oslo is less biased, but uses prescribed dust emissions and is therefore less applicable for climate and Earth system modeling studies.

We have also compared column-integrated optical parameters with estimates from other models, most importantly with ground-based remote sensing data (AERONET). Looking first at the modeled mass extinction coefficients (MECs), we find changes in all components compared to CAM4-Oslo: a ca. 13 % decrease in MEC for sulfate and 30 % for OM, while it has increased by ca. 17 % for BC, 18 % for mineral dust, and as much as 63 % for sea salt, for which considerable changes in assumed particle size at the point of emission have had a large impact. The new estimates are all within the range of models that participated in AeroCom Phase I. The globally averaged mass absorption coefficient (MAC) for BC is smaller or larger than in the predecessor and in observations, depending on how it is being calculated. The practice for evaluating this parameter in climate models is to our knowledge not standardized for internally mixed aerosols and is often estimated based on the assumption that BC is the only aerosol component that contributes to absorption. This approach yields high globally averaged MAC values of about 21–23 $\mathrm{m^2\,g^{-1}}$ in CAM5.3-Oslo and 13.6 $\mathrm{m^2\,g^{-1}}$ in CAM4-Oslo. Adopting the more realistic assumption that mineral dust and OM also contribute to the absorption, a lower bound of the globally averaged modeled MAC is estimated to be approximately 5 $\mathrm{m^2\,g^{-1}}$. If we take this lower bound as a representative model value, it just touches the lower end of a recommended range of 5 to 11 $\mathrm{m^2\,g^{-1}}$ based on in situ measurements. However, even here we find areas regionally where MAC exceeds the recommended central value of 7.5 $\mathrm{m^2\,g^{-1}}$.

Comparing clear-sky aerosol optical depth at 550 nm (OD550CS) with remotely retrieved values from AERONET sun-photometer stations worldwide, we find a negative bias of −16 % globally compared to −22 % in CAM4-Oslo. The respective all-sky bias for CAM5.3-Oslo is positive at 15 %. OD550CS is generally biased low at high NH latitudes and high over and downstream of major mineral dust emission areas. Compared to the eight AP3 models, half of these have smaller bias values globally, while six perform better than CAM5.3-Oslo with respect to correlations. Compared to 20 AP2 models, only 7 of these have lower biases, while correlations are higher in 17 of the models.

For clear-sky absorption optical depth (ABS550CS) there is a slightly stronger negative bias of −25 %, but smaller than in CAM4-Oslo. The all-sky model variable is slightly less biased. The ABS550CS bias is of same sign and roughly the same magnitude as for OD550CS for most regions worldwide. The 1 AP3 model with data available has a stronger low bias, and only 5 of 16 AP2 models have smaller biases than CAM5.3-Oslo. All of these AeroCom models yield better correlation values, however.

The clear-sky Ångström parameter (ANG4487CS) is found to have a relatively small negative bias globally of −17 %, while the all-sky variable has a much stronger negative bias. ANG4487CS is most underestimated in northern Africa, which is consistent with exaggerated dust emissions. Comparing with 13 AP2 models, CAM5.3-Oslo is outperformed by 7 models bias-wise and 5 models with respect to correlation.

In an attempt to also evaluate an important aspect of cloud microphysics with respect to the calculation of cloud–aerosol interactions, we have compared modeled droplet concentrations (CDNC) at the cloud top with remotely retrieved CDNC from MODIS. This is done for ocean areas only, but these are the areas contributing most to the global effective radiative effect due to aerosol–cloud interactions. While overestimating droplet concentrations downwind of major emissions of mineral dust and biomass burning aerosols, CAM5.3-Oslo (in NUDGE_PD) mainly underestimates CDNC over the other coastal areas in East Asia and North America. This might be related to biases in aerosol concentrations in the respective continental source regions, but this cannot be known for sure as long as we only have near-surface concentrations for very limited areas to compare with and only mass (not number) concentrations. The largest regional biases in OD550CS from AERONET, which have mainly continental sites, seem to be consistent with the positive biases in CDNC, however. Globally averaged (low-latitude to midlatitude ocean grid points only), cloud-top CDNC has a low bias of −32 %.

Finally, we have presented and discussed model estimates of effective radiative forcing (ERF) by anthropogenic aerosols for comparison with previous radiative forcing (RF) results from CAM4-Oslo and RF and ERF estimates from IPCC AR5. Globally averaged, the SW direct effect is estimated at −0.095 $\mathrm{W\,m^{-2}}$ compared to −0.100 $\mathrm{W\,m^{-2}}$ in CAM4-Oslo. The LW direct effect was not taken into account in CAM4-Oslo and in CAM5.3-Oslo is estimated to be 0.026 $\mathrm{W\,m^{-2}}$. The joint SW and LW direct effective radiative forcing (−0.069 $\mathrm{W\,m^{-2}}$) lies well within the range of estimates in IPCC AR5. The effective radiative cloud forcing due to anthropogenic aerosols for SW and LW radiation is estimated at −1.50 $\mathrm{W\,m^{-2}}$ and 0.16 $\mathrm{W\,m^{-2}}$, respectively, compared to −0.91 $\mathrm{W\,m^{-2}}$ and 0.01 $\mathrm{W\,m^{-2}}$ in CAM4-Oslo. The joint SW and LW cloud forcing by anthropogenic aerosols in CAM5.3-Oslo ($-1.34\,\mathrm{W\,m^{-2}}$) is at the lower end of the 5–95 % confidence interval of IPCC AR5 based on model and satellite studies, but lies just within 1 standard deviation of the reported multi-model range of the CMIP5 and ACCMIP models.

Whether we use the short (7-year) simulations that have been nudged to ERA-Interim meteorology or the longer (30-year) free AMIP simulations does not make much of a difference for the global averaged results, e.g., for the ERF estimates (only 4 % weaker total aerosol ERF in the free-running simulations). Regionally, differences are larger, however, both for ERF estimates and for anthropogenic contributions to model fields in general (i.e., differences PD–PI).

After the simulations for use in this study were finalized, it was found that the median radius for mixture no. 12 (Aitken-mode BC) with respect to dry deposition had not been increased to the new number in Table 2, as intended. Instead the old value of 0.0118 µm (K13) has been used. This only affects the dry deposition (in OsloAero5.3), while the treatment of aerosol optics and sizes for use in cloud droplet activation (in AeroTab5.3, as well as in the lookup tables and the use of those in the model) is correct and unaffected. The impact of the bug has been tested by rerunning two of the least time-consuming simulations (NUDGE_PD and NUDGE_PI) with the bug fixed. This reveals that the code used in this study has underestimated the BC lifetime and column burden by about 9 % and the globally averaged direct effective radiative forcing by $0.02\,\mathrm{W\,m^{-2}}$. Since the bug affects only a small part of the results discussed in this study and since the exact same model version has been used in several ongoing AeroCom Phase III intercomparison experiments (with additional simulations with finer time-resolved model output), we have decided to keep this model version and the results as they are for this particular study. In addition to correcting this bug for BC, the presented results suggest that we should retune (reduce) the dust emission strength in future work with CAM5.3-Oslo in order to better match remotely retrieved aerosol optical depths over the most dust-dominated areas. The somewhat surprisingly small changes in OM results (including the validation) compared to the predecessor model, in which the SOA treatment is very simplistic, should also be investigated in more detail. Vertical transport and aerosol cloud interactions in convective clouds are other areas of great interest.

Code and data availability. The source code for CAM5.3-Oslo is part of a restricted NorESM2 prerelease and stored within the private GitHub NorESM repository (https://github.com/metno/noresm/tree/NorESM1.2-v1.0.0, last access: 25 September 2018). Access to the code and simulation output data produced in this study can be obtained upon reasonable request to noresm-ncc@met.no and requires entering a NorESM Climate modeling Consortium (NCC) user agreement. The CAM4-Oslo and CAM5.3-Oslo data in Tables 5–8 and Figs. 6 and 7 are available from the AeroCom database at http://aerocom.met.no (last access: 25 September 2018) under the project label NorESM, subset NorESM-Ref2017. Most of the discussed model data (in the form of tables and figures) are also available at http://ns2345k.web.sigma2.no/nudged_NorESM_c12 (last access: 25 September 2018); see especially 53OSLO_PDandPIwPDoxi_vs_AMIP_PDandPIwPDoxi for comparisons of NUDGE_PD with AMIP_PD and NUDGE_PD–NUDGE_PI with AMIP_PD–AMIP_PI.

Competing interests. The authors declare that they have no conflict of interest.

Acknowledgements. This study has been financed by the Research Council of Norway (RCN) through the project EVA (229771) and the NOTUR/Norstore projects (Sigma2 accounts nn2345k and nn9448k; Norstore account NS2345K), by the Nordic projects eSTICC (57001) and CRAICC (26060), and by the EU projects BACCHUS (FP7-ENV-2013-603445), CRESCENDO (641816), and IS-ENES2. Xiaohong Liu was supported by the Office of Science of the US Department of Energy as part of the Earth system modeling program. General NorESM1.2/CAM5.3-Oslo model development has also benefited from contributions by other scientists affiliated with NCAR and PNNL in the USA, member institutions of the Norwegian Climate Centre (BCCR, MET Norway, MetOs-UiO, NERSC, Cicero, NILU and NP), MISU, the Bolin Centre in Sweden, and the University of Helsinki, Finland. Special thanks go to NCAR for granting early access to development versions of CESM, to the AeroCom community for making their model data available at aerocom.met.no (last access: 25 September 2018), and to Jón Egill Kristjánsson at the Department of Geosciences, University of Oslo (UiO), for his dedicated work on cloud microphysics and aerosol–cloud interactions and his leading role in this field at UiO until he passed away on 14 August 2016. Finally, we would like to thank two anonymous reviewers, the topical editor (Graham Mann), and the executive editor (Lutz Gross) of GMD for their very constructive comments and reviews, which significantly improved the clarity and quality of the paper.

Edited by: Graham Mann
Reviewed by: two anonymous referees

References

Abdul-Razzak, H. and Ghan, S. J.: A parameterization of aerosol activation: 2. Multiple aerosol types, J. Geophys. Res., 105, 6837–6844, https://doi.org/10.1029/1999JD901161, 2000.

Albrecht, B. A.: Aerosols, Cloud Microphysics, and Fractional Cloudiness, Science, 245, 1227–1230, 1989.

Arimoto, R., Duce, R. A., Ray, B. J., Ellis, W. G., Cullen, J. D., and Merrill, J. T.: Trace-Elements in the Atmosphere over the North-Atlantic, J. Geophys. Res.-Atmos., 100, 1199–1213, 1995.

Atkinson, R., Baulch, D. L., Cox, R. A., Crowley, J. N., Hampson, R. F., Hynes, R. G., Jenkin, M. E., Rossi, M. J., Troe, J., and IUPAC Subcommittee: Evaluated kinetic and photochemical data for atmospheric chemistry: Volume II – gas phase reactions of organic species, Atmos. Chem. Phys., 6, 3625–4055, https://doi.org/10.5194/acp-6-3625-2006, 2006.

Atkinson, R., Baulch, D. L., Cox, R. A., Crowley, J. N., Hampson, R. F., Hynes, R. G., Jenkin, M. E., Rossi, M. J., and Troe, J.: Evaluated kinetic and photochemical data for atmospheric chemistry: Volume I – gas phase reactions of O_x, HO_x, NO_x and SO_x species, Atmos. Chem. Phys., 4, 1461–1738, https://doi.org/10.5194/acp-4-1461-2004, 2004.

Bennartz, R. and Rausch, J.: Global and regional estimates of warm cloud droplet number concentration based on 13 years of AQUA-MODIS observations, Atmos. Chem. Phys., 17, 9815–9836, https://doi.org/10.5194/acp-17-9815-2017, 2017.

Bentsen, M., Bethke, I., Debernard, J. B., Iversen, T., Kirkevåg, A., Seland, Ø., Drange, H., Roelandt, C., Seierstad, I. A., Hoose, C., and Kristjánsson, J. E.: The Norwegian Earth System Model, NorESM1-M – Part 1: Description and basic evaluation of the physical climate, Geosci. Model Dev., 6, 687–720, https://doi.org/10.5194/gmd-6-687-2013, 2013.

Bergman, T., Kerminen, V.-M., Korhonen, H., Lehtinen, K. J., Makkonen, R., Arola, A., Mielonen, T., Romakkaniemi, S., Kulmala, M., and Kokkola, H.: Evaluation of the sectional aerosol microphysics module SALSA implementation in ECHAM5-HAM aerosol-climate model, Geosci. Model Dev., 5, 845–868, https://doi.org/10.5194/gmd-5-845-2012, 2012.

Berrisford, P., Dee, P. D., Poli, P.,Brugge, R., Fielding, K., Fuentes, M., Kållberg, P. W. Kobayashi, S., Uppala, S., and Simmons, A.: The ERA-Interim archive Version 2.0, ERA report series, number 1, 2011.

Binkowski, F. S. and Shankar, U.: The Regional Particulate Matter Model: 1. Model description and preliminary results, J. Geophys. Res., 100, 26191–26209, https://doi.org/10.1029/95JD02093, 1995.

Bond, T. C. and Bergstrom, R. W.: Light Absorption by Carbonaceous Particles: An Investigative Review, Aerosol Sci. Technol., 40, 27–67, https://doi.org/10.1080/02786820500421521, 2006.

Boucher, O., Randall, D., Artaxo, P., Bretherton, C., Feingold, G., Forster, P., Kerminen, V.-M., Kondo, Y., Liao, H., Lohmann, U., Rasch, P., Satheesh, S., Sherwood, S., Stevens, B., and Zhang, X.: Clouds and aerosols, in: Climate Change 2013: The Physical Science Basis, Contribution of Working Group I to the Fifth Assessment Report of the Intergovernmental Panel on Climate Change, edited by: Stocker, T., Qin, D., Plattner, G.-K., Tignor, M., Allen, S. K., Boschung, J., Nauels, A., Xia, Y., Bex, V., and Midgley, P. M., Chapter 8, 659–740, Cambridge University Press, Cambridge, United Kingdom and New York, NY, USA, 2013.

Boy, M., Thomson, E. S., Acosta Navarro, J.-C., Arnalds, O., Batchvarova, E., Bäck, J., Berninger, F., Bilde, M., Dagsson-Waldhauserova, P., Castarède, D., Dalirian, M., de Leeuw, G., Dragosics, M., Duplissy, E.-M., Duplissy, J., Ekman, A. M. L., Fang, K., Gallet, J.-C., Glasius, M., Gryning, S.-E., Grythe, H., Hansson, H.-C., Hansson, M., Isaksson, E., Iversen, T., Jonsdottir, I., Kasurinen, V., Kirkevåg, A., Korhola, A., Krejci, R., Kristjansson, J. E., Lappalainen, H. K., Lauri, A., Leppäranta, M., Lihavainen, H., Makkonen, R., Massling, A., Meinander, O., Nilsson, E. D., Olafsson, H., Pettersson, J. B. C., Prisle, N. L., Riipinen, I., Roldin, P., Ruppel, M., Salter, M., Sand, M., Seland, Ø., Seppä, H., Skov, H., Soares, J., Stohl, A., Ström, J., Svensson, J., Swietlicki, E., Tabakova, K., Thorsteinsson, T., Virkkula, A., Weyhenmeyer, G. A., Wu, Y., Zieger, P., and Kulmala, M.: Interactions between the atmosphere, cryosphere and ecosystems at northern high latitudes, Atmos. Chem. Phys. Discuss., https://doi.org/10.5194/acp-2018-733, in review, 2018.

Carslaw, K. S., Lee, L. A., Reddington, C. L., Pringle, K. J., Rap., A., Forster, P. M., Mann, G. W., Spracklen, D. V., Woodhouse, M. T., Regayre, L.-A., and Pierce, J. R.: Large contribution of natural aerosols to uncertainty in indirect forcing, Nature, 503, 67–71, https://doi.org/10.1038/nature12674, 2013.

Chen, B., Zhu, Z., Wang, X., Andersson, A., Chen, J., Zhang, Q., and Gustafsson, Ö.: Reconciling modeling with observations of radiative absorption of black carbon aerosols, J. Geophys. Res.-Atmos., 122, 5932–5942, https://doi.org/10.1002/2017JD026548, 2017.

Chen, H. and Finlayson-Pitts, B. J.: New Particle Formation from Methanesulfonic Acid and Amines/Ammonia as a Function of Temperature, Environ. Sci. Technol., 51, 243–252, https://doi.org/10.1021/acs.est.6b04173, 2017.

Chýlek, P., Srivastava, V., Pinnic, R. G., and Wang, R. T.: Scattering of electromagnetic waves by composite spherical particles: experiment and effective medium approximations, Appl. Opt., 27, 2396–2404, 1998.

Dentener, F., Kinne, S., Bond, T., Boucher, O., Cofala, J., Generoso, S., Ginoux, P., Gong, S., Hoelzemann, J. J., Ito, A., Marelli, L., Penner, J. E., Putaud, J.-P., Textor, C., Schulz, M., van der Werf, G. R., and Wilson, J.: Emissions of primary aerosol and precursor gases in the years 2000 and 1750 prescribed data-sets for AeroCom, Atmos. Chem. Phys., 6, 4321–4344, https://doi.org/10.5194/acp-6-4321-2006, 2006.

Emmons, L. K., Walters, S., Hess, P. G., Lamarque, J.-F., Pfister, G. G., Fillmore, D., Granier, C., Guenther, A., Kinnison, D., Laepple, T., Orlando, J., Tie, X., Tyndall, G., Wiedinmyer, C., Baughcum, S. L., and Kloster, S.: Description and evaluation of the Model for Ozone and Related chemical Tracers, version 4 (MOZART-4), Geosci. Model Dev., 3, 43–67, https://doi.org/10.5194/gmd-3-43-2010, 2010.

Formenti, P., Elbert, W., Maenhaut, W., Haywood, J., Osborne, S., and Andreae, M.-O.: Inorganic and carbonaceous aerosols during the Southern African Regional Science Initiative (SAFARI 2000) experiment: Chemical characteristics, physical properties, and emission data for smoke from African biomass burning, J. Geophys. Res., 108, 8488, https://doi.org/10.1029/2002JD002408, 2003.

Gelencsér, A., May, B., Simpson, D., Sánchez-Ochoa,A., Kasper-Giebl, A., Puxbaum, H., Caseiro, A., Pio, C., and Legrand, M.: Source apportionment of PM2.5 organic aerosol over Europe: Primary/secondary, natural/anthropogenic, and fossil/biogenic origin, J. Geophys. Res., 112, D23S04, https://doi.org/10.1029/2006JD008094, 2007.

Gettelman, A. and Morrison, H.: Advanced two-moment bulk microphysics for global models. part I: Off-line tests and comparison with other schemes, J. Climate, 28, 1268–1287, 2015.

Ghan, S. J.: Technical Note: Estimating aerosol effects on cloud radiative forcing, Atmos. Chem. Phys., 13, 9971–9974, https://doi.org/10.5194/acp-13-9971-2013, 2013.

Ghan, S. J. and Easter, R. C.: Impact of cloud-borne aerosol representation on aerosol direct and indirect effects, Atmos. Chem. Phys., 6, 4163–4174, https://doi.org/10.5194/acp-6-4163-2006, 2006.

Ghan, S. J., Laulainen, N., Easter, R., Wagener, R., Nemesure, S., Chapman, E., Zhang, Y., and Leung, R.: Evaluation of aerosol direct radiative forcing in MIRAGE. J. Geophys. Res., 106, 5295–5316, 2001.

Ghan, S. J., Liu, X., Easter, R. C., Zaveri, R., Rasch, P. J., and Yoon, J.-H.: Toward a minimal representation of aerosols in climate models: comparative decomposition of aerosol direct, semidirect, and indirect radiative forcing, J. Climate, 25, 6461–6476, 2012.

Glantz, P., Bourassa, A. E., Herber, A., Iversen, T., Karlsson, J., Kirkevåg, A., Maturilli, M., Seland, Ø., Stebel, K., Struthers, H., Tesche, M., and Thomason, L.: Remote sensing of aerosols in the Arctic for an evaluation of global climate model simulations, J. Geophys. Res.-Atmos., 119, 8169–8188, https://doi.org/10.1002/2013JD021279, 2014.

Guenther, A. B., Jiang, X., Heald, C. L., Sakulyanontvittaya, T., Duhl, T., Emmons, L. K., and Wang, X.: The Model of Emissions of Gases and Aerosols from Nature version 2.1 (MEGAN2.1): an extended and updated framework for modeling biogenic emissions, Geosci. Model Dev., 5, 1471–1492, https://doi.org/10.5194/gmd-5-1471-2012, 2012.

Hess, M., Koepke, P., and Schult, I.: Optical properties of aerosols and clouds: The software package OPAC, B. Am. Meteorol. Assoc., 79, 831–844, 1998.

Holben, B. N., Eck, T. F., Slutsker, I., Tanre, D., Buis, J. P., Setzer, A., Vermote, E., Reagan, J. A., Kaufman, Y., Nakajima, T., Lavenu, F., Jankowiak, I., and Smirnov, A.: AERONET – A federated instrument network and data archive for aerosol characterization, Remote Sens. Environ., 66, 1–16, 1998.

Hoose, C., Kristjánsson, J. E., Chen, J. P., and Hazra, A.: A Classical-Theory-Based Parameterization of Heterogeneous Ice Nucleation by Mineral Dust, Soot and Biological Particles in a Global Climate Model, J. Atmos. Sci., 67, 2483–2503, 2010.

Horowitz, L. W., Walters, S., Mauzerall, D. L., Emmons, L. K., Rasch, P. J., Granier, C., Tie, X., Lamarque, J.-F., Schultz, M. G., Tyndall, G. S., Orlando, J. J., and Brasseur, G. P.: A global simulation of tropospheric ozone and related tracers: Description and evaluation of MOZART, version 2, J. Geophys. Res., 108, 4784, https://doi.org/10.1029/2002JD002853, 2003.

Huneeus, N., Schulz, M., Balkanski, Y., Griesfeller, J., Prospero, J., Kinne, S., Bauer, S., Boucher, O., Chin, M., Dentener, F., Diehl, T., Easter, R., Fillmore, D., Ghan, S., Ginoux, P., Grini, A., Horowitz, L., Koch, D., Krol, M. C., Landing, W., Liu, X., Mahowald, N., Miller, R., Morcrette, J.-J., Myhre, G., Penner, J., Perlwitz, J., Stier, P., Takemura, T., and Zender, C. S.: Global dust model intercomparison in AeroCom phase I, Atmos. Chem. Phys., 11, 7781–7816, https://doi.org/10.5194/acp-11-7781-2011, 2011.

Iversen, T. and Seland, Ø.: A scheme for process-tagged SO_4 and BC aerosols in NCAR CAM3: Validation and sensitivity to cloud processes, J. Geophys. Res., 107, 4751, https://doi.org/10.1029/2001JD000885, 2002.

Iversen, T. and Seland, Ø.: Correction to "A scheme for process-tagged SO_4 and BC aerosols in NCAR-CCM3, Validation and sensitivity to cloud processes", J. Geophys. Res., 108, 4502, https://doi.org/10.1029/2003JD003840, 2003.

Iversen, T., Bentsen, M., Bethke, I., Debernard, J. B., Kirkevåg, A., Seland, Ø., Drange, H., Kristjansson, J. E., Medhaug, I., Sand, M., and Seierstad, I. A.: The Norwegian Earth System Model, NorESM1-M – Part 2: Climate response and scenario projections, Geosci. Model Dev., 6, 389–415, https://doi.org/10.5194/gmd-6-389-2013, 2013.

Iversen, T., Bethke, I., Debernard, J. B., Graff, L. S., Seland, Ø., Bentsen, M., Kirkevåg, A., Li, C., and Olivié, D. J. L.: The "NorESM1-Happi" used for evaluating differences between a global warming of 1.5 °C and 2 °C, and the role of Arctic Amplification, Earth Syst. Dynam. Discuss., https://doi.org/10.5194/esd-2017-115, in review, 2017.

Jiao, C., Flanner, M. G., Balkanski, Y., Bauer, S. E., Bellouin, N., Berntsen, T. K., Bian, H., Carslaw, K. S., Chin, M., De Luca, N., Diehl, T., Ghan, S. J., Iversen, T., Kirkevåg, A., Koch, D., Liu, X., Mann, G. W., Penner, J. E., Pitari, G., Schulz, M., Seland, Ø., Skeie, R. B., Steenrod, S. D., Stier, P., Takemura, T., Tsigaridis, K., van Noije, T., Yun, Y., and Zhang, K.: An AeroCom assessment of black carbon in Arctic snow and sea ice, Atmos. Chem. Phys., 14, 2399–2417, https://doi.org/10.5194/acp-14-2399-2014, 2014.

Jokinen, T., Berndt, T., Makkonen, R., Kerminen, V.-M., Junninen, H., Paasonen, P., Stratmann, F., Herrmann, H., Guenther, A. B., Worsnop, D. R., Kulmala, M., Ehn, M., and Sipilä, M.: Production of extremely low volatile organic compounds from biogenic emissions: Measured yields and atmospheric implications, Proc. Natl. Acad. Sci., 112, 7123–7128, https://doi.org/10.1073/pnas.1423977112, 2015.

Karset, I. H. H., Berntsen, T. K., Storelvmo, T., Alterskjær, K., Grini, A., Olivié, D., Kirkevåg, A., Seland, Ø., Iversen, T., and Schulz, M.: Strong impacts on aerosol indirect effects from historical oxidant changes, Atmos. Chem. Phys., 18, 7669–7690, https://doi.org/10.5194/acp-18-7669-2018, 2018.

Keskinen, H., Virtanen, A., Joutsensaari, J., Tsagkogeorgas, G., Duplissy, J., Schobesberger, S., Gysel, M., Riccobono, F., Slowik, J. G., Bianchi, F., Yli-Juuti, T., Lehtipalo, K., Rondo, L., Breitenlechner, M., Kupc, A., Almeida, J., Amorim, A., Dunne, E. M., Downard, A. J., Ehrhart, S., Franchin, A., Kajos, M. K., Kirkby, J., Kürten, A., Nieminen, T., Makhmutov, V., Mathot, S., Miettinen, P., Onnela, A., Petäjä, T., Praplan, A., Santos, F. D., Schallhart, S., Sipilä, M., Stozhkov, Y., Tomé, A., Vaattovaara, P., Wimmer, D., Prevot, A., Dommen, J., Donahue, N. M., Flagan, R. C., Weingartner, E., Viisanen, Y., Riipinen, I., Hansel, A., Curtius, J., Kulmala, M., Worsnop, D. R., Baltensperger, U., Wex, H., Stratmann, F., and Laaksonen, A.: Evolution of particle composition in CLOUD nucleation experiments, Atmos. Chem. Phys., 13, 5587–5600, https://doi.org/10.5194/acp-13-5587-2013, 2013.

Kettle, A. J. and Andreae, M. O.: Flux of dimethylsulfide from the oceans: A comparison of updated data sets and flux models, J. Geophys. Res., 105, 26793–26808, 2000.

Kinne, S., Schulz, M., Textor, C., Guibert, S., Balkanski, Y., Bauer, S. E., Berntsen, T., Berglen, T. F., Boucher, O., Chin, M., Collins, W., Dentener, F., Diehl, T., Easter, R., Feichter, J., Fillmore, D., Ghan, S., Ginoux, P., Gong, S., Grini, A., Hendricks, J., Herzog, M., Horowitz, L., Isaksen, I., Iversen, T., Kirkevåg, A., Kloster, S., Koch, D., Kristjansson, J. E., Krol, M., Lauer, A., Lamarque, J. F., Lesins, G., Liu, X., Lohmann, U., Montanaro, V., Myhre, G., Penner, J., Pitari, G., Reddy, S., Seland, O., Stier, P., Takemura, T., and Tie, X.: An AeroCom initial assessment – optical properties in aerosol component modules of global models, Atmos. Chem. Phys., 6, 1815–1834, https://doi.org/10.5194/acp-6-1815-2006, 2006.

Kipling, Z., Stier, P., Schwarz, J. P., Perring, A. E., Spackman, J. R., Mann, G. W., Johnson, C. E., and Telford, P. J.: Constraints on aerosol processes in climate models from vertically-resolved aircraft observations of black carbon, Atmos. Chem. Phys., 13, 5969–5986, https://doi.org/https://doi.org/10.5194/acp-13-5969-2013, 2013.

Kipling, Z., Stier, P., Johnson, C. E., Mann, G. W., Bellouin, N., Bauer, S. E., Bergman, T., Chin, M., Diehl, T., Ghan, S. J., Iversen, T., Kirkevåg, A., Kokkola, H., Liu, X., Luo, G., van Noije, T., Pringle, K. J., von Salzen, K., Schulz, M., Seland, Ø., Skeie, R. B., Takemura, T., Tsigaridis, K., and Zhang, K.: What controls the vertical distribution of aerosol? Relationships between process sensitivity in HadGEM3-UKCA and inter-model variation from AeroCom Phase II, Atmos. Chem. Phys., 16, 2221–2241, https://doi.org/10.5194/acp-16-2221-2016, 2016.

Kirkevåg, A. and Iversen, T.: Global direct radiative forcing by process-parameterized aerosol optical properties, J. Geophys. Res., 107, 4433, https://doi.org/10.1029/2001JD000886, 2002.

Kirkevåg, A., Iversen, T., and Dahlback, A.: On radiative effects of black carbon and sulphate aerosols, Atmos. Environ., 33, 2621–2635, 1999.

Kirkevåg, A., Iversen, T., Seland, Ø., and Kristjánsson, J. E.: Revised schemes for optical parameters and cloud condensation nuclei in CCM-Oslo. Institute Report Series, Department of Geosciences, University of Oslo, 29 pp., ISBN 82-91885-31-1, ISSN 1501-6854-128, 2005.

Kirkevåg, A., Iversen, T., Seland, Ø., Debernard, J. B., Storelvmo, T., and Kristjánsson, J. E.: Aerosol-cloud-climate interactions in the climate model CAM-Oslo, Tellus A, 60, 492–512, 2008.

Kirkevåg, A., Iversen, T., Seland, Ø., Hoose, C., Kristjánsson, J. E., Struthers, H., Ekman, A. M. L., Ghan, S., Griesfeller, J., Nilsson, E. D., and Schulz, M.: Aerosol-climate interactions in the Norwegian Earth System Model – NorESM1-M, Geosci. Model Dev., 6, 207–244, https://doi.org/10.5194/gmd-6-207-2013, 2013.

Koehler, K. A., Kreidenweis, S. M., DeMott, P. J., Petters, M. D., Prenni, A. J., and Carrico, C. M.: Hygroscopicity and cloud droplet activation of mineral dust aerosol, Geophys. Res. Lett., 36, L08805, https://doi.org/10.1029/2009GL037348, 2009.

Koffi, B., Schulz, M., Breon, F.-M., Dentener, F., Steensen, B. M., Griesfeller, J., Winker, D., Balkanski, Y., Bauer, S. E., Bellouin, N., Berntsen, T., Bian, H., Chin, M., Diehl, T., Easter, R., Ghan, S., Hauglustaine, D., Iversen, T., Kirkevåg, A., Liu, X., Lohmann, U., Myhre, G., Rasch, P., Seland, Ø., Skeie, R. B., Steenrod, S. D., Stier, P., Tackett, J., Takemura, T., Tsigaridis, K., Vuolo, M. R., Yoon, J., and Zhang, K.: Evaluation of the aerosol vertical distribution in global aerosol models through comparison against CALIOP measurements: AeroCom phase II results. J. Geophys. Res.-Atmos, 121, 7254–7283, https://doi.org/10.1002/2015JD024639, 2016.

Kok, J. F., Ridley, D. A., Zhou, Q., Miller, R. L., Zhao, C., Heald, C. L., Ward, D. S., Albani, S., and Haustein, K.: Smaller desert dust cooling effect estimated from analysis of dust size and abundance, Nat. Geosci., 10, 274–278, https://doi.org/10.1038/ngeo2912, 2017.

Kooperman, G. J., Pritchard, M. S., Ghan, S. J., Wang, M., Somerville, R. C. J., and Russell, L. M.: Constraining the influence of natural variability to improve estimates of global aerosol indirect effects in a nudged version of the Community Atmosphere Model 5, J. Geophys. Res., 117, D23204, https://doi.org/10.1029/2012JD018588, 2012.

Köpke, P., Hess, M., Schult, I., and Shettle, E. P.: Global Aerosol Data Set, MPI Report no. 243, 1997.

Kristjánsson, J. E.: Studies of the aerosol indirect effect from sulfate and black carbon aerosols, J. Geophys. Res.-Atmos, 107, 4246, https://doi.org/10.1029/2001JD000887, 2002.

Kulmala, M., Kerminen, V.-M., Anttila, T., Laaksonen, A., and O'Dowd, C. D.: Organic aerosol formation via sulphate cluster activation, J. Geophys. Res., 109, D04205, https://doi.org/10.1029/2003JD003961, 2004.

Lamarque, J.-F., Bond, T. C., Eyring, V., Granier, C., Heil, A., Klimont, Z., Lee, D., Liousse, C., Mieville, A., Owen, B., Schultz, M. G., Shindell, D., Smith, S. J., Stehfest, E., Van Aardenne, J., Cooper, O. R., Kainuma, M., Mahowald, N., McConnell, J. R., Naik, V., Riahi, K., and van Vuuren, D. P.: Historical (1850–2000) gridded anthropogenic and biomass burning emissions of reactive gases and aerosols: methodology and application, Atmos. Chem. Phys., 10, 7017–7039, https://doi.org/10.5194/acp-10-7017-2010, 2010.

Lana, A., Bell, T. G., Simo, R., Vallina, S. M., Ballabrera-Poy, J., Kettle, A. J., Dachs, J., Bopp, L., Saltzman, E. S., Stefels, J., Johnson, J. E., and Liss, P. S.: An updated climatology of surface dimethylsulfide concentrations and emission fluxes in the global ocean, Global Biogeochem. Cy., 25, GB1004, https://doi.org/10.1029/2010GB003850, 2011

Lehtinen, K. E. J., Dal Maso, M., Kulmala, M., and Kerminen, V-M.: Estimating nucleation rates from apparent particle formation rates and vice versa: Revised formulation of the Kerminen–Kulmala equation, J. Aerosol Sci., 38, 988–994, https://doi.org/10.1016/j.jaerosci.2007.06.009, 2007.

Liu, X., Penner, J. E., Das, B., Bergmann, D., Rodriguez, J. M., Strahan. S., Wang, M., and Feng, Y.: Uncertainties in global aerosol simulations: Assessment using three meteorological data sets, J. Geophys. Res., 112, D11212, https://doi.org/10.1029/2006JD008216, 2007.

Liu, X., Easter, R. C., Ghan, S. J., Zaveri, R., Rasch, P., Shi, X., Lamarque, J.-F., Gettelman, A., Morrison, H., Vitt, F., Conley, A., Park, S., Neale, R., Hannay, C., Ekman, A. M. L., Hess, P., Mahowald, N., Collins, W., Iacono, M. J., Bretherton, C. S., Flanner, M. G., and Mitchell, D.: Toward a minimal representation of aerosols in climate models: description and evaluation in the Community Atmosphere Model CAM5, Geosci. Model Dev., 5, 709–739, https://doi.org/10.5194/gmd-5-709-2012, 2012.

Liu, X., Ma, P.-L., Wang, H., Tilmes, S., Singh, B., Easter, R. C., Ghan, S. J., and Rasch, P. J.: Description and evaluation of a new four-mode version of the Modal Aerosol Module (MAM4) within version 5.3 of the Community Atmosphere Model, Geosci. Model Dev., 9, 505–522, https://doi.org/10.5194/gmd-9-505-2016, 2016.

Makkonen, R., Seland, Ø., Kirkevåg, A., Iversen, T., and Kristjánsson, J. E.: Evaluation of aerosol number concentrations in NorESM with improved nucleation parameterization, Atmos. Chem. Phys., 14, 5127–5152, https://doi.org/10.5194/acp-14-5127-2014, 2014.

Malavelle, F. F., Haywood, J. M., and Jones, A. et al.: Strong constraints on aerosol-cloud interactions from volcanic eruptions, Nature, 546, 485–491, https://doi.org/10.1038/nature22974, 2017.

Mann, G. W., Carslaw, K. S., Spracklen, D. V., Ridley, D. A., Manktelow, P. T., Chipperfield, M. P., Pickering, S. J., and Johnson, C. E.: Description and evaluation of GLOMAP-mode: a modal global aerosol microphysics model for the UKCA composition-climate model, Geosci. Model Dev., 3, 519–551, https://doi.org/10.5194/gmd-3-519-2010, 2010.

Mann, G. W., Carslaw, K. S., Reddington, C. L., Pringle, K. J., Schulz, M., Asmi, A., Spracklen, D. V., Ridley, D. A., Woodhouse, M. T., Lee, L. A., Zhang, K., Ghan, S. J., Easter, R. C., Liu, X., Stier, P., Lee, Y. H., Adams, P. J., Tost, H., Lelieveld, J., Bauer, S. E., Tsigaridis, K., van Noije, T. P. C., Strunk, A., Vignati, E., Bellouin, N., Dalvi, M., Johnson, C. E., Bergman, T., Kokkola, H., von Salzen, K., Yu, F., Luo, G., Petzold, A., Heintzenberg, J., Clarke, A., Ogren, J. A., Gras, J., Baltensperger, U., Kaminski, U., Jennings, S. G., O'Dowd, C. D., Harrison, R. M., Beddows, D. C. S., Kulmala, M., Viisanen, Y., Ulevicius, V., Mihalopoulos, N., Zdimal, V., Fiebig, M., Hansson, H.-C., Swietlicki, E., and Henzing, J. S.: Intercomparison and evaluation of global aerosol microphysical properties among AeroCom models of a range of complexity, Atmos. Chem. Phys., 14, 4679–4713, https://doi.org/10.5194/acp-14-4679-2014, 2014.

Morrison, H. and Gettelman, A.: A new two-moment bulk stratiform cloud microphysics scheme in the community atmosphere model, version 3 (CAM3). Part I: Description and numerical tests, J. Climate, 21, 3642–3659, 2008.

Myhre, G., Shindell, D., Bréon, F.-M., Collins, W., Fuglestvedt, J., Huang, J., Koch, D., Lamarque, J.-F., Lee, D., Mendoza, B., Nakajima, T., Robock, A., Stephens, G., Takemura, T., and Zhang, H.: Anthropogenic and Natural Radiative Forcing, in: Climate Change 2013: The Physical Science Basis, Contribution of Working Group I to the Fifth Assessment Report of the Intergovernmental Panel on Climate Change, edited by: Stocker, T. F., Qin, D., Plattner, G.-K., Tignor, M., Allen, S. K., Boschung, J., Nauels, A., Xia, Y., Bex, V., and Midgley, P. M., Cambridge University Press, Cambridge, UK and New York, NY, USA, 659–740, 2013.

Neale, R. B., Chen, C.-C., Gettelman, A., Lauritzen, P. H., Park, S., Williamson, D. L., Conley, A. J., Garcia, R., Kinnison, D., Lamarque, J.-F., Marsh, D., Mills, M., Smith, A. K., Tilmes, S., Vitt, F., Morrison, H., Cameron-Smith, P., Collins,W. D., Iacono, M. J., Easter, R. C., Ghan, S. J., Liu, X., Rasch, P. J., and Taylor, M. A.: Description of the NCAR Community Atmosphere Model (CAM 5.0), NCAR Tech. Note NCAR-TN-486CSTR, 274 pp., 2012.

Nightingale, P. D., Malin, G., Law, C. S., Watson, A. J., Liss, P. S., Liddicoat, M. I., Boutin, J., and Upstill-Goddard, R. C.: In situ evaluation of air-sea gas exchange parameterizations using novel conservative and volatile tracers, Global Biogeochem. Cy., 14, 373–387, https://doi.org/https://doi.org/10.1029/1999GB900091, 2000.

Ning, Z., Chan, K. L., Wong, K. C., Westerdahl, D., Mocnik, G., Zhou, J. H., and Cheung, C. S.: Black carbon mass size distributions of diesel exhaust and urban aerosols measured using differential mobility analyzer in tandem with Aethalometer, Atmos. Environ., 80, 31–40, 2013

O'Dowd, C., Langmann, B., Varghese, S., Scannell, C., Ceburnis, D., and Facchini, M. C.: A combined organic-inorganic sea-spray source function. Geophys. Res. Lett., 35, L01801, https://doi.org/10.1029/2007GL030331, 2008.

Oleson, K. W., Lawrence, D. M., Bonan, G. B., Drewniak, B., Huang, M., Koven, C. D., Levis, S., Li, F., Riley, W. J., Subin, Z. M., Swenson, S. C., Thornton, P. E., Bozbiyik, A., Fisher, R., Kluzek, E., Lamarque, J.-F., Lawrence, P. J., Leung, L. R., Lipscomb, W., Muszala, S., Ricciuto, D. M., Sacks, W., Sun, Y., Tang, J., and Yang, Z.-L.: Technical Description of version 4.5 of the Community Land Model (CLM), NCAR Technical Note NCAR/TN-503+STR, National Center for Atmospheric Research, Boulder, CO, 422 pp., https://doi.org/10.5065/D6RR1W7M, 2013.

O'Reilly, J. E., Maritorena, S., and O'Brien, M.-C. et al.: SeaWiFS Postlaunch Calibration and Validation Analyses, Part 3. NASA Tech. Memo. 2000–206892, Vol. 11, edited by: Hooker, S. B. and Firestone, E. R., NASA Goddard Space Flight Center, 2000.

Paasonen, P., Nieminen, T., Asmi, E., Manninen, H. E., Petäjä, T., Plass-Dülmer, C., Flentje, H., Birmili, W., Wiedensohler, A., Hõrrak, U., Metzger, A., Hamed, A., Laaksonen, A., Facchini, M. C., Kerminen, V.-M., and Kulmala, M.: On the roles of sulphuric acid and low-volatility organic vapours in the initial steps of atmospheric new particle formation, Atmos. Chem. Phys., 10, 11223–11242, https://doi.org/10.5194/acp-10-11223-2010, 2010.

Poling, B. E., Prausnitz, J. M., and O'Connell, J. P.: The Properties of Gases and Liquids, Fifth Edition, McGRAW-HILL, https://doi.org/10.1036/0070116822, 2001.

Pozzoli, L., Bey, I., Rast, S., Schultz, M. G., Stier, P., and Feichter, J.: Trace gas and aerosol interactions in the fully coupled model of aerosol-chemistry-climate ECHAM5-HAMMOZ: 1. Model description and insights from the spring 2001 TRACE-P experiment, J. Geophys. Res., 113, D07308, https://doi.org/10.1029/2007JD009007, 2008.

Pruppacher, H. R. and Klett, J. D.: Microphysics of Clouds and Precipitation, 954 pp., Kluwer Acad., Norwell, Mass, 1997.

Rasch, P. J. and Kristjánsson, J. E.: A comparison of the CCM3 model climate using diagnosed and predicted condensate parameterizations, J. Climate, 11, 1587–1614, 1998.

Riipinen, I., Pierce, J. R., Yli-Juuti, T., Nieminen, T., Häkkinen, S., Ehn, M., Junninen, H., Lehtipalo, K., Petäjä, T., Slowik, J., Chang, R., Shantz, N. C., Abbatt, J., Leaitch, W. R., Kerminen, V.-M., Worsnop, D. R., Pandis, S. N., Donahue, N. M., and Kulmala, M.: Organic condensation: a vital link connecting aerosol formation to cloud condensation nuclei (CCN) concentrations, Atmos. Chem. Phys., 11, 3865–3878, https://doi.org/10.5194/acp-11-3865-2011, 2011.

Salter, M. E., Zieger, P., Acosta Navarro, J. C., Grythe, H., Kirkevåg, A., Rosati, B., Riipinen, I., and Nilsson, E. D.: An empirically derived inorganic sea spray source function incorporating sea surface temperature, Atmos. Chem. Phys., 15, 11047–11066, https://doi.org/10.5194/acp-15-11047-2015, 2015.

Samset, B. H., Myhre, G., Schulz, M., Balkanski, Y., Bauer, S., Berntsen, T. K., Bian, H., Bellouin, N., Diehl, T., Easter, R. C., Ghan, S. J., Iversen, T., Kinne, S., Kirkevåg, A., Lamarque, J.-F., Lin, G., Liu, X., Penner, J. E., Seland, Ø., Skeie, R. B., Stier, P., Takemura, T., Tsigaridis, K., and Zhang, K.: Black carbon vertical profiles strongly affect its radiative forcing uncertainty, Atmos. Chem. Phys., 13, 2423–2434, https://doi.org/10.5194/acp-13-2423-2013, 2013.

Samset, B. H., Myhre, G., Herber, A., Kondo, Y., Li, S.-M., Moteki, N., Koike, M., Oshima, N., Schwarz, J. P., Balkanski, Y., Bauer,

S. E., Bellouin, N., Berntsen, T. K., Bian, H., Chin, M., Diehl, T., Easter, R. C., Ghan, S. J., Iversen, T., Kirkevåg, A., Lamarque, J.-F., Lin, G., Liu, X., Penner, J. E., Schulz, M., Seland, Ø., Skeie, R. B., Stier, P., Takemura, T., Tsigaridis, K., and Zhang, K.: Modelled black carbon radiative forcing and atmospheric lifetime in AeroCom Phase II constrained by aircraft observations, Atmos. Chem. Phys., 14, 12465–12477, https://doi.org/10.5194/acp-14-12465-2014, 2014.

Schulz, M., Textor, C., Kinne, S., Balkanski, Y., Bauer, S., Berntsen, T., Berglen, T., Boucher, O., Dentener, F., Guibert, S., Isaksen, I. S. A., Iversen, T., Koch, D., Kirkevåg, A., Liu, X., Montanaro, V., Myhre, G., Penner, J. E., Pitari, G., Reddy, S., Seland, Ø., Stier, P., and Takemura, T.: Radiative forcing by aerosols as derived from the AeroCom present-day and pre-industrial simulations, Atmos. Chem. Phys., 6, 5225–5246, https://doi.org/10.5194/acp-6-5225-2006, 2006.

Schwarz, J. P., Samset, B. H., Perring, A. E., Spackman, J. R., Gao, R. S., Stier, P., Schulz, M., Moore, F. L., Ray, E. A., and Fahey, D. W.: Global-scale seasonally resolved black carbon vertical profiles over the Pacific, Geophys. Res. Lett., 40, 5542–5547, https://doi.org/10.1002/2013gl057775, 2013.

Seland, Ø. and Iversen, T.: A scheme for black carbon and sulfate aerosols tested in a hemispheric scale, Eulerian dispersion model, Atmos. Environ., 33, 2853–2879, 1999.

Seland, Ø., Iversen, T., Kirkevåg, A., and Storelvmo, T.: Aerosol-climate interactions in the CAM-Oslo atmospheric GCM and investigations of associated shortcomings, Tellus A, 60, 459–491, 2008.

Simpson, D., Benedictow, A., Berge, H., Bergström, R., Emberson, L. D., Fagerli, H., Flechard, C. R., Hayman, G. D., Gauss, M., Jonson, J. E., Jenkin, M. E., Nyíri, A., Richter, C., Semeena, V. S., Tsyro, S., Tuovinen, J.-P., Valdebenito, Á., and Wind, P.: The EMEP MSC-W chemical transport model – technical description, Atmos. Chem. Phys., 12, 7825–7865, https://doi.org/10.5194/acp-12-7825-2012, 2012.

Spracklen, D. V., Arnold, S. R., Sciare, J., Carslaw, K. S., and Pio, C.: Globally significant oceanic source of organic carbon aerosol, Geophys. Res. Lett., 35, L12811, https://doi.org/10.1029/2008GL033359,2008.

Stjern, C. W., Samset, B. H., Myhre, G., Forster, P. M., Hodnebrog, Ø., Andrews, T., Boucher, O., Faluvegi, G., Iversen, T., Kasoar, M., Kharin, V., Kirkevåg, A., Lamarque, J.-F., Olivié, D., Richardson, T., Shawki, D., Shindell, D., Smith, C. J., Takemura, T., and Voulgarakis, A: Rapid adjustments cause weak surface temperature response to increased black carbon concentrations, J. Geophys. Res.-Atmos., 119, 8169–8188, https://doi.org/10.1002/2017JD027326, 2017.

Stohl, A., Klimont, Z., Eckhardt, S., Kupiainen, K., Shevchenko, V. P., Kopeikin, V. M., and Novigatsky, A. N.: Black carbon in the Arctic: the underestimated role of gas flaring and residential combustion emissions, Atmos. Chem. Phys., 13, 8833–8855, https://doi.org/10.5194/acp-13-8833-2013, 2013.

Ström, J., Okada, S. K., and Heintzenberg, J.: On the state of mixing of particles due to Brownian coagulation, J. Aerosol Sci., 23, 467–480, 1992.

Tang, I. N.: Chemical and size effects of hygroscopic aerosols on light scattering coefficients, J. Geophys. Res., 101, 19245–19250, 1996.

Tang, I . N. and Munkelwitz, H. R.: Aerosol Phase Transformation and Growth in the Atmosphere, J. Appl. Meteorol., 33, 792–796, 1994.

Textor, C., Schulz, M., Guibert, S., Kinne, S., Balkanski, Y., Bauer, S., Berntsen, T., Berglen, T., Boucher, O., Chin, M., Dentener, F., Diehl, T., Easter, R., Feichter, H., Fillmore, D., Ghan, S., Ginoux, P., Gong, S., Grini, A., Hendricks, J., Horowitz, L., Huang, P., Isaksen, I., Iversen, I., Kloster, S., Koch, D., Kirkevåg, A., Kristjansson, J. E., Krol, M., Lauer, A., Lamarque, J. F., Liu, X., Montanaro, V., Myhre, G., Penner, J., Pitari, G., Reddy, S., Seland, Ø., Stier, P., Takemura, T., and Tie, X.: Analysis and quantification of the diversities of aerosol life cycles within AeroCom, Atmos. Chem. Phys., 6, 1777–1813, https://doi.org/10.5194/acp-6-1777-2006, 2006.

Tilmes, S., Lamarque, J.-F., Emmons, L. K., Kinnison, D. E., Ma, P.-L., Liu, X., Ghan, S., Bardeen, C., Arnold, S., Deeter, M., Vitt, F., Ryerson, T., Elkins, J. W., Moore, F., Spackman, J. R., and Val Martin, M.: Description and evaluation of tropospheric chemistry and aerosols in the Community Earth System Model (CESM1.2), Geosci. Model Dev., 8, 1395–1426, https://doi.org/10.5194/gmd-8-1395-2015, 2015.

Tjiputra, J. F., Roelandt, C., Bentsen, M., Lawrence, D. M., Lorentzen, T., Schwinger, J., Seland, Ø., and Heinze, C.: Evaluation of the carbon cycle components in the Norwegian Earth System Model (NorESM), Geosci. Model Dev., 6, 301–325, https://doi.org/10.5194/gmd-6-301-2013, 2013.

Tørseth, K., Aas, W., Breivik, K., Fjæraa, A. M., Fiebig, M., Hjellbrekke, A. G., Lund Myhre, C., Solberg, S., and Yttri, K. E.: Introduction to the European Monitoring and Evaluation Programme (EMEP) and observed atmospheric composition change during 1972–2009, Atmos. Chem. Phys., 12, 5447–5481, https://doi.org/10.5194/acp-12-5447-2012, 2012.

Tsigaridis, K., Daskalakis, N., Kanakidou, M., Adams, P. J., Artaxo, P., Bahadur, R., Balkanski, Y., Bauer, S. E., Bellouin, N., Benedetti, A., Bergman, T., Berntsen, T. K., Beukes, J. P., Bian, H., Carslaw, K. S., Chin, M., Curci, G., Diehl, T., Easter, R. C., Ghan, S. J., Gong, S. L., Hodzic, A., Hoyle, C. R., Iversen, T., Jathar, S., Jimenez, J. L., Kaiser, J. W., Kirkevåg, A., Koch, D., Kokkola, H., Lee, Y. H., Lin, G., Liu, X., Luo, G., Ma, X., Mann, G. W., Mihalopoulos, N., Morcrette, J.-J., Müller, J.-F., Myhre, G., Myriokefalitakis, S., Ng, N. L., O'Donnell, D., Penner, J. E., Pozzoli, L., Pringle, K. J., Russell, L. M., Schulz, M., Sciare, J., Seland, Ø., Shindell, D. T., Sillman, S., Skeie, R. B., Spracklen, D., Stavrakou, T., Steenrod, S. D., Takemura, T., Tiitta, P., Tilmes, S., Tost, H., van Noije, T., van Zyl, P. G., von Salzen, K., Yu, F., Wang, Z., Wang, Z., Zaveri, R. A., Zhang, H., Zhang, K., Zhang, Q., and Zhang, X.: The AeroCom evaluation and intercomparison of organic aerosol in global models, Atmos. Chem. Phys., 14, 10845–10895, https://doi.org/10.5194/acp-14-10845-2014, 2014.

Twomey, S.: The influence of Pollution on the Shortwave Albedo of Clouds, J. Atmos. Sci., 34, 1149–1152, 1977.

Vehkamäki, H., Kulmala, M., Napari, I., Lehtinen, K. E. J., Timmreck, C., Noppel, M., and Laaksonen, A.: An improved parameterization for sulfuric acid–water nucleation rates for tropospheric and stratospheric conditions, J. Geophys. Res., 107, 4622, https://doi.org/10.1029/2002JD002184, 2002.

Vignati, E., Facchini, M. C., Rinaldi, M., Scannell, C., Ceburnis, D., Sciare, J., Kanakidou, M., Myriokefalitakis, S., Dentener, F., and

O'Dowd, C. D.: Global scale emission and distribution of sea-spray aerosol: Sea-salt and organic enrichment, Atmos. Environ., 44, 670–677, 2010.

Wang, Y., Liu, X., Hoose, C., and Wang, B.: Different contact angle distributions for heterogeneous ice nucleation in the Community Atmospheric Model version 5, Atmos. Chem. Phys., 14, 10411–10430, https://doi.org/10.5194/acp-14-10411-2014, 2014.

Willis, M. D., Burkart, J., Thomas, J. L., Köllner, F., Schneider, J., Bozem, H., Hoor, P. M., Aliabadi, A. A., Schulz, H., Herber, A. B., Leaitch, W. R., and Abbatt, J. P. D.: Growth of nucleation mode particles in the summertime Arctic: a case study, Atmos. Chem. Phys., 16, 7663–7679, https://doi.org/10.5194/acp-16-7663-2016, 2016.

Wofsy, S. C. and the HIPPO team: HIAPER Pole-to-Pole Observations (HIPPO): fine-grained, global-scale measurements of climatically important atmospheric gases and aerosols, Philos. T. Ser. A, 369, 207–386, https://doi.org/10.1098/rsta.2010.0313, 2011, 2011.

Yli-Juuti, T., Nieminen, T., Hirsikko, A., Aalto, P. P., Asmi, E., Hõrrak, U., Manninen, H. E., Patokoski, J., Dal Maso, M., Petäjä, T., Rinne, J., Kulmala, M., and Riipinen, I.: Growth rates of nucleation mode particles in Hyytiälä during 2003–2009: variation with particle size, season, data analysis method and ambient conditions, Atmos. Chem. Phys., 11, 12865–12886, https://doi.org/10.5194/acp-11-12865-2011, 2011.

Zender, C. S., Bian H., and Newman, D: Mineral Dust Entrainment and Deposition (DEAD) model: Description and 1990s dust climatology, J. Geophys. Res., 108, 4416, https://doi.org/10.1029/2002JD002775, 2003.

Zhang, K., Wan, H., Liu, X., Ghan, S. J., Kooperman, G. J., Ma, P.-L., Rasch, P. J., Neubauer, D., and Lohmann, U.: Technical Note: On the use of nudging for aerosol-climate model intercomparison studies, Atmos. Chem. Phys., 14, 8631–8645, https://doi.org/10.5194/acp-14-8631-2014, 2014.

Paper II

II

Strong impacts on aerosol indirect effects from historical oxidant changes

Inger Helene Hafsahl Karset, Terje Koren Berntsen, Trude Storelvmo, Kari Alterskjær, Alf Grini, Dirk Olivié, Alf Kirkevåg, Øyvind Seland, Trond Iversen, Michael Schulz

Atmospheric Chemistry and Physics , 2018
doi:10.5194/acp-18-7669-2018

Atmos. Chem. Phys., 18, 7669–7690, 2018
https://doi.org/10.5194/acp-18-7669-2018

Atmospheric Chemistry and Physics
Open Access

Strong impacts on aerosol indirect effects from historical oxidant changes

Inger Helene Hafsahl Karset[1], **Terje Koren Berntsen**[1,2], **Trude Storelvmo**[1], **Kari Alterskjær**[2], **Alf Grini**[3], **Dirk Olivié**[3], **Alf Kirkevåg**[3], **Øyvind Seland**[3], **Trond Iversen**[3], **and Michael Schulz**[3]

[1]University of Oslo, Department of Geosciences, Section for Meteorology and Oceanography, Oslo, Norway
[2]CICERO Center for International Climate Research, Oslo, Norway
[3]Norwegian Meteorological Institute, Oslo, Norway

Correspondence: Inger Helene Hafsahl Karset (i.h.h.karset@geo.uio.no)

Received: 21 December 2017 – Discussion started: 22 January 2018
Revised: 26 April 2018 – Accepted: 15 May 2018 – Published: 1 June 2018

Abstract. Uncertainties in effective radiative forcings through aerosol–cloud interactions (ERF_{aci}, also called aerosol indirect effects) contribute strongly to the uncertainty in the total preindustrial-to-present-day anthropogenic forcing. Some forcing estimates of the total aerosol indirect effect are so negative that they even offset the greenhouse gas forcing. This study highlights the role of oxidants in modeling of preindustrial-to-present-day aerosol indirect effects. We argue that the aerosol precursor gases should be exposed to oxidants of its era to get a more correct representation of secondary aerosol formation. Our model simulations show that the total aerosol indirect effect changes from -1.32 to $-1.07\,\mathrm{W\,m^{-2}}$ when the precursor gases in the preindustrial simulation are exposed to preindustrial instead of present-day oxidants. This happens because of a brightening of the clouds in the preindustrial simulation, mainly due to large changes in the nitrate radical (NO_3). The weaker oxidative power of the preindustrial atmosphere extends the lifetime of the precursor gases, enabling them to be transported higher up in the atmosphere and towards more remote areas where the susceptibility of the cloud albedo to aerosol changes is high. The oxidation changes also shift the importance of different chemical reactions and produce more condensate, thus increasing the size of the aerosols and making it easier for them to activate as cloud condensation nuclei.

1 Introduction

It is well established that changes in atmospheric aerosol abundance since preindustrial times have had a strong, albeit uncertain, influence on Earth's climate over the last century. Atmospheric aerosols are impacting climate not only by directly absorbing and reflecting radiation but also by indirectly acting as cloud condensation nuclei (CCN) and ice nuclei (IN). Through cloud albedo increases mediated by enhancements of CCN, aerosols brighten the clouds and enhance their cooling effect by increasing the reflection of incoming solar radiation (Twomey, 1977). More numerous cloud droplets may also alter rain formation mechanisms, and thus the cooling effect could be further enhanced by suppressed precipitation followed by increased cloud lifetime, cloud amount and cloud extent (Albrecht, 1989; Pincus and Baker, 1994). The impact of IN changes remains uncertain (Storelvmo, 2017; Lohmann, 2017).

Aerosol indirect effects on Earth's radiation budget are often quantified in terms of their effective radiative forcing (Myhre et al., 2013). Unlike instantaneous radiative forcing, effective radiative forcing includes effects from rapid tropospheric adjustments (Boucher et al., 2013). Otherwise, it does not include any feedbacks in the climate system. Model studies of direct and indirect effects typically carry out two simulations, with aerosols and aerosol precursor gases from preindustrial times (PI) and present day (PD), respectively. The difference in cloud forcing, measured as effective radiative forcing between the two simulations, represents the total aerosol indirect effect if the direct aerosol effect in cloudy skies is negligible (Ghan, 2013). Results from sev-

Published by Copernicus Publications on behalf of the European Geosciences Union.

eral model studies show that this number varies considerably. To what extent aerosol–cloud interactions have contributed to the global radiative forcing in the Anthropocene remains highly uncertain and continues to be a research topic of much interest. Lohmann (2017) shows that model estimates of $\mathrm{ERF_{ari+aci}}$ (ari is aerosol–radiation interactions and aci is aerosol–cloud interactions) vary from -0.07 to $-3.41\,\mathrm{W\,m^{-2}}$, while the Fifth Assessment Report (AR5) from the Intergovernmental Panel on Climate Change (IPCC) gives an expert judgement of $\mathrm{ERF_{ari+aci}}$ of $-0.9\,\mathrm{W\,m^{-2}}$, with a 5 to 95 % uncertainty range of -1.9 to $-0.1\,\mathrm{W\,m^{-2}}$ mostly coming from the uncertainties in the aci component (Boucher et al., 2013). Uncertainties in the natural background emissions have been highlighted as a large contributor to the uncertainty in the indirect effects (Lohmann et al., 2000; Kirkevåg et al., 2008; Hoose et al., 2009; Carslaw et al., 2013), while Gettelman (2015) pointed out that its sensitivity to parameterizations of microphysical processes in global models is even higher. In this study, we examine a third factor, namely the oxidants involved in the formation of aerosols.

Aerosols may enter the atmosphere directly, or they can be formed after in situ oxidation of precursor gases to condensable species (Seinfeld and Pandis, 2016). The oxidation process yields secondary gases with lower saturation vapor pressure, which allows them to either condense on already existing particles or nucleate into new particles under atmospheric conditions. Both processes depend on the amount of emitted precursor gases, as well as on the atmospheric oxidation capacity. While model studies of PD–PI aerosol indirect effects usually point out that they use different emissions of aerosols and aerosol precursor gases for the two different time periods, the choice of oxidant levels is usually not specified (Lohmann and Diehl, 2006; Menon and Rotstayn, 2006; Hoose et al., 2008; Storelvmo et al., 2008; Lohmann, 2008; Lohmann and Ferrachat, 2010; Wang et al., 2011; Yun and Penner, 2013; Neubauer et al., 2014; Gettelman, 2015; Gettelman et al., 2015; Tonttila et al., 2015; Sant et al., 2015). A notable exception is Salzmann et al. (2010), who use different oxidant levels for the different eras. Personal communication with scientists from different modeling groups confirms that it is common to use PD oxidants for both PD and PI simulations (U. Lohmann, C. Hoose, A. Kirkevåg, A. Gettelman, and D. Neubauer, personal communication, 2017).

Human activity has influenced the oxidant level mainly through increased emissions of CO, NO_x and $\mathrm{CH_4}$ from fossil fuel combustion, biomass burning and the use of fertilizers in agriculture (Crutzen and Lelieveld, 2001). Due to this anthropogenic activity, precursor gases emitted into the PI atmosphere were exposed to a different oxidant level than the gases emitted today, implying a difference in the rate and distribution of new particle formation in the atmosphere. The aim of this study is to quantify this difference and to give a more realistic estimate of the total PD–PI aerosol indirect effect by letting the precursor gases in the PI simulation (the simulation with emissions of aerosols and aerosol precursor gases from PI) be exposed to an oxidant level that is representative for its era.

Due to counteracting effects, the sign and magnitude of the global mean historical oxidant change is uncertain (Naik et al., 2013a, b; Murray et al., 2014). While in a low NO_x regime CO and $\mathrm{CH_4}$ act as sinks for the hydroxyl radical (OH), one of the most important oxidants in the troposphere, the opposite is the case in a high NO_x regime (Collins et al., 2002). As a consequence, OH has experienced an increase in polluted areas where the NO_x level is high, while it has decreased in remote areas where the NO_x level is low and the $\mathrm{CH_4}$ level is high due to their different lifetimes (Wang and Jacob, 1998; Prinn, 2003). The situation is different for ozone ($\mathrm{O_3}$), where an increase in NO_x, CO or $\mathrm{CH_4}$ usually favors $\mathrm{O_3}$ production in both low and high NO_x regimes (Seinfeld, 1989; Chameides et al., 1992). This also holds for the $\mathrm{NO_3}$ radical, which is produced through reactions between NO_x and $\mathrm{O_3}$ (Wayne et al., 1991) and probably was present at lower levels everywhere in preindustrial times.

Difficulties in measuring the oxidants directly from the atmosphere and the lack of information about oxidants in sediments and ice cores have resulted in limited information about the atmospheric oxidant level (Pavelin et al., 1999). This is especially the case for the time period before the industrial era, where it is limited to simple measurements of surface ozone from a few European stations (Volz and Kley, 1988). Despite this limitation, results from model simulations based on information about emission changes, in combination with the few oxidant measurements that exist, give an indication of how the oxidative power of the atmosphere has changed since preindustrial time (Prinn, 2003; Berntsen et al., 1997; Wang and Jacob, 1998; Tsigaridis et al., 2006; Naik et al., 2013a, b; Young et al., 2013; Murray et al., 2014; Khan et al., 2015).

When trying to get a better understanding of the response of clouds to aerosol perturbations, or when comparing this effect between models, the choice of oxidant level may not be important as long as there is consistency between the different models. However, the oxidant level may be important when the modeled preindustrial-to-present-day total aerosol indirect effect is used as an estimate of the contribution from aerosol–cloud interactions to the total forcing of climate change since PI, as was done in IPCC AR5. Recent global model estimates of the aerosol indirect effects do, to a larger extent than before, represent more of the gas-to-aerosol formation processes through oxidation followed by nucleation (Boucher et al., 2013; Lohmann, 2017), increasing the importance of understanding the effects and the model treatment of the oxidants. More and more models will also incorporate an interactive atmospheric gas-phase chemistry in transient climate studies, making the characterization of effective radiative forcing a larger challenge. With this study we aim to use model simulations to investigate the impact on aerosol indirect effects from historical oxidants changes by letting the aerosol precursor gases in the PI simulation be exposed to PI instead of PD oxidant level.

Information about the model and the configurations applied in this study is found in Sect. 2. The experimental setup for the default model configuration and the experimental setups where the impact of separate oxidant changes is found in Sect. 3. In Sect. 4, the results are presented and discussed, divided into subsections focusing on the effect of the oxidant changes on the aerosol number concentration (Sect. 4.1.1), on the cloud droplet number concentration (Sect. 4.1.2) and on the aerosol indirect effect (Sect. 4.1.3). The results and discussions of the sensitivity tests where the oxidant changes were separated are found in Sect. 4.2, while six other sensitivity tests are studied in Sect. 4.3.

2 Model

2.1 General description

The model used in this study is CAM5.3-Oslo (Kirkevåg et al., 2018), which is an updated version of the atmospheric component of the Norwegian Earth System Model (NorESM) (Bentsen et al., 2013; Iversen et al., 2013; Kirkevåg et al., 2013). CAM5.3-Oslo is based on the Community Atmospheric Model version 5.3 (Neale et al., 2012; Liu et al., 2016), but has its own aerosol module (OsloAero). It also includes other modifications, such as the implementation of heterogeneous ice nucleation (Wang et al., 2014; Hoose et al., 2010). OsloAero has 21 aerosol tracers, distributed among six species (sulfate – SO_4, secondary organic aerosol – SOA, black carbon, organic matter, mineral dust and sea salt), four precursor gases (SO_2, dimethyl sulfide – DMS, isoprene and monoterpene), three condensable gases (sulfuric acid – H_2SO_4, SOA_{LV} and SOA_{SV}) and H_2O_2. DMS emissions are wind-driven and based on Nightingale et al. (2000); emissions of SO_2 are interpolated from a prescribed monthly mean decadal climatology given by Lamarque et al. (2010). The emissions of SO_2 in CAM5.3-Oslo deviate from Lamarque et al. (2010) when it comes to aircraft emissions and volcanic emissions; the former is not included in CAM5.3-Oslo and the latter is included in the model but not in Lamarque et al. (2010). The emissions of the biogenic volatile organic compounds (BVOCs) isoprene and monoterpene are calculated online every time step of half an hour by a satellite phenology version of the Community Land Model version CLM4.5 (Oleson et al., 2013), using the Model of Emissions of Gases and Aerosols from Nature version 2.1 (MEGAN2.1) (Guenther et al., 2012), where the emissions are impacted by both radiation and temperature, inducing a diurnal variation. An overview of global emissions and burdens of the precursor gases in CAM5.3-Oslo is found in Table 1. The aerosol nucleation is based on Makkonen et al. (2014), with improvements described in Kirkevåg et al. (2018). This nucleation scheme is divided into two parts, where the binary homogeneous sulfuric acid–water nucleation based on Vehkamäki et al. (2002) can act in the whole atmosphere, while the activation type nucleation of H_2SO_4 and organic vapor based on Eq. (19) in Paasonen et al. (2010) occurs only in the boundary layer. The survival rate of particles with diameter from 2 to 23.6 nm (where the upper limit corresponds to the smallest-sized particles that are accounted for in the aerosol number concentration in the model) follows Lehtinen et al. (2007). The stratiform clouds are described by the two-moment bulk microphysics scheme MG1.5, which is almost identical to MG1 described in Morrison and Gettelman (2008), but with cloud droplet activation moved before the cloud microphysical process rate calculations (Gettelman, 2015; Gettelman and Morrison, 2015).

Table 1. Overview of global emission rates and burdens of the precursor gases in CAM5.3-Oslo. The values come from three different simulations using aerosols and oxidants from present day, aerosols from preindustrial and oxidants from present day (in round brackets) and aerosols and oxidants from preindustrial (in curly brackets).

Species	Emission rates ($Tg\,yr^{-1}$)	Burdens (Tg)
SO_2	130 (29.0) {29.0}	0.705 (0.319) {0.380}
DMS	66.3 (66.2) {66.2}	0.276 (0.274) {0.417}
Isoprene	406 (418) {417}	0.148 (0.150) {0.287}
Monoterpene	114 (116) {116}	0.0358 (0.0341) {0.0697}

Methods by Ghan (2013) are used for calculating the effective radiative forcing of aerosols. The part called “cloud radiative forcing”, or ΔC_{clean}, is often used as a measure of the total aerosol indirect effect, where it represents the difference in the top of the atmosphere total cloud forcing between simulations performed with different aerosols. The “clean” subscript indicates that the cloud forcing is based on separate calls to the radiation code where the scattering and absorption of radiation by the aerosols in the air around the cloud is neglected. ΔC_{clean} also includes semi-direct effects, but additional simulations with CAM5.3-Oslo with non-absorptive aerosols have shown that this term is negligible compared to the indirect effects in the model global mean PD–PI values (Kirkevåg et al., 2018). Henceforth we use ΔC_{clean} as a measure of the total aerosol indirect effect in this study.

Table 2. Chemical reactions with corresponding rate coefficients. For Reaction (R1), $fc = 3 \times 10^{-31} \cdot \left(\frac{300}{T}\right)^{3.3}$, and $ko = \frac{fc \cdot M}{1 + (fc \cdot M \cdot 1.5 \times 10^{12})}$, where M is the number concentration of all molecules that can act as a third body (cm^{-3}). If the model does not trace an end product of a chemical reaction, the product is lost in the model and not written down in this table, explaining why the stoichiometry is not exact in all of the reactions.

Reaction number	Reaction	Rate coefficient (cm^3 molecule^{-1} s^{-1})
(R1)	$SO_2 + OH + M \rightarrow H_2SO_4 + M$	$ko \cdot 0.6^{\left(1+\left(\log_{10}(fc \cdot M \cdot 1.5\times10^{12})\right)^2\right)^{-1}}$
(R2)	$DMS + OH \rightarrow SO_2$	$9.6 \times 10^{-12} \cdot e^{-234/T}$
(R3)	$DMS + OH \rightarrow 0.75 \cdot SO_2 + 0.5 \cdot HO_2 + 0.029 \cdot SOA_{LV} + 0.114 \cdot SOA_{SV}$	$\frac{(1.7\times10^{-42} \cdot e^{7810/T}[O_2])}{(1+5.5\times10^{-31} e^{7460/T}[O_2])}$
(R4)	$DMS + NO_3 \rightarrow SO_2 + HNO_3$	$1.9 \times 10^{-13} \cdot e^{-520/T}$
(R5)	monoterpene $+ OH \rightarrow 0.15 \cdot SOA_{SV}$	$1.2 \times 10^{-11} \cdot e^{-440/T}$
(R6)	monoterpene $+ O_3 \rightarrow 0.15 \cdot SOA_{LV}$	$8.05 \times 10^{-16} \cdot e^{-640/T}$
(R7)	monoterpene $+ NO_3 \rightarrow 0.15 \cdot SOA_{SV}$	$1.2 \times 10^{-12} \cdot e^{-490/T}$
(R8)	isoprene $+ OH \rightarrow 0.05 \cdot SOA_{SV}$	$2.7 \times 10^{-11} \cdot e^{-390/T}$
(R9)	isoprene $+ O_3 \rightarrow 0.05 \cdot SOA_{SV}$	$1.03 \times 10^{-14} \cdot e^{-1995/T}$
(R10)	isoprene $+ NO_3 \rightarrow 0.05 \cdot SOA_{SV}$	$3.15 \times 10^{-12} \cdot e^{-450/T}$
(R11)	$HO_2,+ HO_2 \rightarrow H_2O_2$	$(3.5 \times 10^{-13} \cdot e^{430/T} + 1.7 \times 10^{-33} \cdot e^{1000/T}) \cdot (1 + 1.4 \times 10^{-21} \cdot [H_2O] \cdot e^{2200/T})$
(R12)	$H_2O_2 + OH \rightarrow H_2O_2 + HO_2$	$2.9 \times 10^{-12} \cdot e^{-160/T}$
(R13)	$H_2O_2 + h\nu \rightarrow 2 \cdot OH$	

2.2 Oxidant chemistry

CAM5.3-Oslo includes simple chemistry for sulfur and SOA species, which makes use of the chemical preprocessor MOZART (Emmons et al., 2010) modified for the CAM framework (Liu et al., 2012). The preprocessor is a numerical scheme that generates code for the model based on some input chemical reactions and rates. The generated code provides information of how the chemical tracers evolve as a function of concentration of chemical species. Reactions (R1)–(R10) in Table 2 represent the gas-phase oxidation of the precursor gases in the model. Both SOA_{LV} and SOA_{SV} are gaseous SOA (SOA(g)), low volatile and semi-volatile, respectively, where only 50 % of the former can take part in nucleation, while both can condense on already existing aerosols. While Reaction (R2) represents the H abstraction part of the complex reaction where DMS is oxidized by OH, Reaction (R3) represents the OH addition part. At standard conditions (temperature of 273.13 K and pressure of 1013 hPa), the ratio between the reaction rates of Reactions (R2) and (R3) is 7/13 (Reactions R2/R3). Methanesulfonic acid (MSA) is produced in Reaction (R3) following Chin et al. (1996). Since CAM5.3-Oslo does not trace MSA, 20 % of the MSA is put into the SOA_{LV} tracer, while 80 % is put into the SOA_{SV} tracer. The exact yields are unknown, but there are studies supporting that MSA can obtain low enough volatility to contribute to new particle formation and growth (Bork et al., 2014; Willis et al., 2016; Chen and Finlayson-Pitts, 2017). The oxidation of BVOCs in Reaction (R5)–(R10) is based on Makkonen et al. (2014), but with some extensions explained by Kirkevåg et al. (2018). The yield of 15 % for monoterpenes (considered to be α-pinene in this model) is widely used in other global models (Dentener et al., 2006; Tsigaridis et al., 2014). The yield for isoprene varies more between different laboratory and model-based studies (0.9–12 %) (Lee et al., 2006; Kroll et al., 2005; Spracklen et al., 2011; Jokinen et al., 2015), where the yield applied in CAM5.3-Oslo of 5 % is within this range.

The model also includes aqueous-phase oxidation of SO_2 by H_2O_2 and O_3 (Tie et al., 2001; Neale et al., 2012). H_2O_2 production and loss are calculated online through Reactions (R11)–(R13) in Table 2.

The concentrations of the other oxidants (NO_3, O_3, OH and HO_2) are prescribed by monthly mean values produced by the global full chemistry model CAM-chem v3.5 in the study of Lamarque et al. (2010). PD and PI values used in this study are taken from decadal climatologies around year 2000 and 1855, respectively, and the percent change in the annual mean values can be seen in Fig. 1. NO_3 experiences a very large change between PI and PD (up to more than 1000 % in the Northern Hemisphere), which is also seen in other model studies that show good agreement between modeled present-day concentrations of NO_3 and observations (Khan et al., 2015). The prescribed PI values of surface layer O_3 in the region around Paris used in this study are around a factor of 2 higher than the measured PI values at a station near Paris in the study of Volz and Kley (1988) (∼ 10 ppb). This overestimation of the PI level of O_3 compared to observations

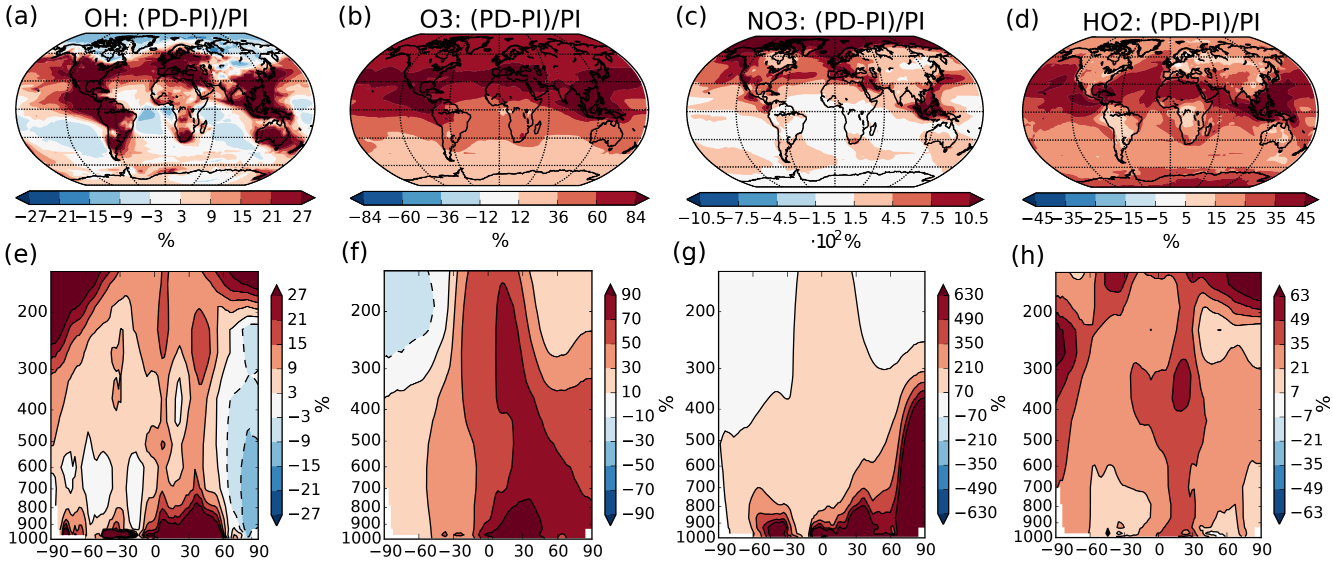

Figure 1. Percent-wise change in the annual mean oxidant mixing ratio (mol mol^{-1}) between PI and PD in the dataset from Lamarque et al. (2010) used in this study. **(a)–(d)** Mean change from surface and up to 550 hPa. **(e)–(h)** Zonal mean change. Please note the different scales on the color bars.

corresponds with findings from other studies (Parrish et al., 2014). Evaluation of present-day concentrations of OH in a comparable version of CAM-chem shows reasonable agreement with the Spivakovsky et al. (2000) climatology (Lamarque et al., 2012). Simulated tropospheric concentrations of O_3 also agree well with ozone sondes, except for an overestimation over eastern USA and Europe (Lamarque et al., 2012; Brown-Steiner et al., 2018).

CAM5.3-Oslo applies a daily cycle to OH and HO_2, which is not included in CAM5.3. One should also be aware that the ozone climatology used for the radiation in the model is different from the ozone climatology used for the chemistry (the ozone climatology for radiation is the same in the PI and PD simulations).

2.3 Configurations

The model was configured with a horizontal resolution of 0.9° (latitude) by 1.25° (longitude) and 30 hybrid levels between the surface and ~3 hPa. The simulations were carried out using nudged meteorology produced by the model itself to constrain the natural variability (Kooperman et al., 2012). The horizontal wind components (U, V) were nudged with a relaxation timescale of 6 h, while the temperature was freely evolving, allowing impacts by aerosol perturbations, which could be important when calculating indirect effects (Zhang et al., 2014). Prescribed climatological sea surface temperatures and sea ice extent from the mean of 1982–2001 were used in all simulations, as well as greenhouse gas concentrations and land use information from the year 2000.

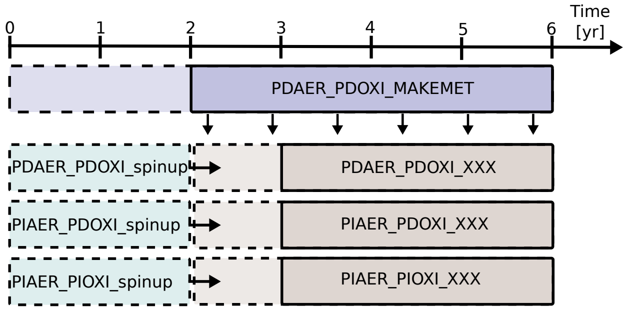

Figure 2. Overview of how the simulations were carried out. PDAER_PDOXI_MAKEMET produced meteorology for the other simulations from its last 4 years. Dashed lines show the part of the simulations used as spin-up. Horizontal arrows show that the simulations to the right of the arrow restarted from the already spun up simulation to the left. The spin-up cases were not nudged, but started with free-running meteorology from the same state as PDAER_PDOXI_MAKEMET. XXX refers to either ORG (original model setup), or the name of the sensitivity tests described in Sects. 3.2 and 4.3.

3 Experimental setup

3.1 General

Figure 2 describes how the simulations were carried out. The model was first run for 6 years to generate instantaneous meteorological data using PD conditions for emissions, prescribed oxidant and all other boundary conditions. All other simulations were nudged to the meteorology of this simulation. For each modification to the default model setup, three

Table 3. Overview of the prescribed precursor and aerosol emissions and prescribed oxidant concentrations used in the three different simulations that were carried out for each modification to the default model setup.

Name of simulations	Prescribed emissions of aerosols and precursor gases	Prescribed concentrations of oxidants	SSTs, sea ice extent, greenhouse gases and land use
PDAER_PDOXI_XXX	PD	PD	PD
PIAER_PDOXI_XXX	PI	PD	PD
PIAER_PIOXI_XXX	PI	PI	PD

different simulations were carried out. These three simulations used the prescribed precursor and aerosol emissions and oxidant concentrations given in Table 3. Each of them was restarted from an earlier simulation that was already spun up for 2 years with free meteorology, applying emissions and oxidants from the same era. The nudged simulations were then run for 4 years, and the last 3 years were analyzed. Sensitivity tests with CAM5.3-Oslo (not shown here) show that analyzing only these 3 years gives a standard error due to natural variability of only 0.01 $\mathrm{W\,m^{-2}}$ for the total aerosol indirect effect and a magnitude of the total aerosol indirect effect that is the same as when running the nudged simulations for 11 years and analyzing the last 10 years. To lower the computational cost, the simulations in this study apply the setup described above, except for one sensitivity test in Sect. 4.3 where longer simulations with free meteorology are examined. The first set of simulations used CAM5.3-Oslo as described in the previous section, without any other modifications to the code. We name these simulations ORG, and the impact of historical oxidant changes on the PD–PI total aerosol indirect effect in CAM5.3-Oslo are quantified by the difference we obtain (relative to the PD simulation PDAER_PDOXI_ORG) when switching between the two PI simulations PIAER_PDOXI_ORG and PIAER_PIOXI_ORG.

3.2 Decomposing the oxidant change

To estimate the importance of the different changes in the individual oxidants between PI and PD, four additional simulations with PI aerosols were carried out. In these simulations, the oxidant of interest was changed to PI concentrations, while all other oxidants were kept at PD levels. Acknowledging the complexity of oxidant chemistry, one cannot expect that separate oxidant changes in separate simulations will add up to the same result as changing them all simultaneously. To explore the importance of this nonlinearity, another four additional simulations were performed, keeping all oxidants from PI except the one of interest, which was set to PD levels.

4 Results and discussion

4.1 Original setup

The top panels of Fig. 3 show the PD–PI indirect effect for (a) shortwave radiation, (b) longwave radiation and (c) total radiation when using the standard setup with PD oxidants in both simulations. The bottom panels of Fig. 3 show the impact of historical oxidant changes on the PD–PI indirect effect. Figure 3d shows that letting the precursor gases in the PI simulation be exposed to oxidants from its era, instead of oxidants from PD, makes the shortwave indirect effect 0.39 $\mathrm{W\,m^{-2}}$ less negative (changing from -1.48 to $-1.09\,\mathrm{W\,m^{-2}}$). This implies that the clouds in the PI simulation with PI oxidants are cooling the climate more through shortwave (SW) effects than the clouds in the PI simulation with PD oxidants, reducing the difference in shortwave cloud forcing between PI and PD. Figure 3e shows that the change in longwave indirect effect is $-0.14\,\mathrm{W\,m^{-2}}$ (from 0.16 to 0.02 $\mathrm{W\,m^{-2}}$), meaning that the clouds in the PI simulation with PI oxidants are warming the climate more through increased absorption of longwave radiation, reducing the difference in longwave cloud forcing between PI and PD. Figure 3f shows a total (shortwave + longwave) change in the indirect effects of $+0.25\,\mathrm{W\,m^{-2}}$ (changing from -1.32 to $-1.07\,\mathrm{W\,m^{-2}}$), meaning that the PI clouds with PI oxidants are cooling the climate more than the PI clouds with PD oxidants, thus making the indirect effect less negative. The largest changes in the shortwave indirect effect occur over ocean, especially over the North Pacific, off the west coast of America, in remote areas between 30 and 60° S and over the Indian Ocean. The changes in the longwave indirect effect mainly take place in the polar regions and over the Indian Ocean.

Different cloud and aerosol changes can help explain the resulting change in the indirect effect. Some of these are presented in Fig. 4. In the global mean, switching to PI oxidants in the PI simulation results in (a) more numerous aerosol particles (+9.2 %), (b) more numerous cloud droplets (CDNC) (+3.7 %), (c) smaller cloud droplets (−1.5 %), (d) larger cloud fraction (+0.26 %), which is mainly caused by changes in the low cloud fraction, and (e) larger total grid box aver-

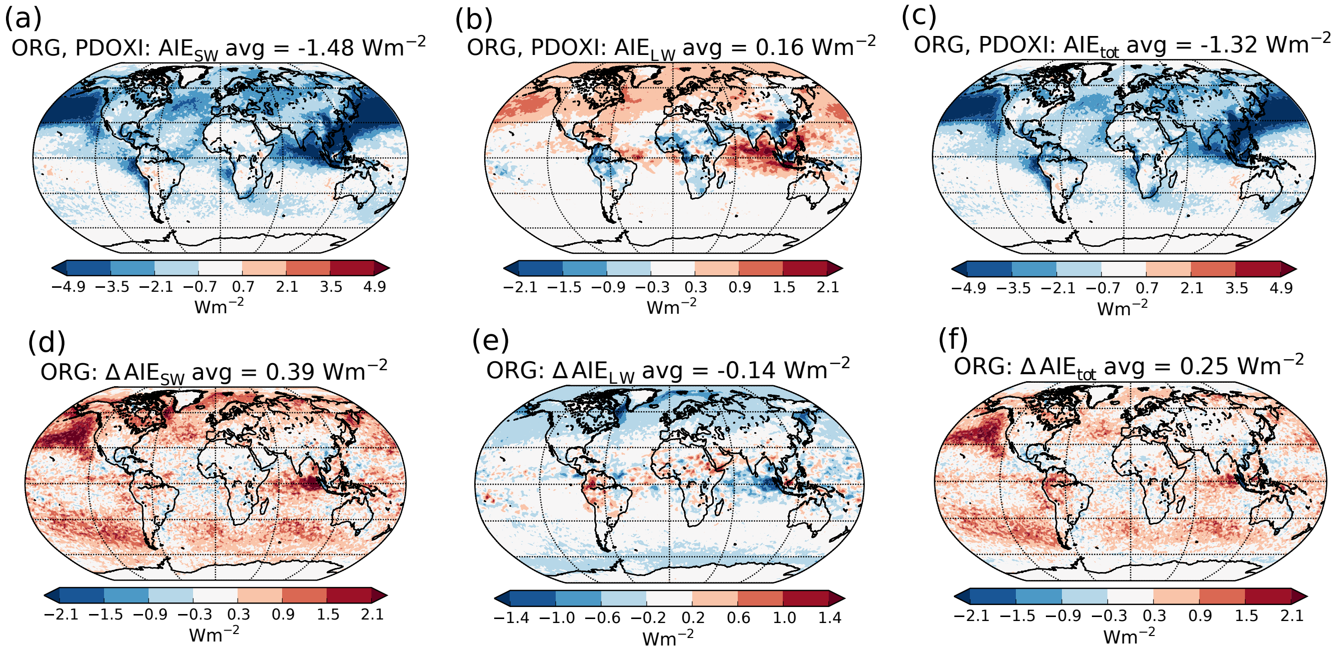

Figure 3. **(a)**–**(c)** PD–PI aerosol indirect effect when using the standard setup with PD oxidants in both simulations: **(a)** shortwave, **(b)** longwave and **(c)** total. **(d)**–**(f)** Differences in the PD–PI indirect effect between simulations performed with PI and PD oxidants in the PI simulation.

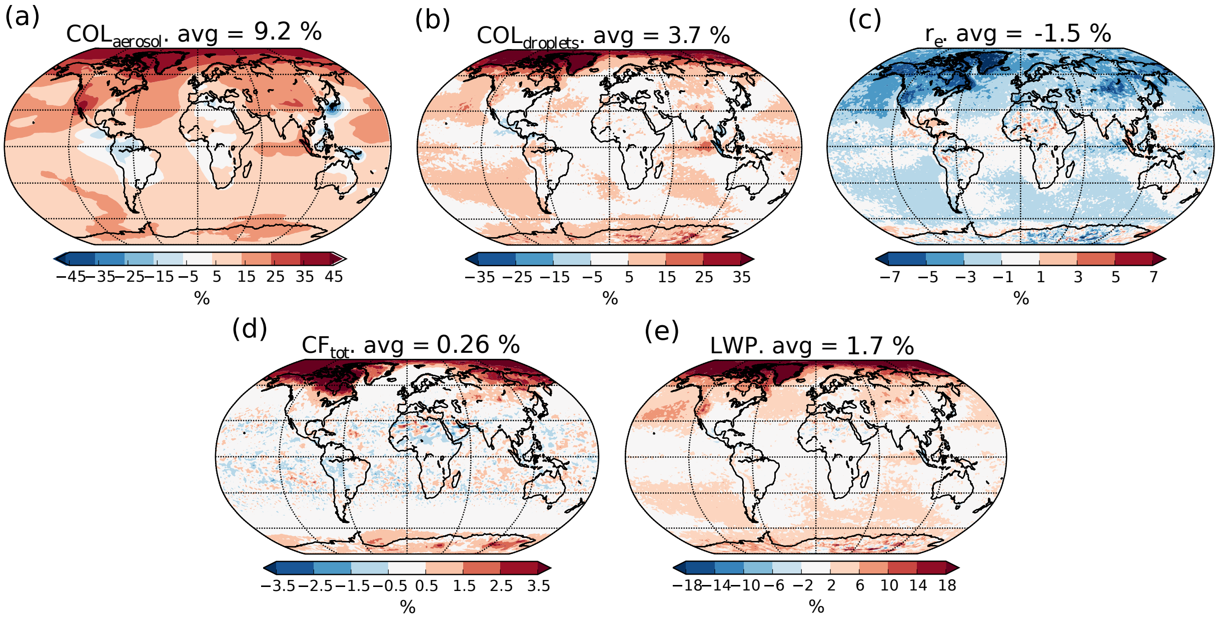

Figure 4. Relative change in aerosol and cloud properties in the PI simulation when switching from PD to PI oxidants. **(a)** Column number of aerosols, **(b)** column number of cloud droplets, **(c)** effective radius of cloud droplets in the cloud top layer, **(d)** total cloud fraction and **(e)** total grid box averaged liquid water path.

aged liquid water path (LWP) (+1.7 %). The size of the cloud droplets in Fig. 4c is taken from the cloud top layer of the stratiform clouds.

The sign of the changes in the global mean cloud and radiative properties seen in Figs. 3 and 4 is as expected for an increase in the global mean aerosol number concentration. We will now further investigate why the oxidant changes enhance the aerosol number concentration. Figures 3 and 4 show that the distribution of the changes in aerosol number concentration does not always correspond directly to the dis-

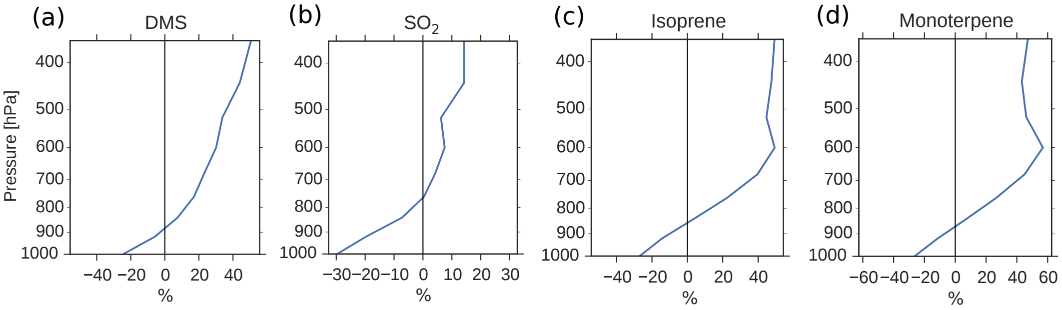

Figure 5. Global mean relative change in chemical loss of **(a)** DMS, **(b)** SO_2, **(c)** isoprene and **(d)** monoterpene when switching from PD to PI oxidants in the PI simulation.

tribution of the changes in the cloud and radiative properties. This indicates that it is not only the change in aerosol number concentration that is important for the result but also changes in the composition of the aerosols and in the atmospheric conditions where the aerosol changes take place.

4.1.1 The increase in aerosol number concentration

Since the formation of new aerosols depends on the availability of low-volatility gases, and the PI atmosphere consisted of relatively small amounts of oxidants to produce secondary gases with reduced volatility, one could expect a reduction in the aerosol number concentration when switching from PD to PI oxidants. This is the opposite of what Fig. 4a shows. The increased lifetime of the precursor gases and the aerosols seen in Table 4 partly explains this. When the oxidizing power of the atmosphere is reduced, the precursor gases with high volatility are transported higher up in the atmosphere before they are oxidized. This is seen in Fig. 5, where the relative change in chemical loss of (a) DMS, (b) SO_2, (c) isoprene and (d) monoterpene through oxidation is negative close to the surface, but positive higher up in the atmosphere when switching from PD to PI oxidants in the PI simulation. This pattern corresponds well with the change in the vertical profile of the aerosol number concentration seen in Fig. 9a, with lower values close to the surface, but larger values above ~ 900 hPa. Aerosols formed from gases higher up in the atmosphere are not removed by deposition as easily as aerosols formed closer to the surface (Jaenicke, 1980; Williams et al., 2002). This is seen in the results of this study where the dry deposition of the newly formed nucleation mode SO_4 and SOA decreases by 2.6 %. The wet deposition stays the same. This total decrease in deposition is one of the factors contributing to the increase in the aerosol number concentration seen in Fig. 4a.

It is not only the vertical transport of the gases that changes. The reduced oxidation capacity also increases the horizontal transport of the primary precursors away from the source regions. This is seen, for example, in Fig. 6 for DMS, the main precursor gas over ocean, where most of the aerosol, cloud and radiation changes occur. Figure 6a shows the distribution of DMS emissions, which is equal in all PI simulations, while Fig. 6b shows the change in the chemical loss of DMS through oxidation when switching from PD to PI oxidants. Increased horizontal transport happens from areas with negative values to areas with positive values, since chemical loss through oxidation is the only way DMS can be lost in the model. The increase is especially pronounced in the North Pacific, with increased transport further south and towards the Arctic, but is also found in the Southern Ocean with increased transport from the large emission sources close to the coast towards the remote ocean. Figure 6c shows that this transport results in increased aerosol formation close to the surface in areas that receive more DMS with PI oxidants. Since the precursor gases are spread more in space with PI oxidants, towards more remote areas where the background concentration of aerosols are low, the coagulation sink during the nucleation process is reduced, contributing to an increase in the formation rate. In CAM5.3-Oslo, "formation rate" describes the formation of aerosol particles with diameters of 23.6 nm, which is the size limit a particle must achieve to be accounted for in the aerosol number concentration (Figs. 4a and 6e). "Nucleation rate" describes the formation of aerosol

Table 4. Global mean lifetime of different gaseous and aerosol species (g: gas; a: aerosol) when applying PD and PI oxidants in the PI simulation. The lifetime is calculated as (global mean burden) / (global mean loss).

Species	Lifetime, PD (h)	Lifetime, PI (h)	Change in lifetime (%)
SO_2 (g)	29	34	+17
DMS (g)	36	55	+53
Isoprene (g)	3.2	6.0	+88
Monoterpene (g)	2.6	5.3	+104
H_2SO_4 (g)	0.91	1.0	+9.9
SOA_{LV} (g)	0.65	0.82	+26
SOA_{SV} (g)	0.75	1.0	+9.9
SO_4 (a)	78	84	+7.7
SOA (a)	115	116	+0.9

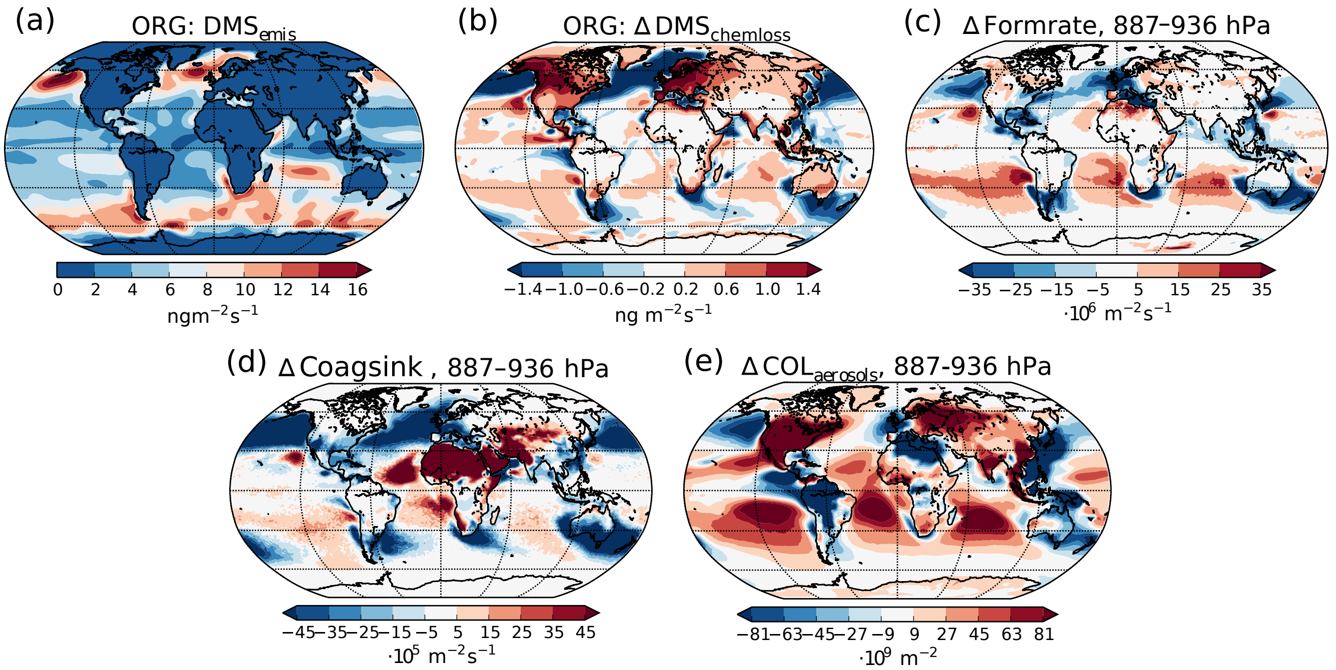

Figure 6. **(a)** Emission rate of DMS (same for both PI simulations). **(b)** Difference in net chemical loss of DMS though oxidation. **(c)** Difference in aerosol formation rate in the 887–936 hPa layer. **(d)** Difference in the coagulation sink during nucleation in the 887–936 hPa layer. **(e)** Difference in column burden of aerosols in the 887–936 hPa layer. All differences show values from the PI simulation using PI oxidants minus values from the PI simulation using PD oxidants.

particles with diameters of 2 nm. As for all aerosols, the particles between 2 and 23.6 nm can be lost through coagulation with background aerosols. Figure 6d shows how the coagulation sink of these particles changes when switching from PD to PI oxidants in the PI simulation. The reduction in the coagulation sink is especially large close to the strong DMS emissions sources (Fig. 6d). The areas over ocean with increased formation rate close to the surface correspond well with the areas in Fig. 6e with increased aerosol number concentrations, indicating that the horizontal transport of DMS due to its longer lifetime in an atmosphere with PI oxidants is important for the increase in aerosol number concentration. Higher up in the atmosphere (above ∼ 850 hPa), the formation rate of aerosols also increases over the emission sources and at higher latitudes (not shown). The change in the total vertically integrated coagulation sink decreases by 17.7 % when switching from PD to PI oxidants in the PI simulation, favoring enhanced formation of new aerosols. As the lifetime of the precursor gases and the cloud amount increases, the total deposition rate of SO_2 increases with 7.4 % (DMS, isoprene and monoterpene are only lost through atmospheric chemistry), favoring a decrease in the formation of new aerosols. As a result of all the competing effects, the total vertically integrated formation of new aerosols increases by 5.4 %.

Some of the newly formed SO_4 and SOA are lost through coagulation with the background aerosols. This coagulation sink is also reduced (−3.6 %) when switching from PD to PI oxidants for the same reasons as for the particles between 2 and 23.6 nm, contributing to the change in the aerosol number concentration seen in Fig. 4a.

Even though Fig. 6 shows that the increased lifetime of the precursor gases partly can explain why the aerosol number concentration increases when switching from PD to PI oxidants, other factors could also play a role. The precursor gases have the potential of being oxidized in three different ways, resulting in different amounts of the end products H_2SO_4, SOA_{LV} and SOA_{SV}. While both H_2SO_4 and SOA_{LV} can take part in nucleation (to nucleation mode SO_4 and nucleation mode SOA, respectively), SOA_{SV} can only condense onto already existing particles. If changes in the oxidation pathways favor more production of H_2SO_4 or SOA_{LV}, it can contribute to the increase in the aerosol number concentration seen in Fig. 4a. The left panels of Fig. 7 show the contribution of the different reactions to the oxidation of the precursor gases. The largest change in the oxidant level when switching from PD to PI oxidants is found for NO_3 in the Northern Hemisphere (Fig. 1c). When switching to PI oxidants, the relative fraction of DMS, isoprene and monoterpene oxidized by NO_3 is reduced (Fig. 7a, c, d, red curves), while the oxidation involving the other oxidants become more important. For DMS, Fig. 7a shows that this change in the oxidation pathway will reduce the formation of species that can take part in nucleation since some of it will

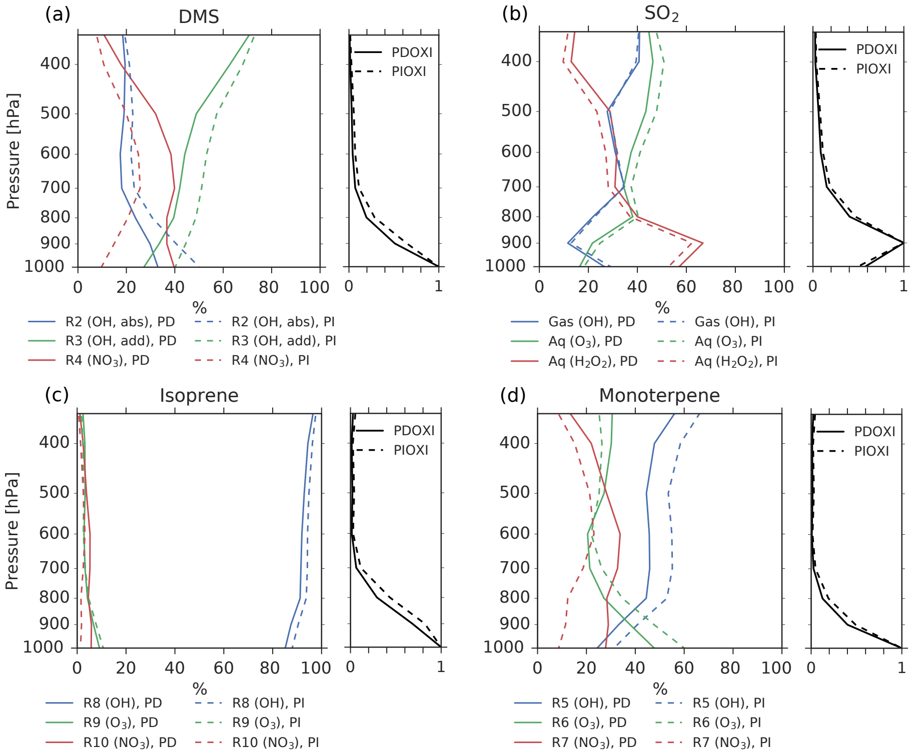

Figure 7. The left panel of each figure shows the importance of different oxidant reactions at different levels for **(a)** DMS, **(b)** SO_2, **(c)** isoprene and **(d)** monoterpene. Solid lines: PD-oxidants, dashed lines: PI-oxidants. The curves indicate the percentage of the total oxidation for each specie that occurs through the specified reactions at a specific height. The sum of the three reactions at each level is equal to 100 % in all cases. The right panel of each figure shows how much of the specie is oxidized at each level relative to the level of maximum oxidation.

be converted to SOA_{SV} instead of SO_2 (that later becomes H_2SO_4). For monoterpene, switching to PI oxidants favors an oxidation pathway that gives more SOA_{LV} (Fig. 7d), thus favoring an increase in the aerosol number concentration. An overview of all the conversion rates for the oxidation reactions in the two simulations with different oxidants is found in Table 5. Even though the global burden of nucleation mode SO_4 aerosols increases (+0.00650 Tg, +8.8 %), Table 5 shows that the production of H_2SO_4 decreases when switching from PD to PI oxidants ($-0.5\,\mathrm{Tg\,yr^{-1}}$), indicating that a shift towards more production of H_2SO_4 that can nucleate is not an explanation for the increase in the aerosol number concentration seen in Fig. 4a. The global burden of nucleation mode SOA aerosols is also increasing (+0.00450 Tg, +12 %). Contrary to the case of SO_4, Table 5 shows that this could partly be due to a shift towards more production of a gas that can take part in nucleation since the production of SOA_{LV} increases ($+1.63\,\mathrm{Tg\,yr^{-1}}$). Sensitivity tests in Sect. 4.3 will show that this increase in production of SOA_{LV} has a negligible impact on the results in this study.

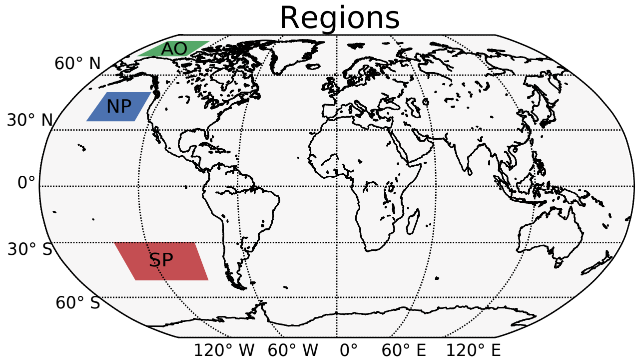

Figure 8. Selected regions with extra focus. AO is the Arctic Ocean (70–82° N, 130–170° W). NP is the North Pacific (35–50° N, 130–160° W). SP is the South Pacific (30–50° S, 90–140° W).

4.1.2 The increase in cloud droplet number concentration

Figure 4b shows that the CDNC increases in regions that experience large relative changes in the aerosol number concentration (Fig. 4a). The aerosol number concentration and CDNC increases are linked to the extended DMS lifetime discussed above (Fig. 6b), which in turn allows for more

Table 5. Conversion rates using present-day (preindustrial) oxidants.

Reaction			Loss (Tg yr^{-1})		Production (Tg yr^{-1})	
(R2)	DMS + OH	[DMS]	24.0 (31.4)	$\rightarrow$	24.7 (32.4)	[SO_2]
(R3)	DMS + OH	[DMS]	20.6 (26.7)	$\xrightarrow{0.75}$	16.0 (20.7)	[SO_2]
				$\xrightarrow{0.029}$	1.62 (2.10)	[SOA_{LV}]
				$\xrightarrow{0.114}$	6.38 (8.26)	[SOA_{SV}]
(R4)	DMS + NO_3	[DMS]	26.3 (10.4)	$\rightarrow$	27.1 (10.7)	[SO_2]
(R5)	monoterpene + OH	[monoterpene]	41.3 (50.6)	$\xrightarrow{0.15}$	7.65 (9.37)	[SOA_{SV}]
(R6)	monoterpene + O_3	[monoterpene]	45.2 (51.4)	$\xrightarrow{0.15}$	8.38 (9.53)	[SOA_{LV}]
(R7)	monoterpene + NO_3	[monoterpene]	32.8 (12.7)	$\xrightarrow{0.15}$	6.09 (2.36)	[SOA_{SV}]
(R8)	isoprene + OH	[isoprene]	376 (376)	$\xrightarrow{0.05}$	46.4 (46.4)	[SOA_{SV}]
(R9)	isoprene + O_3	[isoprene]	26.7 (27.6)	$\xrightarrow{0.05}$	3.30 (3.41)	[SOA_{SV}]
(R10)	isoprene + NO_3	[isoprene]	21.8 (6.72)	$\xrightarrow{0.05}$	2.70 (0.830)	[SOA_{SV}]
(R2)	$SO_2 + OH + M$	[SO_2]	10.4 (10.1)	$\rightarrow$	16.0 (15.5)	[H_2SO_4]
(aq)	$SO_2 + O_3$	[SO_2]	14.6 (14.8)	$\rightarrow$	21.9 (22.3)	[SO_4]
(aq)	$SO_2 + H_2O_2$	[SO_2]	28.4 (22.5)	$\rightarrow$	42.6 (33.7)	[SO_4]
	SO_2 dry deposition	[SO_2]	16.5 (16.5)			
	SO_2 wet deposition	[SO_2]	22.5 (25.4)			

DMS transport to and subsequently increased aerosol formation in remote regions like the South Pacific (SP) and the Arctic Ocean (AO), as defined in Fig. 8. The region named North Pacific (NP) in Fig. 8 experiences a local minimum in the change in the aerosol number concentration. Figure 6 shows that this is caused by less aerosol formation in this region. Nevertheless, NP also experiences a relatively large increase in CDNC. The vertical profiles in Fig. 9 show that the regions which receive more precursor gases with PI oxidants (AO and SP) experience an increase in both aerosol number concentration and CDNC for all altitudes, while the NP region experiences a decrease close to the surface, but an increase higher aloft. The latter can be explained by the vertical shift in the oxidation (Fig. 5). In NP, the height above which the change in CDNC is positive is located lower down in the atmosphere than the height at which the aerosol number concentration starts to increase (Fig. 9i and l). This can be explained by the change in the size of the aerosols (Fig. 9j), caused by the increased aerosol condensate relative to the aerosol number concentration (Fig. 9k). The relative amount of condensate increases in the global mean (Fig. 9c) and in the Northern Hemisphere (Fig. 9g and k) because of the strong shift in the importance of the different oxidation reactions (Fig. 7). This means that for DMS, the dominant precursor gas over the remote oceans, instead of mostly getting $1 \cdot SO_2$ and no SOA from an oxidation of DMS through Reaction (R4), the PI atmosphere will produce to a larger extent $0.75 \cdot SO_2$ and some SOA through Reaction (R3). After SO_2 has been oxidized to H_2SO_4, it nucleates easier than SOA, and 80 % of the SOA from Reaction (R3) comes as SOA_{SV},

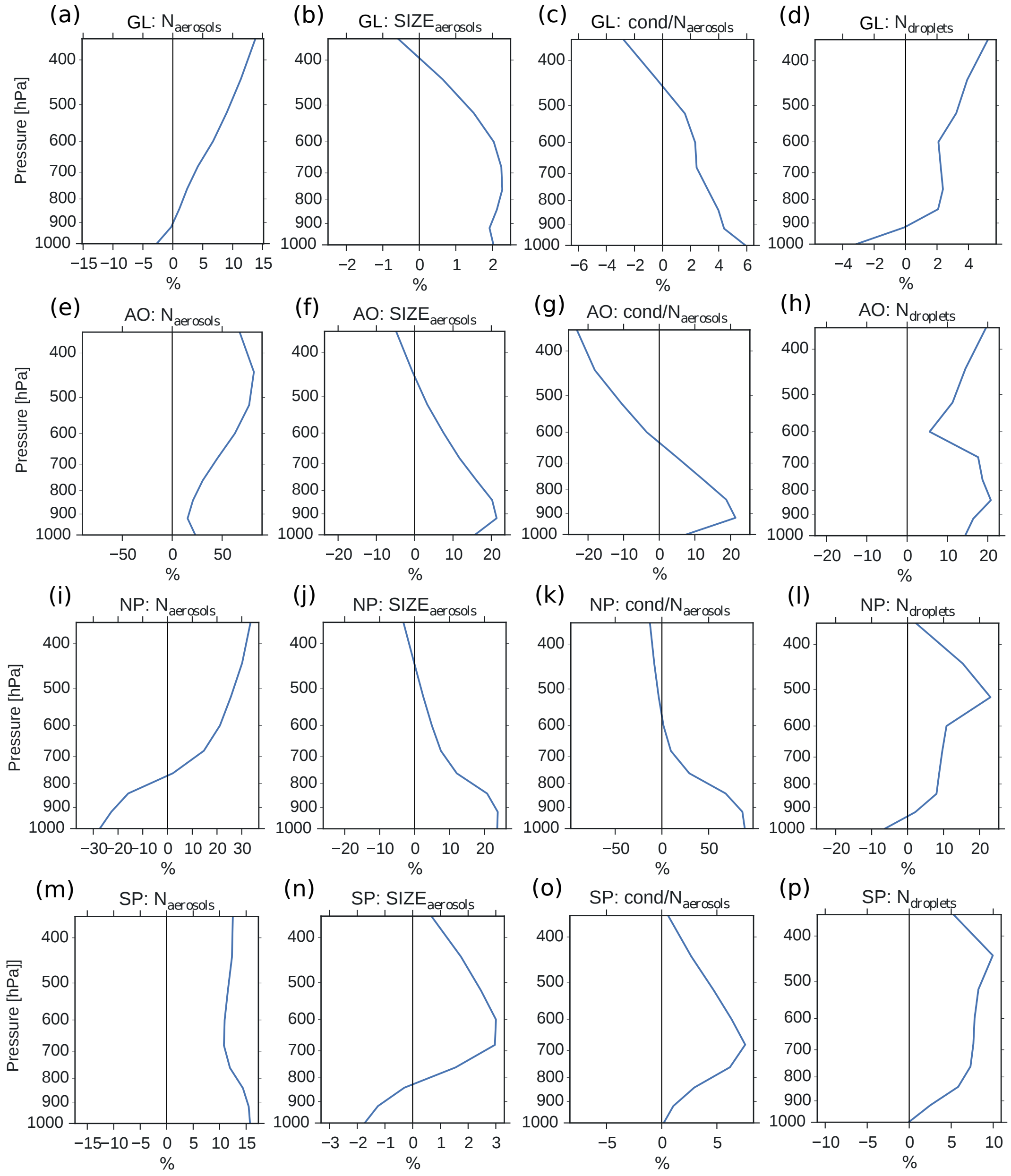

Figure 9. Vertical profiles of annual averaged changes in aerosol number concentration **(a, e, i, m)**, aerosol size **(b, f, j, n)**, aerosol condensate divided by the aerosol number concentration **(c, g, k, o)** and CDNC **(d, h, l, p)** on a global mean (GL) and in the three different regions from Fig. 8 (Arctic Ocean – AO, North Pacific – NP and South Pacific – SP), when switching from PD to PI oxidants in the PI simulation. The mean size of the aerosols in panels **(b, f, j, n)** is calculated as a mean of the number mean radius of all mixtures in the model, weighted by the number of aerosols in each mixture.

which is only allowed to condense. The change in aerosol size in SP (Fig. 9n) deviates from the other regions. This is due to the increase in OH in SP when switching to PI oxidants (blue colors in Fig. 1a), giving rise to enhanced nucleation of small SO_4 aerosols followed by an enhanced H_2SO_4 production through Reaction (R1). This also happens in AO, where the OH level also is larger in PI, but here this effect is small relative to the effect of the increased SOA_{SV} production due to the large NO_3 change in the Northern Hemisphere (Fig. 1c).

4.1.3 The change in aerosol indirect effect

The SW radiative effect of a change in CDNC varies depending on where these changes take place. Twomey (1991) showed that $dA/d(CDNC)$, where A is the cloud albedo, is largest in clean regions with low CDNC and where the

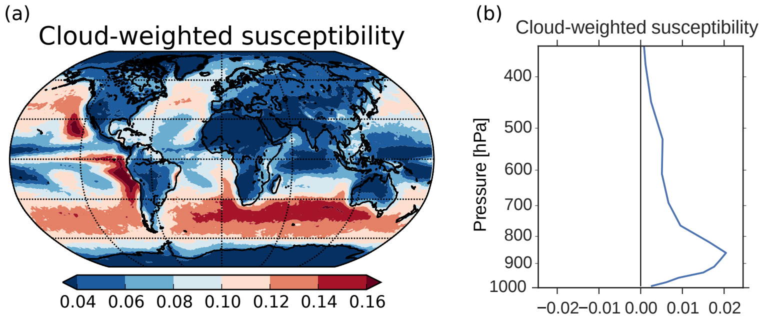

Figure 10. **(a)** Cloud-weighted susceptibility using Eq. (6) in Alterskjær et al. (2012). Cloud droplet size and numbers from the cloud top layer and the total cloud fraction were applied. **(b)** Vertical profile of the global mean cloud-weighted susceptibility.

cloud albedo is approximately 0.5. The SW radiative effect will also be larger in areas with low surface albedo, in areas close to the Equator due to more incoming solar radiation and in areas where the cloud fraction is high. The last two factors, in addition to the factors in Twomey (1991), are taken into account in Eq. (6) in Alterskjær et al. (2012) when finding a cloud-weighted susceptibility function. This is a hybrid of the simplified $dA/d(\mathrm{CDNC})$ of Twomey and the more complex d(ERFaci)/d(CDNC), which we see in Fig. 3. It only includes the first aerosol indirect effect and not secondary aerosol indirect effects (such as increased lifetime, cloud amount and cloud extent). The susceptibility function gives an indication of which areas over ocean that are relatively more susceptible than others to cloud albedo changes caused by changes in CDNC. The cloud-weighted susceptibility function is normalized by its maximum value. Applying this function to 3 years of daily output from the PIAER_PDOXI_ORG simulation in this study results in Fig. 10a. Areas with high cloud-weighted susceptibility are found off the west coast of the continents and in the remote Southern Ocean storm tracks. The large increase in CDNC (Fig. 4b) in the North and South Pacific regions efficiently increases the albedo of the clouds, thus resulting in the large change in the SW indirect effect seen in Fig. 3d. Due to less insolation in the Arctic, the cloud-weighted susceptibility in this region is low, resulting in a negligible effect on the SW indirect effect, even though this is the region that experiences the relatively largest increase in both CDNC (Fig. 4b), cloud fraction (Fig. 4d) and LWP (Fig. 4e) due to the oxidant changes. The longwave (LW) indirect effect is not dependent on the incoming solar radiation, so the large changes in cloud properties seen in the Arctic affect the LW indirect effect. The thicker and longer-lived clouds in the simulation with PI oxidants act to reduce the difference in LW heating between the PD and PI simulations (Fig. 3e). Figure 10b shows the vertical profile of the global mean cloud-weighted susceptibility. It shows that the decrease in CDNC close to the surface (Fig. 9d) does not affect the cloud albedo as much as the increase in CDNC between 900 and 800 hPa.

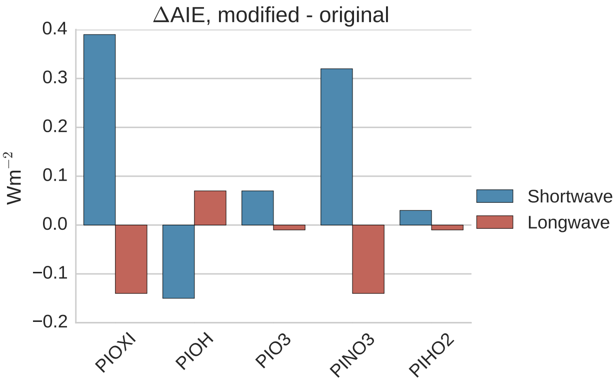

Figure 11. Differences in global mean shortwave and longwave aerosol indirect effect between the setups with modified PI simulations (PIOXI, PIOH, PINO3 and PIHO2) and the original setup.

4.2 Decomposing the oxidant change

To get a better understanding of the results in the original experiment, results from the sensitivity tests where only one oxidant at a time was changed are analyzed. Figure 11 shows differences in the global mean shortwave and longwave indirect effect between the setups with modified PI simulations (PIOXI, PIOH, PIO3, PINO3 and PIHO2) and the original setup with only PD oxidants in both simulations. Figure 12 shows the same for the horizontal distribution. Changing only NO_3 (PINO3) gives almost the same result as changing all of the oxidants (PIOXI), indicating that the historical change in NO_3 is the most important oxidant change for indirect effect calculations. This corresponds well with Fig. 1, which shows that NO_3 is the oxidant that has experienced the largest relative change since PI, and Fig. 7, which shows that the importance of the oxidation reactions involving NO_3 drops the most when switching from PD to PI oxidants in the PI simulation. The negative pattern over land in the tropics in PINO3 that is missing in PIOXI (Fig. 12) seems to be explained by the changes in O_3. Analysis of the PIO3 simulation shows that replacing only the O_3 oxidant with PI values reduces the importance of Reaction (R6) where monoterpene

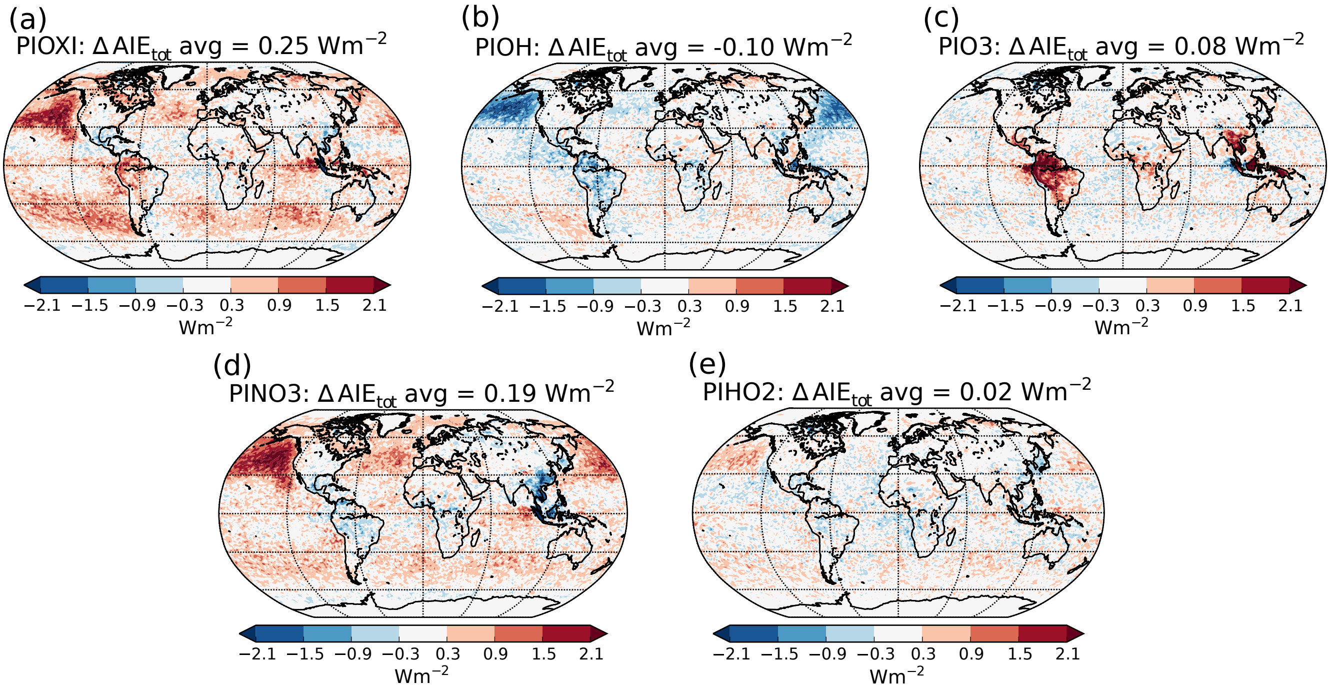

Figure 12. Differences in total aerosol indirect effect between the PI simulation with **(a)** PIOXI, **(b)** PIOH, **(c)** PIO3, **(d)** PINO3, **(e)** PIHO2 and the original PI simulation with only PD oxidants.

Table 6. Difference in global mean SW and LW indirect effects between setups with the modified PI simulation in the second column and the default PI simulation with PD oxidants. The bottom row shows the effect of changing all of the oxidants at the same time (similar to Fig. 3c and d), the other odd numbered rows show the effect of changing one oxidant at the time in the PI simulation, while the even numbered rows show the difference in switching all oxidants (PIOXI) and all but one (PIOXI_PDXXX) in the PI simulation.

Row number	Description of the modified PI simulation	Change in shortwave aerosol indirect effect (W m^{-2})	Change in longwave aerosol indirect effect (W m^{-2})
1	PDOXI_PIOH	−0.15	+0.07
2	PIOXI – PIOXI_PDOH	−0.06	+0.02
3	PDOXI_PIO3	+0.07	−0.01
4	PIOXI – PIOXI_PDO3	+0.12	0.00
5	PDOXI_PINO3	+0.32	−0.14
6	PIOXI – PIOXI_PDNO3	+0.41	−0.11
7	PDOXI_PIHO2	+0.03	−0.01
8	PIOXI – PIOXI_PDHO2	+0.03	+0.01
9	PIOXI	+0.39	−0.14

is oxidized by O_3 giving SOA_{LV}, while the other oxidation reactions of monoterpene giving SOA_{SV} become more important. This results in less new aerosol formation and increased growth of the already existing aerosols through condensation, increasing the CCN concentration and the following cloud droplet activation and CDNC.

Table 6 shows that there are some nonlinearities associated with changing one oxidant at a time. The odd numbered rows show the impact on the indirect effects when changing one oxidant at a time, while the even rows show the difference in the effect of changing all oxidant and changing all except for one oxidant. If there were no nonlinearities involved in the oxidant chemistry, an odd numbered row and the following row would have shown the same numbers. This is not the case, but the differences are relatively small, supporting the indication that the contributions to the total result mainly stem from the historical changes in NO_3.

4.3 Sensitivity tests

Due to nonlinear processes and feedbacks in the model, it is difficult to separate the different effects and to estimate how much each of them contributes to the final result. As an example, enhanced formation of new aerosols can be explained as in Sect. 4.1.1, starting by the increase in lifetime of the precursor gases, but the enhanced importance of reactions giving SOA with sufficiently low volatility to nucleate new aerosols (Reactions R3 and R6) can also be a part of the explanation. To get a better understanding of the importance of the various factors and processes, extra sensitivity tests with six new setups were carried out. All tests consist of three different simulations, as illustrated in Fig. 2. They

Table 7. Information about how the setup for the sensitivity tests deviates from the default original setup. The right column shows how the total aerosol indirect effect changes when switching from PD to PI oxidants in the PI simulation. ΔAIE_{tot} with the default model setup was $+0.25\,W\,m^{-2}$.

Name of simulations	Description of setup	ΔAIE_{tot} ($W\,m^{-2}$)
NOSOALVDMS	None of the SOA produced through Reaction (R3) is allowed to nucleate new particles. Reaction (R3) is thus replaced with $DMS + OH \rightarrow 0.75 \cdot SO_2 + 0.5 \cdot HO_2 + 0.143 \cdot SOA_{SV}$.	$+0.25$
NOSOALVBVOC	None of the SOA produced through Reaction (R6) is allowed to nucleate new particles. Reaction (R6) is thus replaced with monoterpene $+ O_3 \rightarrow 0.15 \cdot SOA_{SV}$.	$+0.26$
NOSOA	No SOA production from DMS oxidation. Reaction (R3) is thus replaced with $DMS + OH \rightarrow 0.75 \cdot SO_2 + 0.5 \cdot HO_2$.	$+0.14$
NACTOFF	No activation from particle mixture number 1 (Kirkevåg et al., 2018). This mixture corresponds to the nucleation mode in modal aerosol schemes, and this is where we find the newly formed SOA and SO_4 aerosols.	-0.03
DIURNALNO3	Add a daily cycle to the concentrations of NO_3 that come from prescribed monthly mean values.	$+0.26$
FREEMET	Apply free meteorology instead of nudged winds.	$+0.3 \pm 0.2$

all deviate from the original setup as well as from Kirkevåg et al. (2018), through either changes in some of the chemical Reactions (R1)–(R10), manipulating the aerosol input to the code for cloud droplet activation, manipulating the code that treats the oxidants or changing the constraint on the meteorology. Information about the setups for the sensitivity tests is found in Table 7.

4.3.1 NOSOALVDMS and NOSOALVBVOC

When moving from a high NO_3 regime (PD oxidants) to a low NO_3 regime (PI oxidants), the oxidation reactions giving SOA_{LV} as a product (Reactions R3 and R6) become more important. This is seen from the large change in the global mean column burden of SOA_{LV} (+49.6 %). Since SOA_{LV} can take part in nucleation and can give rise to the increased aerosol number concentration seen in Fig. 4a, the additional SOA_{LV} that is produced when using PI oxidants may explain the change in the indirect effects seen in Fig. 3. When replacing all of the standard produced SOA_{LV} from the DMS oxidation in Reaction (R3) with SOA_{SV} in the NOSOALVDMS simulations, the change in the total aerosol indirect effect is almost the same as for the original setup (ΔAIE_{tot}: $+0.25\,W\,m^{-2}$), and the geographical pattern looks largely the same (not shown here). This also holds when doing the same for the oxidation of monoterpene (Reaction R6) (ΔAIE_{tot}: $+0.26\,W\,m^{-2}$). The pattern of the resulting AIE from the oxidant changes in the NOSOALVBVOC simulations looks almost the same as for the original simulations, except over the Amazon where the signal from the O_3 changes explained in the last section is gone. This does not change the global mean AIE by more than $0.01\,W\,m^{-2}$, however. These sensitivity tests indicate that even though the global mean burden of SOA_{LV} changes a lot when using PI oxidants, this plays a minor role for the change in the indirect effects seen in Fig. 3.

4.3.2 NOSOA

The increased production of total SOA(g) (SOA_{SV} and SOA_{LV}) when switching from PD to PI oxidants has the potential to cause changes in the indirect effects even though the nucleation effect is negligible. All SOA(g) can condense onto already nucleated aerosols and make it easier for them to grow to the critical size for cloud droplet activation, except for cases where the reduction in hygroscopicity is more important than the increase in size. The impact of the hygroscopicity changes due to the changes in the oxidant levels has been tested and found to be negligible (not shown here). The change in total global mean column burden of SOA(g) due to changes in the oxidant level with the original setup was +40.7 %. To find out whether this increase is causing the change in the indirect effects seen in Fig. 3, the model was run with the NOSOA setup described in Table 7. This resulted in a change in the total aerosol indirect effects (ΔAIE_{tot}) of $+0.14\,W\,m^{-2}$, deviating by more than $0.10\,W\,m^{-2}$ from the original setup. Removing products from the reaction makes the atmosphere cleaner, thus creating a different regime both for aerosol growth through reduced competition for condensable gases as for aerosol activation through reduced competition for water vapor. This means that one cannot conclude that $0.11\,\mathrm{W\,m^{-2}}$ of the $0.25\,\mathrm{W\,m^{-2}}$ is caused by an increase in condensable SOA(g) when switching from PD to PI oxidants, but this sensitivity test indicates that it may have contributed to the overall result seen in Fig. 3.

4.3.3 NACTOFF

This test is performed in order to see how important the change in the droplet activation on the smallest aerosols is. When modifying the oxidant level, the smallest aerosols are affected by the change in formation rate, while all aerosols are affected by the change in condensation. The results from this test give an indication of how important the changes associated with the smallest aerosols are. When not allowing the smallest aerosols in mixture number 1 (corresponding to the nucleation mode in modal aerosol schemes) to activate, the change in the total aerosol indirect effects found when switching from PD or PI oxidants in the PI simulation is small ($\Delta\mathrm{AIE_{tot}}$: $-0.03\,\mathrm{W\,m^{-2}}$). This confirms that it is the difference in the number concentration of the smallest SO_4 and SOA aerosols between the simulations with different oxidant levels that gives the large difference in the indirect effect seen in Fig. 3.

4.3.4 DIURNALNO3

The tests where the oxidant changes where studied individually identified the historical change in NO_3 as having the largest impact on the result. As described in the model description, OH and HO_2 have a diurnal cycle added to the prescribed monthly climatology in CAM5.3-Oslo. This is not the case for NO_3, even though it is well known that concentrations of NO_3 drop during daytime due to rapid photolysis (Wayne et al., 1991; Seinfeld and Pandis, 2016). To see how this lack of a diurnal cycle for NO_3 impacts the results in this study, another set of simulations was carried out. The daytime concentration of NO_3 was set to zero, while the nighttime concentration was increased, such that the daily averaged and the monthly averaged values stayed the same as in the original setup. This treatment of the diurnal cycle is the same as that for HO_2 and OH, but with a shift from day to night. Carrying out the same three model simulations with this new setup as for the original default model setup gives a change in the total aerosol indirect effect of $+0.26\,\mathrm{W\,m^{-2}}$ (from -1.32 to $-1.06\,\mathrm{W\,m^{-2}}$) when applying PI instead of PD oxidants. In other words, this test shows that the lack of a diurnal cycle for NO_3 only has a minor influence on the result in this study. The reason for this minor impact is that the main effect of oxidation by NO_3 is of DMS over the oceans. Since the lifetime of DMS is 36 and 55 h (present day and preindustrial, respectively), the reduction in the nighttime oxidation when not applying a diurnal cycle will have time to be compensated by an increase in the daytime oxidation.

4.3.5 FREEMET

Constraining the natural variability by nudging the meteorology has been shown to be an efficient way of identifying the effect of a model perturbation since it reduces the computational cost and time significantly (Kooperman et al., 2012). In this study, nudging has been applied in order to model $\mathrm{ERF_{aci}}$. According to the definition of effective radiative forcing in Myhre et al. (2013, p. 665), "ERF represents the change in net top-of-the-atmosphere downward radiative flux after allowing for atmospheric temperatures, water vapor and clouds to adjust, but with global mean surface temperature or a portion of surface conditions unchanged". In the simulations presented here, nudged winds are not fully impacted by rapid adjustments in the atmosphere due to an aerosol perturbation, which again could give a response by the clouds. Thus, parts of this rapid wind–aerosol–cloud–radiation feedback could be missing from the calculated values of ERF in this study. Running all the simulations in this study with free meteorology is computationally very expensive. Instead we performed sensitivity tests for the three simulations with the original model setup to estimate the bias introduced by the method of nudging. The length of the simulations is 53 years, where the last 50 are analyzed. The total aerosol indirect effect changes by $0.3 \pm 0.2\,\mathrm{W\,m^{-2}}$ (from -1.3 ± 0.2 to $-1.0 \pm 0.2\,\mathrm{W\,m^{-2}}$) when switching from PD to PI oxidants in the PI simulation. Even though the uncertainties due to natural variability still are large after 50 years, this change in the total aerosol indirect effect due to historical oxidant changes fall in the same range as when nudging the winds with a relaxation timescale of 6 h. Analyzing only the last 30 years of the simulations gives the same change in the total aerosol indirect effect, indicating that there is no drift in the signal.

5 Summary and conclusions

We have used the global atmospheric model CAM5.3-Oslo to study the effect of historical oxidant changes on the PD–PI aerosol indirect effect. The precursor gases in the PI simulation were exposed to PI oxidants instead of PD oxidants. Our main findings are the following:

- The total aerosol indirect effect is reduced from -1.32 to $-1.07\,\mathrm{W\,m^{-2}}$, mainly due to a cloud brightening in the modified PI simulation.
- NO_3 is the oxidant that contributes the most to the changes.
- When the precursor gases are exposed to an atmosphere with relatively lower oxidative power (PI oxidants vs. PD oxidants), their lifetimes increase and they

are transported higher up in the atmosphere and horizontally towards more remote areas before they are oxidized.

- The increased lifetime of the precursor gases contributes to an increase in the formation of new aerosol and a decrease in the deposition and in the coagulation sink of the newly formed aerosols, contributing to an increase in the aerosol number concentration.
- A large portion of the new aerosol formation and the increase in aerosol number concentration occurs where the cloud-weighted susceptibility is high, giving a large impact on the radiative effects.
- The change from PD to PI oxidants in the PI simulation yields a shift in the chemical reactions towards increased production of condensate relative to the amount of gases that can nucleate, which increases the size of the aerosols, making it easier for them to activate.

Note that the magnitude of the sensitivity of the total aerosol indirect effect to the choice of the oxidants in this study is as large as the total sulfur direct forcing (Myhre et al., 2013), thus contributing significantly to the total preindustrial-to-present-day anthropogenic forcing. Overviews of model results of the PD–PI aerosol indirect effect show occasionally so negative values that they even offset the warming from the greenhouse gases (Boucher et al., 2013; Lohmann, 2017). Our results suggest that such unrealistic cooling may appear less often if the precursor gases are exposed to oxidants of their era, instead of applying PD oxidants for both PD and PI simulations.

The results in this study are based on simulations from just one model, with its model-specific treatments of oxidants, aerosols, clouds and radiation that all include uncertainties and simplifications. This also holds for the single input dataset used for the prescribed oxidants. An evaluation of the extent to which uncertainties in the different parameterizations and in the prescribed oxidant fields affect the result is beyond the scope of this paper, but should be focus for future studies. The treatment of the MSA product from DMS oxidation by OH (Reaction R3) should be looked at in particular, since the changes in SOA condensate from that reaction seem to contribute to the resulting changes in the total aerosol indirect effect. Different choices of yields for the oxidation reactions in Table 2 should also be in focus since these yields are uncertain and vary between different models and observations (Kroll et al., 2005; Lee et al., 2006; Dentener et al., 2006; Spracklen et al., 2011; Neale et al., 2012; Tsigaridis et al., 2014; Jokinen et al., 2015). The impact of the lack of pure biogenic new particle formation in the model applied in this study could also be studied, since this mechanism has been shown to be important for radiative forcing calculations, especially in clean regions (Gordon et al., 2016). When it comes to the oxidant input dataset, it would be interesting to see how the result is affected by using a model with online oxidant chemistry. Upcoming studies should also see how the result is affected by using other input datasets produced by more advanced models than the model applied in Lamarque et al. (2010), which for example did not include online aerosol–cloud radiative interactions or different land cover information in the two different eras, which could have impacted the oxidant level through different photolysis rates and different emissions from the land model.

The impact of the oxidant changes also depends on the emissions of precursor gases. Carslaw et al. (2013) show that there are large uncertainties linked to natural emissions, even when assuming that they do not vary between PI and PD. This was shown especially for DMS (Woodhouse et al., 2010), which is found to be one of the most important precursor gases in this study. Changes in temperature and pH in the ocean, as well as changes in land use, insolation and CO_2 may also have contributed to a change in the emissions since preindustrial time (Charlsson et al., 1987; Guenther et al., 2012; Unger, 2014). CAM5.3-Oslo is also lacking some emissions that could be important for the magnitude of the effect of the oxidant changes, for example emissions of BVOC from the ocean, which can contribute significantly to the marine aerosol loading (Shaw et al., 2010), creating a more polluted regime with the potential of different susceptibilities.

Despite the large uncertainties and simplifications mentioned above, we find that the treatment of the oxidants is open for discussion. We suggest that a common way of treating the oxidants must be agreed upon when modeling aerosol effective radiative forcings. We also encourage other researchers to specify which oxidants are used in their studies of historical changes in aerosol–cloud interactions.

Simulations from the Aerosol Chemistry Model Intercomparison Project (AerChemMIP), endorsed by the Coupled Model Intercomparison Project 6 (CMIP6), can be used to quantify preindustrial-to-present-day effective radiative forcings. Comparing the cloud forcings from the simulations called piClim-aer and piClim-control (Collins et al., 2017) will be approximately the same as done in the original default setup in this study, with the same oxidant level in both simulations. For models without tropospheric chemistry, AerChemMIP does not include a setup that takes into account historical oxidant changes. However, models that include tropospheric chemistry can perform the simulation piClim-NTCF, which includes different ozone precursors in the two different simulations, giving a different oxidation capacity. The piClim-NTCF simulation does not include all the factors that contribute to the differences in the oxidant level between PD and PI (for example methane), but it includes some of them, so we suggest that a comparison of the cloud forcings in piClim-NTCF and piClim-control will facilitate calculations of the PD–PI aerosol indirect effect, including changes due to different oxidant level, for the CMIP6 models as well.

Data availability. The CAM5.3-Oslo code is available for registered users through signing a respective license. In order to initiate this process please contact noresm-ncc@met.no. Users should briefly state themselves as CESM users at the CESM website (http://www.cesm.ucar.edu/models/register/register.html). Output from the three simulations with the default model setup (named PDAER_PDOXI_ORG, PIAER_PDOXI_ORG and PIAER_PIOXI_ORG) is available here: https://doi.org/10.11582/2018.00014. Output from the sensitivity simulations are available upon request. The reason why we only have output stored online from the three simulations with the default model setup is that the rest of the simulations count 31 in total, which requires too big storage space for our online storage. We are more than happy to share the output upon request.

Competing interests. The authors declare that they have no conflict of interest.

Acknowledgements. Inger Helene Hafsahl Karset, Alf Grini, Dirk Olivié, Alf Kirkevåg, Øyvind Seland, Trond Iversen and Michael Schulz have been financed by the research council of Norway (RCN) through the project EVA and the NOTUR/Norstore projects (Sigma2 account: nn2345k; Norstore account: NS2345K). We gratefully acknowledge Sara Marie Blichner and Moa Sporre for scientific discussions.

Edited by: Barbara Ervens
Reviewed by: four anonymous referees

References

Albrecht, B. A.: Aerosols, cloud microphysics, and fractional cloudiness, Science, 245, 1227–1230, https://doi.org/10.1126/science.245.4923.1227, 1989.

Alterskjær, K., Kristjánsson, J. E., and Seland, O.: Sensitivity to deliberate sea salt seeding of marine clouds – Observations and model simulations, Atmos. Chem. Phys., 12, 2795–2807, https://doi.org/10.5194/acp-12-2795-2012, 2012.

Bentsen, M., Bethke, I., Debernard, J. B., Iversen, T., Kirkevåg, A., Seland, Ø., Drange, H., Roelandt, C., Seierstad, I. A., Hoose, C., and Kristjánsson, J. E.: The Norwegian Earth System Model, NorESM1-M – Part 1: Description and basic evaluation of the physical climate, Geosci. Model Dev., 6, 687–720, https://doi.org/10.5194/gmd-6-687-2013, 2013.

Berntsen, T. K., Isaksen, I. S., Myhre, G., Fuglestvedt, J. S., Stordal, F., Alsvik Larsen, T., Freckleton, R. S., and Shine, K. P.: Effects of anthropogenic emissions on tropospheric ozone and its radiative forcing, J. Geophys. Res., 102, 101–128, https://doi.org/10.1029/97JD02226, 1997.

Bork, N., Elm, J., Olenius, T., and Vehkamäki, H.: Methane sulfonic acid-enhanced formation of molecular clusters of sulfuric acid and dimethyl amine, Atmos. Chem. Phys., 14, 12023–12030, https://doi.org/10.5194/acp-14-12023-2014, 2014.

Boucher, O., Randall, D., Artaxo, P., Bretherton, C., Feingold, G., Forster, P., Kerminen, V.-M., Kondo, Y., Liao, H., Lohmann, U., Rasch, P., Satheesh, S., Sherwood, S., Stevens, B., and Zhang, X.: Clouds and aerosols, in: Climate Change 2013: The Physical Science Basis, Contribution of Working Group I to the Fifth Assessment Report of the Intergovernmental Panel on Climate Change, chap. 8, edited by: Stocker, T., Qin, D., Plattner, G.-K., Tignor, M., Allen, S., Boschung, J., Nauels, A., Xia, Y., and Midgley, V., Cambridge University Press, Cambridge, UK and New York, NY, USA., 659–740, 2013.

Brown-Steiner, B., Selin, N. E., Prinn, R., Tilmes, S., Emmons, L., Lamarque, J.-F., and Cameron-Smith, P.: Evaluating Simplified Chemical Mechanisms within CESM Version 1.2 CAM-chem (CAM4): MOZART-4 vs. Reduced Hydrocarbon vs. Super-Fast Chemistry, Geosci. Model Dev. Discuss., https://doi.org/10.5194/gmd-2018-16, in review, 2018.

Carslaw, K. S., Lee, L. A., Reddington, C. L., Pringle, K. J., Rap, A., Forster, P. M., Mann, G. W., Spracklen, D. V., Woodhouse, M. T., Regayre, L. A., and Pierce, J. R.: Large contribution of natural aerosols to uncertainty in indirect forcing, Nature, 503, 67–71, https://doi.org/10.1038/nature12674, 2013.

Chameides, W. L., Fehsenfeld, F., Rodgers, M. O., Cardelino, C., Martinez, J., Parrish, D., Lonneman, W., Lawson, D. R., Rasmussen, R. A., Zimmerman, P., Greenberg, J., Mlddleton, P., and Wang, T.: Ozone precursor relationships in the ambient atmosphere, J. Geophys. Res., 97, 6037, https://doi.org/10.1029/91JD03014, 1992.

Charlsson, R. J., Lovelock, J., Andreae, M. O., and Warren, S. G.: Oceanic phytoplankton, atmospheric sulphur, cloud albedo and climate, Nature, 326, 655–661, https://doi.org/10.1038/326655a0, 1987.

Chen, H. and Finlayson-Pitts, B. J.: New Particle Formation from Methanesulfonic Acid and Amines/Ammonia as a Function of Temperature, Environ. Sci. Technol., 51, 243–252, https://doi.org/10.1021/acs.est.6b04173, 2017.

Chin, M., Jacob, D. J., Gardner, G. M., Foreman-Fowler, M. S., Spiro, P. A., and Savoie, D. L.: A global three-dimensional model of tropospheric sulfate, J. Geophys. Res.-Atmos., 101, 18667–18690, https://doi.org/10.1029/96JD01221, 1996.

Collins, J. W., Lamarque, J. F., Schulz, M., Boucher, O., Eyring, V., Hegglin, I. M., Maycock, A., Myhre, G., Prather, M., Shindell, D., and Smith, J. S.: AerChemMIP: Quantifying the effects of chemistry and aerosols in CMIP6, Geosci. Model Dev., 10, 585–607, https://doi.org/10.5194/gmd-10-585-2017, 2017.

Collins, W. J., Derwent, R. G., Johnson, C. E., and Stevenson, D. S.: The oxidation of organic compounds in the troposphere and their global warming potentials, Climatic Change, 52, 453–479, https://doi.org/10.1023/A:1014221225434, 2002.

Crutzen, P. and Lelieveld, J.: Human impacts on atmospheric chemistry, Annu. Rev. Earth Planet. Sci., 29, 17–45, 2001.

Dentener, F., Kinne, S., Bond, T., Boucher, O., Cofala, J., Generoso, S., Ginoux, P., Gong, S., Hoelzemann, J. J., Ito, A., Marelli, L., Penner, J. E., Putaud, J. P., Textor, C., Schulz, M., Van Der Werf, G. R., and Wilson, J.: Emissions of primary aerosol and precursor gases in the years 2000 and 1750 prescribed data-sets for AeroCom, Atmos. Chem. Phys., 6, 4321–4344, https://doi.org/10.5194/acp-6-4321-2006, 2006.

Emmons, L. K., Walters, S., Hess, P. G., Lamarque, J.-F., Pfister, G. G., Fillmore, D., Granier, C., Guenther, A., Kinnison, D., Laepple, T., Orlando, J., Tie, X., Tyndall, G., Wiedinmyer, C., Baughcum, S. L., and Kloster, S.: Description and evaluation of the Model for Ozone and Related chemical Tracers, version 4 (MOZART-4), Geosci. Model Dev., 3, 43–67, https://doi.org/10.5194/gmd-3-43-2010, 2010.

Gettelman, A.: Putting the clouds back in aerosol-cloud interactions, Atmos. Chem. Phys., 15, 12397–12411, https://doi.org/10.5194/acp-15-12397-2015, 2015.

Gettelman, A. and Morrison, H.: Advanced two-moment bulk microphysics for global models. Part I: Off-line tests and comparison with other schemes, J. Climate, 28, 1268–1287, https://doi.org/10.1175/JCLI-D-14-00102.1, 2015.

Gettelman, A., Morrison, H., Santos, S., Bogenschutz, P., and Caldwell, P. M.: Advanced two-moment bulk microphysics for global models. Part II: Global model solutions and aerosol-cloud interactions, J. Climate, 28, 1288–1307, https://doi.org/10.1175/JCLI-D-14-00103.1, 2015.

Ghan, S. J.: Technical note: Estimating aerosol effects on cloud radiative forcing, Atmos. Chem. Phys., 13, 9971–9974, https://doi.org/10.5194/acp-13-9971-2013, 2013.

Gordon, H., Sengupta, K., Rap, A., Duplissy, J., Frege, C., Williamson, C., Heinritzi, M., Simon, M., Yan, C., Almeida, J., Tröstl, J., Nieminen, T., Ortega, I. K., Wagner, R., Dunne, E. M., Adamov, A., Amorim, A., Bernhammer, A.-K., Bianchi, F., Breitenlechner, M., Brilke, S., Chen, X., Craven, J. S., Dias, A., Ehrhart, S., Fischer, L., Flagan, R. C., Franchin, A., Fuchs, C., Guida, R., Hakala, J., Hoyle, C. R., Jokinen, T., Junninen, H., Kangasluoma, J., Kim, J., Kirkby, J., Krapf, M., Kürten, A., Laaksonen, A., Lehtipalo, K., Makhmutov, V., Mathot, S., Molteni, U., Monks, S. A., Onnela, A., Peräkylä, O., Piel, F., Petäjä, T., Praplan, A. P., Pringle, K. J., Richards, N. A. D., Rissanen, M. P., Rondo, L., Sarnela, N., Schobesberger, S., Scott, C. E., Seinfeld, J. H., Sharma, S., Sipilä, M., Steiner, G., Stozhkov, Y., Stratmann, F., Tomé, A., Virtanen, A., Vogel, A. L., Wagner, A. C., Wagner, P. E., Weingartner, E., Wimmer, D., Winkler, P. M., Ye, P., Zhang, X., Hansel, A., Dommen, J., Donahue, N. M., Worsnop, D. R., Baltensperger, U., Kulmala, M., Curtius, J., and Carslaw, K. S.: Reduced anthropogenic aerosol radiative forcing caused by biogenic new particle formation, P. Natl. Acad. Sci. USA, 43, 12053–12058, https://doi.org/10.1073/pnas.1602360113, 2016.

Guenther, A. B., Jiang, X., Heald, C. L., Sakulyanontvittaya, T., Duhl, T., Emmons, L. K., and Wang, X.: The model of emissions of gases and aerosols from nature version 2.1 (MEGAN2.1): An extended and updated framework for modeling biogenic emissions, Geosci. Model Dev., 5, 1471–1492, https://doi.org/10.5194/gmd-5-1471-2012, 2012.

Hoose, C., Lohmann, U., Erdin, R., and Tegen, I.: The global influence of dust mineralogical composition on heterogeneous ice nucleation in mixed-phase clouds, Environ. Res. Lett., 3, 025003, https://doi.org/10.1088/1748-9326/3/2/025003, 2008.

Hoose, C., Kristjánsson, J. E., Iversen, T., Kirkevåg, A., Seland, Ø., and Gettelman, A.: Constraining cloud droplet number concentration in GCMs suppresses the aerosol indirect effect, Geophys. Res. Lett., 36, 1–5, https://doi.org/10.1029/2009GL038568, 2009.

Hoose, C., Kristjánsson, J. E., Chen, J.-P., and Hazra, A.: A Classical-Theory-Based Parameterization of Heterogeneous Ice Nucleation by Mineral Dust, Soot, and Biological Particles in a Global Climate Model, J. Atmos. Sci., 67, 2483–2503, https://doi.org/10.1175/2010JAS3425.1, 2010.

Iversen, T., Bentsen, M., Bethke, I., Debernard, J. B., Kirkevåg, A., Seland, Ø., Drange, H., Kristjansson, J. E., Medhaug, I., Sand, M., and Seierstad, I. A.: The Norwegian Earth System Model, NorESM1-M – Part 2: Climate response and scenario projections, Geosci. Model Dev., 6, 389–415, https://doi.org/10.5194/gmd-6-389-2013, 2013.

Jaenicke, R.: Natural Aerosols, Ann. New York Acad. Sci., 338, 317–329, https://doi.org/10.1111/j.1749-6632.1980.tb17129.x, 1980.

Jokinen, T., Berndt, T., Makkonen, R., Kerminen, V.-M., Junninen, H., Paasonen, P., Stratmann, F., Herrmann, H., Guenther, A. B., Worsnop, D. R., Kulmala, M., Ehn, M., and Sipilä, M.: Production of extremely low volatile organic compounds from biogenic emissions: Measured yields and atmospheric implications, P. Natl. Acad. Sci. USA, 112, 7123–7128, https://doi.org/10.1073/pnas.1423977112, 2015.

Karset, I. H.: Oxidant impact on indirect effects – Model output from the three simulations with original model setup, Data set, Norstore, https://doi.org/10.11582/2018.00014, 2018.

Khan, M. A. H., Cooke, M. C., Utembe, S. R., Archibald, A. T., Derwent, R. G., Xiao, P., Percival, C. J., Jenkin, M. E., Morris, W. C., and Shallcross, D. E.: Global modeling of the nitrate radical (NO_3) for present and pre-industrial scenarios, Atmos. Res., 164–165, 347–357, https://doi.org/10.1016/j.atmosres.2015.06.006, 2015.

Kirkevåg, A., Iversen, T., Seland, Ø., Debernard, J. B., Storelvmo, T., and Kristjánsson, J. E.: Aerosol–cloud–climate interactions in the climate model CAM-Oslo, Tellus A, 60, 492–512, https://doi.org/10.1111/j.1600-0870.2008.00313.x, 2008.

Kirkevåg, A., Iversen, T., Seland, Ø., Hoose, C., Kristjánsson, J. E., Struthers, H., Ekman, A. M. L., Ghan, S., Griesfeller, J., Nilsson, E. D., and Schulz, M.: Aerosol–climate interactions in the Norwegian Earth System Model – NorESM1-M, Geosci. Model Dev., 6, 207–244, https://doi.org/10.5194/gmd-6-207-2013, 2013.

Kirkevåg, A., Grini, A., Olivié, D., Seland, Ø., Alterskjær, K., Hummel, M., Karset, I. H. H., Lewinchal, A., Liu, X., Makkonen, R., Bethke, I., Griesfeller, J., Schulz, M., and Iversen, T.: A production-tagged aerosol module for earth system models, OsloAero5.3 – extensions and update for CAM5.3-Oslo, Geosci. Model Dev. Discuss., https://doi.org/10.5194/gmd-2018-46, in review, 2018

Kooperman, G. J., Pritchard, M. S., Ghan, S. J., Wang, M., Somerville, R. C. J., and Russell, L. M.: Constraining the influence of natural variability to improve estimates of global aerosol indirect effects in a nudged version of the Community Atmosphere Model 5, J. Geophys. Res.-Atmos., 117, 025003, https://doi.org/10.1029/2012JD018588, 2012.

Kroll, J. H., Ng, N. L., Murphy, S. M., Flagan, R. C., and Seinfeld, J. H.: Secondary organic aerosol formation from isoprene photooxidation under high-NO_x conditions, Geophys. Res. Lett., 32, L18808, https://doi.org/10.1029/2005GL023637, 2005.

Lamarque, J. F., Bond, T. C., Eyring, V., Granier, C., Heil, A., Klimont, Z., Lee, D., Liousse, C., Mieville, A., Owen, B., Schultz, M. G., Shindell, D., Smith, S. J., Stehfest, E., Van Aardenne, J., Cooper, O. R., Kainuma, M., Mahowald, N., McConnell, J. R., Naik, V., Riahi, K., and Van Vuuren, D. P.: Historical (1850–2000) gridded anthropogenic and biomass burning emissions of reactive gases and aerosols: Methodology and application, Atmos. Chem. Phys., 10, 7017–7039, https://doi.org/10.5194/acp-10-7017-2010, 2010.

Lamarque, J. F., Emmons, L. K., Hess, P. G., Kinnison, D. E., Tilmes, S., Vitt, F., Heald, C. L., Holland, E. A., Lauritzen, P. H., Neu, J., Orlando, J. J., Rasch, P. J., and Tyndall, G. K.: CAM-chem: Description and evaluation of interactive atmospheric chemistry in the Community Earth System Model, Geosci. Model Dev., 5, 369–411, https://doi.org/10.5194/gmd-5-369-2012, 2012.

Lee, A., Goldstein, A. H., Kroll, J. H., Ng, N. L., Varutbangkul, V., Flagan, R. C., and Seinfeld, J. H.: Gas-phase products and secondary aerosol yields from the photooxidation of 16 different terpenes, J. Geophys. Res.-Atmos., 111, 1–25, https://doi.org/10.1029/2006JD007050, 2006.

Lehtinen, K. E., Dal Maso, M., Kulmala, M., and Kerminen, V. M.: Estimating nucleation rates from apparent particle formation rates and vice versa: Revised formulation of the Kerminen-Kulmala equation, J. Aerosol Sci., 38, 988–994, https://doi.org/10.1016/j.jaerosci.2007.06.009, 2007.

Liu, X., Easter, R. C., Ghan, S. J., Zaveri, R., Rasch, P., Shi, X., Lamarque, J. F., Gettelman, A., Morrison, H., Vitt, F., Conley, A., Park, S., Neale, R., Hannay, C., Ekman, A. M., Hess, P., Mahowald, N., Collins, W., Iacono, M. J., Bretherton, C. S., Flanner, M. G., and Mitchell, D.: Toward a minimal representation of aerosols in climate models: Description and evaluation in the Community Atmosphere Model CAM5, Geosci. Model Dev., 5, 709–739, https://doi.org/10.5194/gmd-5-709-2012, 2012.

Liu, X., Ma, P. L., Wang, H., Tilmes, S., Singh, B., Easter, R. C., Ghan, S. J., and Rasch, P. J.: Description and evaluation of a new four-mode version of the Modal Aerosol Module (MAM4) within version 5.3 of the Community Atmosphere Model, Geosci. Model Dev., 9, 505–522, https://doi.org/10.5194/gmd-9-505-2016, 2016.

Lohmann, U.: Global anthropogenic aerosol effects on convective clouds in ECHAM5-HAM, Atmos. Chem. Phys., 8, 2115–2131, https://doi.org/10.5194/acpd-7-14639-2007, 2008.

Lohmann, U.: Anthropogenic Aerosol Influences on Mixed-Phase Clouds, Curr. Clim. Change Rep., 3, 32–44, https://doi.org/10.1007/s40641-017-0059-9, 2017.

Lohmann, U. and Diehl, K.: Sensitivity Studies of the Importance of Dust Ice Nuclei for the Indirect Aerosol Effect on Stratiform Mixed-Phase Clouds, J. Atmos. Sci., 63, 968–982, https://doi.org/10.1175/JAS3662.1, 2006.

Lohmann, U. and Ferrachat, S.: Impact of parametric uncertainties on the present-day climate and on the anthropogenic aerosol effect, Atmos. Chem. Phys., 10, 11373–11383, https://doi.org/10.5194/acp-10-11373-2010, 2010.

Lohmann, U., Feichter, J., Penner, J., and Leaitch, R.: Indirect effect of sulfate and carbonaceous aerosols: A mechanistic treatment, J. Geophys. Res.-Atmos., 105, 12193–12206, https://doi.org/10.1029/1999JD901199, 2000.

Makkonen, R., Seland, Ø., Kirkevåg, A., Iversen, T., and Kristjánsson, J. E.: Evaluation of aerosol number concentrations in NorESM with improved nucleation parameterization, Atmos. Chem. Phys., 14, 5127–5152, https://doi.org/10.5194/acp-14-5127-2014, 2014.

Menon, S. and Rotstayn, L.: The radiative influence of aerosol effects on liquid-phase cumulus and stratiform clouds based on sensitivity studies with two climate models, Clim. Dynam., 27, 345–356, https://doi.org/10.1007/s00382-006-0139-3, 2006.

Morrison, H. and Gettelman, A.: A new two-moment bulk stratiform cloud microphysics scheme in the community atmosphere model, version 3 (CAM3). Part I: Description and numerical tests, J. Climate, 21, 3642–3659, https://doi.org/10.1175/2008JCLI2105.1, 2008.

Murray, L. T., Mickley, L. J., Kaplan, J. O., Sofen, E. D., Pfeiffer, M., and Alexander, B.: Factors controlling variability in the oxidative capacity of the troposphere since the Last Glacial Maximum, Atmos. Chem. Phys., 14, 3589–3622, https://doi.org/10.5194/acp-14-3589-2014, 2014.

Myhre, G., Shindell, D., Bréon, F.-M., Collins, W., Fuglestvedt, J., Huang, J., Koch, D., Lamarque, J.-F., Lee, D., Mendoza, B., Nakajima, T., Robock, A., Stephens, G., Takemura, T., and Zhang, H.: Anthropogenic and Natural Radiative Forcing, in: Climate Change 2013: The Physical Science Basis, Contribution of Working Group I to the Fifth Assessment Report of the Intergovernmental Panel on Climate Change, chap. 7, edited by: Stocker, T., Qin, D., Plattner, G.-K., Tignor, M., Allen, S., Boschung, A., Nauels, Y., Xia, V., and Midgley, B., Cambridge University Press, Cambridge, UK and New York, NY, USA, 659–740, https://doi.org/10.1017/CBO9781107415324.018, 2013.

Naik, V., Horowitz, L. W., Fiore, A. M., Ginoux, P., Mao, J., and Aghedo, A. M.: Impact of preindustrial to present-day changes in short-lived pollutant emissions on atmospheric composition and climate forcing, J. Geophys. Res.-Atmos., 118, 8086–8110, https://doi.org/10.1002/jgrd.50608, 2013a.

Naik, V., Voulgarakis, A., Fiore, A. M., Horowitz, L. W., Lamarque, J. F., Lin, M., Prather, M. J., Young, P. J., Bergmann, D., Cameron-Smith, P. J., Cionni, I., Collins, W. J., Dalsøren, S. B., Doherty, R., Eyring, V., Faluvegi, G., Folberth, G. A., Josse, B., Lee, Y. H., MacKenzie, I. A., Nagashima, T., Van Noije, T. P., Plummer, D. A., Righi, M., Rumbold, S. T., Skeie, R., Shindell, D. T., Stevenson, D. S., Strode, S., Sudo, K., Szopa, S., and Zeng, G.: Preindustrial to present-day changes in tropospheric hydroxyl radical and methane lifetime from the Atmospheric Chemistry and Climate Model Intercomparison Project (ACCMIP), Atmos. Chem. Phys., 13, 5277–5298, https://doi.org/10.5194/acp-13-5277-2013, 2013b.

Neale, R. B., Chen, C.-C., Gettelman, A., Lauritzen, P. H., Park, S., Williamson, D. L., Conley, A. J., Garcia, R., Kinnison, D., Lamarque, J.-F., Marsh, D., Mills, M., Smith, A. K., Tilmes, S., Vitt, F., Morrison, H., Cameron-Smith, P., Collins, W. D., Iacono, M. J., Easter, R. C., Ghan, S. J., Liu, X., Rasch, P. J., and Taylor, M. A.: Description of the NCAR Community Atmosphere Model (CAM 5.0), NCAR Technical Note, http://www.cesm.ucar.edu/models/cesm1.0/cam/docs/description/cam5_desc.pdf (last access: 29 May 2018), 2012.

Neubauer, D., Lohmann, U., Hoose, C., and Frontoso, M. G.: Impact of the representation of marine stratocumulus clouds on the anthropogenic aerosol effect, Atmos. Chem. Phys., 14, 11997–12022, https://doi.org/10.5194/acp-14-11997-2014, 2014.

Nightingale, P. D., Malin, G., Law, C. S., Watson, A. J., Liss, P. S., Liddicoat, M. I., Boutin, J., and Upstill-Goddard, R. C.: In situ evaluation of air–sea gas exchange parameterizations using novel conservative and volatile tracers, Global Biogeochem. Cy., 14, 373–387, https://doi.org/10.1029/1999GB900091, 2000.

Oleson, K. W., Lawrence, D. M., Authors, L., Bonan, G. B., Drewniak, B., Huang, M., Koven, C. D., Levis, S., Li, F., Riley, W. J., Subin, Z. M., Swenson, S. C., Thornton, P. E., Bozbiyik, A., Fisher, R., Heald, C. L., Kluzek, E., Lamarque, J.-F., Lawrence, P. J., Leung, L. R., Lipscomb, W., Muszala, S., Ricciuto, D. M., Sacks, W., Sun, Y., Tang, J., and Yang, Z.-L.: Technical Description of version 4.5 of the Community Land Model (CLM), https://doi.org/10.5065/D6RR1W7M, 2013.

Paasonen, P., Nieminen, T., Asmi, E., Manninen, H. E., Petäjä, T., Plass-Dülmer, C., Flentje, H., Birmili, W., Wiedensohler, A., Hõrrak, U., Metzger, A., Hamed, A., Laaksonen, A., Facchini, M. C., Kerminen, V. M., and Kulmala, M.: On the roles of sulphuric acid and low-volatility organic vapours in the initial steps of atmospheric new particle formation, Atmos. Chem. Phys., 10, 11223–11242, https://doi.org/10.5194/acp-10-11223-2010, 2010.

Parrish, D. D., Lamarque, J. F., Naik, V., Horowitz, L., Shindell, D. T., Staehelin, J., Derwent, R., Cooper, O. R., Tanimoto, H., Volz-Thomas, A., Gilge, S., Scheel, H. E., Steinbacher, M., and Fröhlich, M.: Long-term changes in lower tropospheric baseline ozone concentrations: Comparing chemistry-climate models and observations at northern midlatitudes, J. Geophys. Res., 119, 5719–5736, https://doi.org/10.1002/2013JD021435, 2014.

Pavelin, E. G., Johnson, C. E., Rughooputh, S., and Toumi, R.: Evaluation of pre-industrial surface ozone measurements made using Schonbein's method, Atmos. Environ., 33, 919–929, https://doi.org/10.1016/S1352-2310(98)00257-X, 1999.

Pincus, R. and Baker, M. B.: Effect of precipitation on the albedo susceptibility of clouds in the marine boundary layer, Nature, 372, 250–252, 1994.

Prinn, R. G.: The cleansing capacity of the atmosphere, Annu. Rev. Environ. Resour., 28, 29–57, https://doi.org/10.1146/annurev.energy.28.011503.163425, 2003.

Salzmann, M., Ming, Y., Golaz, J. C., Ginoux, P. A., Morrison, H., Gettelman, A., Kramer, M., and Donner, L. J.: Two-moment bulk stratiform cloud microphysics in the GFDL AM3 GCM: Description, evaluation, and sensitivity tests, Atmos. Chem. Phys., 10, 8037–8064, https://doi.org/10.5194/acp-10-8037-2010, 2010.

Sant, V., Posselt, R., and Lohmann, U.: Prognostic precipitation with three liquid water classes in the ECHAM5-HAM GCM, Atmos. Chem. Phys., 15, 8717–8738, https://doi.org/10.5194/acp-15-8717-2015, 2015.

Seinfeld, J. H.: Urban Air Pollution: State of the Science, Science, 243, 745–752, https://doi.org/10.1126/science.243.4892.745, 1989.

Seinfeld, J. H. and Pandis, S. N.: Atmospheric Chemistry and Physics: From Air Pollution to Climate Change, 3rd Edn., John Wiley & Sons Inc., Hoboken, New Jersey, 2016.

Shaw, S. L., Gantt, B., and Meskhidze, N.: Production and Emissions of Marine Isoprene and Monoterpenes: A Review, Adv. Meteorol., 2010, 1–24, https://doi.org/10.1155/2010/408696, 2010.

Spivakovsky, C. M., Logan, J. A., Montzka, S. A., Balkanski, Y. J., Foreman-Fowler, M., Jones, D. B. A., Horowitz, L. W., Fusco, A. C., Brenninkmeijer, C. A. M., Prather, M. J., Wofsy, S. C., and McElroy, M. B.: Three-dimensional climatological distribution of tropospheric OH: Update and evaluation, J. Geophys. Res.-Atmos., 105, 8931–8980, https://doi.org/10.1029/1999JD901006, 2000.

Spracklen, D. V., Jimenez, J. L., Carslaw, K. S., Worsnop, D. R., Evans, M. J., Mann, G. W., Zhang, Q., Canagaratna, M. R., Allan, J., Coe, H., McFiggans, G., Rap, A., and Forster, P.: Aerosol mass spectrometer constraint on the global secondary organic aerosol budget, Atmos. Chem. Phys., 11, 12109–12136, https://doi.org/10.5194/acp-11-12109-2011, 2011.

Storelvmo, T.: Aerosol Effects on Climate via Mixed-Phase and Ice Clouds, Annu. Rev. Earth Planet. Sci., 45, 199–222, https://doi.org/10.1146/annurev-earth-060115-012240, 2017.

Storelvmo, T., Kristjánsson, J. E., Lohmann, U., Iversen, T., Kirkevåg, A., and Seland, Ø.: Modeling of the wegener-bergeron-findeisen process – Implications for aerosol indirect effects, Environ. Res. Lett., 3, 045001, https://doi.org/10.1088/1748-9326/3/4/045001, 2008.

Tie, X., Brasseur, G., Emmons, L., Horowitz, L., and Kinnison, D.: Effects of aerosols on tropospheric oxidants: A global model study, J. Geophys. Res.-Atmos., 106, 22931–22964, https://doi.org/10.1029/2001JD900206, 2001.

Tonttila, J., Jarvinen, H., and Raisanen, P.: Explicit representation of subgrid variability in cloud microphysics yields weaker aerosol indirect effect in the ECHAM5-HAM2 climate model, Atmos. Chem. Phys., 15, 703–714, https://doi.org/10.5194/acp-15-703-2015, 2015.

Tsigaridis, K., Krol, M., Dentener, F. J., Balkanski, Y., Lathière, J., Metzger, S., Hauglustaine, D. A., and Kanakidou, M.: Change in global aerosol composition since preindustrial times, Atmos. Chem. Phys., 6, 5143–5162, https://doi.org/10.5194/acp-6-5143-2006, 2006.

Tsigaridis, K., Daskalakis, N., Kanakidou, M., Adams, P. J., Artaxo, P., Bahadur, R., Balkanski, Y., Bauer, S. E., Bellouin, N., Benedetti, A., Bergman, T., Berntsen, T. K., Beukes, J. P., Bian, H., Carslaw, K. S., Chin, M., Curci, G., Diehl, T., Easter, R. C., Ghan, S. J., Gong, S. L., Hodzic, A., Hoyle, C. R., Iversen, T., Jathar, S., Jimenez, J. L., Kaiser, J. W., Kirkevåg, A., Koch, D., Kokkola, H., Lee, Y., Lin, G., Liu, X., Luo, G., Ma, X., Mann, G. W., Mihalopoulos, N., Morcrette, J. J., Müller, J. F., Myhre, G., Myriokefalitakis, S., Ng, N. L., O'donnell, D., Penner, J. E., Pozzoli, L., Pringle, K. J., Russell, L. M., Schulz, M., Sciare, J., Seland, Shindell, D. T., Sillman, S., Skeie, R. B., Spracklen, D., Stavrakou, T., Steenrod, S. D., Takemura, T., Tiitta, P., Tilmes, S., Tost, H., Van Noije, T., Van Zyl, P. G., Von Salzen, K., Yu, F., Wang, Z., Wang, Z., Zaveri, R. A., Zhang, H., Zhang, K., Zhang, Q., and Zhang, X.: The AeroCom evaluation and intercomparison of organic aerosol in global models, Atmos. Chem. Phys., 14, 10845–10895, https://doi.org/10.5194/acp-14-10845-2014, 2014.

Twomey, S.: The Influence of Pollution on the Shortwave Albedo of Clouds, J. Atmos. Sci., 34, 1149–1152, https://doi.org/10.1175/1520-0469(1977)034<1149:TIOPOT>2.0.CO;2, 1977.

Twomey, S.: Aerosols, clouds and radiation, Atmos. Environ. A, 25, 2435–2442, https://doi.org/10.1016/0960-1686(91)90159-5, 1991.

Unger, N.: Human land-use-driven reduction of forest volatiles cools global climate, Nat. Clim. Change, 4, 907–910, https://doi.org/10.1038/nclimate2347, 2014.

Vehkamäki, H., Kulmala, M., Napari, I., Lehtinen, K. E. J., Timmreck, C., Noppel, M., and Laaksonen, A.: An improved parameterization for sulfuric acid–water nucleation rates for tropospheric and stratospheric conditions, J. Geophys. Res., 107, 4622, https://doi.org/10.1029/2002JD002184, 2002.

Volz, A. and Kley, D.: Evaluation of the Montsouris series of ozone measurements made in the nineteenth century, Nature, 332, 240–242, https://doi.org/10.1038/332240a0, 1988.

Wang, M., Ghan, S., Ovchinnikov, M., Liu, X., Easter, R., Kassianov, E., Qian, Y., and Morrison, H.: Aerosol indirect effects in a multi-scale aerosol-climate model PNNL-MMF, Atmos. Chem. Phys., 11, 5431–5455, https://doi.org/10.5194/acp-11-5431-2011, 2011.

Wang, Y. and Jacob, D. J.: Anthropogenic forcing on tropospheric ozone and OH since preindustrial times, J. Geophys. Res., 103, 31123–31135, https://doi.org/10.1029/1998JD100004, 1998.

Wang, Y., Liu, X., Hoose, C., and Wang, B.: Different contact angle distributions for heterogeneous ice nucleation in the Community Atmospheric Model version 5, Atmos. Chem. Phys., 14, 10411–10430, https://doi.org/10.5194/acp-14-10411-2014, 2014.

Wayne, R. P., Barnes, I., Biggs, P., Burrows, J. P., Canosa-Mas, C. E., Hjorth, J., Le Bras, G., Moortgat, G. K., Perner, D., Poulet, G., Restelli, G., and Sidebottom, H.: The nitrate radical: Physics, chemistry, and the atmosphere, Atmos. Environ. A, 25, 1–203, https://doi.org/10.1016/0960-1686(91)90192-A, 1991.

Williams, J., de Reus, M., Krejci, R., Fischer, H., and Ström, J.: Application of the variability–size relationship to atmospheric aerosol studies: estimating aerosol lifetimes and ages, Atmos. Chem. Phys., 2, 133–145, https://doi.org/10.5194/acp-2-133-2002, 2002.

Willis, M. D., Burkart, J., Thomas, J. L., Köllner, F., Schneider, J., Bozem, H., Hoor, P. M., Aliabadi, A. A., Schulz, H., Herber, A. B., Leaitch, W. R., and Abbatt, J. P.: Growth of nucleation mode particles in the summertime Arctic: A case study, Atmos. Chem. Phys., 16, 7663–7679, https://doi.org/10.5194/acp-16-7663-2016, 2016.

Woodhouse, M. T., Carslaw, K. S., Mann, G. W., Vallina, S. M., Vogt, M., Halloran, P. R., and Boucher, O.: Low sensitivity of cloud condensation nuclei to changes in the sea-air flux of dimethyl-sulphide, Atmos. Chem. Phys., 10, 7545–7559, https://doi.org/10.5194/acp-10-7545-2010, 2010.

Young, P. J., Archibald, A. T., Bowman, K. W., Lamarque, J.-F., Naik, V., Stevenson, D. S., Tilmes, S., Voulgarakis, A., Wild, O., Bergmann, D., Cameron-Smith, P., Cionni, I., Collins, W. J., Dalsøren, S. B., Doherty, R. M., Eyring, V., Faluvegi, G., Horowitz, L. W., Josse, B., Lee, Y. H., MacKenzie, I. A., Nagashima, T., Plummer, D. A., Righi, M., Rumbold, S. T., Skeie, R. B., Shindell, D. T., Strode, S. A., Sudo, K., Szopa, S., and Zeng, G.: Preindustrial to end 21st century projections of tropospheric ozone from the Atmospheric Chemistry and Climate Model Intercomparison Project (ACCMIP), Atmos. Chem. Phys., 13, 2063–2090, https://doi.org/10.5194/acp-13-2063-2013, 2013.

Yun, Y. and Penner, J. E.: An evaluation of the potential radiative forcing and climatic impact of marine organic aerosols as heterogeneous ice nuclei, Geophys. Res. Lett., 40, 4121–4126, https://doi.org/10.1002/grl.50794, 2013.

Zhang, K., Wan, H., Liu, X., Ghan, S. J., Kooperman, G. J., Ma, P. L., Rasch, P. J., Neubauer, D., and Lohmann, U.: Technical note: On the use of nudging for aerosol-climate model intercomparison studies, Atmos. Chem. Phys., 14, 8631–8645, https://doi.org/10.5194/acp-14-8631-2014, 2014.

Paper III

Strong constraints on aerosol-cloud interactions from volcanic eruptions

Florent F. Malavelle, Jim M. Haywood, Andy Jones, Andrew Gettelman, Lieven Clarisse, Sophie Bauduin, Richard P. Allan, **Inger Helene H. Karset**, Jón Egill Kristjánsson, Lazaros Oreopoulos, Nayeong Cho, Dongmin Lee, Nicolas Bellouin, Olivier Boucher, Daniel P. Grosvenor, Ken S. Carslaw, Sandip Dhomse, Graham W. Mann, Anja Schmidt, Hugh Coe, Margaret E. Hartley, Mohit Dalvi, Adrian A. Hill, Ben T. Johnson, Colin E. Johnson, Jeff R. Knight, Fiona M. O'Connor, Daniel G. Partridge, Philip Stier, Gunnar Myhre, Steven Platnick, Graeme L. Stephens, Hanii Takahashi and Thorvaldur Thordarson
Nature , 2017
doi:10.1038/nature22974

Paper IV

Exploring impacts of size-dependent evaporation and entrainment in a global model

Inger Helene H. Karset, Andrew Gettelman, Trude Storelvmo, Kari Alterskjær, Terje Koren Berntsen

Journal of Geophysical Research - Atmospheres, *in review*

Exploring impacts of size-dependent evaporation and entrainment in a global model

I. H. H. Karset[1], A. Gettelman[2], T. Storelvmo[1], K. Alterskjær[3], T. K. Berntsen[1,3]

[1]University of Oslo, Department of Geosciences, Section for Meteorology and Oceanography, Oslo, Norway
[2]National Center for Atmospheric Research, Colorado, USA
[3]CICERO Center for International Climate Research, Oslo, Norway

Key Points:

- Enhanced evaporation does not necessarily result in decreased cloud liquid water.
- Differences in cloud droplet sizes between PI and PD are too small for size-dependent evaporation, scaled by only surface area differences, to give large impacts on aerosol indirect effects.
- Size-dependent entrainment dampens the second aerosol indirect effect, but not as much as damping the dependency of cloud droplet number in rain formation calculations.

Corresponding author: Inger H. H. Karset, `i.h.h.karset@geo.uio.no`

Abstract

While most observations indicate well buffered clouds to aerosol perturbations, global models do not. Among the suggested mechanisms for this discrepancy is the models' lack of connections between cloud droplet size and two processes that can contribute to reduced cloudiness when droplets become more numerous and smaller; evaporation and entrainment. In this study, we explore different implementations of size-dependent evaporation and entrainment in the global atmospheric model CAM5.3-Oslo. We study their impact on the preindustrial-to-present day change in liquid water path (LWP_{PD-PI}) and the corresponding aerosol indirect effect (AIE_{PD-PI}). Impacts of the 2014-2015 fissure eruption in Holuhraun, Iceland, are also presented. Our entrainment modifications only have a moderate effect on AIE_{PD-PI} (changes from -1.07 Wm^{-2} to -0.98 Wm^{-2}), and a small impact on the signal from the Holuhraun eruption compared to other suggested compensating mechanisms. Simulations with added size-dependent evaporation in the top of the stratiform clouds also show small evaporation differences between PI and PD. Moderate changes in AIE_{PD-PI} were achieved when also including an entrainment feedback to the evaporation changes, mixing air between the cloudtop layer and the layer above. These changes were not associated with the size-dependency, but changes in the cloud susceptibility to aerosols in both PI and PD when adding evaporation. We find that increased evaporation of smaller droplets at stratiform cloud tops can reduce LWP, but can increase LWP in some areas due to enhanced shallow convection caused by destabilization.

1 Introduction

Aerosol-cloud interactions are singled out by the Intergovernmental Panel on Climate Change (IPCC) as the largest contributor to the uncertainty in present day global radiative forcing (Boucher et al., 2013; Myhre et al., 2013). An increase in the atmospheric aerosol concentration usually favors more numerous, but smaller cloud droplets that scatter more of the incoming solar radiation back to space (Twomey, 1977). The uncertainty in this so-called "Twomey effect", "albedo effect" or "first aerosol indirect effect" has been reduced during the last decades, and there is strong confidence that it is cooling the climate on a global scale (Bréon et al., 2002; Feingold et al., 2003; Quaas et al., 2008; Lebsock et al., 2008; Bellouin et al., 2013; Ghan et al., 2016; McCoy et al., 2017). However, estimates of the total magnitude of radiative effects by aerosol-cloud interactions remain highly uncertain, mainly due to the modulation of clouds through fast cloud adjustments that follow a reduction in cloud droplet size. This effect is often referred to as the "second aerosol indirect effect". Since smaller cloud droplets decrease the efficiency of precipitation formation by suppressing the collision-coalescence process, aerosols may increase the water content and the lifetime of clouds (Albrecht, 1989; Pincus & Baker, 1994). This is illustrated in the left branch of Fig. 1, which shows how different cloud processes can affect LWP when the cloud droplet size is reduced. This so-called "Albrecht effect" or "lifetime effect" has, for a long time, been the only cloud process included in global models that can affect how aerosol perturbations impact cloud water content or extent through cloud physics (Neale et al., 2012; K. Zhang et al., 2012; Kirkevåg et al., 2013; Walters et al., 2014; Kirkevåg et al., 2018). As a consequence, estimates by these models of the total effective radiative forcing through aerosol-cloud interactions (ERF_{aci}, including both the first and the second aerosol indirect effect) are not complete (Boucher et al., 2013).

Several recent studies have shown a muted response, and sometimes even a reduction in LWP when cloud droplet concentrations (N_c) or aerosol number concentrations (N_a) increase. Studies of correlations between LWP and N_a from satellites have shown both positive and negative signals (Quaas et al., 2009; M. Wang et al., 2012; Chen et al., 2014; Lebsock et al., 2008), but the reliability of these results as measures of LWP responses to aerosol perturbations are questionable due to the difficulty of measuring aerosols

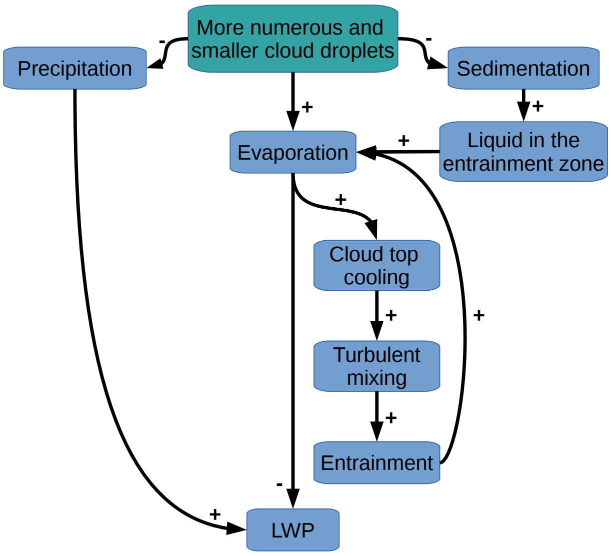

Figure 1. Fast cloud adjustments that follow a reduction in cloud droplet size.

and clouds simultaneously. Toll et al. (2017, 2019) compared satellite measurements of clouds downwind of known aerosol sources, like cities, volcanoes, shiptracks and fires, to unpolluted clouds nearby, showing a weak average decrease in LWP in the polluted clouds. Gryspeerdt et al. (2019) found both positive and negative relations between N_c and LWP, with a domination of reduced LWP in clouds with high N_c. McCoy et al. (2018) used a combination of satellite measurements and aqua planet simulations to show that high values of LWP in midlatitude cyclone clouds are associated with high values of N_c. Malavelle et al. (2017) studied satellite retrievals of LWP during the 2014-2015 fissure eruption in Holuhraun, finding no significant increase in LWP compared to previous years. Thus the sign of the second aerosol indirect effect is under debate, which makes it worth investigating cloud processes that can contribute to a reduction in cloudiness associated with increased aerosol loadings.

Sensitivity tests turning off the dependency of precipitation on droplet number in global models have shown better agreement with observations (Quaas et al., 2009; M. Wang et al., 2012; Gettelman et al., 2013; Gettelman, 2015; Malavelle et al., 2017), but can not explain situations where LWP decreases with increased droplet concentrations. Another suggested reason for observed constant or decreasing LWP with increasing aerosol loading is the lack of representation of processes in the models that buffer cloud responses to aerosol perturbations (Stevens & Feingold, 2009). Some of these processes are seen in Fig. 1. The middle branch shows that more numerous, but smaller droplets results in more evaporation. This size dependent evaporation mechanism is not represented in most global models (Ackerman et al., 2004; Malavelle et al., 2017; Zhou & Penner, 2017). As for the growth rate of cloud droplets by condensation, the rate of evaporation also varies with the cloud droplet size. The characteristic phase relaxation time, $\tau \propto (Nr)^{-1}$ (Squires, 1952a, 1952b), where N is the cloud droplet number concentration and r is the mean radius of the cloud droplets, is used as a measure of the conversion rate between the liquid and the vapor phase. If a clean cloud (N_1, r_1) is perturbed to a polluted cloud $(N_2 > N_1, r_2 < r_1)$ and the total liquid water content (M_c) is conserved, the phase relaxation time is reduced (see Supplementary Information, Sect. S1), so that

$$\tau_1 > \tau_2. \tag{1}$$

This change in τ is due to the larger total surface area compared to the total volume of the more numerous but smaller cloud droplets in the polluted cloud.

As seen in Fig. 1, enhanced evaporation of cloud water will not only directly result in decreased LWP, but also trigger other fast feedback processes. When water at the cloudtop evaporates, the temperature drops, which promotes sinking of air masses, enhancing the turbulent mixing and entrainment of air from above, which again can result in more evaporation. Results from fine-scale modeling have shown examples of decreased cloud fraction and LWP caused by increased aerosol loading, probably due to enhanced evaporation and evaporation-entrainment feedbacks when the droplets become smaller (Ackerman et al., 2004; Jiang & Feingold, 2006; Feingold et al., 2006; Xue & Feingold, 2006; Xue et al., 2008; Altaratz et al., 2008; Hill et al., 2009; Zhou & Penner, 2017). Small et al. (2009) presents observations from a flight campaign of non-precipitating clouds that support these results. Bretherton et al. (2007) also points out that sedimentation of droplets away from the entrainment zone is suppressed when droplets are smaller, which can result in more liquid water available for evaporation in the entrainment zone, more evaporation and thus enhanced entrainment efficiency and reduced LWP. This is seen in the right branch of Fig. 1.

The aim of this study is to implement size-dependent evaporation and size-dependent entrainment into a global model and see how that affects the second aerosol indirect effect. The hypothesis is that enhanced evaporation and entrainment in a polluted cloud will counteract the increase in water content due to suppressed autoconversion. This will make a perturbed cloud less reflective compared to a similar cloud without size-dependency.

Size-dependent evaporation and entrainment are implemented separately into the model, and both setups are described in Sect. 3. The first part of the result section focuses on results from the evaporation cases, where the impact on LWP_{PD} is presented and analyzed in Sect. 4.1.1-4.1.2, the impacts on changes between PI and PD are presented and analyzed in Sect. 4.1.3, while Sect. 4.1.4 shows results from sensitivity tests with various implementations of the evaporation. Results from simulations with size-dependent entrainment are presented and analyzed in Sect. 4.2, with sensitivity test in Sect. 4.2.2. Although we know that aerosol concentrations have increased since preindustrial times, it is highly uncertain to which extent and how they have contributed to cloud changes (Boucher et al., 2013). Recent volcanic eruptions are on the other hand better documented and well observed by both satellites and ground based instruments, and can serve as testbeds when modelling aerosol-cloud interactions. In Sect. 4.3, we investigate how the inclusion of size-dependency affects the modelled changes in cloud properties caused by a volcanic eruption. We also compare the impact of implementing size-dependency to the impact of corrections of other processes that have been suggested to affect modelled aerosol indirect effects.

2 Model

2.1 General description

This study uses the global model CAM5.3-Oslo, which is the atmospheric component of the Norwegian Earth System Model (NorESM). While CAM4-Oslo was used in the first version of NorESM (Bentsen et al., 2013; Iversen et al., 2013; Kirkevåg et al., 2013) and CAM6-Oslo (under development) will be the atmospheric component of the second version of NorESM, CAM5.3-Oslo is an intermediate version of the atmospheric component, documented by Kirkevåg et al. (2018). It is based on the Community Atmospheric Model version 5.3 (Neale et al., 2012; Liu et al., 2016). The main difference between CAM5.3 and CAM5.3-Oslo is that the latter has its own aerosol module, OsloAero. This module is neither modal or sectional, but so-called "production tagged". In OsloAero, background tracers form lognormal distrubutions, but process-tracers resulting from con-

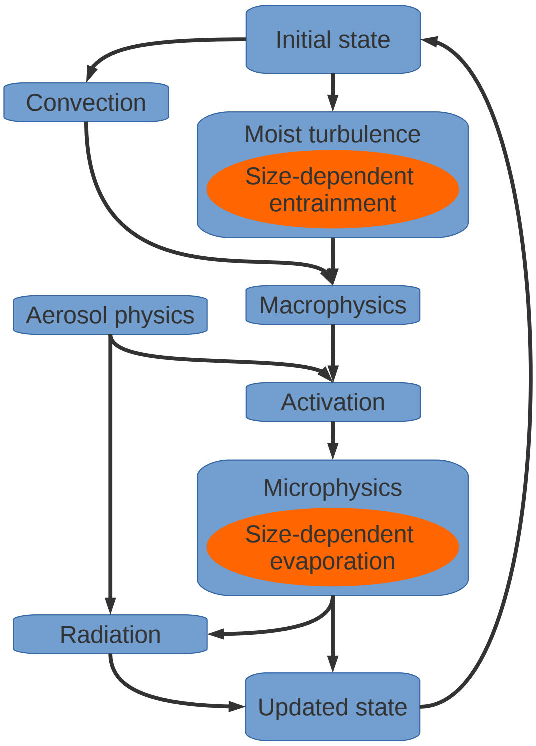

Figure 2. A simplified picture of the workflow in CAM5.3-Oslo. This figure does not include all parts of the model. It is meant as an illustration of the order of some of the most important processes governing the cloud physics. The orange boxes indicate where size-dependency is included in the modified simulations of this study, which will be described in detail in Sect. 3.

densation, coagulation and cloud processes change the shape of the distribution. Lookup tables produced by a sectional model are applied to obtain optical propterties. More detailed description of the module is found in Kirkevåg et al. (2018). The stratiform clouds are treated by the double moment bulk microphysics scheme MG1.5, which is almost the same as MG1 (Morrison & Gettelman, 2008; Gettelman et al., 2008), but with cloud droplet activation moved before the rest of the microphysical process rate calculations (Gettelman, 2015). The scheme applies autoconversion parameterizations based on Khairoutdinov and Kogan (2000). The treatment of shallow convective clouds and moist turbulence are based on work done at the University of Washington (Park & Bretherton, 2009; Bretherton & Park, 2009), while the parameterizations of deep convective clouds are based on G. J. Zhang and McFarlane (1995). Aerosols are activated following Abdul-Razzak and Ghan (2000). The macrophysics is described in Park et al. (2014) and includes saturation adjustment.

The blue boxes and the arrows in between in Fig. 2 show the order of some of the most important processes in CAM5.3-Oslo that affect the cloud water mass, q_c, and droplet number, N_c. The aerosols are only impacting the stratiform clouds, which means that aerosol-cloud interactions lack from the convective clouds. Detrained convective condensate is added to the stratiform clouds, with a number concentration estimated by assuming a constant mean volume cloud droplet radius of 10 and 8 μm for shallow and deep convective clouds respectively. The implementation of size-dependency, indicated by the orange boxes in Fig. 2, are described later.

Emissions of aerosols and aerosol precursor gases, and the concentrations of greenhouse gases in the atmosphere follow the standard of the Coupled Model Intercomparison Project number 5 (CMIP5) (Lamarque et al., 2010). The atmospheric component is coupled to a satellite phenology version of the Community Land Model version CLM4.5 (Oleson et al., 2013) and an ocean with prescribed climatological sea surface temperatures and sea ice extent. Methods by Ghan (2013) are used for calculating the effective radiative forcing of aerosols. For more detailed descriptions of the model, see Kirkevåg et al. (2018) and Karset et al. (2018).

2.2 Configurations

The model was configured with 30 levels in the vertical and a horizontal resolution of 0.9° (latitude) by 1.25° (longitude). Nudged meteorology was applied to constrain the natural variability (Kooperman et al., 2012). This meteorology was generated by the model itself in an earlier simulation, applying all present day conditions (emissions, oxidants, land use, sea surface temperatures, etc.). The horizontal wind components and the surface pressure were nudged with a relaxation time scale of 6 hours, corresponding to a nudging intensity of 8.3 % when the timestep of the model is 30 minutes. The air temperature was freely evolving (K. Zhang et al., 2014), as were all other variables.

3 Experimental setup

To find out how the clouds in the model respond to aerosol perturbations, two simulations with the default model setup, N, were carried out. The simulations applied emissions of aerosol precursor gases, aerosols and prescribed oxidants from present day (PD, year 2000) and pre-industrial times (PI, year 1850) respectively. The simulation length is six years, where the last four are analyzed. Simulations from a previous study, applying a similar setup, showed a standard error of only 0.01 $\mathrm{Wm^{-2}}$ for the total aerosol indirect effect, and the same result, with no drift in the signal, when extending the simulation length to 11 years and analyzing the last 10 years (Karset et al., 2018). The results from the nudging simulations of that study were also in the uncertainty range of the simulated total aerosol indirect effect with free meteorology, running for 50 years, where the last 30 were analyzed. The impact of including size-dependency on the evaporation and the entrainment processes are investigated separately in the following sections.

3.1 Size-dependent evaporation

An additional evaporation is implemented in the top layer of clouds without ice. The argument of adding extra evaporation, on top of the one already calculated by the model itself, is that we assume the model is underestimating the amount of evaporation and entrainment, thus the reduction in cloud water, due to the lack of an evaporation-entrainment feedback parameterization. Size-dependent evaporation occurs in both warm and mixed-phased clouds, but we choose to only focus on the warm clouds to better understand the physical mechanisms behind the results, without possible impacts by complex processes including ice. In a later study, mixed-phase clouds should also be included. Figure 3(a) shows the effective radius of the cloud droplets in the top layer of stratiform clouds without ice in the default PD-simulation, while Fig. 3(b) shows the difference in the effective radius between PI and PD. The effective radius of cloud droplets in CAM5.3-Oslo is slightly lower than that of MODIS (Moderate Resolution Imaging Spectroradiometer) (Rausch et al., 2017), which we find acceptable due to the positive biases associated with the r_e-products coming from MODIS (Painemal & Zuidema, 2011; Liang et al., 2015). Changes in r_e between PI and PD are mostly negative, owing to the Twomey effect when aerosol concentrations increase. Positive areas over land are associated with reduced emissions from forest and grass fires since PI, while positive areas over remote oceans are due

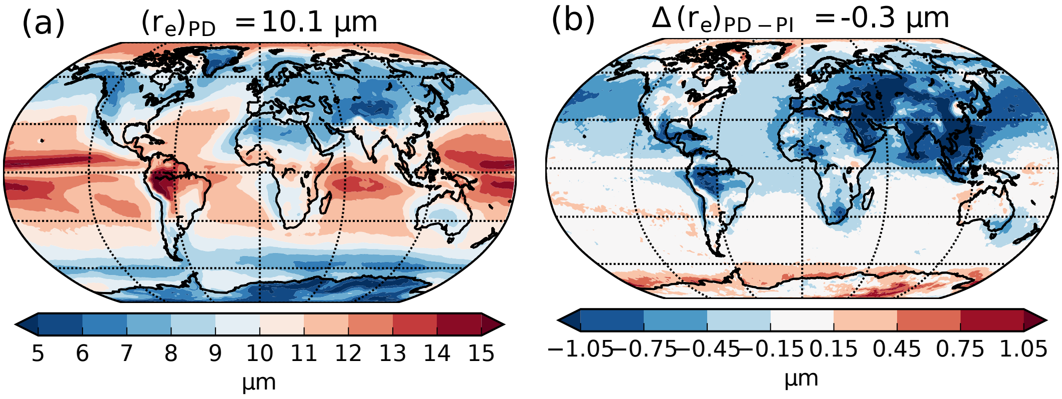

Figure 3. **(a)** Annual mean effective radius of the cloud droplets in the cloudtop layer of stratiform clouds without ice in the PD-simulation with default model setup. **(b)** Difference in effective radius between PI and PD.

to oxidant differences between PI and PD, resulting in a shift in the location of secondary aerosol formation (Karset et al., 2018).

As a first approach to the question of how size-dependent evaporation will affect cloud responses to aerosol perturbations, 5 % of the liquid in the cloudtop layer is evaporated if the cloud droplets are smaller than 4 μm. Since this can occur every timestep of 0.5 h, it results in an evaporation rate in the cloud top layer of up to 10 %h^{-1}. As we do not have good global constraints by observations of this quantity at this point, a higher evaporation factor of up to 50 % is also tested. This corresponds to an evaporation rate in the cloud top layer of up to 100 %h^{-1}.

The rate of evaporation depends on the surface area. If the total volume of water in a cloud, V, is constant, the total surface area, A, of all the cloud droplets is given as

$$A = \frac{3V}{r}. \tag{2}$$

Since A is proportional to r^{-1}, we let the additional evaporation of droplets larger than 4 μm also vary with r^{-1}. This results in an evaporation rate seen in Fig. 4(a). The horizontal distribution of the evaporation rate from the PD-simulation is seen in Figure 4(b) with its global mean value in the heading.

The standard evaporation calculations in the model is a part of the macrophysics (see Fig. 2). The evaporation changes in this study are applied to the model code right after the microphysics (see Fig. 2). One reason why we do not add it right after the standard evaporation in the macrophysics is the way activation is calculated. The activation process makes assumptions based on saturation-adjustment, which is not the case if we add extra evaporation. If trying to evaporate cloud droplets between the macrophysics and activation, the scheme will activate back the number, but not the mass, resulting in an unphysical reduction in cloud droplet size. Another reason why the code changes are applied where they are is because a the residual condensation term in the microphysics scheme that condenses all excess vapor before entering radiation. With our implementation, excess vapor will condense in the next timestep, but not before the condensation calculations in the macrophysics scheme. This allows our changes to affect both radiation, turbulence, entrainment, convection and detrainment (see Fig. 2).

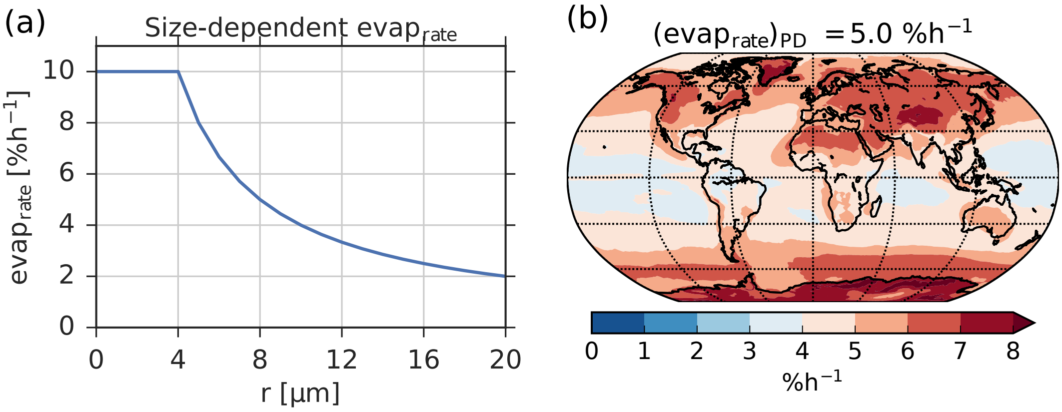

Figure 4. **(a)** Evaporation rate of the liquid in the cloudtop layer as a function of the effective radius of the cloud droplets. **(b)** Horizontal distribution of the evaporation factor in the PD simulation where additional size-dependent evaporation is applied.

Table 1. Overview of the main setups applied for the inclusion of size-dependent evaporation. CT is the cloudtop layer, while CT+1 is the layer above. More simulations exploring the sensitivity of different uncertain choices are presented in Sect. 4.1.4.

Casename	Move between CT and CT+1	max $evap_{rate}$ [%h^{-1}]	Mixing type
EVAP_NOMIX	-	10	50-50^a
EVAP_NOMIX_HIGH	-	100	50-50^a
EVAP_MIX	released q_v and θ, moist and dry air (q_v,θ)	10	50-50^a

^{a}50-50 means an equal mix between homogeneous and heterogeneous mixing.

When water evaporates, vapor is released and the temperature drops. The change in vapor can be implemented in the model in different ways, and several options were tested in this study by different sets of PD- and PI-simulations. The main part of this study will focus on the three setups listed in Tab. 1, while others will be studied and presented in Sect. 4.1.4. In EVAP_NOMIX and EVAP_NOMIX_HIGH, the released vapor is kept inside the same gridbox as the evaporation of cloud water occurred. These setups indicate no vertical mixing between the cloudtop layer (CT) and the layer above (CT+1). In EVAP_MIX, the evaporation is assumed to either stem from mixing of air from above the cloudtop or that it initiates downdrafts at the cloudtop due to evaporative cooling, which also contributes to enhanced turbulence, entrainment and mixing of air between the cloudtop layer and the layer above (see Fig. 1). The released vapor is therefore moved one layer up. The released vapor is given as $q_c \cdot evap_{rate}$, where q_c is the liquid water content in the cloudtop layer. When this mass moves, the air around also moves. Due to conservation of mass, the same amount of air moves down from the layer above the cloudtop and mixes into the cloudtop layer. This is taken into account in EVAP_MIX. The mixed variables are mixing ratio of water vapor (q_v, [kgkg^{-1}]) and potential temperature (θ, [K]). The amounts are calculated as follows in Eq. (3-6).

$$\Delta q_{v,CT} = evap_{rate} \cdot CF \cdot \frac{m_{v,CT+1} - m_{v,CT}}{\rho_{a,CT}} \cdot dt \tag{3}$$

$$\Delta q_{v,CT+1} = -evap_{rate} \cdot CF \cdot \frac{m_{v,CT+1} - m_{v,CT}}{\rho_{a,CT+1}} \cdot dt \tag{4}$$

$$\Delta \theta_{CT} = evap_{rate} \cdot CF \cdot \frac{T_{CT+1} - T_{CT}}{\nu_{CT}} \cdot dt \tag{5}$$

$$\Delta \theta_{CT+1} = -evap_{rate} \cdot CF \cdot \frac{T_{CT+1} - T_{CT}}{\nu_{CT+1}} \cdot dt \tag{6}$$

CF is the cloud fraction in the layer the evaporation occurred, m_v is the mass of water vapor [kgm^{-3}], ρ_a is the air density [kgm^{-3}] and ν is a factor converting from absolute temperature, T, to potential temperature, θ. $\nu = \left(\frac{p_s}{p}\right)^{c_p}$. Sensitivity simulations with different choices of which quantities to move between CT and CT+1 are also carried out and analyzed in Sect. 4.1.4.

The mixing of cloudy air with drier air from outside the edges of a cloud can take place in different ways, resulting in different impact on the cloud droplet number concentration after the following evaporation (Latham & Reed, 1977; Baker et al., 1980). The two extremes are commonly referred to as homogeneous and extreme inhomogeneous mixing (Korolev et al., 2015; Pinsky et al., 2015; Lehmann et al., 2009). Homogeneous mixing occurs on a much shorter time scale than evaporation. The drier air has time to be mixed with all the cloudy air, which results in some evaporation of all droplets. In this scenario, none of the droplets evaporate completely, keeping the cloud droplet number concentration constant. This is illustrated in the left column of Fig. 5. On the other hand, extreme inhomogeneous mixing will evaporate some droplets completely, keeping the sizes of the remaining droplets the same due to the much slower mixing than evaporation. This is illustrated in the right column of Fig. 5. A number of observational based studies have documented that both types of mixing, and also a mix between the two, can occur in liquid clouds, but it is not well understood when and under which conditions one or the other will take place (Painemal & Zuidema, 2011; Freud et al., 2011; Korolev et al., 2015). We use a 50 % mix between the two, but results from simulations with purely homogeneous and purely extreme inhomogeneous mixing (from now referred to as heterogeneous mixing) are also shown in Sect. 4.1.4.

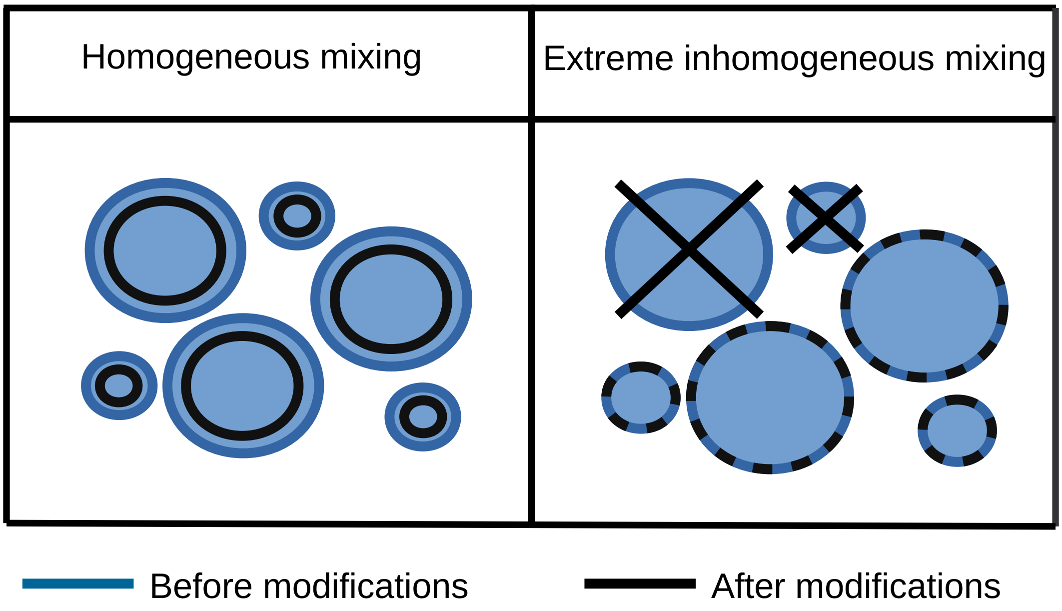

Figure 5. An overview of how different sized cloud droplets are treated in the simulations with size-dependent evaporation. For the homogeneous mixing case (left column), all droplets evaporate to some extent, but the number stays the same. For the extreme inhomogeneous mixing case (right column), some droplets evaporate completely, while the others remain unchanged. Exteme inhomogeneous mixing are also reffered to as heterogeneous mixing in this paper.

3.2 Size-dependet entrainment

The entrainment rate at the top of stratiform clouds in the model is calculated within the moist turbulence scheme, based on Bretherton and Park (2009), which again is based on the entrainment closure of Nicholls and Turton (1986). Its strength is, among others, given by an entrainment efficiency factor, A, which is affected by the evaporative cooling at the cloudtop. A is given by Eq. (7),

$$A = 0.1\left(1 + \frac{0.8a_2 L_v q_l}{\Delta s}\right) \tag{7}$$

where L_v is the latent heat of vaporization, q_l is the liquid water content at the cloudtop, and Δs is the jump of mean liquid static energy across the entrainment interface. a_2 is a tuning parameter that is commonly used to tune global models with a CAM-based atmospheric component to retrieve radiative balance and a realistic cloud deck. Bretherton and Park (2009) uses $a_2 = 15$, based on observations by Stevens and Feingold (2009) and Caldwell et al. (2005), while Nicholls and Turton (1986) bases their choice of $a_2 = 60$ on aircraft measurements. Bretherton and Park (2009) suggest tuning of a_2 within the range of 10−100. The default value of a_2 in CAM5.3-Oslo is 30. In this study, size-dependent entrainment is implemented in the model by letting a_2 vary with the effective radius of the cloud droplets in the cloudtop layer. As a first approach, the values in Eq. (8) are applied.

$$\begin{aligned} a_2 &= 100, & r_e &< 4\ \mu m \\ a_2 &= 400 r_e^{-1}, & r_e &> 4\ \mu m \end{aligned} \tag{8}$$

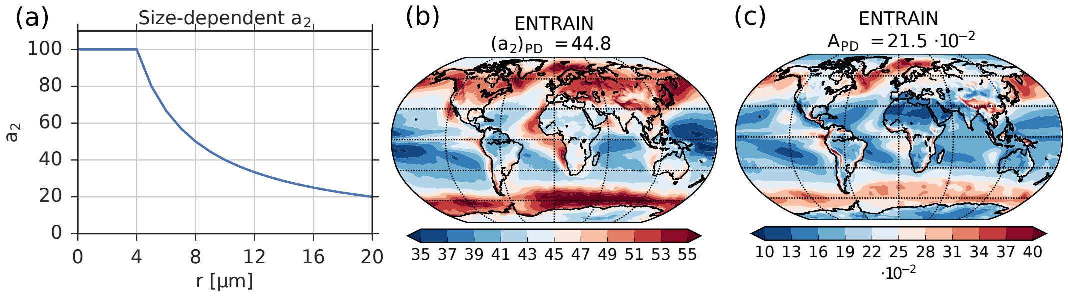

Figure 6. **(a)** a_2 as a function of the effective radius in the cloudtop layer when entrainment closure is calculated. **(b)** Horizontal distribution of the tuning parameter a_2. **(c)** Horizontal distribution of the entrainment efficiency factor, A, in the PD-simulation.

This is also seen in Fig. 6(a). The r^{-1} relation is applied for the same reason as for the evaporation case. The horizontal distribution of a_2 and A from the PD-simulation is seen in Fig. 6(b-c).

4 Results

4.1 Size-dependent evaporation

4.1.1 PD-changes in LWP

Before looking at changes in LWP between PI and PD caused by differences in the additional size-dependent evaporation, we first examine how LWP in the PD-simulations of EVAP_NOMIX, EVAP_NOMIX_HIGH and EVAP_MIX (see Tab. 1) differ from that of the original default model setup, N (Fig. 7(a)). Results from EVAP_NOMIX in Fig. 7(b) shows that evaporating up to 10 $\%\text{h}^{-1}$ of the liquid in the cloudtop layer has a negligible effect on LWP when keeping all changes inside the gridbox of evaporation. In EVAP_NOMIX_HIGH, the maximum evaporation rate is tuned up. Fig. 7(c) shows that this results in a change in global mean LWP of -3.7 gm^{-2} (-6.9 %). Since the simulations are carried out with the use of nudging, the signal vary little from year to year, with a standard error of 0.1 gm^{-2} for LWP. When allowing the evaporated liquid and the surrounding air masses to be mixed with the layer above, LWP changes as shown in Fig. 7(d). The global mean value in Fig. 7(d) is negative, but there are areas with large positive values, especially outside the west coast of Africa.

4.1.2 How can LWP_{PD} increase with increased evaporation?

When adding evaporation, reduced LWP is expected. The result from EVAP_MIX in Fig. 7(d) shows that the opposite can occur. A closer look at the mechanisms behind this signal indicates that this is linked to changes in shallow convection. Figure 8 shows that the frequency of occurence of shallow convection is enhanced in many of the same areas as LWP_{PD} increase in EVAP_MIX. Enhanced shallow convection can be caused by reduced CIN (convective inhibition), which can occur when the gradient in virtual potential temperature is affected when the evaporation changes dry the cloudtop layer and moisten the layer above (Park & Bretherton, 2009). Figure S1 in the supplementary shows that this drying and moistening occur in the simulations of EVAP_MIX, especially in the regions where the vapor differences between the cloudtop layer and the layer above is large. Figure S2(a) in the supplementary shows reduced CIN in the same areas. When shallow convection is enhanced, more liquid cloud water is detrained to the stratiform clouds (Fig. S3 in the supplementary).

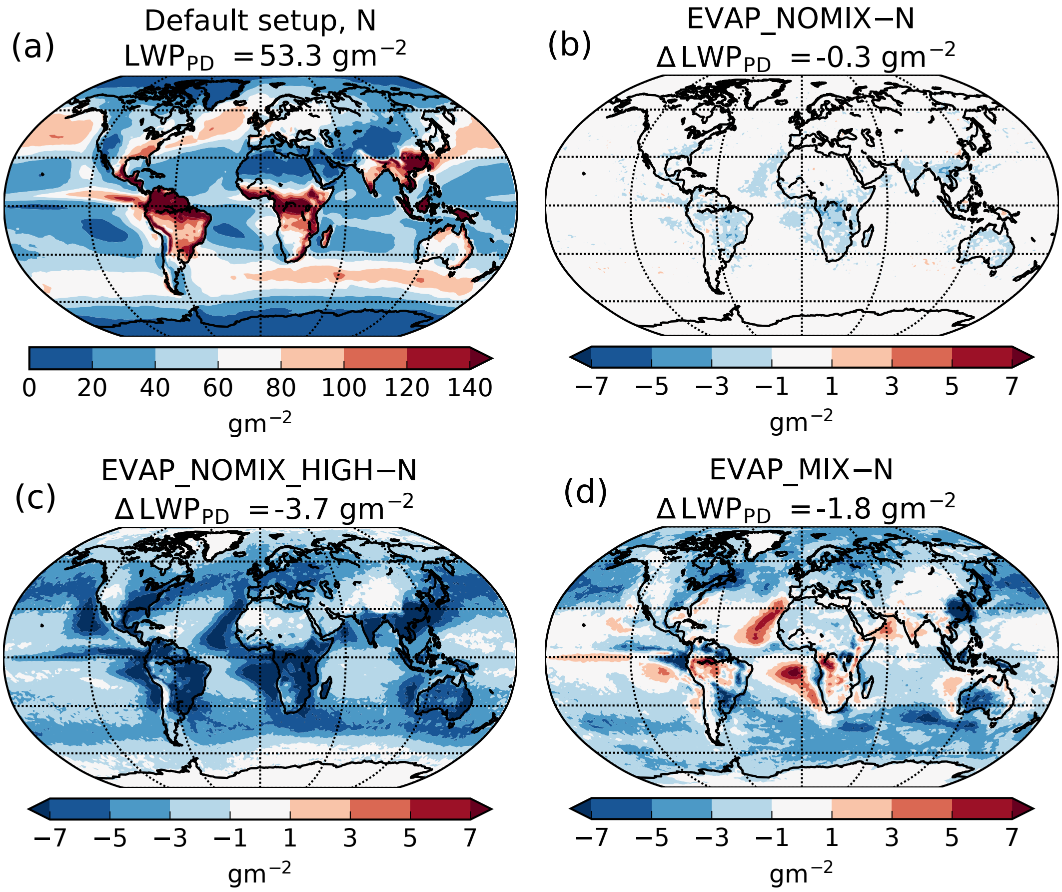

Figure 7. **(a)** Total gridbox average LWP in the PD simulation with default model setup, N. **(b-d)** Change in LWP in PD caused by enhanced evaporation in the setups EVAP_NOMIX **(b)** and EVAP_NOMIX_HIGH **(c)**, and EVAP_MIX **(d)**. Description of the setups are found in Tab. 1.

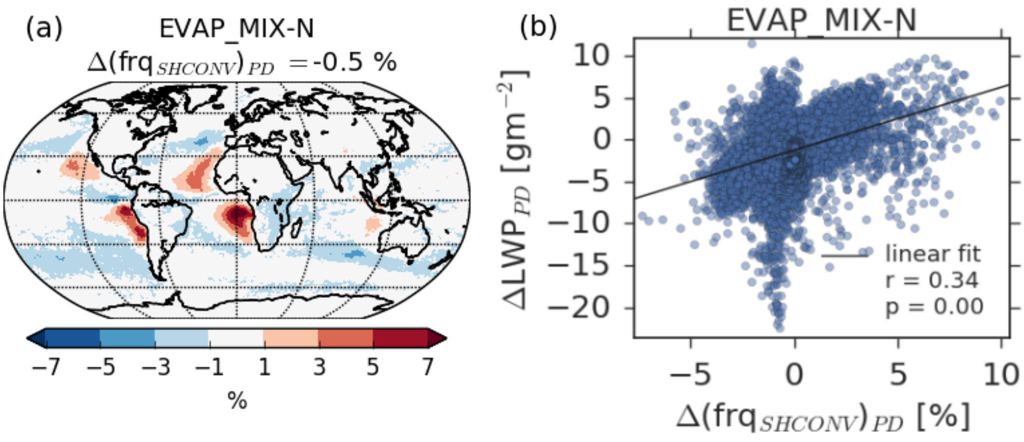

Figure 8. **(a)** Changes in frequency of occurrence of shallow convection when switching from the default model setup, N, to EVAP_MIX, where evaporation is enhanced for the smaller droplets and vertical mixing between the cloud top layer and the layer above is allowed. **(b)** Scatter plot showing how ΔLWP_{PD} from Fig. 7(d) correlate with $\Delta\text{frq}(_{SHCONV})_{PD}$ in (a). r is the Pearson's correlation coefficient and p is its respective p-value.

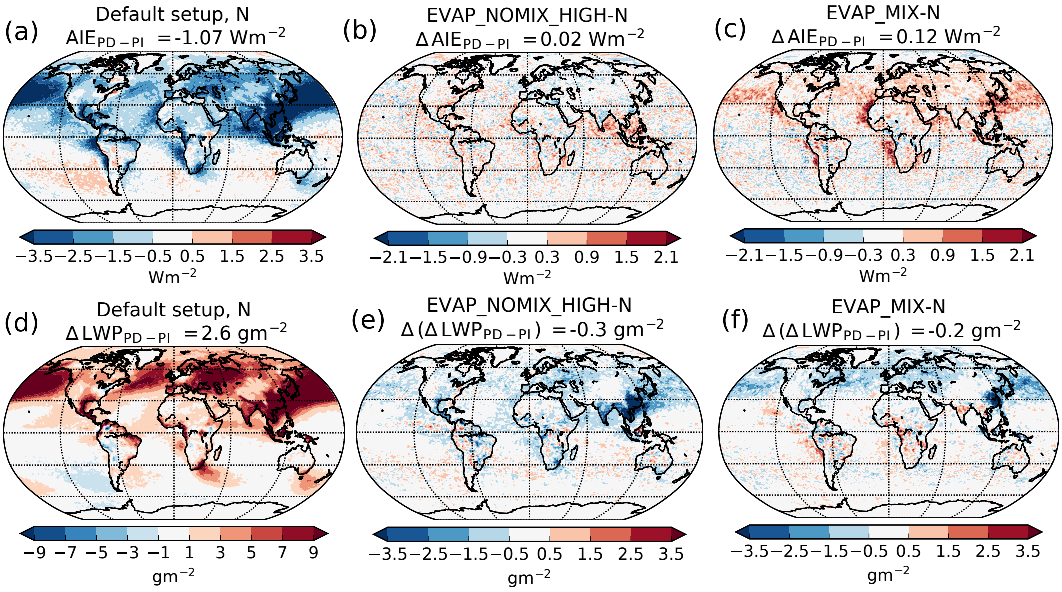

Figure 9. Total aerosol indirect effect (AIE_{PD-PI}) from simulations with default model setup, N. **(a)**. Change from N in AIE_{PD-PI} when adding evaporation with size-dependency to setups without (EVAP_NOMIX_HIGH) **(b)** and with (EVAP_MIX) **(c)** mixing between the cloudtop layer and the layer above. Change in LWP between PI and PD in the simulations with the default model setup **(d)**. Change from N in ΔLWP_{PD-PI} when adding evaporation with size-dependency to setups without (EVAP_NOMIX_HIGH) **(e)** and with (EVAP_MIX) **(f)** mixing between the cloudtop layer and the layer above.

While cloud top evaporation seems to enhance shallow convection through its impact on the stability, the Pearson's correlation coefficient in Fig. 8(b) is only weakly positive, indicating other mechanisms involved. Fig. S2(b) in the supplementary shows that the estimated inversion strength (EIS), which is a good indicator for the stratiform cloud cover (Wood & Bretherton, 2006), decreases in the same areas. While unstable regimes favor convective clouds, stable regimes favor stratiform cloud formation, trapping the moisture under the inversion. When the inversion strength is reduced, the cloud can break up, and LWP is reduced. The combination of reduced LWP due to evaporation, enhanced LWP due to shallow convection, and reduced LWP due to reduced EIS, give us a complex picture of the LWP response to enhanced evaporation of small droplets in EVAP_MIX seen in Fig. 7(d).

4.1.3 Changes in aerosol indirect effects due to evaporation

Figure 9 shows how the total aerosol indirect effect (AIE_{PD-PI}) and the LWP change between PI and PD are affected when size-dependent evaporation is added. The left column shows results from the default model setup. The middle column shows results from the simulation EVAP_NOMIX_HIGH (see Tab. 1). Figure 9(b) shows a negligible impact on AIE_{PD-PI}, even though we look at the case with high additional evaporation rate. Since the implementation of this effect resulted in a reduction in LWP of 6.9 % (see Fig. 7(c)) in the PD-simulation, and a corresponding change in radiative balance on the top of the atmosphere of 1.09 Wm^{-2} (not shown here), the lack of result on AIE_{PD-PI} is not due to weak evaporation. It is also not caused by PD-PI differences in compensating processes due to for example residual condensation or feedbacks on other processes, such as convection and mixing, since the evaporation modifications are implemented right before the radiation calculations in the code. The lack of a result stems from the r^{-1}-relation giving a small difference in the amount of evaporated liquid between PI and PD, resulting in the small change in ΔLWP_{PD-PI} seen in Fig. 9(e). Even though the global mean evaporation rate for the additional evaporation in the cloudtop layer of the PD-simulation of EVAP_NOMIX_HIGH is as high as 51 $\%h^{-1}$, it is only 1.4 $\%h^{-1}$ lower in the corresponding PI-simulation. As described in Sect. 3.1, the r^{-1}-relation stems from surface area to volume relation of a collection of cloud droplets, and the assumption of the strength of the evaporation being proportional to the total cloud droplet surface area. Going away from the r^{-1}-relation means going away from this assumption.

When also including vertical mixing between the cloudtop layer and the layer above after the evaporation (case EVAP_MIX), AIE_{PD-PI} gets less negative (Fig. 9(c)) , which was our expected change when implementing size-dependent evaporation. This occurs even though we only allow for up to 10 $\%h^{-1}$ additional evaporation rate for the smaller droplets. But, when looking at Fig. 9(f), which shows how the change in LWP between PI and PD (ΔLWP_{PD-PI}) differs compared to the default model simulations, N, it is clear that the change in AIE_{PD-PI} does not correspond everywhere with the change in ΔLWP_{PD-PI}, at least not south of 30 °N. The hypothesis before this study was that the higher aerosol concentration in PD would evaporate more liquid in PD compared to that in PI due to the larger total cloud droplet surface area, dampening the positive signal in ΔLWP_{PD-PI} in Fig. 9(d) caused by suppressed autoconversion, giving negative patterns in Fig. 9(f). This could have been the reason for the signal north of 30 °N, where ΔLWP_{PD-PI} is negative and AIE_{PD-PI} is positive, but we question this link since EVAP_NOMIX showed almost equal dampening in the change in LWP_{PD-PI}, without any impact on AIE_{PD-PI}. Since analysis in Sect. 4.1.2 showed that adding evaporation to the PD-simulation EVAP_MIX did not result in reduced LWP everywhere, but also increased LWP some places due to enhanced shallow convection, positive signals in Fig. 9(f) are expected. Positive patterns in Fig. 9(f) means that LWP changes more between PI and PD compared to that of the default setup. This should result in more negative AIE_{PD-PI} in these regions than what seen in Fig. 9(a), which is not the case. Neither changes between PI and PD in the effective radius ($\Delta(\Delta r_{e,PD-PI}) = -0.0$ μm), cloud droplet number concentration ($\Delta(\Delta N_{d,PD-PI}) = -1.5$ cm^{-3}) or cloud fraction ($\Delta(\Delta CF_{PD-PI}) = -0.0$ %) caused by the implemented size-dependent evaporation correspond with ΔAIE_{PD-PI} in Fig. 9(c). The positive signal in ΔAIE_{PD-PI} in Fig. 9(c) must stem from changes in the susceptibility of the clouds to aerosol perturbations when adding extra evaporation, rather than effects from the size-dependency. Section 4.1.2 showed that adding more evaporation at the cloud tops facilitates shallow convective clouds rather than stratiform clouds in some areas. The former is associated with reduced horizontal extent, promoting a reduction in the total cloud fraction, giving a global mean absolute change in total cloud fraction of -1.8 % from that of the default model setup in PD. Clouds with reduced horizontal extent no longer have the same potential to impact the radiative balance when imposing an aerosol perturbation through their reduced cloud weighted susceptibility (Alterskjær et al., 2012; Karset et al., 2018). With the same imposed aerosol perturbation in the different setups, this change in cloud weighted susceptibility could explain the dampening of the total aerosol indirect effect seen in Figure 9(c).

4.1.4 Sensitivity tests - Evaporation

Five sets of simulations are carried out to study how sensitive our results are to the treatment of exchange of mass between the cloudtop layer and the layer above followed by the evaporation, and to the type of mixing. Table 2 gives an overview of the simulations. It also includes the three simulations discussed earlier in this paper for comparison. When it comes to the exchange of mass between the layers, the similar results between EVAP_MIX and EVAP_MIX3, where moist air is mixed between the layers, clearly shows that the previously discussed signals in ΔAIE_{PD-PI} and ΔLWP_{PD} come when not only mixing the released vapor and temperature (EVAP_MIX2) or the released va-

Table 2. Overview of the simulations with additional size-dependent evaporation. CT is the cloudtop layer, while CT+1 is the layer above. Cases in bold are discussed in the main part of this paper. The changes are values compared to those of the default model setup, N.

Casename	Move between CT and CT+1	max $evap_{rate}$ [%h^{-1}]	Mixing type	ΔLWP_{PD} [gm^{-2}]	ΔAIE_{PD-PI} [Wm^{-2}]
EVAP_NOMIX	-	10	50-50	-0.3	-0.04
EVAP_NOMIX_HIGH	-	100	50-50	-3.7	+0.02
EVAP_NOMIX_HIGH_HOMO	-	100	HOMO	-3.4	+0.02
EVAP_NOMIX_HIGH_HETERO	-	100	HETERO	-4.0	+0.02
EVAP_MIX	released q_v and θ, moist and dry air (q_v,θ)	10	50-50	-1.8	+0.12
EVAP_MIX2	released q_v and θ,	10	50-50	-1.1	+0.01
EVAP_MIX3	released q_v and θ, moist air (q_v)	10	50-50	-1.8	+0.12
EVAP_MIX4	released q_v and θ, dry air (θ)	10	50-50	-1.1	+0.02

[a] 50-50 means an equal mix between homogeneous and heterogeneous mixing.

por, temperature and dry air (EVAP_MIX4), but also the moist air (EVAP_MIX3). Assuming purely homogeneous mixing slightly reduces the impact on ΔLWP_{PD}, while purely heterogeneous mixing has the opposite effect. This could be due to their different impact on the cloud droplet size, resulting in different autoconversion rates. Homogeneous mixing results in smaller droplets, which suppresses the autoconversion rate, contributing to a less negative signal in ΔLWP_{PD} for EVAP_NOMIX_HIGH_HOMO compared to the other setups. In our study, the mixing assumption does not affect ΔAIE_{PD-PI}, but this is probably due to the small difference in evaporation factor between PI and PD. With larger differences in the evaporation between PI and PD, using purely heterogeneous mixing would probably enhance the signal due to the same reasons as for ΔLWP_{PD}.

4.2 Size-dependent entrainment

4.2.1 Changes in aerosol indirect effects due to entrainment

Figure 10 shows how the total aerosol indirect effect and the change in LWP between PI and PD are affected when adding size-dependency on the entrainment rate at the top of the clouds. As seen in Fig. 6(a), the entrainment is more efficient for the smaller droplets in PD compared to those in PI (Fig. 3(b)), resulting in a less negative indirect effect in the case named ENTRAIN compared to that of the default model setup ($\Delta AIE_{PD-PI} =$ 0.09 Wm^{-2}, 8.4 %), as seen in Fig. 10. Parts of this result are caused by a reduction in the increase in LWP between PI and PD ($\Delta LWP_{PD-PI} =$ -0.19 gm^{-2}, 7.3 %). While enhanced evaporation resulted in various complex responses in LWP, the signal due to enhanced entrainment is more as expected, with reduced LWP in all areas with enhanced entrainment (not shown here). As for the result in EVAP_MIX, dampened indirect effect could be due to changes in the the susceptibility rather than due to the difference in cloud droplet size between PI and PD, but one of the sensitivity tests in the following section shows that this is not the case.

4.2.2 Sensitivity tests - Entrainment

Four sets of simulations are carried out to study how sensitive our results are to the entrainment modifications. Table 3 gives an overview of the simulations. It also includes the simulations discussed in the previous section for comparison. As seen in Fig. 6(b), the global mean value of a_2 in ENTRAIN_PD is 44.8, which is higher than that of the default model setup (30.0). A higher value of a_2 means stronger entrainment efficiency, which eventually results in a reduction in the cloud water content. This can change how susceptible clouds are to aerosol perturbations, meaning that the result seen in Fig. 10 could be a result of this rather than size-dependency. To check if this is the case, the sensitivity test ENTRAIN_CONST is carried out applying the same constant high a_2-value of 44.8 in both PI and PD. These simulations only gave a change in ΔAIE_{PD-PI} of +0.02 Wm^{-2} compared to that of the default model setup, indicating that most of the signal in Fig. 10(a) stems from the size-dependency rather than susceptibility changes.

Even though some observations suggest a_2-values ranging from 10-100 (see Sect. 3.2), large uncertainties are still associated with this parameter. In ENTRAIN_HIGHLIM, larger values of a_2 are allowed. The results in Tab. 3 show that this increases ΔAIE_{PD-PI} slightly, but not much, probably due to its similar high impact in PI and PD. Going away from the r^{-1}-relation could create larger differences between the eras. This means allowing for evaporation or entrainment differences caused by other reasons than the surface area difference. One such reason could be that smaller droplets often are associated with more liquid water due to dampened autoconversion, thus even larger total surface area. In ENTRAIN_HIGHSENS, the sensitivity of cloud droplet size is increased, and the relation $r^{-1.5}$ is applied. The results from ENTRAIN_HIGHSENS show almost the same ΔAIE_{PD-PI} as ENTRAIN_PD, probably due to the reduction in global mean value of a_2 in both PI and PD. By combining higher sensitivity to cloud droplet size and higher

Table 3. Overview of the simulations with size-dependent entrainment. Case in bold is discussed in 4.2. The changes are values compared to those of the default model setup, N.

Casename	Relation	$a_{2,max}$	$\overline{a_{2,PD}}$	ΔLWP$_{PD}$ [gm^{-2}]	ΔAIE_{PD-PI} [Wm^{-2}]
ENTRAIN	$\frac{1}{r}$	100	44.8	-1.6	+0.09
ENTRAIN_CONST	const	44.8	44.8	-2.3	+0.02
ENTRAIN_HIGHLIM	$\frac{1}{r}$	200	89.4	-4.9	+0.11
ENTRAIN_HIGHSENS	$\frac{1}{r^{1.5}}$	100	31.5	+1.2	+0.10
ENTRAIN_HIGHSENSLIM	$\frac{1}{r^{1.5}}$	200	63.4	-2.8	+0.13

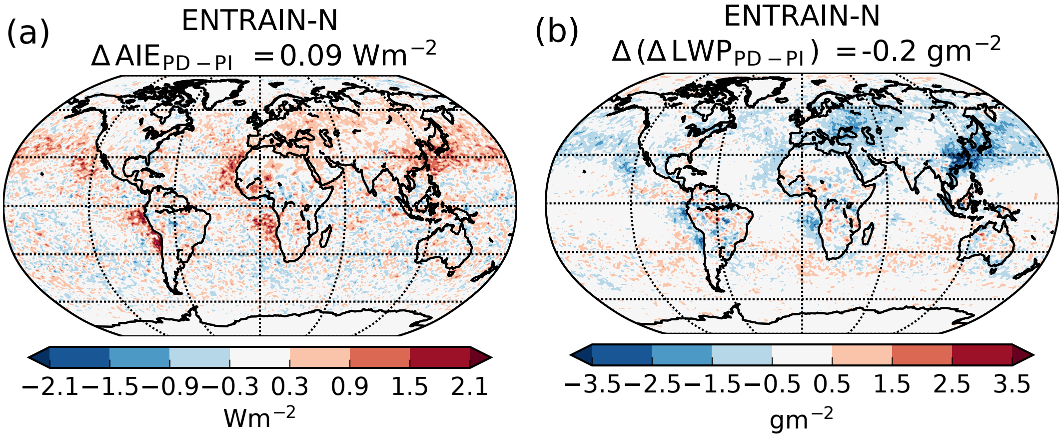

Figure 10. Difference in AIE_{PD-PI} between the cases ENTRAIN and N **(a)**. Positive values means that the total aerosol indirect effect with the setup ENTRAIN is less negative than that of the default setup, N. Difference in the change in LWP between the simulations from ENTRAIN and from N, when switching between PI and PD aerosols (b).

upper limit if a_2, ENTRAIN_HIGHSENSLIM gives the largest change in ΔAIE_{PD-PI} among our setups, but even with the doubling of the upper limit of a_2, and the much higher sensitivity of the entrainment rate to cloud droplet size, ENTRAIN_HIGHSENSLIM does not give more than a moderate impact on ΔAIE_{PD-PI} of 0.13 Wm^{-2}.

4.3 Size-dependency applied to the Holuhraun eruption

The 2014-2015 fissure eruption in Holuhraun, Iceland, ejected large amounts of the aerosol precursor gas sulfur dioxide (SO_2) into the troposphere (Gettelman et al., 2015). When SO_2 is oxidized to sulfate (SO_4), the SO_4 particles can act as cloud condensation nuclei, increasing the cloud droplet number concentration. Satellite retrievals show that this resulted in smaller cloud droplets during the eruption, thus a first aerosol indirect effect as expected (McCoy & Hartmann, 2015; Malavelle et al., 2017). Second aerosol indirect effects were not observed since cloud amounts and liquid water path did not change significantly (Malavelle et al., 2017). Simulations by four global models, including CAM5.3-Oslo, replicated the effect on the sizes of the cloud droplets when modelling the eruption in the study of Malavelle et al. (2017), but they failed in modelling the second in-

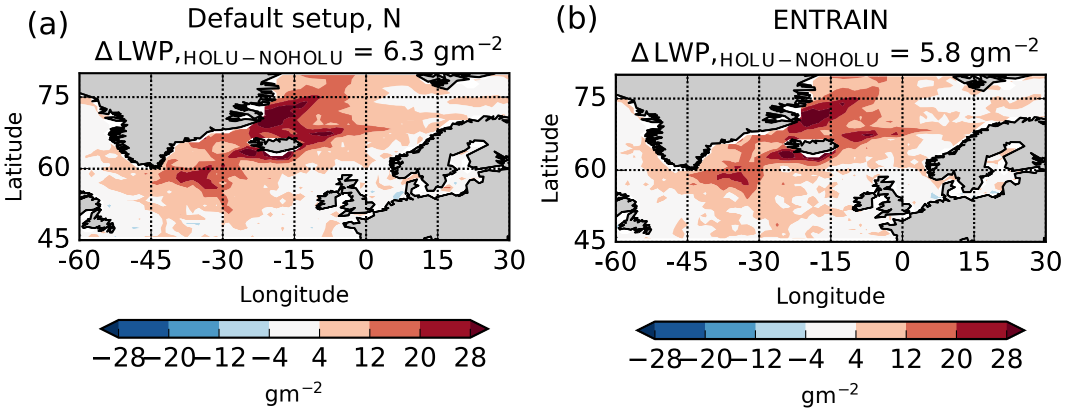

Figure 11. Change in LWP in October 2014 caused by the Holuhraun eruption in the default model setup, N **(a)**, and the setup ENTRAIN, including size-dependent entrainment **(b)**.

direct effect, reporting large increases in LWP that were not clearly observed by satellite. We want to check if adding size-dependency to the model code could make the models agree better with observations. Since size differences had a small impact on the different amounts of evaporated liquid between small and large droplets, we focus on implementing our size-dependent entrainment.

4.3.1 Including size-dependent entrainment

Two simulations were carried out with the default model setup, with and without the eruption. The simulations without the eruption (NOHOLU_N) starts on January 1st 2013, and last for two years. Concerning the nudging, the model-produced meteorology applied for the PD-PI aerosol indirect effect is replaced by meteorology from ERA-interim (Berrisford et al., 2009). The simulation including the eruption (HOLU_N) restarts from NOHOLU_N on January 1st, 2014, but include the emissions from the eruption from August 31, 2014, as described in Malavelle et al. (2017). Similar simulations are carried out, including size-dependent entrainment, resulting in the two cases HOLU_ENTRAIN and NOHOLU_ENTRAIN.

The resulting impact on the October 2014 changes in LWP are found in Fig. 11. While the change in LWP, averaged over the domain 44° N - 80° N, 60° W - 30° E, was 6.3 gm^{-2} (8.2 %) in the simulations with the default model setup, including size-dependent entrainment dampens the signal only slightly to 5.8 gm^{-2} (7.7 %). As for the PD-PI indirect effect, adding size-dependent entrainment described in Sect. 3.2 is not very efficient in dampening the LWP-response to aerosol perturbations, even though we are using the outer most recommended values for the tuning parameter a_2 to enhance the entrainment efficiency for the smaller droplets. Our implementation of size-dependent entrainment cannot alone make the simulated change in LWP correspond with the observed lack of positive change (Malavelle et al., 2017).

4.3.2 Including other processes

When it comes to simulating aerosol-cloud interactions, other weaknesses of global models, beside the lack of size-dependency, are already known. Since the impact of adding size-dependent entrainment could differ in more updated model versions due to these weaknesses, additional sensitivity experiments, using the Holuhraun eruption as a testbed, are carried out. One of the known weaknesses is the lack of indirect effects in clouds other than the stratiform clouds (Kirkevåg et al., 2018). Another is the too strong sensitivity of the autoconversion rate to cloud droplet number concentration (Quaas et al., 2009; M. Wang et al., 2012; Gettelman et al., 2013; Malavelle et al., 2017). We carry out three sets of simulations, with and without the eruption, modeling the impact adjustments of these weaknesses can have on the aerosol indirect forcing alone (SCONVAIE and AUTOLOW), and together combined with the inclusion of size-dependent entrainment (ENTRAIN_SCONVAIE_AUTOLOW). In the setup SCONVAIE, detrained droplets from shallow convection are not all set to 10 μm, as in the default model setup, but they differ in size based on the background aerosol number concentration. If the column integrated aerosol number concentration, N_a, is larger than $9{\cdot}10^{12}$ m^{-2}, the mean volume radius of the droplets, r_{vol} is set to 8 μm. If N_a is smaller than $3{\cdot}10^{12}$ m^{-2}, r_{vol} is set to 12 μm, while a linear relationship is applied for concentrations in between. The N_a-limits are chosen to optimize the effect of the size-dependency, without the need of increasing or decreasing the r_{vol}-limits to unrealistic values. When more clouds are susceptible to aerosol perturbations, it is likely that both the impact on the radiative forcing due to the eruption, and the effect of adding size-dependent entrainment is enhanced. In the setup AUTOLOW, we reduce the sensitivity of autoconversion rate to cloud droplet number concentration. Like many other models, CAM5.3-Oslo applies the autoconversion scheme of Khairoutdinov and Kogan (2000). This scheme is given by Eq. (9), where q_r and q_c are the mixing ratios of rain and cloud liquid water, E is a constant representing subgrid variability, k, α and β are constants and N_c is the cloud droplet number concentration.

$$\left(\frac{\partial q_r}{\partial t}\right)_{auto} = Ekq_c^{\alpha}N_c^{-\beta} \tag{9}$$

In the default scheme, k is 1350, α is 2.47 and β is 1.79. In the simulations with the setup AUTOLOW, α and β are changed to 1.67 and 0.67 respectively, based on a suggested relation between the two in the study of Feingold et al. (2013). k is tuned to $9.5{\cdot}10^{-2}$ so that the LWP in the simulation without the eruption is similar to the LWP in NOHOLU_N.

Allowing for indirect effects also for the detrained water from shallow convective clouds only increases the signal slightly from 6.3 gm^{-2} (8.2 %) in the default model setup to 6.7 gm^{-2} (8.8 %). Dampening the dependency on N_d and q_c on the autoconversion rate almost halves the signal to 3.6 gm^{-2} (4.6 %). The combination of all three cases, SCONVAIE_AUTOLOW_ENTRAIN, results in a change in LWP caused by the Holuhraun eruption of 2.9 gm^{-2} (3.8 %). Based on the individual cases, the large dampening from the default model setup is dominated by AUTOLOW, with a smaller contribution from size-dependent entrainment. Figures of the horizontal distribution of LWP changes caused by the eruption with the different setups are found in Fig. S4 in the supplementary information.

5 Summary and conclusions

We have explored different implementations of size-dependent evaporation and entrainment in the global atmospheric model CAM5.3-Oslo. The impacts on the total aerosol indirect effect and the second indirect effect, using the change in LWP caused by an aerosol perturbation as a measure, are studied. Our main findings are the following:

1. Size-dependent entrainment, implemented by varying a tuning parameter in the expression for the entrainment efficiency between its maximum recommended values, had a moderate impact on the PD-PI total aerosol indirect effect, with a dampening from -1.07 Wm^{-2} to -0.98 Wm^{-2}. The result was mostly caused by a reduction in the PD-PI change in LWP. (Sect. 4.2-4.2.2).

2. The same size-dependent entrainment reduced the LWP-response of the Holuhraun eruption slightly from +8.2 % to +7.8 %, much less than the impact of adding a suggested dampening of the dependency of cloud droplet number concentration to the autoconversion rate (+4.6%). (Sect. 4.3.1-4.3.2).
3. An additional size-dependent evaporation was also implemented, but the resulting change in the total aerosol indirect effect was caused by susceptibility changes due to enhanced evaporation rather than the size-dependency. (Sect. 4.1.3).
4. Scaling the additionally implemented evaporation by the surface area differences between the PI- and the PD-droplets gave too small differences between the eras to impact aerosol indirect effects. (Sect. 4.1.3).
5. Enhanced evaporation of small droplets only resulted in large impacts on LWP when either increasing the evaporation factor up to very large values, or allowing for mixing of moist air (q_v) between the cloudtop layer and the layer above. (Sect. 4.1.1).
6. When allowing for mixing between the layers, LWP increased in some areas as a response to enhanced evaporation. This increase in LWP was caused by enhanced shallow convection due to stability changes. We also show that the stability changes can have the opposite effect on LWP through altering EIS. (Sect. 4.1.2).

While previous studies have highlighted the lack of buffering effects when modelling aerosol-cloud interactions with global models as a big reason why models overestimate the LWP-response to aerosol perturbations (Stevens & Feingold, 2009; S. Wang et al., 2003; Malavelle et al., 2017; Zhou & Penner, 2017), our simulations show a more complex picture of the cloud response when including these mechanisms. When previous studies have mentioned the lack of processes that buffer cloud responses to aerosol perturbations, enhanced evaporation of smaller cloud droplets are associated with a reduction in cloud water. Our study highlight that the response in LWP is more complex due to competing effects acting in opposite directions. Even though enhanced evaporation at the top of the stratiform clouds reduces their liquid content and extent, the following response by shallow convective clouds can act in the opposite way due to reduced stability (reduced CIN). On the other hand, reduced stability (reduced EIS) in regions dominated by stratiform clouds captured under inversions are associated with reduced cloudiness. This could mean that global mean values of AIE_{PD-PI} and ΔLWP_{PD-PI} may be results of compensating effects in different regions, especially with buffering processes as clouds are more or less shallow convective of sensitive to EIS. These mechanisms may not be captured by regional LES or cloud resolving models, which usually do not cover large areas with different cloud regimes and may not capture the interaction between them, since the modeled domain usually is nested one way with large scale dynamics and boundary conditions from reanalysis data or a coarser model. Our results indicate some buffering by entrainment effects, but not comparable to the magnitude of the potential of dampening the response in LWP to aerosol perturbations through altering the autoconversion process. With the large amounts of various sensitivity simulations giving small impact on aerosol indirect effects, our study indicates that discrepancies between global model estimates of LWP responses to aerosol perturbations are dominated by overestimations in the dependency of autoconversion to cloud droplet number rather than the lack of size-dependency in the evaporation or the entrainment process.

Acknowledgments

I. H. H. K has been financed by the research council of Norway (RCN) through the project EVA and the NOTUR/Norstore projects (Sigma2 account: nn2345k; Norstore account: NS2345K). T. S. has been financed by the European Research Council (ERC), Grant StG 758005. The National Center for Atmospheric Research (where A. G. works) is sponsored by the U.S. National Science Foundation. Output from the simulations are available here: `https://archive.sigma2.no/pages/public/datasetDetail.jsf?id=10.11582/2019`

.00022. Please follow the instructions in this link: `https://wiki.met.no/noresm/start` to obtain the source code for CAM5.3-Oslo.

References

Abdul-Razzak, H., & Ghan, S. J. (2000). A parameterization of aerosol activation 2. Multiple aerosol types. *Journal of Geophysical Research Atmospheres*, *105*(D5), 6837–6844. doi: 10.1029/1999JD901161

Ackerman, A. S., Kirkpatrick, M. P., Stevens, D. E., & Toon, O. B. (2004). The impact of humidity above stratiform clouds on indirect aerosol climate forcing. *Nature*, *432*(7020), 1014–1017. doi: 10.1038/nature03137.1.

Albrecht, B. A. (1989). Aerosols, cloud microphysics, and fractional cloudiness. *Science*, *245*(4923), 1227–1230. doi: 10.1126/science.245.4923.1227

Altaratz, O., Koren, I., Reisin, T., Kostinski, A., Feingold, G., Levin, Z., & Yin, Y. (2008). Aerosols' influence on the interplay between condensation, evaporation and rain in warm cumulus cloud. *Atmospheric Chemistry and Physics*, *8*(1), 15–24. doi: 10.5194/acp-8-15-2008

Alterskjær, K., Kristjánsson, J. E., & Seland, O. (2012). Sensitivity to deliberate sea salt seeding of marine clouds - Observations and model simulations. *Atmospheric Chemistry and Physics*, *12*(5), 2795–2807. doi: 10.5194/acp-12-2795-2012

Baker, M. B., Corbin, R. G., & Latham, J. (1980). The influence of entrainment on the evolution of cloud droplet spectra: I. A model of inhomogeneous mixing. *Quarterly Journal of the Royal Meteorological Society*, *106*(449), 581–598. doi: 10.1002/qj.49710644914

Bellouin, N., Quaas, J., Morcrette, J. J., & Boucher, O. (2013). Estimates of aerosol radiative forcing from the MACC re-analysis. *Atmospheric Chemistry and Physics*, *13*(4), 2045–2062. doi: 10.5194/acp-13-2045-2013

Bentsen, M., Bethke, I., Debernard, J. B., Iversen, T., Kirkevåg, A., Seland, Ø., ... Kristjánsson, J. E. (2013). The Norwegian Earth System Model, NorESM1-M Part 1: Description and basic evaluation of the physical climate. *Geoscientific Model Development*, *6*(3), 687–720. doi: 10.5194/gmd-6-687-2013

Berrisford, P., Dee, D., Poli, P., Brugge, R., Fielding, K., Fuentes, M., ... Simmons, A. (2009). The ERA-Interim Archive Version 2.0. *ERA report series*, *1*(1), 1–16.

Boucher, O., Randall, D., Artaxo, P., Bretherton, C., Feingold, G., Forster, P., ... Zhang, X. (2013). Clouds and aerosols. In T. Stocker et al. (Eds.), *Climate change 2013 the physical science basis: Working group i contribution to the fifth assessment report of the intergovernmental panel on climate change* (Vol. 9781107057, pp. 571–658). Cambridge, United Kingdom and New York, NY, USA.: Cambridge University Press. doi: 10.1017/CBO9781107415324.016

Bréon, F. M., Tanré, D., & Generoso, S. (2002). Aerosol effect on cloud droplet size monitored from satellite. *Science*, *295*(5556), 834–838. doi: 10.1126/science.1066434

Bretherton, C. S., Blossey, P. N., & Uchida, J. (2007). Cloud droplet sedimentation, entrainment efficiency, and subtropical stratocumulus albedo. *Geophysical Research Letters*, *34*(3). doi: 10.1029/2006GL027648

Bretherton, C. S., & Park, S. (2009). A new moist turbulence parameterization in the community atmosphere model. *Journal of Climate*, *22*(12), 3422–3448. doi: 10.1175/2008JCLI2556.1

Caldwell, P., Bretherton, C. S., & Wood, R. (2005). Mixed-layer budget analysis of the diurnal cycle of entrainment in southeast Pacific stratocumulus. *Journal of the Atmospheric Sciences*, *62*(10), 3775–3791. doi: 10.1175/JAS3561.1

Chen, Y. C., Christensen, M. W., Stephens, G. L., & Seinfeld, J. H. (2014). Satellite-based estimate of global aerosol-cloud radiative forcing by marine warm clouds. *Nature Geoscience*, *7*(9), 643–646. doi: 10.1038/ngeo2214

Feingold, G., Eberhard, W. L., Veron, D. E., & Previdi, M. (2003). First measurements of the Twomey indirect effect using ground-based remote sensors. *Geophysical Research Letters*, *30*(6). doi: 10.1029/2002GL016633

Feingold, G., Jiang, H., Xue, H., Teller, A., & Levin, Z. (2006). Aerosol effects on the lifetime of shallow cumulus. *12th Conference on Cloud Physics, and 12th Conference on Atmospheric Radiation*, *33*(February), 2–5. doi: 10.1029/2006GL026024

Feingold, G., McComiskey, A., Rosenfeld, D., & Sorooshian, A. (2013). On the relationship between cloud contact time and precipitation susceptibility to aerosol. *Journal of Geophysical Research Atmospheres*, *118*(18), 10544–10554. doi: 10.1002/jgrd.50819

Freud, E., Rosenfeld, D., & Kulkarni, J. R. (2011). Resolving both entrainment-mixing and number of activated CCN in deep convective clouds. *Atmospheric Chemistry and Physics*, *11*(24), 12887–12890. doi: 10.5194/acp-11-12887-2011

Gettelman, A. (2015). Putting the clouds back in aerosol-cloud interactions. *Atmospheric Chemistry and Physics*, *15*(21), 12397–12411. doi: 10.5194/acp-15-12397-2015

Gettelman, A., Morrison, H., & Ghan, S. J. (2008). A new two-moment bulk stratiform cloud microphysics scheme in the community atmosphere model, version 3 (CAM3). Part II: Single-column and global results. *Journal of Climate*, *21*(15), 3660–3679. doi: 10.1175/2008JCLI2116.1

Gettelman, A., Morrison, H., Terai, C. R., & Wood, R. (2013). Microphysical process rates and global aerosol-cloud interactions. *Atmospheric Chemistry and Physics*, *13*(19), 9855–9867. doi: 10.5194/acp-13-9855-2013

Gettelman, A., Schmidt, A., & Kristjánsson, J. E. (2015). Icelandic volcanic emissions and climate. *Nature Geoscience*, *8*(4), 243. doi: 10.1038/ngeo2376

Ghan, S. (2013). Technical note: Estimating aerosol effects on cloud radiative forcing. *Atmospheric Chemistry and Physics*, *13*(19), 9971–9974. doi: 10.5194/acp-13-9971-2013

Ghan, S., Wang, M., Zhang, S., Ferrachat, S., Gettelman, A., Griesfeller, J., ... Zhang, K. (2016). Erratum: Challenges in constraining anthropogenic aerosol effects on cloud radiative forcing using present-day spatiotemporal variability (Proceedings of the National Academy of Sciences of the United States of America (2016) 113 (5804-5811)). *Proceedings of the National Academy of Sciences of the United States of America*, *113*(21), E3049. doi: 10.1073/pnas.1604888113

Gryspeerdt, E., Goren, T., Sourdeval, O., Quaas, J., Mülmenstädt, J., Dipu, S., ... Christensen, M. (2019). Constraining the aerosol influence on cloud liquid water path. *Atmospheric Chemistry and Physics*, *19*(8), 5331–5347. doi: 10.5194/acp-19-5331-2019

Hill, A. A., Feingold, G., & Jiang, H. (2009). The influence of entrainment and mixing assumption on aerosol-cloud interactions in marine stratocumulus. *Journal of the Atmospheric Sciences*, *66*(5), 1450–1464. doi: 10.1175/2008JAS2909.1

Iversen, T., Bentsen, M., Bethke, I., Debernard, J. B., Kirkevåg, A., Seland, Ø., ... Seierstad, I. A. (2013). The Norwegian Earth System Model, NorESM1-M Part 2: Climate response and scenario projections. *Geoscientific Model Development*, *6*(2), 389–415. doi: 10.5194/gmd-6-389-2013

Jiang, H., & Feingold, G. (2006). Effect of aerosol on warm convective clouds: Aerosol-cloud surface flux feedbacks in a new coupled large eddy model. *Journal of Geophysical Research Atmospheres*, *111*(1), 1–12. doi: 10.1029/2005JD006138

Karset, I. H. H., Koren Berntsen, T., Storelvmo, T., Alterskjær, K., Grini, A., Olivié, D., ... Schulz, M. (2018). Strong impacts on aerosol indirect effects from historical oxidant changes. *Atmospheric Chemistry and Physics*, *18*(10), 7669–7690. doi: 10.5194/acp-18-7669-2018

Khairoutdinov, M., & Kogan, Y. (2000). A new cloud physics parameterization in a large-eddy simulation model of marine stratocumulus. *Monthly Weather Review*, *128*(1), 229–243. doi: 10.1175/1520-0493(2000)128⟨0229:ANCPPI⟩2.0.CO;2

Kirkevåg, A., Grini, A., Olivié, D., Seland, Ø., Alterskjær, K., Hummel, M., ... Iversen, T. (2018). A production-tagged aerosol module for earth system models, OsloAero5.3-extensions and updates for CAM5.3-Oslo. *Geoscientific Model Development*, *11*(10), 3945–3982. doi: 10.5194/gmd-11-3945-2018

Kirkevåg, A., Iversen, T., Seland, Ø., Hoose, C., Kristjánsson, J. E., Struthers, H., ... Schulz, M. (2013). Aerosolclimate interactions in the Norwegian Earth System Model NorESM1-M. *Geoscientific Model Development*, *6*(1), 207–244. doi: 10.5194/gmd-6-207-2013

Kooperman, G. J., Pritchard, M. S., Ghan, S. J., Wang, M., Somerville, R. C., & Russell, L. M. (2012). Constraining the influence of natural variability to improve estimates of global aerosol indirect effects in a nudged version of the Community Atmosphere Model 5. *Journal of Geophysical Research Atmospheres*, *117*(23). doi: 10.1029/2012JD018588

Korolev, A., Khain, A., Pinsky, M., & French, J. (2015). Theoretical study of mixing in liquid clouds - Part 1: Classical concept. *Atmospheric Chemistry and Physics Discussions*, *15*(21), 30211–30267. doi: 10.5194/acpd-15-30211-2015

Lamarque, J. F., Bond, T. C., Eyring, V., Granier, C., Heil, A., Klimont, Z., ... Van Vuuren, D. P. (2010). Historical (1850-2000) gridded anthropogenic and biomass burning emissions of reactive gases and aerosols: Methodology and application. *Atmospheric Chemistry and Physics*, *10*(15), 7017–7039. doi: 10.5194/acp-10-7017-2010

Latham, J., & Reed, R. L. (1977). Laboratory studies of the effects of mixing on the evolution of cloud droplet spectra. *Quarterly Journal of the Royal Meteorological Society*, *103*(436), 297–306. doi: 10.1002/qj.49710343607

Lebsock, M. D., Stephens, G. L., & Kummerow, C. (2008). Multisensor satellite observations of aerosol effects on warm clouds. *Journal of Geophysical Research Atmospheres*, *113*(15), 1–12. doi: 10.1029/2008JD009876

Lehmann, K., Siebert, H., & Shaw, R. A. (2009). Homogeneous and inhomogeneous mixing in cumulus clouds: Dependence on local turbulence structure. *Journal of the Atmospheric Sciences*, *66*(12), 3641–3659. doi: 10.1175/2009JAS3012.1

Liang, L., Di Girolamo, L., & Sun, W. (2015). Bias in MODIS cloud drop effective radius for oceanic water clouds as deduced from optical thickness variability across scattering angles. *Journal of Geophysical Research*, *120*(15), 7661–7681. doi: 10.1002/2015JD023256

Liu, X., Ma, P. L., Wang, H., Tilmes, S., Singh, B., Easter, R. C., ... Rasch, P. J. (2016). Description and evaluation of a new four-mode version of the Modal Aerosol Module (MAM4) within version 5.3 of the Community Atmosphere Model. *Geoscientific Model Development*, *9*(2), 505–522. doi: 10.5194/gmd-9-505-2016

Malavelle, F. F., Haywood, J. M., Jones, A., Gettelman, A., Clarisse, L., Bauduin, S., ... Thordarson, T. (2017). Strong constraints on aerosol-cloud interactions from volcanic eruptions. *Nature*, *546*(7659), 485–491. doi: 10.1038/nature22974

McCoy, D. T., Bender, F. A., Mohrmann, J. K., Hartmann, D. L., Wood, R., & Grosvenor, D. P. (2017). The global aerosol-cloud first indirect effect estimated using MODIS, MERRA, and AeroCom. *Journal of Geophysical Research*, *122*(3), 1779–1796. doi: 10.1002/2016JD026141

McCoy, D. T., Field, P. R., Schmidt, A., Grosvenor, D. P., Bender, F. A., Shipway, B. J., ... Elsaesser, G. S. (2018). Aerosol midlatitude cyclone indirect effects in observations and high-resolution simulations. *Atmospheric Chemistry and Physics*, *18*(8), 5821–5846. doi: 10.5194/acp-18-5821-2018

McCoy, D. T., & Hartmann, D. L. (2015). Observations of a substantial cloud-aerosol indirect effect during the 2014-2015 Bár arbunga-Vei IVötn fissure eruption in Iceland. *Geophysical Research Letters*, *42*(23), 10409–10414. doi: 10.1002/2015GL067070

Morrison, H., & Gettelman, A. (2008). A new two-moment bulk stratiform cloud microphysics scheme in the community atmosphere model, version 3 (CAM3). Part I: Description and numerical tests. *Journal of Climate*, *21*(15), 3642–3659. doi: 10.1175/2008JCLI2105.1

Myhre, G., Shindell, D., Br{\'{e}}on, F.-M., Collins, W., Fuglestvedt, J., Huang, J., … Zhang, H. (2013). Anthropogenic and Natural Radiative Forcing. In T. Stocker et al. (Eds.), *Climate change 2013: The physical science basis. contribution of working group i to the fifth assessment report of the intergovernmental panel on climate change* (pp. 657–740). Cambridge University Press. doi: 10.1017/CBO9781107415324.018

Neale, R. B., Chen, C.-C., Gettelman, A., Lauritzen, P. H., Park, S., Williamson, D. L., … Taylor, M. A. (2012). *CAM5 Description.*

Nicholls, S., & Turton, J. D. (1986). An observational study of the structure of stratiform cloud sheets: Part II. Entrainment. *Quarterly Journal of the Royal Meteorological Society*, *112*(472), 461–480. doi: 10.1002/qj.49711247210

Oleson, K. W., Lawrence, D. M., Bonan, G. B., Drewniak, B., Huang, M., Koven, C. D., … Yang, Z.-L. (2013). *Technical Description of version 4.5 of the Community Land Model (CLM).*

Painemal, D., & Zuidema, P. (2011). Assessment of MODIS cloud effective radius and optical thickness retrievals over the Southeast Pacific with VOCALS-REx in situ measurements. *Journal of Geophysical Research Atmospheres*, *116*(24), 1–16. doi: 10.1029/2011JD016155

Park, S., & Bretherton, C. S. (2009). The University of Washington shallow convection and moist turbulence schemes and their impact on climate simulations with the community atmosphere model. *Journal of Climate*, *22*(12), 3449–3469. doi: 10.1175/2008JCLI2557.1

Park, S., Bretherton, C. S., & Rasch, P. J. (2014). Integrating cloud processes in the Community Atmosphere Model, version 5. *Journal of Climate*, *27*(18), 6821–6856. doi: 10.1175/JCLI-D-14-00087.1

Pincus, R., & Baker, M. B. (1994). Effect of precipitation on the albedo susceptibility of clouds in the marine boundary layer. *Nature*, *372*(6503), 250–252. doi: 10.1038/372250a0

Pinsky, M., Khain, A., Korolev, A., & Magaritz-Ronen, L. (2015). Theoretical investigation of mixing in warm clouds - Part 2: Homogeneous mixing. *Atmospheric Chemistry and Physics Discussions*, *15*(21), 30269–30320. doi: 10.5194/acpd-15-30269-2015

Quaas, J., Boucher, O., Bellouin, N., & Kinne, S. (2008). Satellite-based estimate of the direct and indirect aerosol climate forcing. *Journal of Geophysical Research Atmospheres*, *113*(5), 1–9. doi: 10.1029/2007JD008962

Quaas, J., Ming, Y., Menon, S., Takemura, T., Wang, M., Penner, J. E., … Schulz, M. (2009). Aerosol indirect effects ” general circulation model intercomparison and evaluation with satellite data. *Atmospheric Chemistry and Physics*, *9*(22), 8697–8717. doi: 10.5194/acp-9-8697-2009

Rausch, J., Meyer, K., Bennartz, R., & Platnick, S. (2017). Differences in liquid cloud droplet effective radius & number concentration estimates between MODIS collections 5.1 & 6 over global oceans. *Atmospheric Measurement Techniques*, *10*(6), 2105–2116. doi: 10.5194/amt-10-2105-2017

Small, J. D., Chuang, P. Y., Feingold, G., & Jiang, H. (2009). Can aerosol decrease cloud lifetime? *Geophysical Research Letters*, *36*(16), 1–5. doi: 10.1029/

2009GL038888

Squires, P. (1952a). The growth of cloud drops by condensation. I. General characteristics. *Australian Journal of Chemistry*, *5*(1), 59–86. doi: 10.1071/CH9520059

Squires, P. (1952b). The growth of cloud drops by condensation. I. General characteristics. *Australian Journal of Chemistry*, *5*(1), 59–86. doi: 10.1071/CH9520059

Stevens, B., & Feingold, G. (2009). Untangling aerosol effects on clouds and precipitation in a buffered system. *Nature*, *461*(7264), 607–613. doi: 10.1038/nature08281

Toll, V., Christensen, M., Gassó, S., & Bellouin, N. (2017). Volcano and Ship Tracks Indicate Excessive Aerosol-Induced Cloud Water Increases in a Climate Model. *Geophysical Research Letters*, *44*(24), 12,492–12,500. doi: 10.1002/2017GL075280

Toll, V., Christensen, M., Quaas, J., & Bellouin, N. (2019). Weak average liquid-cloud-water response to anthropogenic aerosols. *Nature*, *572*(7767), 51–55. doi: 10.1038/s41586-019-1423-9

Twomey, S. (1977). The Influence of Pollution on the Shortwave Albedo of Clouds. *Journal of the Atmospheric Sciences*, *34*(7), 1149–1152. doi: 10.1175/1520-0469(1977)034⟨1149:tiopot⟩2.0.co;2

Walters, D. N., Williams, K. D., Boutle, I. A., Bushell, A. C., Edwards, J. M., Field, P. R., … Vidale, P. L. (2014). The Met Office Unified Model Global Atmosphere 4.0 and JULES Global Land 4.0 configurations. *Geoscientific Model Development*, *7*(1), 361–386. doi: 10.5194/gmd-7-361-2014

Wang, M., Ghan, S., Liu, X., L'Ecuyer, T. S., Zhang, K., Morrison, H., … Penner, J. E. (2012). Constraining cloud lifetime effects of aerosols using A-Train satellite observations. *Geophysical Research Letters*, *39*(15), 3–9. doi: 10.1029/2012GL052204

Wang, S., Wang, Q., & Feingold, G. (2003). Turbulence, condensation, and liquid water transport in numerically simulated nonprecipitating stratocumulus clouds. *Journal of the Atmospheric Sciences*, *60*(2), 262–278. doi: 10.1175/1520-0469(2003)060⟨0262:TCALWT⟩2.0.CO;2

Wood, R., & Bretherton, C. S. (2006). On the relationship between stratiform low cloud cover and lower-tropospheric stability. *Journal of Climate*, *19*(24), 6425–6432. doi: 10.1175/JCLI3988.1

Xue, H., & Feingold, G. (2006). Large-eddy simulations of trade wind cumuli: Investigation of aerosol indirect effects. *Journal of the Atmospheric Sciences*, *63*(6), 1605–1622. doi: 10.1175/JAS3706.1

Xue, H., Feingold, G., & Stevens, B. (2008). Aerosol effects on clouds, precipitation, and the organization of shallow cumulus convection. *Journal of the Atmospheric Sciences*, *65*(2), 392–406. doi: 10.1175/2007JAS2428.1

Zhang, G. J., & McFarlane, N. A. (1995). Sensitivity of climate simulations to the parameterization of cumulus convection in the canadian climate centre general circulation model. *Atmosphere - Ocean*, *33*(3), 407–446. doi: 10.1080/07055900.1995.9649539

Zhang, K., O'Donnell, D., Kazil, J., Stier, P., Kinne, S., Lohmann, U., … Feichter, J. (2012). The global aerosol-climate model ECHAM-HAM, version 2: Sensitivity to improvements in process representations. *Atmospheric Chemistry and Physics*, *12*(19), 8911–8949. doi: 10.5194/acp-12-8911-2012

Zhang, K., Wan, H., Liu, X., Ghan, S. J., Kooperman, G. J., Ma, P. L., … Lohmann, U. (2014). Technical note: On the use of nudging for aerosol-climate model intercomparison studies. *Atmospheric Chemistry and Physics*, *14*(16), 8631–8645. doi: 10.5194/acp-14-8631-2014

Zhou, C., & Penner, J. E. (2017). Why do general circulation models overestimate the aerosol cloud lifetime effect? A case study comparing CAM5 and a CRM. *Atmospheric Chemistry and Physics*, *17*(1), 21–29. doi: 10.5194/acp-17-21-2017

JOURNAL OF GEOPHYSICAL RESEARCH

Supporting Information for "Exploring impacts of size-dependent evaporation and entrainment in a global model"

I. H. H. Karset[1], A. Gettelman[2], T. Storelvmo[1], K. Alterskjær[3], T. K. Berntsen[1,3]

[1]University of Oslo, Department of Geosciences, Section for Meteorology and Oceanography, Oslo, Norway

[2]National Center for Atmospheric Research, Colorado, USA

[3]CICERO Center for International Climate Research, Oslo, Norway

Contents of this file

1. Derivation of the change in phase relaxation time, τ, when a clean cloud (r_1, N_1) is perturbed to a polluted cloud (r_2, N_2).
2. Figure S1, S2, S3 and S4

Introduction This file contain supporting information to the manuscript ”Exploring impacts of size-dependent evaporation and entrainment in a global model”.

Derivation of Eq. (1) in the main paper

$$\begin{aligned}
M_{c,1} &= M_{c,2} \\
\frac{N_1 \rho_L \pi r_1^3}{3} &= \frac{N_2 \rho_L \pi r_2^3}{3} \\
N_1 r_1^3 &= N_2 r_2^3 \\
(N_1 r_1)\, r_1^2 &= (N_2 r_2)\, r_2^2
\end{aligned}$$

Since $r_1 > r_2$, we have that $r_1^2 > r_2^2$. For the above to be equal on both sides, we have that

$$(N_1 r_1) < (N_2 r_2)$$

Resulting in a reduction in the phase relaxation time since

$$\begin{aligned}
\frac{1}{N_1 r_1} &> \frac{1}{N_2 r_2} \\
\tau_1 &> \tau_2
\end{aligned}$$

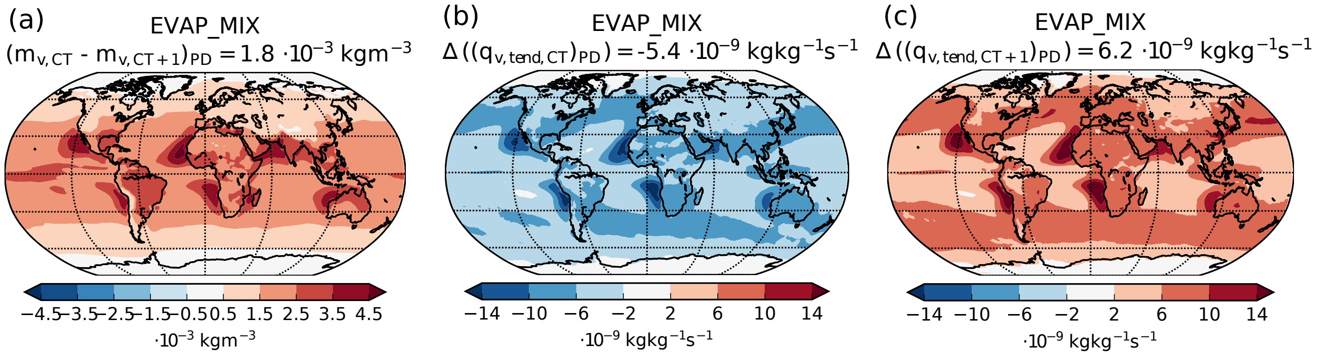

Figure S1. **(a)** Difference in mass of water vapor, m_v between the cloudtop layer and the layer above. Positive values means drier air aloft. The global mean absolute difference between the layers correspond to a relative difference of 32 %. **(b-c)** Changes in tendency of water vapor in the cloudtop layer and the layer above due to our implemented evaporation and mixing. Positive values means that more water vapor comes into the layer due to our changes. All values are taken from the PD-simulation using the setup EVAP_MIX. The tendencies are written out by the model right before andre right after our code changes, resulting in the Δq_v-values.

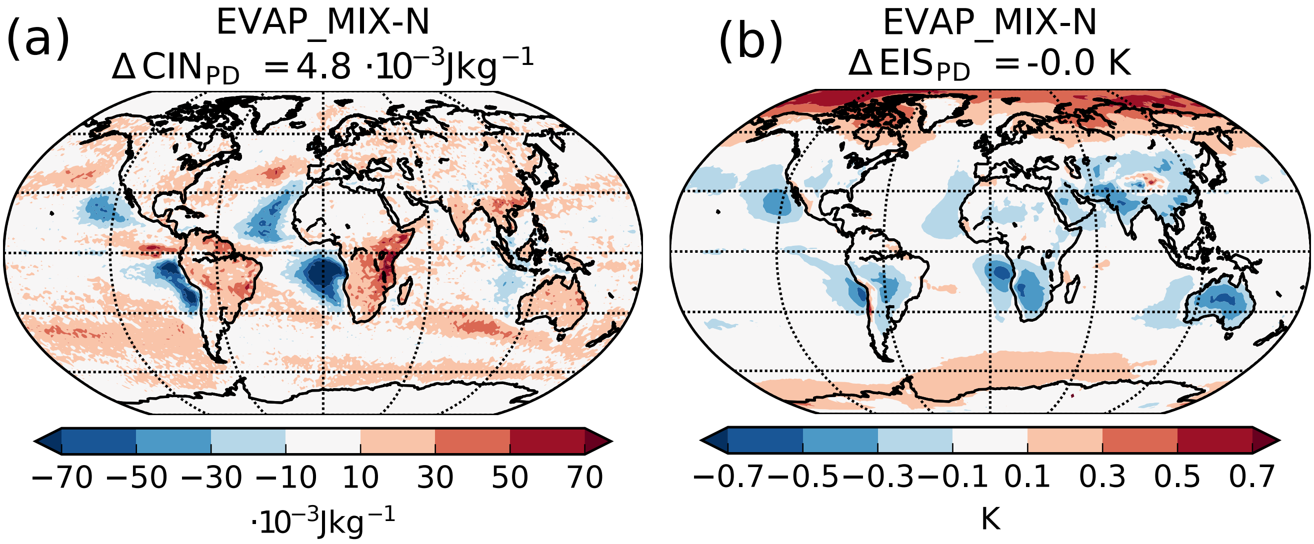

Figure S2. Changes in **(a)** convective inhibition (CIN) and **(b)** estimated inversion strength (EIS) when switching from the default model setup, N, to EVAP_MIX, where evaporation is enhanced for the smaller droplets and vertical mixing between the cloud top layer and the layer above is allowed.

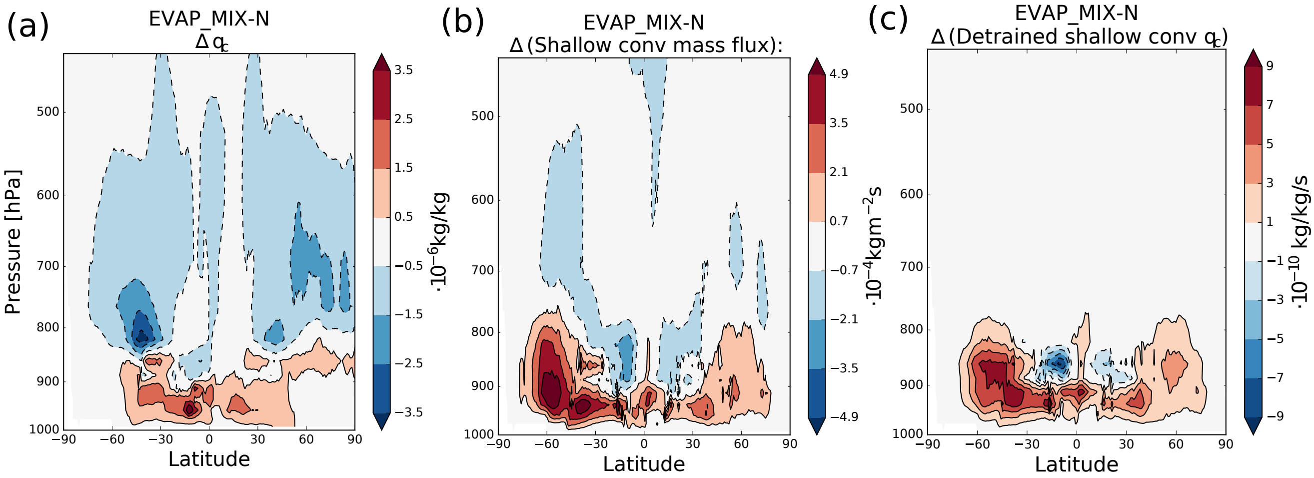

Figure S3. Changes in zonal mean mass mixing ratio of liquid cloud water, q_c **(a)**, shallow convective mass flux **(b)** and detrained q_c from shallow convection **(c)** when switching from the default model setup, N, to EVAP_MIX, where evaporation is enhanced for the smaller droplets and vertical mixing between the cloudtop layer and the layer above is allowed.

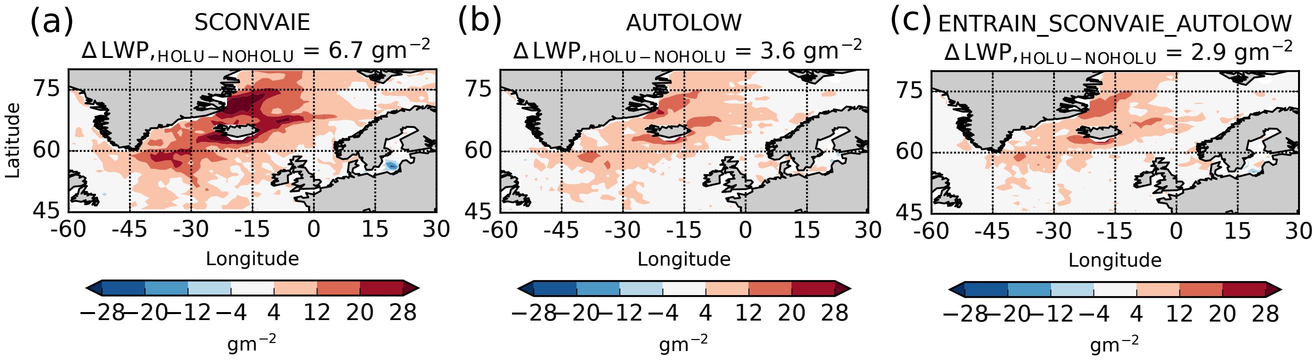

Figure S4. Change in LWP in October 2014 caused by the Holuhraun eruption in the setups **(a)** SCONVAIE, including size-dependency on the detrained cloud droplets from shallow convective clouds, **(b)** AUTOLOW, with dampened dependency on N_d and q_c on the autoconversion rate, and **(c)** a combination of SCONVAIE, AUTOLOW and ENTRAIN, where also size-dependent entrainment is included.